



# Landmine Detection Algorithm Design Based on Data Fusion Technology

---

Thesis submitted for the degree of  
Doctor of Philosophy

Hongyuan Jing (M.Sc.)  
Department of Engineering  
University of Leicester

September 2018

## Abstract

This research has focused on close-in landmine detection, which aims to identify landmines in a particular landmine area. Close-range landmine detection requires both sub-surface sensors, such as metal detectors and ground penetrating radar (GPR), and surface sensors, such as optical cameras.

A new multi-focus image fusion algorithm is proposed which outperforms the existing intensity-hue-saturation (IHS) and principle components analysis (PCA) algorithms on both visual and fusion parameter analysis. In addition, the proposed algorithm can save 30.9% running time than the IHS algorithm, which is the same level as the existing PCA algorithm.

A novel single GPR sensor landmine detection algorithm entropy-based region selecting algorithm is proposed which uses the entropy value of the region as the feature and continuous layers instead of a hard threshold. Two A-scan based statistics algorithms and a GPR signal oscillation feature based detection algorithm are also proposed. The results show that the proposed entropy-based algorithm outperforms the existing region selection algorithm on both detection accuracy and running time. The proposed statistics algorithms and GPR feature-based algorithm outperform the edge histogram descriptor and edge energy algorithms on both detection accuracy range, running time and memory usage. In addition, the GPR feature-based algorithm can reduce the false alarm rate (FAR) by 22% for all targets at 90% probability of detection.

With regards to data fusion system design, this research overcomes the limitations of the existing Bayesian fusion approach. A new Kalman-Bayes based fusion system is developed which reduces the system uncertainty and improves the fusion process. The experimental results have shown that the proposed Kalman-Bayes fusion system and enhanced fuzzy fusion system can reach 7.8% FAR at 91.1% detection rate and 6.30% FAR at 92.4% detection rate, correspondingly, outperforming the existing Bayes and fuzzy fusion systems in terms of detection ability.

## **Acknowledgements**

Firstly, I would like to express my sincere appreciation to my supervisor Professor Tanya Vladimirova for giving me the chance to work in her friendly research team and for all her excellent guidance, advice and supervision.

I would like to thank my second supervisor Dr David R. Siddle for his kind advice and support. I am extremely grateful to Dr Xiaojun Zhai and Dr Danothy Bennett for their insightful advice on my project and warm encouragement in my life.

I would like to thank the D-Box project for sponsoring me to complete this landmine detection work. Special thanks to Stewart Grainger and Franco Curatella for helping and teaching me to understand what a real landmine area looks like. I also would like to thank Yann Yvinec and Jon Dittmer for giving me access to the MsMs dataset. Thanks to Dr Fayyaz Muhammad, Ian Griffiths, Dr Muhammad Ziya Komsul and Dr Irfan F. Mir as well as everyone in the embedded research group.

Thanks go to my family for their unwavering encouragement and unconditional love.

Finally, thanks to Enjie for her support, love and company during these last four years.

September 2018, Leicester

# Table of Contents

Abstract .....	i
Acknowledgements .....	ii
Table of Contents .....	iii
List of Figures .....	viii
List of Tables.....	xiv
Abbreviations .....	xv
Chapter 1: Introduction .....	1
1.1 Background .....	1
1.2 Research Aims .....	3
1.3 Problems and Challenges .....	4
1.3.1 Limitations of Landmine Detection Sensors.....	4
1.3.2 Challenges of the Landmine Area Clearing Process.....	6
1.3.3 Challenges of Data Fusion System Design for Landmine Detection.....	7
1.4 Novel Contributions .....	8
1.5 Structure of the Thesis .....	11
1.6 Related Publications.....	12
Chapter 2: Literature Survey .....	14
2.1 Data Fusion Technology .....	14
2.2 Current Landmine Detection Technology.....	18

2.2.1 Landmine Detection Systems Review .....	18
2.2.2 Landmine Detection Sensor Review .....	22
2.2.3 Landmine Detection Related Projects .....	28
2.2.4 Landmine Detection Algorithms Review .....	35
2.3 Image Fusion Technology .....	41
2.3.1 General Principle of Image Fusion .....	41
2.3.2 Image Fusion Algorithms .....	44
2.4 Summary .....	49
Chapter 3: Design of a Pixel-based Multi-Focus Image Fusion Algorithm .....	50
3.1 Introduction .....	50
3.2 Multi-focus Image Fusion Algorithm Design .....	52
3.3 Simulation Results and Analysis .....	58
3.3.1 Visual Analysis .....	59
3.3.2 Computational Complexity Evaluation .....	74
3.3.3 Quantitative Performance Evaluation .....	78
3.4 Summary .....	82
Chapter 4: Design of Landmine Detection Algorithms for a Single Sensor .....	84
4.1 Landmine Detection Definitions .....	84
4.2 GPR Sensor Test Data .....	88
4.2.1 GPR Data from the Naples Outdoor Simulated Landmine Area .....	89
4.2.2 GPR Data from an Indoor Simulated Landmine Area .....	93

4.3 Landmine Detection Algorithm Design .....	96
4.3.1 Entropy-based Algorithm.....	97
4.3.2 Statistics-based Algorithm .....	105
4.3.3 GPR Array Feature-based Algorithm.....	112
4.4 Evaluation of the Algorithms .....	117
4.4.1 ROC Curve Analysis.....	117
4.4.2 Detection Accuracy Range Analysis.....	121
4.4.3 Operation Time Analysis .....	124
4.4.4 Memory Usage Analysis .....	125
4.5 Summary .....	130
Chapter 5: Data Fusion System Design for Landmine Detection .....	132
5.1 D-Box System and Data Resources .....	132
5.1.1 D-Box System Design.....	133
5.1.2 Robot Arm Data Re-build .....	136
5.1.3 Metal Detector Image Simulation .....	140
5.1.4 GPR Image Analysis .....	142
5.2 Fusion System Design.....	143
5.2.1 Kalman-Bayes Fusion System Design .....	144
5.2.2 Dempster-Schafer Theory-Based System Design.....	155
5.2.3 Fuzzy Logic Data Fusion System Design .....	160
5.3 ROC Analysis.....	171

5.4 Summary .....	173
Chapter 6: Case Study - Multi-Sensor Data Fusion using the MsMs Dataset .....	176
6.1 Overview of the MsMs Project .....	176
6.2 Sensor Data Analysis .....	180
6.2.1 MD Sensor Data Analysis .....	180
6.2.2 GPR Sensor Data Analysis.....	187
6.3 Evaluation Results.....	193
6.4 Summary .....	196
Chapter 7: Conclusions and Future Work .....	198
7.1 Research Summary.....	198
7.2 Novel Contributions .....	200
7.3 Future Work .....	202
Appendices.....	204
Appendix A: Surface Landmine Detection Algorithm .....	204
Appendix B: General GPR Analysis.....	207
Appendix C: TIR Image Analysis.....	208
Appendix D: Metal Detector Image Re-build.....	212
Appendix E: Re-built GPR Image.....	215
Appendix F: GPS Location Analysis .....	218
Appendix G: Computational Complexity of Single-Sensor Detection Algorithms .....	220
Appendix H: Simulation of the IR Camera Image.....	224

Appendix I: The Metal Detector Data Analysis.....	224
Appendix J: Data Fusion Models Review.....	225
Appendix K: MsMs Landmine Detection Sensor Analysis .....	233
References.....	236

## List of Figures

Figure 2-1. Types of data fusion [27].....	15
Figure 2-2. Landmine detection system architecture [35]. .....	19
Figure 2-3. Vehicle-mounted tele-operated mine detection system architecture [48]. .....	21
Figure 2-4. LIBS working structure [14]. .....	23
Figure 2-5. Scheme (a) and photography of a portable nitrogen dioxide sensor (b) [17]. .....	25
Figure 2-6. The AN/PSS-14 hand-held landmine detection sensor [42]. .....	25
Figure 2-7. GPR array from the Wrocott research group [43].....	26
Figure 2-8. Foerster Minex 2FD 4.500 hand-held MD equipment [44]. .....	27
Figure 2-9. Cross-track and down-track 3D GPR images.....	28
Figure 2-10. ATR function description of the ARC project[49].....	31
Figure 2-11. Flowchart of the edge-energy-based landmine detection algorithm. ....	38
Figure 2-12. Application of multi-sensor data fusion [32]. .....	43
Figure 2-13. Wavelet representation and a tour representation [45].....	48
Figure 3-1. Flowchart of the new proposed PCA-based multi-focus image fusion algorithm. ....	53
Figure 3-2. Multi-focus image fusion matrix. ....	55
Figure 3-3. Confidence level of neighbour pixels for a normal case in the fusion result. .....	57

Figure 3-4. Multi-focus image fusion results. ....	63
Figure 3-5. Multi-focus image fusion result. ....	66
Figure 3-6. Multi-focus image fusion result. ....	68
Figure 3-7. Multi-focus image fusion results. ....	70
Figure 3-8. Change track for multi-focus image fusion. ....	73
Figure 4-1. ROC curve of the landmine detection process. ....	88
Figure 4-2. UAV image and the position of the landmine targets in the Naples simulated desert landmine area. ....	91
Figure 4-3. Outdoor environment ground truth map-building process. ....	92
Figure 4-4. Ground truth map of the Naples simulated landmine area. ....	93
Figure 4-5. Position and nature of the targets in the public domain test area. ....	94
Figure 4-6. Rebuilt ground truth map of the public domain test area. ....	95
Figure 4-7. Flowchart of an entropy-based algorithm. ....	98
Figure 4-8. Average mapping result of an entropy-based algorithm. ....	101
Figure 4-9. Entropy-based algorithm test result with the average mapping method using the Naples GPR dataset. ....	102
Figure 4-10. Continuous-layer counting method for entropy-based algorithm for an indoor environment. ....	104
Figure 4-11. Continuous-layers counting method for entropy-based algorithm test results using the Naples GPR dataset. ....	104
Figure 4-12. Flow chart of the statistics-based algorithm. ....	106
Figure 4-13. Pixel plot of the GPR signal. ....	108

Figure 4-14. Model signal of the GPR array signal (public domain dataset). .....	109
Figure 4-15. Cross-comparing method of statistics-based algorithm for the public domain dataset.....	110
Figure 4-16. Self-comparing method of statistics-based algorithm for the public domain dataset.....	112
Figure 4-17. Flowchart of the GPR feature-based landmine detection algorithm. ..	114
Figure 4-18. Testing result of the feature-based algorithm.....	116
Figure 4-19. 2D detection map of the feature-based algorithm. ....	117
Figure 4-20. Reference algorithms' test results with the indoor environment dataset. ....	119
Figure 4-21. ROC curve of the proposed algorithms for the indoor test dataset (section 4.2.2). ....	120
Figure 4-22. Operation time of the proposed algorithms in the MATLAB environment. ....	124
Figure 4-23. The memory usage change trend.....	129
Figure 5-1. Multi-sensor data fusion for AP landmine clearance. ....	133
Figure 5-2. Close range detection sensor data fusion functionality. ....	135
Figure 5-3. Centralized feature level Naïve Bayes fusion system flowchart. ....	136
Figure 5-4. How to re-build the position of the MD arm.....	137
Figure 5-5. Metal detector image re-build process flowchart.....	138
Figure 5-6. Re-built landmine location (grass in the top, desert in the bottom). ....	139
Figure 5-7. Simulated metal detector image output. ....	141

Figure 5-8. GPR image input for data fusion system.....	143
Figure 5-9. Distributions of the sensor output (a) MD, (b) GPR. ....	148
Figure 5-10. Kalman filter result of the input sensor (a) MD (b) GPR.....	151
Figure 5-11. Bayesian fusion existing method fusion result.....	152
Figure 5-12. Distributions of the Bayes fusion system .....	153
Figure 5-13. Bayesian-Kalman method fusion result .....	154
Figure 5-14. Dempster-Schafer theory fusion result.....	157
Figure 5-15. Dempster-Schafer fusion result $u_{GPR} = 0.5$ and $u_{MD} = 0.3$ .....	158
Figure 5-16. The influence of the uncertainty rate changed in Dempster-Schafer System.....	160
Figure 5-17. Membership function of GPR and MD sensor input data.....	161
Figure 5-18. Membership function of the output .....	162
Figure 5-19. Fuzzy rules surface map .....	163
Figure 5-20. Fuzzy fusion algorithm test result .....	166
Figure 5-21. P.D Grader research group's fuzzy fusion system output function.....	167
Figure 5-22. Fuzzy fusion result by using Gaussian output membership function..	168
Figure 5-23. Input and output membership function of the novel fuzzy fusion system .....	169
Figure 5-24. Fusion result of the novel fuzzy fusion system .....	170
Figure 5-25. Screenshot of the C# D-Box software.....	171
Figure 5-26. ROC analysis of the fusion system.....	173

Figure 6-1. Area map of the test lane [44]. .....	177
Figure 6-2. Ground truth information of the MsMs dataset [44]. .....	178
Figure 6-3. Ground truth map of area 3A (a), Dangerous range of the area 3A (b)	179
Figure 6-4. A feature of MD02 signals. ....	181
Figure 6-5. The MD023A01 output data.....	182
Figure 6-6. Flow chart of the metal detector image pre-processing algorithm. ....	183
Figure 6-7. Entropy average mapping algorithm detection result for MD sensor in area 3A.....	184
Figure 6-8. The detection result of the MD sensor; left, the optimised image; right, compared to ground truth. ....	186
Figure 6-9. C++ code for reading the .rad file. ....	189
Figure 6-10. The detection result of the GPR sensor.. ....	190
Figure 6-11. The detection result of the GPR feature algorithm.....	191
Figure 6-12. Data fusion system inputs. Left: MD image; right: GPR image .....	193
Figure 6-13. Data fusion system result. (a): Kalman-Bayes fusion system; (b): fuzzy fusion system.....	194
Figure A-1. 'G' label GPR image. ....	207
Figure B-1. Flow chart of the proposed multi-modal image fusion algorithm. ....	204
Figure C-1. Simulation IR camera's landmine map.....	224
Figure D-1. TIR image for the landmine area.....	208
Figure D-2. Entropy-based algorithm for TIR image detection.....	209

Figure D-3. FLIR landmine area normal image.....	209
Figure D-4. GLIR landmine area image with filter.....	210
Figure D-5. Ground truth of landmine area. ....	211
Figure D-6. Landmine area TIR image in MATLAB version with filter. ....	211
Figure E-1. U-blox version of MD altitude information.....	212
Figure E-2. MATLAB version of MD altitude information. ....	213
Figure E-3. U-blox version of the deviation map. ....	213
Figure E-4. MATLAB version for the route of MD operator.....	214
Figure F-1. Flow chart of the re-building GPR image.....	215
Figure F-2. Anti-tank mines in a desert area.....	215
Figure F-3. 300*300 matrix (left) and 500*500 matrix (right) of the statistics algorithm result.....	216
Figure F-4. GPR entropy map using the simple average method. ....	217
Figure F-5. GPR entropy map using the threshold value method.....	217
Figure G-1. Robot-based MD detection result from Naples.....	225
Figure I-1. CW metal detector data.....	233
Figure I-2. Infrared camera output of MsMs dataset. ....	234
Figure J-1. Operation surface of the RTKCONV software.....	218
Figure J-2. GPS route of the Poland landmine area.....	219
Figure K-1. Multisensory ocean surveillance [28].....	226

## List of Tables

Table 1-1 <i>Landmine Detection Sensor Review</i> [16].....	5
Table 3-1 <i>Classical IHS Algorithm Complexity Evaluation</i> .....	75
Table 3-2 <i>Classical PCA Algorithm Complexity Evaluation</i> .....	75
Table 3-3 <i>Proposed PCA Algorithm Complexity Evaluation</i> .....	76
Table 3-4 <i>Number of Operations and Execution Time</i> .....	77
Table 3-5 <i>Quantitative Evaluation of the Multi-Focus Image Fusion Results</i> .....	81
Table 4-1 <i>Detection Accuracy Range Analysis</i> .....	123
Table 4-2 <i>Memory Usage by the Landmine Detection Algorithms</i> .....	127
Table 5-1 <i>The Dempster-Schafer Fusion Rules</i> .....	156
Table 5-2 <i>Fuzzy Fusion Table</i> .....	163
Table 5-3 <i>Fuzzy Logic Mapping Rules</i> .....	164
Table 6-1 <i>Detailed Results of the MD Detection</i> .....	187
Table 6-2 <i>Detailed Results of the GPR Detection Test</i> .....	192
Table 6-3 <i>Detailed Fusion Results with the MsMs Dataset (a) Kalman-Bayes Fusion System, (b) Fuzzy Fusion System</i> .....	196
Table H-1 <i>Computational Complexity Analysis for Proposed Algorithm</i> .....	222
Table H-2 <i>Computational Complexity Analysis for Proposed Algorithm with the Public Domain GPR Image</i> .....	223

## Abbreviations

ADD	Addition
AHS	Adaptive Hardware and Systems
APM	Anti-Personnel Mines
ARC	Airborne Minefield Area Reduction
ATM	Anti-Tank Mines
ATR	Automatic Target Recognition
BT	Brovey Transform
CE	Cross Entropy
CF	Column Frequency
CP	Contrast Pyramid
CPU	Centre Processing Unit
CWMD	Counties Wave metal Detector
D-BOX	Demining tool-BOX for humanitarian clearing of large-scale areas from anti-personnel landmines and cluster munitions
DIV	Division
DNT	Dinitro Toluene

DOD	Department of Defense
DWT	Discrete Wavelet Transform
EGDN	Ethylene Glycol Denigrate
EMI	Electro-Magnetic Induction
EOD	Explosive Ordnance Disposal
EST	Emerging Security Technologies
FAR	False Alarm Rate
FMC	Fusion Matrix Covariance
FMI	Fusion Mutual Information
GEODE	Ground Explosive Ordnance Detection system
GIS	Geography Information Systems
GPR	Ground-Penetrating Radar
GPS	Global Positioning System
HMM	Hidden Markov Model
HSTAMIDS	Handheld STAndoff MIne Detection System
IHS	Intensity-Hue-Saturation
IR	Infrared Radiation
JDL	Joint Directors of Laboratories

JPDA	Joint Probabilistic Data Association
KA	Knowledge Acquisition
K-NN	K-Nearest Neighbour
LDS	Landmine Detection Systems
LIBS	Laser Induced Breakdown Spectroscopy
LOTUS	Light Ordnance detection with Teleoperated Unmanned System
MD	Metal Detector
MMW	Millimeter Wave
MS	Multi-Spectral
MSA	Mine Suspected Areas
MsMs	The Multi-Sensor Mine Signatures
MUL	Multiplication
NBS	National Bureau of Standard
NG	Nitroglycerin
NN	Nearest Neighbour
PAN	PANchromatic
PCA	Principle Components Analysis

PMA	Yugoslavian Blast Antiersonnel Mines
PMN	Yugoslavian Blast Antitank Mines
RF	Row Frequency
RGB	Red-Green-Blue
ROC	Receiver Operating Characteristic
SAR	Synthetic Aperture Radar
SF	Spatial Frequency
SMART	Space and Airborne Mined Area Reduction Tool
SUB	Subtraction
TNA	Thermal Neutron Activation
UAV	Unmanned Aerial Vehicle
UV	Ultra Violet
VIS	Video Inspection System
WT	Wavelet Transform

# **Chapter 1: Introduction**

## **1.1 Background**

A landmine is an explosive device concealed below or on the ground and is designed to destroy or disable enemy targets (e.g. a group of soldiers, vehicles, military tanks) when they move past it [1, 2]. Normal landmines are typically automatically detonated by pressure when a target steps on or drives over them. Landmines are prominent devices employed by the military, where they are generally used to prevent the movement of the enemy. However, not all undetonated landmines are recycled immediately following periods of conflict, due to the dangerous nature and safety costs of the landmine removal process.

Presently, more than 100 million landmines are buried in more than 80 countries around the world. Every year, roughly 26,000 people are killed or maimed by landmines, most of these being non-militarily individuals [1]. The presence of landmines also influences human confidence in that area: no one wants to work in such an unsafe environment. Safe Explosive Ordnance Disposal (EOD) [3, 4] and landmine area clearing have therefore become extremely urgent and significant issues in many countries.

The two important research aspects of landmine area clearing are landmine detection and safe landmine removal. The landmine detection process includes long-range mine area reduction and close-range landmine detection [5]. By analysing information feedback pertaining to the landmine area, long-range mine area reduction aims to reduce unnecessary close-range landmine detection [6]. The most difficult aspect of the landmine detection process is accurate detection, which aims to identify a

landmine's location correctly. Once landmines have been detected, there are many methods for eliminating them.

Different types of landmines are used throughout the world, with each country having its own techniques for creating them. Landmines can be distinguished according to many different features. There are wooden landmines, metal landmines and plastic landmines, distinguished by the materials used in the landmine's shell [2]. Landmines can also be distinguished according to how they are used: Anti-Personnel Mines (APM) aim to disable infantry while the Anti-Tank Mines (ATM) seek to destroy military vehicles and tanks [7]. Generally, the ATM will include more explosives and more metal than the APM. In addition, some APMs are made using low-metal materials, which are difficult to detect using current metal detector (MD) devices.

A landmine detection system should be able to detect mines regardless of the type of explosives used. The detection system must also be sensitive to the geometrical shape of the mine and type of casing material and preferably provide imaging information. These features will enable the system to distinguish mines from background and clutter such as metal shreds, rocks, etc. These features can also help to reduce false-positive alarm rates and time wasted trying to clear an innocuous object believed to be a landmine [8]. Since mines can be buried at various depths underground, the detection system should not overly rely on the depth of burial. In addition, the cost of a landmine detection system is another aspect that requires evaluation.

The two main humanitarian mine actions that may benefit from multi-sensor data fusion technology are close-range APM detection and mined area reduction [9]. Close-range mine detection consists of surface-anomalies detection, metal detection (metal detector), and temperature-differences detection (infrared camera). Mined area reduction aims to identify mine free areas from the mine suspected areas (MSA). In

terms of mined-area reduction, the European Commission and participating member states funded a ‘pilot project on airborne minefield detection in Mozambique’, focusing on mined area reduction [10]. In 1997, this project showed that it is impossible to find anti-personnel landmines using extremely high-resolution airborne sensors; instead, multi-sensor data fusion is needed. Image fusion technology can be used to reduce a mine area using long-range sensors such as satellite synthetic aperture radar (SAR) imagers. The images produced by close-range working sensors, such as ground penetrating radar (GPR) and metal detectors (MDs), can then be incorporated to identify mines in the reduced mine suspect area.

## **1.2 Research Aims**

The motivation for this research is to improve landmine detection in order to save the lives of people living in landmine areas. Accordingly, the research has several aims: firstly, to improve optical camera output quality to reduce redundant information in such images. This point will mainly focus on improving the quality of the outputs and reduce the operation time of the existing multi-focus image fusion algorithm, the reference algorithms will be the Intensity-Hue-Saturation (IHS) and Principle Components Analysis (PCA). Secondly, to improve landmine detection algorithms for processing single-sensor data, thus improving the detection ability of landmine detection sensors. This point will mainly focus on finding the feature of the detection sensors and designing suitable detection algorithm which will use the features effectively. Thirdly, to build a suitable data fusion system for the incorporation of different types of landmine detection sensors to improve the quality of landmine detection results. This point will mainly focus on improve the detection ability of the existing multi-sensor fusion system, the candidate systems includes the Bayes fusion system and the Fuzzy fusion system.

## **1.3 Problems and Challenges**

To achieve the aims of this research (as noted in section 1.2), several problems and challenges must be addressed. The first problem is that landmine detection sensor outputs are always large in terms of bit size and contain repeated information; for example, an optical camera must take several images from different visual angles to analyse the ground environment. These images all include the same background information, which, in terms of processing, is redundant. The second problem is that the sensors used for landmine detection have their own limitations. For example, the MD sensor is only suitable for use in metal-free environments; otherwise, it will produce many false alarms during the detection process. The first challenge therefore concerns improving the detection rate and lowering the false alarm rate in a single sensor system, for example, using only an MD or GPR sensor. The second challenge concerns the need to have the same format for all landmine detection process inputs. In a bid to achieve heterogeneous multi-sensor data-level fusion, a substantial preliminary work is required to make the sensor data outputs suitable to fuse.

### **1.3.1 Limitations of Landmine Detection Sensors**

Many types of sensors are used in the landmine detection process, including electromagnetic induction (EMI) sensors, metal detector (MDs), GPR, GPR arrays, electrical impedance tomography, X-ray sensors, infrared/hyperspectral cameras, acoustic/seismic sensors and others. However, each sensor has its own benefits and limitation, and no type of sensor can achieve landmine detection work in all types of ground environment[11].

The MD sensor is good for detecting metal-containing landmines under the ground surface, but it cannot detect landmines made of plastic or those that contain little or no

metal [12]. The GPR sensor can detect many discontinuities in the ground, including landmines with little or no metal content; however, it can also yield a high rate of false detections (e.g., bones, rocks and the roots of plants) [13]. The X-ray sensor uses an X-ray to scan the underground environment; it has very good imaging ability and can output an image indicating the location of landmines. Hence, while it is expensive and can currently only be employed in a lab environment, the X-ray sensor will nonetheless be a good landmine detection sensor in the future [14]. The infrared/hyperspectral cameras have been used to detect surface landmines. The strength of this type of cameras is the fact that operators can keep far away from the landmine area. However, it cannot deal with buried landmines within a short response time [15]. The acoustic sensor is a new technique, which, by counting the reflection of sound waves, aims to identify landmines. However, currently, this type of sensor is generally not suitable for outdoor environments.

Table 1-1 below summarises the principle, strengths and limitations of landmine detection sensors. It indicates that, to achieve a successful landmine detection process, the use of only one type of sensor is insufficient.

Table 1-1 *Landmine Detection Sensor Review* [16]

Sensor type	Operating principle	Strengths	Limitations
MD	Induces electric currents in the metal components of mines.	Performs in a range of environments.	Metal clutter; low-metal-content mines.
GPR	Reflects radio waves off mine/soil interface.	Detects all anomalies.	Roots, rocks water pockets.
Electrical impedance tomography	Determines electrical conductivity distribution.	Detects all anomalies.	Dry environments; can detonate mine.
X-ray	Images buried objects using X-rays.	Advanced imaging ability.	Slow; emits radiation.

Infrared/hyper spectral	Assesses temperature and light-reflectance differences.	Operates from safe stand-off distance and scans a large area quickly.	Cannot locate individual mines.
Acoustic/seismic	Reflects sound or seismic waves off mines.	Low FAR; not reliant on electromagnetic properties.	Deep mines; vegetation cover and frozen ground.

### 1.3.2 Challenges of the Landmine Area Clearing Process

Both anti-tank and anti-personnel mines come in many different shapes and sizes, and they can be encased in metal, plastic or wood. Their triggering mechanisms vary from simple pressure triggers, tilt rods, acoustic and seismic fuses and even light- or magnetically influenced fuses. Landmines can be embedded in a field cluttered with various materials and objects like metal cans, keys, bones, and even simulated mines. Furthermore, landmines can also be scattered on the ground surface, covered by plant overgrowth or buried at various depths from the surface. All of these aspects impede the landmine area clearing process.

Research on demining can be divided into two areas: civilian demining and military demining. The requirements of civilian demining (mine clearance) are very different from military demining, thereby affecting detection strategies. The objective of military demining is to move across a minefield as rapidly as possible; therefore, using brute force to achieve landmine removal is acceptable. However, the mine clearance process requires a complete removal of all mines in the field, meaning that absolutely no explosive material can be left in the landmine field [17]. The present research focuses on close-range landmine detection, which refers to civilian demining. In these

cases, the requirements for the detection results are extremely strict and necessitate all landmines to be detected while keeping the false alarm rate as low as possible.

The false alarm rate (FAR) is an important parameter for evaluating landmine detection systems. The Geo-centres VMMD system can achieve a higher than 90% detection rate and 4% FAR in field testing on ATM [10]. Via the Hidden Markov Models (HMM) algorithm, the detection rate of the ATM has been able to reach above 95% with a FAR of less than 2% [18]. The handheld system used for APM detection in [19] has a higher FAR than the ATM detection system. The challenge of this research is to improve the detection rate and lower the FAR of both APM and deep buried ATM detection process. The existing acceptable detection rate for a single sensor detect the APM is 60% false alarm rate at the detection rate is 90% and for deep buried ATM it will be 70% false alarm rate at 90% detection rate[20]. Therefore, the challenge of this research is to assure the proposed work on single sensor landmine detection can reach beyond the boundary of the existing algorithms.

### **1.3.3 Challenges of Data Fusion System Design for Landmine Detection**

According to Nuzzo et al.,

*“The challenge of landmine detection is not only to develop techniques that can meet this demanding problem, but to also tailor such techniques to local conditions. It is difficult to apply any one technique unless the nature of the mine, soil and background clutter is well known, and it is inconceivable that a single detection technology will be able to meet all needs. A fusion of systems is needed as a solution to the landmine detection problem. Radiation-based*

*techniques have the unique ability to identify the presence of an explosive material in an anomaly detected by other methods.” [21]*

The literature shows that sensor type, mine type, geographical site, soil type, weather conditions, and the burial depth of mines limit the landmine detection process [22]. Currently, if mine density is high or environmental conditions change too rapidly, detection sensors will fail to find landmines.

The challenge of designing a data fusion system for landmine detection is that not all types of detection sensors are suitable for fusing in an outdoor environment [23]. For example, the IR camera can output images with surface landmine information whilst the acoustic sensor can output sound wave signals for identifying buried landmines. Combining these two types of sensors may help to identify both on- and below-surface landmines; however, the precondition for doing so is having an extremely accurate GPS system to ensure that the two detection sensors are collecting the data from the same point. Since there is currently no such GPS system for use in an outdoor environment, the IR camera is not suitable for fusion with the acoustic sensor.

The method for evaluate the existing landmine detection system is detection rate and false alarm rate. The HSTAMIDS system in [24] reduces the FAR of APM detection from 38% to 9%, a significant improvement for landmine detection in an outdoor environment. In addition, the current boundary of the fusion-based detection system is less than 10% FAR with over 90% detection rate[25]. The challenge of this research is not only select the suitable sensors for the data fusion system, but also to assure the proposed fusion system can reach the boundary of the existing system.

## **1.4 Novel Contributions**

The novel aspects of this research are listed below:

*Firstly*, this research proposes a new PCA-based multi-focus image fusion algorithm. When compared to the famous existing multi-focus image fusion algorithms (IHS and PCA), the proposed algorithm improves the existing PCA algorithm through comparing the feature relevance between the main components and other components of multi-layer images. It achieves better fusion results than the IHS and PCA algorithms but has the same operation time as the PCA algorithm. In addition, the multi-focus-image fusion algorithm can assist a landmine detection system by reducing the redundant information captured from different optical cameras. The algorithm can also be used in autonomous driving systems to help the system understand the road conditions, as such systems have multiple optical cameras, producing multi-focus images.

*Secondly*, the research proposes three different types of single-sensor landmine detection algorithms:

(a) entropy-based landmine detection algorithm: the proposed algorithm is suitable for rough detection in a minefield using the entropy value as the feature to distinguish the landmine area from the background, enabling it to be used for reducing the suspect landmine area for detailed detection. The entropy-based algorithm belongs to the spatial region feature detection algorithm, which is suitable for mine area reduction work. It will be shown in Chapter 4 of the thesis that the proposed algorithm outperforms the existing energy-based region selection algorithm reaching 33% FAR rate with 80% detection rate. In addition, it only takes 33.8% of the operation time of the existing region selection algorithm.

(b) statistics-based detection algorithm: this is an A-scan GPR signal based landmine detection algorithm. The proposed statistics-based detection algorithm has reduced the requirements of the GPR sensor inputs from B-scan signal to A-scan signal, which can

reduce the computational complexity of the existing spatial-feature based algorithms. In addition, as detailed in Chapter 4, the detection rate of the proposed statistics-based algorithm has achieved 35% FAR at 90% detection rate, which is a great improvement than the existing detection rate boundary EHD algorithm (60% FAR at 90% detection rate). The proposed statistics-based algorithm can also save 51.1% operation time than the EHD algorithm.

(c) GPR feature-based algorithm: a new feature of the C-scan GPR image has been proposed, which is oscillation feature. This new feature has been found when the GPR signals across the buried object, as the shape and material of object change the oscillation time and oscillation range will be changed. The proposed algorithm through distinguish the oscillation features of landmine pixel and the background pixel to identify the buried landmine in the mine area. The GPR feature-based algorithm aims to challenge the existing best GPR sensor detection algorithm, which is edge energy algorithm. The detection ability results presented in Chapter 4 have shown that both the proposed algorithm and edge energy algorithm can reach a 22% FAR at a 90% detection rate. However, the proposed algorithm only spends 18.5% operation time of the edge energy algorithm. In addition, the proposed algorithm will use less memory than the edge energy algorithm. The aim of single-sensor landmine detection research is to improve the existing single-sensor detection algorithm, which also aims to improve the inputs signals for the data fusion system.

*Thirdly*, the research proposes two different novel fusion systems, which are a Kalman-Bayes fusion system and a fuzzy logic based fusion system. The Kalman-Bayes system argues that the existing Bayes system does not process the system uncertainty during the fusion process, therefore a Kalman filter has been introduced before the decision level fusion in the Bayes system. The detection ability results in

Chapter 5 show that the proposed Kalman-Bayes fusion can reach 7.25% FAR with 91.1% detection rate, outperforming the existing Bayes fusion system. The proposed fuzzy fusion system argues that the existing fuzzy fusion system only uses triangle inputs membership functions, which do not consider the uncertainty and features of the input sensors. The proposed fuzzy fusion system employs the distributions of the input sensors to design the input membership functions. The result has shown that the proposed fuzzy fusion algorithm can reach 6.3% FAR with 92.4 detection rate, which is an improvement of the existing fuzzy fusion system. The proposed system is able to fuse different types of sensors for conducting the landmine detection process.

The data fusion techniques can assist in improving the detection performance, thus increasing the detection rate. The results also prove that data fusion technology can enhance the performance of the landmine detection process, resulting in a significant improvement when comparing the fusion results with the single-sensor detection results.

## **1.5 Structure of the Thesis**

The structure of this thesis is as follows:

Chapter 2 reviews the relevant literature on landmine detection and data fusion aspects to formulate a research method.

Chapter 3 proposes a PCA-based novel multi-focus image fusion algorithm suitable for improving the quality of an optical image used in the landmine detection process. The test results have shown that the proposed multi-focus image fusion algorithm has improved the quality of the fusion result when compared to other existing fusion algorithms.

Chapter 4 is concerned with the use of the GPR sensor as a specific sensor for the design of landmine detection algorithms. The test results have shown that the proposed single-sensor detection algorithm could improve the current landmine detection process by increasing the detection rate and lowering the calculation time of the algorithm. This will be the primary novelty aspect of this research.

Chapter 5 focuses on the integration of data fusion techniques with the landmine detection system to improve detection performance.

Chapter 6 presents a case study confirming the performance improvement achieved by the landmine detection algorithms proposed in this thesis using the Multi-Sensor Mine Signatures (MsMs) dataset.

Chapter 7 summarises the thesis and presents future research aspects.

The Appendices contain experimental results illustrating the landmine detection process as discussed in this thesis.

## **1.6 Related Publications**

Parts of the research presented in this thesis have been reported in the following publications:

- Jing, H. and Vladimirova, T. 2017, September. Novel algorithm for landmine detection using C-scan ground penetrating radar signals. In *Proceedings of Seventh International Conference on Emerging Security Technologies (EST)*, 2017, pp. 68-73, IEEE.
- Jing, H. and Vladimirova, T., 2013, September. Image fusion for an EOD Robot Wireless Visual Module, in *Proceedings of 2013 Fourth International Conference Emerging Security Technologies (EST)*, pp. 125-126, IEEE.

- Jing, H. and Vladimirova, T., 2014, July. Novel PCA-based pixel-level multi-focus image fusion algorithm, in *Proceedings of 2014 NASA/ESA Conference on Adaptive Hardware and Systems (AHS)*, pp. 135-142. IEEE.
- Zhai, X., Jing, H. and Vladimirova, T., 2014, July. Multi-sensor data fusion in wireless sensor networks for planetary exploration, in *Proceedings of 2014 NASA/ESA Conference, Adaptive Hardware and Systems (AHS)*, pp. 188-195. IEEE.
- Bennett, D., Jing, H., Fayyaz, M. and Vladimirova, T., 2016, April. Generation and fusion of landmine detection intensity maps using a three-stage algorithm in *Proceedings of International Symposium "Mine Action 2016"*, pp. 149-153.
- Bennett, D., Jing, H., and Vladimirova, T., 2016, March. Software tools for close-in detection of landmines. Poster presentation, D-Box Final Demonstration, Naples Italy, 28<sup>th</sup> March 2016.

Other publications:

- Rodrigues, P., Oliveira, A., Alvarez, F., Cabas, R., Oddi, G., Liberati, F., Vladimirova, T., Zhai, X., Jing, H. and Crosnier, M., 2014, July. Space wireless sensor networks for planetary exploration: node and network architectures, in *Proceedings of 2014 NASA/ESA Conference on Adaptive Hardware and Systems (AHS)*, (pp. 180-187). IEEE.

## **Chapter 2: Literature Survey**

This chapter aims to review the existing work on data fusion systems and landmine detection methods. Section 2.1 is a general review of data fusion technology. Section 2.2 includes a review of landmine detection systems, sensors, previous projects and useful algorithms. Section 2.3 is a review of image fusion technologies, which could contribute to surface landmine detection. Section 2.4 summarises the chapter.

### **2.1 Data Fusion Technology**

Data fusion techniques combine data from multiple sensors and related information to achieve more specific inferences than could be accomplished by using a single, independent sensor. Data fusion refers to the combination of data from multiple sensors (either of the same or different types), whereas information fusion refers to the combination of data and information from sensors, human reports, databases, etc. [26].

Based on the input data relation, it is possible to divide the data fusion process into cooperative, redundant and complementary data fusion. Figure 2-1 shows the three different types of data fusion processes.

In Figure 2-1, the A, B and C represent three different sensors, which produce input data referred to as a, b, c, and c'. Complementary data fusion aims to fuse different data from different sensors; in Figure 2-1, the fused result could represent both A and B features. Redundant data fusion aims to reduce the amount of redundant data during data processing. In addition, cooperative data fusion combines different data from the same sensor or sensor group with the aim of producing more informative output data.

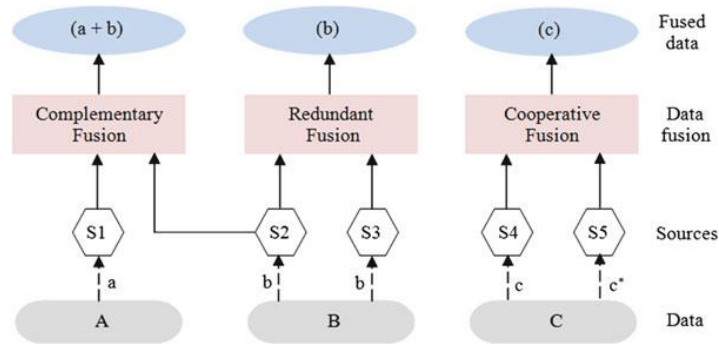


Figure 2-1. Types of data fusion [27].

The fusion methods can be categorised as ‘decision-level’, ‘feature-level’ or ‘data-level’ [1]:

- In decision-level fusion, each component sensor of the system provides the operator with a decision from independently processed signals, and these are combined to make the overall decision. ‘Hard’ decision-level fusion bases the overall decision on only the individual binary decisions of the component sensors, generally using simple rules (e.g. Boolean ‘and’, ‘or’ or majority voting). Alternatively, if individual decisions are augmented with some measure of confidence, ‘soft’ decision rules that give more weight to more reliable decisions are possible. In either case, the overall decision is based on only the independently processed signals from the individual sensors.
- In feature- and data-level fusion, the signals generated by each sensor are combined algorithmically to present the operator with a single signal on which to base the decision. That is, rather than combining the processed outputs of various sensors, these lower-level fusion methods jointly process the received physical information at the signal level. Data-level fusion combines the raw

data collected by each sensor, while feature-level fusion combines information about informative ‘features’ extracted from the raw signals.

The data fusion process includes two types of rules: inference rules and estimation rules [28]. The inference method is known for adhering to decision-making rules, which are applied in the decision-based data fusion system. Classical inference methods include the Bayesian method, Dempster–Shafer, Fuzzy logic, and neural networks.

The naïve Bayesian method requires the inputs to determine the confidence level of the detection sensor and the sensor values in  $[0, 1]$  intervals, where 0 is false and 1 is true [29]. The naïve Bayes approach is a naïve implementation of the likelihood ratio. In this case, it is capable of fusing the different confidence levels of the multi-sensor signals to determine the confidence level of the object suspected to be a landmine. The advantage of this method is that it is easy to achieve whilst the drawback is the high FAR of the fusion result. The challenge of using this method in the landmine detection system is to build a reasonable confidence evolution system, since the performance of the detection sensor can be influenced by many conditions (e.g. soil condition, clutter and weather conditions).

The Dempster [30]-Shafer [31] inference is based on the Bayesian method. It deals with beliefs or mass functions just as the Bayes rule does with probabilities. The Dempster-Shafer inference has been used to build dynamic operational pictures of battlefields for situational evaluation. In this case, the Dempster-Shafer methods need the input signals to include two parts: the suspect object’s probability mass assigned to a landmine of each sensor and the probability mass assigned to the background of each sensor. By using the Dempster-Shafer-based fusion method to fuse the input data, the system can provide the probability mass of a suspect object assigned to a landmine,

which is more accurate than the Bayesian method. A benefit of this method is that it can more effectively reduce the FAR than the Bayesian method. However, the drawback of this method is that it requires more input than the Bayesian method and introduces the burden of much more calculation in the fusion process.

Fuzzy-data fusion is a type of decision-level data fusion technology. This method requires building different fuzzy sets based on the features of the raw data. In addition, when proposing a practical solution, the fuzzy rules are adopted to overcome any shortcomings of the mathematical approaches. Fuzzy data fusion technology can be used for intelligent data fusion system design. For example, by correcting slow sensor drift faults, Goebel presented a hybrid method using fuzzy logic with genetic algorithms [32]. To exploit the advantages of both fuzzy logic and the Kalman filter, Escamilla suggested a hybrid Kalman filter fuzzy logic that adapted multisensory data fusion architecture [33], an efficient intelligent fusion method. The fuzzy logic approach has been widely used in decision-level data fusion systems. In a landmine detection system, rule-based fusion algorithms normally represent the fuzzy-logic-fusion method. Through the creation of fusion rules, this method is able to classify the sensor input data using such rules to determine whether the probability mass of an object is a landmine. The benefit of this method is that it can output a description language of the suspect object. However, the drawback of this method is that it cannot provide a crispy result (i.e. whether the suspect object is a landmine or not). The existing fuzzy-logic-based landmine detection systems use decision-level data as the inputs signals. The advantage of the existing system is it can detect the landmines correctly and effectually; however, the disadvantage is it requires processing the raw data to the decision level first. Therefore, using the feature-level or data-level inputs

signals to build a fuzzy-logic-based landmine detection system can improve extant detection systems by reducing the input requirements.

## **2.2 Current Landmine Detection Technology**

This section will review the relevant literature on landmine detection with the aim to identify the research gaps. Section 2.2.1 reviews existing landmine detection systems. Section 2.2.2 reviews the existing landmine detection sensors. Section 2.2.3 reviews several landmine detection projects outlining the contributions of each project. Section 2.2.4 reviews landmine detection algorithms for GPR sensors and methods to improve the 3D-GPR landmine detection performance.

### **2.2.1 Landmine Detection Systems Review**

A landmine detection system is similar to the explosive detection system, with the difference being that landmines are normally concealed under or on the ground; hence, to verify landmines, the sensors should be able to detect the underground environment [34]. However, a bomb is normally on the ground or hidden in some object; thus, bomb detection will not need high-performance sensors to search underground. Nonetheless, some explosive detection techniques could be used in the landmine detection process as well. In this section, existing popular landmine detection and explosive detection equipment will be reviewed.

#### **2.2.1.1 Improved Landmine Detection System**

The Improved Landmine Detection System (ILDS) is a remotely operated vehicle-mounted multiple-sensor mine detection system belonging to the Defense Research Establishment at Suffield (DRES) and General Dynamics Canada Group. The ILDS uses a data fusion centre to carry out multi-type landmine detection sensor fusion work.

Figure 2-2 shows the architecture of the ILDS, which represents the classic system. Four kinds of detection sensors are used in this figure: Infrared camera, Metal Detector, GPR and Thermal Neutron Activation (TNA) detection sensor [35]. The system uses IR, MD and GPR sensors to achieve the landmine detection process separately; then, through the fusion centre, it uses decision-level data to identify the input signals as belonging to a landmine or not. A navigation system is attached to the landmine detection system to provide the position information of the suspected landmine. The TNA detection sensor has been introduced as proof-level fusion after the suspect landmines have been located, which aims to confirm whether the detection result is correct or not. The point marking (marking the location of the determined landmines) is the final work of this system: the detection result. In addition, the point marking is connected with the end-user's interface [36].

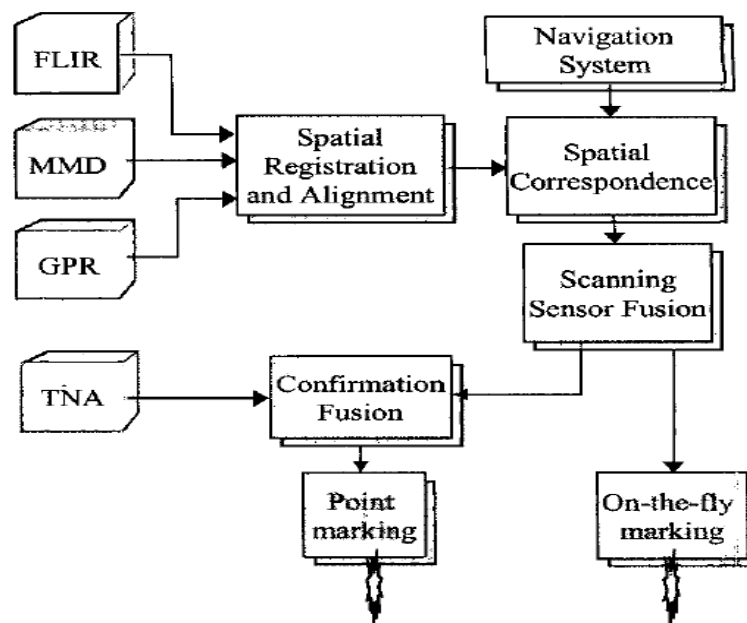


Figure 2-2. Landmine detection system architecture [35].

The ILDS is a successful system, which can be used as the model of the data fusion system design. The beneficial part of a system using a decision-level data fusion technique is its improvement in the detection ability and adding a confirmation fusion block to prove whether the result is correct or not. The drawback of such a system is, when adding or deleting one of the detection sensors in the system, the fusion block needs to be re-designed again. The research gap here is to design an adaptive landmine detection algorithm which can improve the detection ability of the existing system. The other research gap is using the feature-level data instead of the decision-level data, offering another idea to design an LDS.

#### **2.2.1.2 Vehicle-mounted Tele-operated Mine Detection System**

Other explosive detection systems have been built by different research groups. A Canada research group has built a vehicle-mounted tele-operated mine detection system, which uses data fusion technology to detect landmines. The system's architecture is shown in Figure 2-3 [37, 38]:

This system is constructed via a remote detector vehicle, confirmation detector trailer and a vehicle control station. The remote detector vehicle uses IR and VIS cameras (visible camera) to achieve landmine detection, and the trailer uses the TNA camera to confirm the suspicious landmine, and the vehicle control station controls the vehicle. The remote detector vehicle has a marker controller to mark the detected landmines. This system is quite huge and suitable only for battlefield landmine detection.

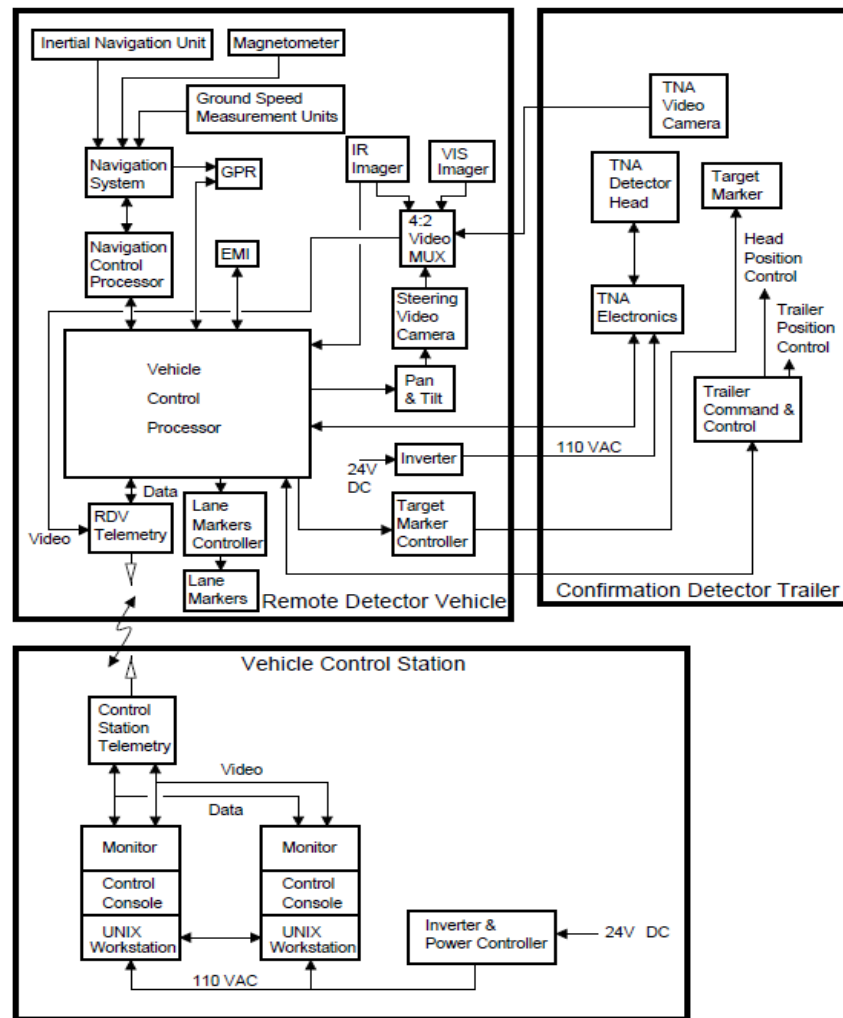


Figure 2-3. Vehicle-mounted tele-operated mine detection system architecture [48].

According to Figure 2-3, some important points of a landmine detection system can be determined. The first one is that the operator needs to work in a safe condition; therefore, the remote-control system has been introduced. The second point is that image fusion is a part of the landmine detection research since this system has fused the IR image data with the VIS camera data. The third point is that both the image sensor and the signal sensor are important in a landmine detection system; therefore, the IR camera, VIS camera, GPR sensor and EMI sensor are inputs of this system. The last point is the GPR sensor needs a navigation system to help locate positions in the

detection process. The above four points are very useful rules when designing the landmine detection system in this research.

## **2.2.2 Landmine Detection Sensor Review**

This subsection aims to review the existing landmine detection sensors, finding their advantages and limitations. The purpose of this review is to identify which types of detection sensor will be used in this research.

### **2.2.2.1 Elemental Composition Equipment**

The working principle of an elemental composition sensor is based on the explosive material which presents different features when exposed to some kinds of radiation. The classic radiation sensor uses gamma rays, which are detected using an array of detectors placed near the object and analysed using a computer. The computer program will study the nature of the radiation and indicate the subject type. Explosive detection is based on a benchmark of gamma ray exposure such as photoelectric absorption, Compton scattering, and positron and electron production. Laser-Induced Breakdown Spectroscopy (LIBS) [14] is another form of radiation detection which could be used for explosive detection. LIBS an atomic emission spectroscopy method used for testing the elemental composition of materials. LIBS is based on plasma generation by a sufficiently intense laser pulse. In a LIBS sensor, optical plasma radiation is collected and spectrally analysed in the spectral range covering near UV, visible and near IR. The spectrum appears as the spectral signature of the sampled material. Figure 2-4 shows a LIBS module structure.

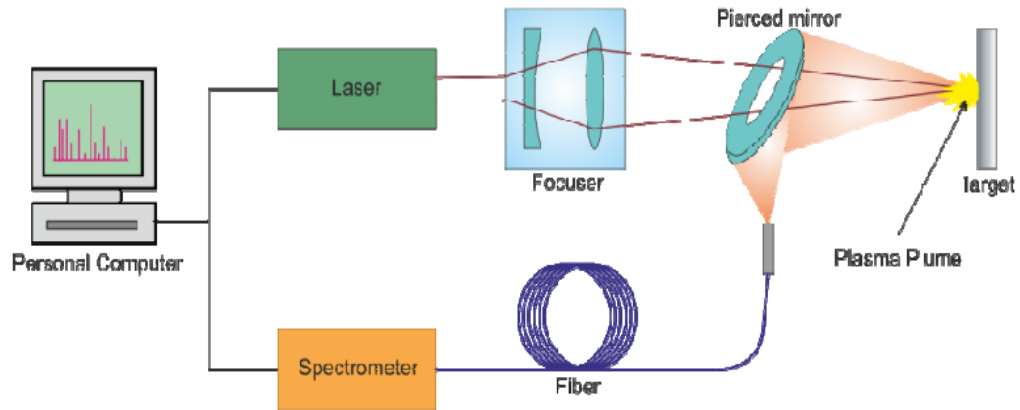


Figure 2-4. LIBS working structure [14].

The LIBS spectra of energy materials contain atomic lines of these elements and molecular bands of CN and C<sub>2</sub>, which can be attributed to native C=C and C-N bonds of explosive molecules and to radicals formed in chemical processes proceeding the plasma plume. Based on the spectrum analysis, most of explosives can be targeted.

Microwave radiation is a popular method to detect the landmines. The operating principle of microwave radiation is based on measuring very small temperature differences (microwave thermograph) [39]. Physically, there is a difference between characteristics of the heating and cooling time of the ground surface with and without buried objects. Most elemental composition sensors are suitable for an explosive detection process; however, some of these techniques could be employed in a landmine detection process as well.

Overall, both of the LIBS sensor and the microwave sensor are good performed in the explosive detection process. However, in the landmine detection process, these sensors will be limited by the response time, working environment, prices and other reasons. The elemental composition sensor will have a good performance in the landmine detection process in the future.

#### 2.2.2.2 Vapor-emissions equipment

Vapor detection refers to gas-phase molecules emitted by a solid or liquid explosive. The concentration of explosives in the air is related to the vapor pressure of the explosive material and to other factors, such as the duration of the presence of explosive material in the given location, its packing, temperature and air circulation in the location. Basically, a vapor-emissions sensor could be divided into three types: electronic/chemical sensors, optical sensors and biosensors. Most explosives will contain some organic chemical material such as ethylene glycol denigrate (EGDN), nitro-glycerine (NG), and 2, 4-dinitrotoluene (DNT) [3]. All kinds of explosives will volatilise parts of these molecule into the environment. Using the vapor-emissions sensor to analyse the air in the environment, it is easy to target suspicious bombs. Figure 2-5 shows an example of a nitrogen dioxide sensor which could detect nitrogen dioxide in the environment. Once the concentration of nitrogen dioxide reaches a limit, it is proof an explosive is near [40]. The drawback of vapor detection is that each explosive has its own material composition. It is not possible to have a sensor that could detect all kinds of explosive. If the material of an explosive is unusual, then vapor detection would not work. In addition, this type of sensor is a very new technique, and it might not be suitable for a landmine detection process. Moreover, a vapor-emissions sensor is very expensive; consequently, it is hardly used in most existing landmine detection processes. Another drawback of this sensor is its working principle is not suitable for accuracy in the detection process, which seeks to locate the position of the landmines.

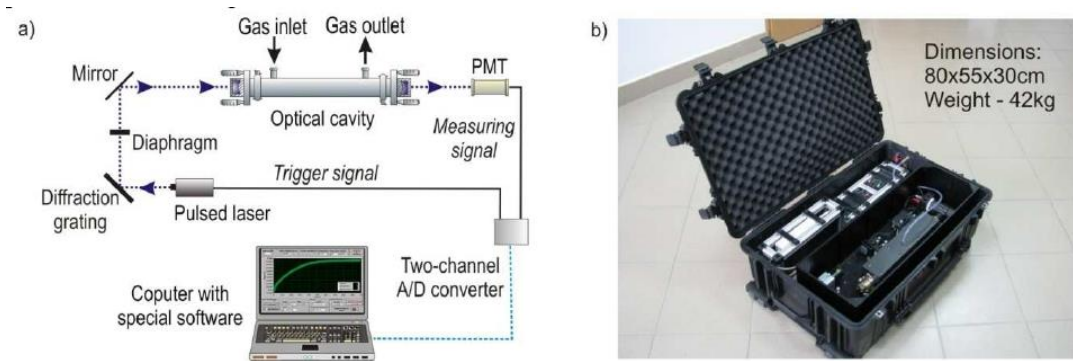


Figure 2-5. Scheme (a) and photography of a portable nitrogen dioxide sensor (b) [17].

### 2.2.2.3 Ground Penetrating Radar

Ground-Penetrating Radar is the most popular landmine detection sensor in the current landmine detection process. The working principle of the GPR sensor is sending different high-frequency (as frequency increases, the penetrating power will decrease) electrical signals to ground surface, thereby detecting the reflected signals from subsurface structures [41]. Generally, the Ground-Penetrating Radar sensor can be divided into two different types: hand-held GPR and as GPR array. The hand-held GPR is easy to use but cannot locate a landmine's position under the ground surface; it often used by the military. Figure 2-6 shows a military hand-held GPR sensor.



Figure 2-6. The AN/PSS-14 Hand-held landmine detection sensor [42].

The GPR array is a complex GPR system consisting of several electrical signal transmitters and receivers. The GPR array can supply a 3D GPR image for the landmine detection process. The 3D GPR image is a kind of multi-spectral image, the detailed information of which will be introduced in section 4.1. The GPR array has the ability to locate the actual position of the landmines. However, this type of equipment is too large. Therefore, the GPR array is often used by large landmine detection systems (i.e. vehicle-based) and indoor laboratories. Figure 2-7 shows a GPR array used by the Wrocott research group [43].



Figure 2-7. GPR array from the Wrocott research group [43].

#### 2.2.2.4 Metal Detector

A metal detector is another popular landmine detection sensor, which is used by the military. A feature of MD sensor-based detection equipment is ease of operation and low cost. The working principle of the MD detector is electromagnetic induction, meaning MD-based equipment can only report an object containing metal; hence, the metal detector will treat every object containing metal as a landmine. The MD can only show good performance in non-metal-clutter areas. Normally, when a metal

object has been detected by the MD sensor, a beep will be produced to report that a landmine has been found. Two types of MD sensor will be explained in sections 5.1 and 6.2. Figure 2-8 below shows hand-held MD equipment:



Figure 2-8. Foerster Minex 2FD 4.500 hand-held MD equipment [44].

#### 2.2.2.5 3D GPR Image

The 3D GPR image produced by a GPR array is known as ‘C-scan GPR data’; it is mainly using for describing the under-surface environment. Generally, the GPR array data could be divided via three types of description method: A-scan, B-scan and C-scan. The A-scan GPR signal means the GPR array is only scanning one location with different frequencies; with only a line representing the reflection strength of the under-surface environment. The B-scan GPR signal uses a series of A-scan GPR signals to build a 2D image; the edge-energy landmine detection algorithm (see section 2.3.3) is a B-scan-based landmine detection algorithm. The C-scan GPR signal consists of a series of B-scan GPR signals; however, it could be treated as a multi-spectrum image

as well. There are two different methods by which to analyse C-scan GPR signals: cross-track analysis and down-track analysis. Cross-track analysis aims to use surface depth changes to detect landmines. In addition, the down-track analysis aims to divide the C-scan signals into B-scan signals, and then detect the landmines. The C-scan GPR signals contains the information of the shape of the detected object, which B-scan GPR signals do not have. Figure 2-9 below shows the difference between cross-track and down-track.

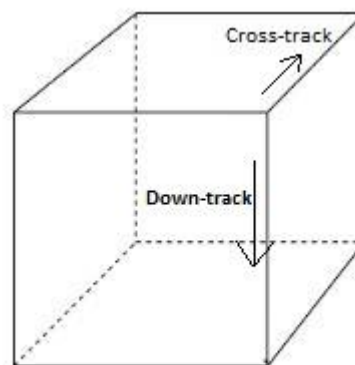


Figure 2-9. Cross-track and down-track 3D GPR images.

### 2.2.3 Landmine Detection Related Projects

Space and Airborne Mined Area Reduction Tools (SMART) and ARC are two previous landmine area reduction projects funded by the European Community. The aim of the SMART project is not to solve the problem of mine suspected area automatically, but to help human analysts in their interpretation. The ARC project aims to reduce landmine areas by identifying mine free areas on a map. A review of some other landmine detection projects conducted in other countries follows.

### 2.2.3.1 Airborne Minefield Area Reduction (ARC)

The ARC project uses different types of airborne camera images as the input and utilises the fusion process to determine which area is free of landmines. The core technology of the ARC project is data fusion, whereby Geography Information Systems (GIS) functions as the fusion centre to fuse measured image data, ground truth, mine information, minefield history, and geographical information[10]. In the ARC project, image data are divided into several levels: global, regional, UAV, local, and minefield level. The global-level image derives from the Synthetic Aperture Radar (SAR) image, which covers an area of 50x50 km at a resolution of 30m-15m/pixel.

The global-level image provides an overall map of the landmine area. The regional-level image data are come from a high-resolution satellite with an area of 20x20 km and a resolution of 1m/pixel, used to detect the ground truth information from the map [45].

The UAV-level image is taken from the infrared optronic image of the UAV camera and provides a visual image that covers a range of 10x5 km at a resolution of 0.5m/pixel [38]. The UAV image helps close-range landmine disposal by giving the GIS information of a landmine area.

The local image is taken from the Camcopter, which includes IR and a visible image, covering a range of 2x0.5 km at a resolution of 20cm/pixel. This type of image helps the landmine disposal operator find the general location of the suspected landmine. The minefield image also comes from the Camcopter, with coverage of 200x200m at a resolution of 10cm/pixel. This image can provide useful information during the close-range landmine detection process; 10cm/pixel means that one landmine occupies one pixel in the image [46]. The Knowledge Acquisition (KA) system is the

core of the ARC project, wherein a data fusion engine identifies different ground truth information. The work process begins by recovering the photographs of the area, which are then imposed onto the map [6]. The next step is to define the feature types (e.g. building, road, terrain), a process aided by the image fusion algorithms, which segment the image and locate these defined feature types. Finally, the system is based on the segment information of the image in order to verify the distance between two segments.

The feature type of the mine area is a very important point in determining whether an area is landmine free or remains suspect [47]. Based on human observation and expert analysis, the existing available sources of data can be divided into several types: suspected area, demolished house, house, demolished vehicle, unused road, bunker, hole, crater, cultivated area, formerly cultivated area, former wall, and dry wall. All of these features can be identified in the SAR image.

The data fusion engine in the ARC project is a knowledge model, which aims to transform the signal and features from the landmine detection sensor to a higher degree of abstraction signal (feature or decision) and write the feedback to the sensor. In the ARC system, each sensor datum contains four attributes: the value, the position, the uncertainty and the physical definition (based on the sensor). Based on the Automatic Target Recognition (ATR) technology, the image data are transferred to the feature level, which aims to recognise the landmine free area or the dangerous area on the SAR map [48]. The ATR is a particularly common approach as a pattern-recognition field, which involves classifying the fixed input feature vectors into output target classes when using an  $n$ -dimensional feature space. Figure 2-10 below shows the working principles of the ATR function in the ARC project[49]:

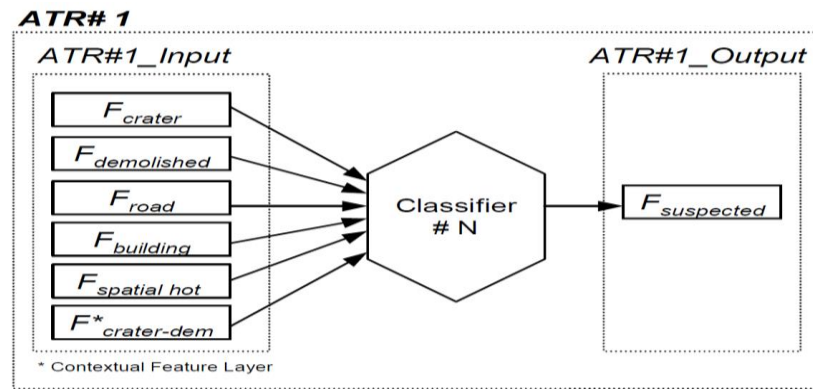


Figure 2-10. ATR function description of the ARC project[49].

According to Figure 2-10, the system extracts certain feature information from the input image, which is used to determine whether the area is mine free or remains suspect. The advantage of the ATR algorithm is it can clearly identify the object features, helping to reduce the mine area effectively. The drawback of this algorithm is its need for a large dataset of the object features which is hard to build. In addition, in some cases, the object feature is unknown for the system and even the operator. The ATR algorithm not only used for mine area reduction, but also for close-range detection as well. However, considering the cost and effectiveness of the system, a non-dataset-based landmine detection method is still needed.

### 2.2.3.2 Space and Airborne Mined Area Reduction Tool (SMART)

The SMART project ran between 2002–2005, with the goal of providing a GIS-based system augmented by dedicated tools and methods designed to be used in a multispectral way, as well as radar data to assist human analysts in the interpretation of a mined area [50]. During its time in operation, SMART focused on landmine presence; it was not a mine detection technology but rather a methodology that integrated a variety of geographical data. The final output of the SMART project was a danger map of the mine area.

The available data for the SMART project include SAR, multi-spectral, high-resolution optical, and satellite data. The SAR data were collected with the ESAR system of DLR in v-polarisation x-band and C-band, as well as in fully polar metric L and P band. The multi-spectral data were collected at a very low altitude (330 m to get a high spatial resolution) in 12 different channels [50], ranging from visible blue to thermal infrared. It is worth noting that the SMART system did not use the GPR image, as such an approach is used for close-range landmine detection whilst the SMART project was used to reduce the mine area. The main contribution of the SMART project was to focus on the multi-model image fusion system design, for, in such a system, the SAR and multi-spectral images have been fused and analysed in the feature level. The available features include bushes/hedges, trees, water, radar shadow, power lines, hilltop detection, roads and abandoned roads [6]. These features are known as landmine suspect marks; if detected, it means that the area is not safe. The danger map has been introduced in this project as the final output: a map produced on the basis of the location and confidence of the fusion result. The danger map contains a complete scene and the main decision as to which locations are mine areas. It is a good idea to have such a map, which could help the end-user understand the environment of the landmine area and the confidence of the SMART systems. Although the danger map idea was designed for the mine area reduction process, it will be worthwhile to implement it in the close-range landmine detection process.

### **2.2.3.3 Ground Explosive Ordinance Detection System (GEODE)**

The Ground Explosive Ordinance Detection (GEODE) project is a FP7 project, which aims to create a vehicle-mounted, multi-sensory, anti-personnel landmine detection system for humanitarian demining. In this project, three types of sensors are used: metal detector (MD), infrared camera (IR), and ground-penetrating radar (GPR) [51].

The sensor's output is processed to produce confidence levels on a grid covering the test bed. The confidence level relates to the confidence or belief in landmine detection at a certain position [52]. The core technology of this GEODE project is based on the decision-level sensor-fusion and co-registration of the sensors. The applied fusion methods include naïve Bayes approaches [29], the Dempster-Shafer theory, fuzzy probabilities and rule-based methods. The results of this research have shown that the rule-based fusion method is better than all other methods regarding the same training and evaluation set. However, the core technique of the rule-based methods is based on the experiences of human experts; hence, the detection ability will also be influenced by human experts.

#### **2.2.3.4 Light Ordnance Detection with Tele-operated Unmanned System**

The Light Ordnance Detection with Tele-operated Unmanned System (LOTUS) project is another landmine detection project sponsored by FP7. The aim of the LOTUS system is to construct a multi-sensor, vehicle-mounted platform for the demining process [53]. The LOTUS PLUS system searches the ground with a metal detector from Foerser (Germany), a downward infrared camera and a ground-penetrating radar from Emrad (UK). The data are analysed in real time at a maximum search rate of 1m/s (forward speed). As the vehicle moves forward, the position of the detected targets are marked, and the data are stored to allow more extensive offline evaluation between the real-time search and any subsequent mine clearance operation.

The IR camera in the LOTUS system includes a 3-5 $\mu$ m (MWIR) Radiance HS camera and a polarimetric IR camera. The HS camera runs at a frame rate of 25Hz and the image is acquired every 0.42m. The polarimetric IR camera is used to acquire the image sequences continuously. The pre-processing of the IR camera data and the polarimetric IR camera aims to calculate the confidence level of the camera outputs.

The pre-processing algorithm performs a normalisation of the image (to remove global variations) as well as certain additional morphology operations to select objects that conform to specified size and shape criteria [53].

The outcome of the LOTUS project is a demonstration of detection capability: in other words, the confidence level of the IR sensors. The confidence level of the sensor outputs can be used for decision-level multi-sensor data fusion to carry out the landmine detection process. The drawback of the LOTUS project is that it only considers the dimensional translation of the platform over the minefield [54].

#### **2.2.3.5 NIITEK**

The NIITEK landmine detection system comprises 24 vehicle-mounted channels of the GPR array and is used to collect data from a variety of test sites (dirt and gravel, roads and lanes, and both landmines and clutter objects) [55]. The NIITEK project uses several algorithms to detect landmines from the GPR images. The only inputs of the NIITEK project are the GPR images, from which a Hidden Markov Model (HMM) and geometric feature FOWA ROCA algorithms are used to find the landmines from the background [56]. This project is different from the GEODE project, since input data are only a raw GPR image. The results of this project show that, by using the HMM algorithm, the NIITEK GPR detection system works more effectively than any other algorithm.

#### **2.2.3.6 D-Box project**

The D-Box is short for a demining tool-box used for humanitarian clearing large-scale areas of anti-personnel landmines and cluster munitions [57]. The D-Box tackles the burning issue of anti-personal landmines and cluster munitions remaining from armed conflicts. It provides demining stakeholders with innovative, ‘easy to use’ and low-

cost solutions interfaced and/or integrated in a comprehensive toolbox [58]. One of the D-Box work packages (WP4) includes the task of designing a data fusion system which will be explained in detail in section 5.1.

#### **2.2.4 Landmine Detection Algorithms Review**

This section reviews the existing landmine detection algorithms for GPR sensors, with the aim to find the advantages and limitations of the current detection algorithms. Methods for automated landmine detection with GPR sensors employ features arising from GPR signals, which can be divided into three types: spatial edge features, spectral features and spatial region features [59]

**Spatial edge features:** The spatial edge features are related to the location and the spatial organisations of changes in a radar reflection signal. In this approach, a high value of the spatial edge feature is associated with the presence of a landmine. Existing landmine detection algorithms employing spatial edge features include the edge histogram descriptor (EHD) and the Hidden Markov Model (HMM).

The edge histogram descriptor is an edge-information-based landmine detection algorithm. It subdivides the raw C-scan 3D GPR image into several down-track overlapping sub-images. For each sub-image, four categories of edge strength (vertical, horizontal, diagonal, and anti-diagonal) and one non-edge category are computed for each neighbored pixel [24]. A static parameter of how many times each category applies in each sub-image is then calculated. If the result for the diagonal category is higher than the result for the anti-diagonal category in the left side of the image and lower in the right side of the image, it indicates the presence of a landmine. If the edge does not follow a specific structure, this represents the absence of a landmine. Hichem Frigui published a journal paper in which a GPR system was used in the landmine

detection process [60]. The GPR sensor used in the study was the NITTEK GPR, which has 51 channels; the adjacent channels are spaced approximately 5cm apart in the cross-track direction and the sequences are taken at approximately 6cm down-track intervals. The following details the EHD algorithm:

1. Consider a 3D image  $C_{(x,y,z)}$  representing the 3D-GPR image, where the  $x$  is the surface horizontal axis,  $y$  is the surface vertical axis and  $z$  represent the depth axis. Then, based on the size of the original image in selecting the window, in the test case, the window is selected as  $30 \times 15 \times 7$ . The size of the window normally depends on the size of the 3D image; in the normal case, the size will allow more than 50% overlap between two continuous windows.
2. Find the edge strength for each pixel under the window. There are a maximum of eight neighbourhood pixels for one pixel in the window; therefore, the large difference between the neighbourhood pixel and the pixel will be the edge strength. If the edge strength is greater than an experienced threshold value  $\theta$ , this pixel will be marked as an edge strength pixel. The  $\theta$  will be manually selected by the operator.
3. Make a histogram of edge strength for the window; the histogram will be the feature of the 3D-GPR image. The detection process can be achieved by comparing the histogram with the existing dataset of the histogram.

Overall, the EHD algorithm is a good landmine detection algorithm. However, the limitation of the EHD algorithm is that window selection does not have rules, and the edge strength calculation depends on an ad hoc parameter. In addition, the EHD algorithm is a feature-extraction algorithm which does not have the ability to detect landmines; it needs a classification algorithm in the detection process.

The Hidden Markov Model (HMM) algorithm treats the down-track dimension as a time variable and produces a confidence value that a mine is present at various positions on the surface being traversed [61]. The HMM algorithm has a background and a mine model. Each model has three states and produces a probability value by backtracking through the model state using the Viterbi algorithm.

**Spectral feature:** Spectral features are related to the energy frequency spectrum of the radar return signal. The rationale behind this GPR feature type is that '*landmine targets and clutter objects have different shapes and/or composition that yield different energy density spectrum (EDS)*' [62]. Spectral feature-based algorithms seek to capture the characteristics of a target in the frequency domain.

The spectral feature algorithm aims to capture the characteristics of a target in the frequency domains. It extracts a false-alarm spectral feature and formulates a confidence value based on similarities to the characteristics of mine objects. The spectral features are derived from the energy-density spectrum of an alarm [63].

An edge-energy-based landmine detection algorithm, developed in our group by M Fayyaz [7], which is aimed at GPR sensor data, has shown very good performance. The edge-energy algorithm was developed based on an existing landmine detection algorithm (edge histogram model [64, 65]); the literature survey has shown that the edge-energy-based algorithm outperforms than other landmine detection algorithms in the out-door environment. The edge-energy algorithm will be used to evaluate the proposed algorithm in sections 4.3, 5.2 and 5.3. Figure 2-11 below shows the flowchart of the edge-energy-based landmine detection algorithm.

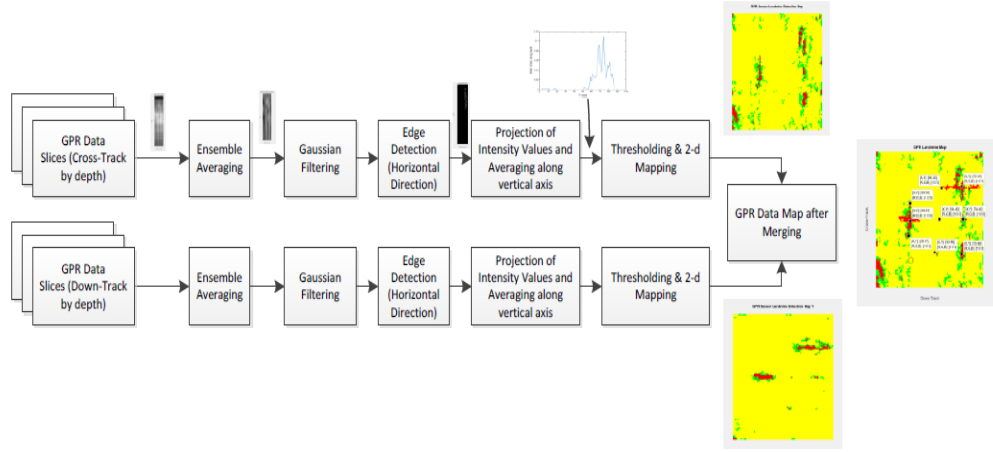


Figure 2-11. Flowchart of the edge-energy-based landmine detection algorithm.

Figure 2-11 has shown that the edge-energy-based algorithm can be divided into four main steps. For each vertical slice of the GPR data, the edge energy is calculated via the following steps:

(1) Ensemble average: consider one of the vertical slices of the raw 3D GPR image as  $A$  and the removed reflections image as  $B$ .  $X(i)$  represents the index of horizontal rows and  $Y(j)$  represents the vertical columns,  $\forall j \in [1, M], \forall i \in [1, N]$ .  $M$  and  $N$  are the length and width of the vertical sliced images. Equation (2.1) shows the ensemble average works.

$$B_{(X(i),Y(j))} = A_{(X(i),Y(j))} - \overline{X(i)} \quad (2.1)$$

(2) Gaussian (low pass) filtering, in which a 3x3 Gaussian kernel is convolved with the data slice in order to remove noise that may be detected during the edge detection phase.

$$B_G \quad (2.2)$$

$$= B * \begin{bmatrix} 0.0113 & 0.0838 & 0.0113 \\ 0.0838 & 0.6193 & 0.0838 \\ 0.0113 & 0.0838 & 0.0113 \end{bmatrix}$$

(3) Horizontal Sobel edge detection, in which a  $3 \times 3$  horizontal Sobel edge detection kernel is convolved with the data slice, calculating the horizontal edge energies at each point.

$$B_S = B_G * G_x \quad (2.3)$$

$$G_x = \begin{bmatrix} -1 & -2 & -1 \\ 0 & 0 & 0 \\ 1 & 2 & 1 \end{bmatrix} \quad (2.4)$$

(4) Use the maximum rules to combine the cross-track and down-track slices into a 3D landmine detection report. Finally, take the mean values of vertical columns to build the 2D landmine report.

The edge-energy algorithm is an existing well-performing landmine detection algorithm, as it can detect landmines without a landmine feature dataset. However, the drawback of this algorithm is it requires lots of calculations. The challenge of this research is to design a landmine detection algorithm which can reach the same level of detection rate with a lower computational complexity.

**Spatial region features:** The spatial region features exploit similarity properties of spatially contiguous radar returns. This approach is based on finding connected components of high energy and calculating region properties. The popular spatial region features algorithm includes the region-selection thresholding algorithm and the K-NN algorithm.

The region-selection thresholding algorithm in [13] employs a spatial energy feature and region features to find the actual landmine in the test area. The energy feature is defined as the square of the GPR reflection value, and a local maxima search method is employed to select the maximum energy value in each region. The decision-making performance of the algorithm is improved by modelling and combining the GPR features in terms of belief functions with the Dempster-Shafer theory. The equation below shows the core of the region-selection thresholding algorithm:

$$E_{(window)} = \sum_{x=1,y=1}^{X,Y} C_{(x,y)}^2 \quad (2.5)$$

Where the  $X$  and  $Y$  represent the size of the window and the  $C$  represents the GPR image, as the  $E_{(window)}$  can only represent the energy level of the window. It is only a feature-extraction algorithm, which still needs a classification algorithm to achieve the detection process. The simplest classification algorithm is hard thresholding. The region-based algorithm offer a good idea of the landmine detection process, as it is simple to implement. However, the detection accuracy is not good, so the challenge is to design a high-performing, region-based landmine detection algorithm.

The K-NN classification rule is a voting scheme that is widely used in pattern recognition and classification problems [37]. It can work with the EHD algorithm to detect landmines. A common drawback of the crisp K-NN classification rule is that the K-nearest training patterns are treated as equally important in the confidence assignment of the test pattern. In some cases, the K-NN classifiers cannot discriminate between neighbours that are equally close and neighbours that are equally far way.

In summary, this sub-section has reviewed existing landmine detection algorithms, most of which are feature-extraction algorithms, which still need a classification

algorithm to support detection. The research gap here is to design a feature-based landmine detection algorithm which can use an appropriate signal feature to represent landmine presence and improve the region-based detection algorithm.

## **2.3 Image Fusion Technology**

The image fusion module in the landmine detection system is capable of providing a visual interface of the upper computer system. This sub-section will review image fusion applications, algorithms, and evaluation parameters in detection systems.

### **2.3.1 General Principle of Image Fusion**

Image fusion is a research area belonging to data fusion. Image fusion is the fusing of two or more images to output a new image, emphasising the colour, resolution or sharpness of the original images [66]. The steps of image fusion can be divided into image registration, image filtering, pixel-level evaluation, selection or fuse, image rebuilding and optimisation. The image registration controls the image's size or visual angle, as well as its store format [67]. To fuse image data, the source images should have at least one relevant point. All image data should then be pre-processed to filter the noise signal before the fusion process. The CPU subsequently evaluates image data by using fixed algorithms. The data fusion centre uses corresponding fusion algorithms or selection rules to fuse the image data. According to the timing sequence of the input image data, the data fusion centre starts rebuilding the image before it is eventually released as an output.

Image fusion derives from image processing [68], and both use pixel data as the input signal. However, whilst the output of image processing can be text data, image data or a decision, the output of image fusion can only be image data. Image fusion processing normally includes multi-modal, multi-type and multi-focus image fusion. Multi-modal

image fusion combines two different types of images [67, 69]. This technology is normally used in remote sensing. In multi-type image fusion, two images from different sensors are fused (e.g. an image from the infrared camera with an image from a millimetre wave sensor) [70]. This technology is usually used in crime detection. In multi-focus image fusion, two or more images are fused from the same type of camera, meaning the image has the same visual angle but different foci [71]. This technology can be used in the military for precision guiding.

Multi-modal image fusion is often considered as remote sensing. Although remote sensing is not that relevant when it comes to landmine detection system design, some of its achievements can be used as reference points. The image fusion part of remote sensing is mainly concerned with fusing a panchromatic (PAN) [72] image with a multispectral (MS) image. The fundamental problem of remote sensing is data association. The multi-modal image fusion algorithm includes the nearest neighbour (NN), joint probabilistic data association (JPDA) [69] and the multiple hypothesis testing approach. JPDA uses a weighted average of all measurements as a selection standard [73].

Multi-type image fusion has been used in many studies relating to terrorism detection, such as airport security, bomb detection, and object tracking. To date, only the airport security system has been used in daily life. Figure 2-12 shows how an IR sensor and MMW sensor can be fused to detect guns [74]. The left image is taken by an IR camera, good for presenting human features but not good at gun detection. The right image is from a MMW sensor, which is sensitive to guns but loses human features. The bottom image is the fusion result, which tries to fuse these two different types of sensors. The result confirms that multi-type data fusion works well in terrorism detection. This is a successful application, having proved useful in building explosive detection systems.

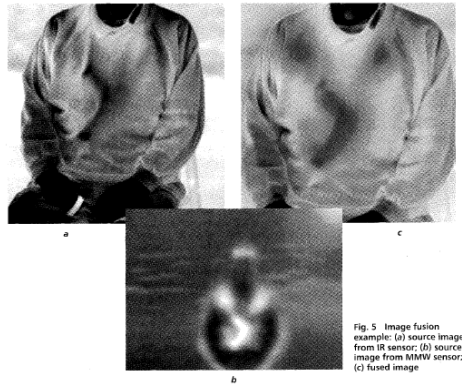


Figure 2-12. Application of multi-sensor data fusion [32].

Multi-focus image fusion processing can be done at the pixel level, feature level and decision level, according to the requirements of the design. Pixel-level image fusion processes each pixel separately using a selection method to determine the useful pixels from the original images and to re-organise the image to produce the fusion result [75]. Feature-level image fusion is concerned with finding the feature for each image and representing the main feature of each image in the fusion result. Decision-level image fusion focuses on selecting and subsequently displaying the most useful image from a group of images.

Pixel-level multi-focus image fusion can be achieved through two common schemes. The first is based in the frequency domain and uses a multi-resolution approach to fuse the image. The general methods in the frequency domain are Discrete Wavelet Transform (DWT) [76], Contrast Pyramid (CP) [77] and Wavelet Transform (WT) [78]. These methods are complicated and difficult to implement. The second scheme is based in the time domain and uses general selection rules to rebuild images. Several fusion algorithms in the time domain have already been discovered, such as Intensity-Hue-Saturation (IHS), Principle Components Analysis (PCA) [79] and Brovey Transform (BT).

### 2.3.2 Image Fusion Algorithms

Wide ranges of algorithms have been developed to achieve image fusion. Different algorithms have their own features, some of which suit multi-modal image fusion whilst others are more relevant to multi-type sensor fusion. It is logical to divide image fusion algorithms into fusion algorithms and selection rules. As previously described, a fused algorithm is mainly concerned with transforming image data into another state whereas selection rules focus on how to determine the final fusion result. In the following section, a number of classical fused algorithms will be explored.

#### 2.3.2.1 Intensity-Hue-Saturation method (IHS)

Intensity-Hue-Saturation transformation (IHS) is widely used in RGB format image fusion. The principle of the IHS transformation is to represent the spectral information of the RGB composition in the  $H$  and  $S$  components and separate most of the spatial information in the  $I$  component [80]. As such, the  $H$  and  $S$  components represent the main feature of RGB format images. The  $I$  component describes the total colour brightness of the images [81]. In multi-modal image fusion, the main step involves swapping the  $I$  component to produce a high-resolution colour image [78]. However, in multi-focus image fusion, swapping the  $I$  component does not work. The fusion result can only be achieved by using the likelihood ratio method or by taking the average method to evaluate the  $H$  and  $S$  components. The  $I$ ,  $H$ , and  $S$  components are subsequently swapped to gain the fusion units. The details of the IHS algorithm will be describe below.

The first step is to transform the visible image into an Intensity-Hue-Saturation matrix using IHS transformation rules. The equation is shown below:

$$\begin{bmatrix} I \\ v_1 \\ v_2 \end{bmatrix} = \begin{bmatrix} \frac{1}{3} & \frac{1}{3} & \frac{1}{3} \\ -\frac{\sqrt{2}}{6} & -\frac{\sqrt{2}}{6} & \frac{\sqrt{2}}{6} \\ \frac{1}{\sqrt{2}} & -\frac{1}{\sqrt{2}} & 0 \end{bmatrix} \begin{bmatrix} R \\ G \\ B \end{bmatrix} \quad (2.6)$$

Several different fusion methods can be used to fuse the intensive matrix, once the intensive matrix of  $I_v$  is obtained. The simplest method to fuse two images is to use the average of the two matrixes to re-build the  $I_f$ . The following set uses the fused matrix to re-build the fused image; the equation of the inverse transformation rules is shown as follows:

$$\begin{bmatrix} F(R) \\ F(G) \\ F(B) \end{bmatrix} = \begin{bmatrix} 1 & \frac{-1}{\sqrt{2}} & \frac{1}{\sqrt{2}} \\ 1 & \frac{-1}{\sqrt{2}} & -\frac{1}{\sqrt{2}} \\ 1 & \sqrt{2} & 0 \end{bmatrix} \begin{bmatrix} I_f \\ v_1 \\ v_2 \end{bmatrix} \quad (2.7)$$

Based on the method mentioned above, the fusion result, containing both features of the two originals, is obtained. The IHS algorithm is easy to implement; however, it can only work for an RGB format image. In this case, most of the time, the IHS algorithm is not a good choice, since the input image format will be changed.

### 2.3.2.2 Principle Components Analysis (PCA)

As a way of describing image information in a hierarchical decomposition, PCA has been successfully applied in the field of digital signal processing [79]. The PCA algorithm is based on the eigenvector of covariance matrices of the source image, which represents the weight of the images. The PCA transformation uses the source image to multiply the eigenvector to represent the components of the original image. It is possible to combine the PCA fusion method with the pyramid-based fusion method, resulting in the images being divided into several parts. Each part is subject

to the PCA transformation, which uses a set of chosen selection rules to re-configure every part together as a new fusion result [82]. Although such an approach could be particularly effective in multi-modal image fusion, the evidence suggests it would be less so in multi-focus image fusion processing.

### 2.3.2.3 Brovey Transform Algorithm (BT)

The Brovey transform algorithm is normally used to fuse multispectral and panchromatic images. This is a pixel level-based method; the equation below describes how three multispectral images and one panchromatic image are fused. The fusion result equals the weight of the band plus the weight of the panchromatic image. Regarding the three multispectral images with respect to the RGB value, the fused red layer will be equal to  $R/(R+G+B)+P$ .  $P$  is the panchromatic image value [83, 84].

$$DN_{fused_i} = \frac{DN_{band_i}}{DN_{band_1}+DN_{band_2}+DN_{band_3}} + DN_{pan} \quad (2.8)$$

The Brovey transform is an efficient algorithm in the field of image fusion, which generates good visual performance for images. The benefit of this algorithm is that it is easy to achieve, and the fusion result is capable of representing all band image information with a high-colour attribute. The drawback of this method is that the average pixel weight does not represent the importance of the pixel properly.

### 2.3.2.4 Wavelet Transform Algorithm (WT)

The wavelet transform algorithm is a traditional frequency domain fusion algorithm, which is itself an extension of the ideas behind high-pass filtering [85]. The main principle of this algorithm is the transference of signals from the time domain to the frequency domain using Fourier transforms. The image signals are then fused to

produce a more informative image. The equation of the wavelet transform is shown below:

$$WT(a, b) = \frac{1}{\sqrt{a}} \int_{-\infty}^{+\infty} f(t) \Psi\left(\frac{t-b}{a}\right) dt \quad (2.9)$$

Where  $WT(a, b)$  is the wavelet coefficient of the function  $f(t)$ ,  $\Psi$  is the analysing wavelet, and  $a$  ( $a > 0$ ) and  $b$  are scaling and translational parameters, respectively [86].

This algorithm provides a multi-resolution framework where the signal is decomposed into several components, which capture the information present at any given scale. This enables the introduction of the concept of details between successive levels of scale or resolution, and, if the process is inverted, the original image can be reconstructed from one approximation and different wavelet coefficients [87]. Image fusion using the WT approach can improve the spatial resolution with minimal distortion of the spectral content of the source image. The drawback of the WT algorithm is that the image's column and row should be to the power of 2 [88]. Consequently, if the fusion centre wants fused parts of the whole image, the selection part size also needs to be to the power of 2. The drawback of the wavelet transform algorithm is that it cannot provide a shift-invariant system, so this algorithm is not suitable for certain unique image fusion cases.

#### 2.3.2.5 Tour Algorithm

Being a subset of the wavelet transform, the tour algorithm is also known as the discrete wavelet transform [89], used to obtain shift-invariant discrete wavelet decomposition for images. Figure 2-13 shows the different WTs as well as the tour algorithm itself.

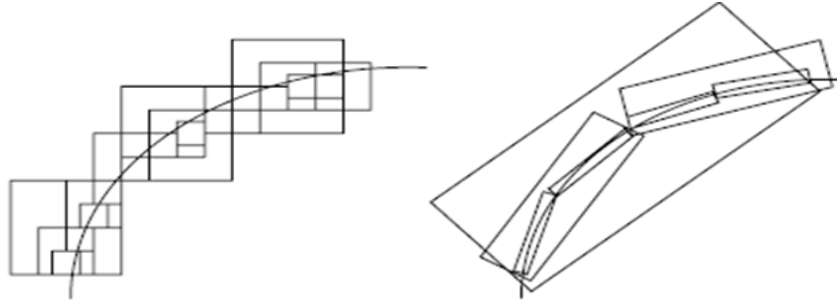


Figure 2-13. Wavelet representation and a tour representation [45].

According to Figure 2-13, the design principle of these two methods are clearly different. Where WT is applied to determine the isotropy of images, the tour method presents the singularity of their anisotropy (i.e. the whole feature of the images). Therefore, in some unique image fusion cases, using the tour method could gain better results than the WT [80].

If we consider  $f(x, y)$  as the given image, the first step involves doing the Laplace transform.

$$L[f(x, y)] = f_1(x, y) \quad (2.10)$$

The wavelet planes are computed as the differences between two consecutive approximations:  $f_{j-1}(x, y)$  and  $f_j(x, y)$ . If we consider  $w_j(x, y)$  as wavelet coefficients of two dimensions at resolution level  $j$ , then  $w_j(x, y) = f_{j-1}(x, y) - f_j(x, y)$ ;  $j=1 \dots j$ . Based on this, we have the reconstruction equation, as shown below [90]:

$$f(x, y) = \sum_{j=1}^j w_j(x, y) + f_1(x, y) \quad (2.11)$$

The likelihood ratio selection rule is one of the most popular selection rules in the field of data fusion, as it can fit into the multi-focus image fusion model. The selection rule is based on statistical methods, which work on the basis that the fusion pixel follows

discrete probability distributions. The step of this method involves using fusion methods to process the original images to produce the fusion unit [91]. The distance between fusion unit and two original pixels is then measured. Finally, the corresponding pixel is selected to rebuild the fusion result. These selection rules judge the pixel based on which image has the most probability of being represented.

## **2.4 Summary**

This chapter reviewed the principles of data fusion technology and introduced the concept of data fusion with regards to landmine detection. The review of the existing landmine detection systems identified the need of feature-level data fusion methods in landmine detection. The literature survey on the existing landmine detection sensors showed that the GPR and MD sensors were suitable for feature-level fusion algorithm design.

Several existing landmine detection projects were reviewed, including the ARC, SMART and GEOGE, showing that data fusion technology can help current landmine detection systems to either reduce redundant data or improve detection performance. Existing landmine detection algorithms were also reviewed, with a particular focus on the GPR sensor. Findings indicate that the use of 3D-GPR landmine detection algorithms can reduce the false alarm rate and improve detection accuracy.

Finally, image fusion technology, a specific research topic in the data fusion field, was also addressed in this chapter. This study showed that multi-modal and multi-focus image fusion technology methods can be used to improve the output performance of optical cameras, which may assist in surface landmine detection processes. The literature survey on the image fusion algorithms indicated that image fusion algorithms can improve the fusion visual results and reduce computational complexity.

# **Chapter 3: Design of a Pixel-based Multi-Focus Image**

## **Fusion Algorithm**

This chapter focuses on multi-focus image fusion algorithm design, with the aim to improve the output quality of optical cameras in surface landmine detection.

Section 3.1 provides the background and objectives of multi-focus image fusion research. Section 3.2 explains how the new proposed multi-focus image fusion algorithm works. Section 3.3 demonstrates the fusion result of the proposed algorithm. Section 3.4 summarises the whole chapter.

### **3.1 Introduction**

Multi-sensor data fusion is a set of techniques that process the data collected from different types of sensors to make a decision or to generate a higher level of information content than that provided by single sensor data. Normally, data fusion includes image fusion, sound fusion and decision-making. Image fusion involves combining two or more image signals to output a new image, whereby the colour, resolution or sharpness of the original images have been enhanced. Image fusion processing normally includes multi-modal, multi-sensor, and multi-focus image fusion [92]. Multi-modal image fusion combines two different types of images, such as fusing a high-resolution image with a high-colour image [93]. This technology is normally used in remote sensing, in this research a multi-modal image fusion algorithm has been designed, which aims to using the IR images and optical images to identify landmines laid on the surface of mine area (see Appendix A). Multi-sensor image fusion fuses images from different kinds of sensors, such as fusing an image from an infrared sensor with an image from a millimetre wave sensor. Such a data fusion type is

typically employed in crime detection. Multi-focus image fusion is a kind of cooperative data fusion process, which aims to fuse two or more images captured by the same type of camera with the same visual angle but with different foci to produce a more informative image. This technology is often used in military applications, such as precision guidance.

Landmine detection systems (LDS) are one targeted application area for multi-focus image fusion algorithms [94]. Preliminary investigations have shown that two main types of humanitarian mine actions may benefit from multi-sensor data fusion technology: mined area reduction and close-range antipersonnel mine detection. The former aims to identify the mine free area from the mine suspected areas, while the latter is concerned with detecting surface anomalies and underground metal in the suspected area. Close-range antipersonnel mine detection involves the collection and integration of multi-focus images from a range of cameras to identify features of the environments and objects in the suspected landmine area. Since an optical camera cannot capture more than one region of interest, several images with the same visual angle but a different focus are normally taken. This leads to a lot of redundant information in the LDS. Multi-focus image fusion algorithms can remove the redundant information from the input images and re-construct the output image without compromising the useful information content. Such algorithms can help to reduce the image size and save energy in the analysis process.

The multi-focus image fusion technique could also be employed by other applications. The unmanned ground vehicle binocular system uses two optical cameras, simulating the two eyes of human beings, to collect road information. In such a case, the multi-focus image fusion algorithm could help to fuse the input images from two optical

cameras and generate a more informative image, which could be applied to object detection and distance detection processes.

Multi-focus image fusion research belongs to the field of adaptive image processing techniques. Simply put, the basic requirements of multi-focus image fusion are to select useful pixels from the two original input images and to build a new output image that includes the features of both images. The higher-level requirement of the multi-focus algorithm is a high-quality visual of the fusion result, effective and easy to implement. This technique can be applied to the fusion of close shot images in many applications that require adaptation, such as adaptive close-range landmine detection systems. In addition, multi-focus image fusion algorithms can reduce the amount of redundant image pixel data, which can reduce the data size of the final output image. Overall, multi-focus image fusion algorithms can improve the quality of the captured raw sensor images and save energy during their subsequent transference to the user.

### **3.2 Multi-focus Image Fusion Algorithm Design**

The main aim of multi-focus image fusion is to fuse two or more images with the same visual angles but with different foci to output one image that is more informative than any of the other input images. A new algorithm based on the PCA fusion method has been proposed in this research. Figure 3-1 below shows the flowchart of the new proposed PCA-based multi-focus image fusion algorithm.

The original inputs are two different focus images from two optical cameras, referred to as  $I_{1(x, y, z)}$  and  $I_{2(x, y, z)}$ . Both of these two images are represented in RGB format and should incorporate the same visual angle. Each image will have  $M \times N \times 3$  pixels.  $M$  and  $N$  represent the number of rows and columns, respectively, in each image; the  $x$  and  $y$

represent the index of the rows and columns, and  $z$  represents the index of layers, in this case  $x \in [1, M]$ ,  $y \in [1, N]$ ,  $z \in [1, 3]$ .

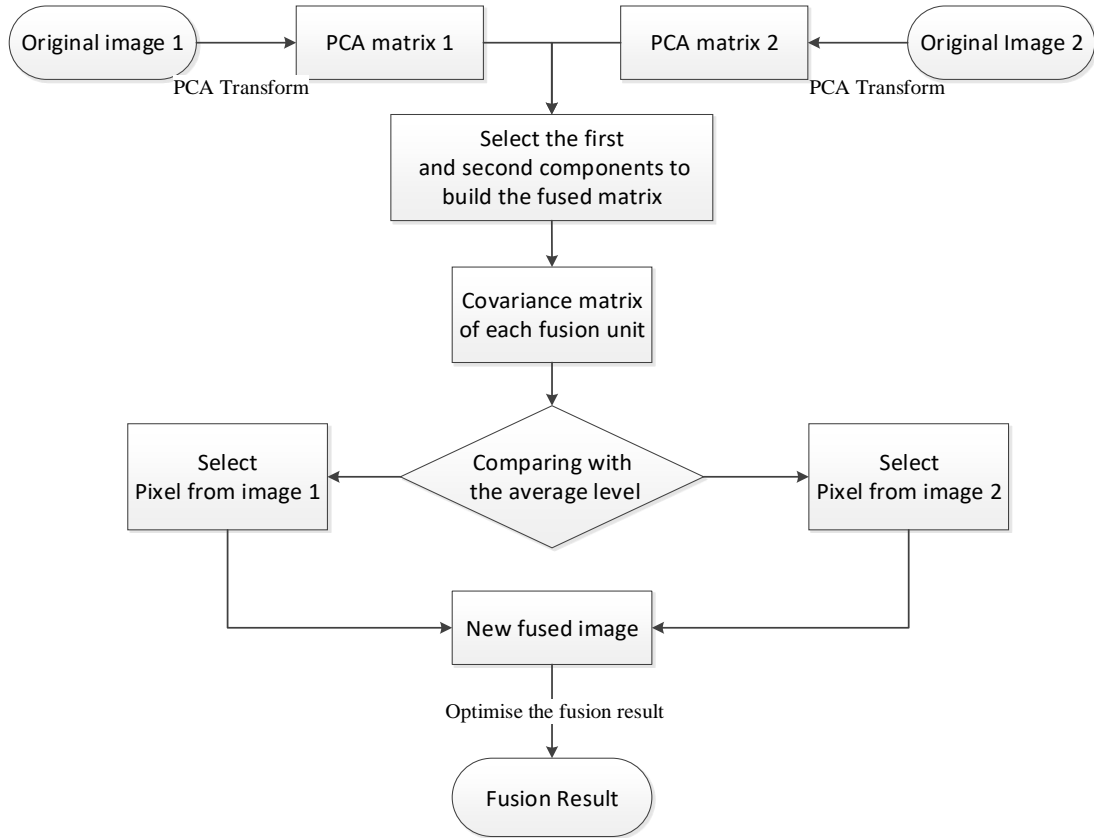


Figure 3-1. Flowchart of the new proposed PCA-based multi-focus image fusion algorithm.

The steps of the proposed PCA-based algorithm are, first, the first step is running a PCA transform for both image1 and image2. The covariance matrices of  $I_{1(x, y, z)}$  and  $I_{2(x, y, z)}$  are calculated separately. Because these two matrices are three-dimensional images, each pixel group at  $X_{(x, y)}$  is represented as a column matrix:  $X=[R; G; B]$  and  $X^T=[R, G, B]$ . Thus, the equation of the covariance matrix becomes:

$$COV(I) = \sum(X \times X^T) / M \times N - (\sum X / M \times N) \times (\sum X^T / M \times N) \quad (3.1)$$

This matrix represents the population variance of  $I_{(x, y, z)}$ , where the size of the matrix is  $3 \times 3$ . Each eigenvector of the  $COV(I_1)$  and  $COV(I_2)$  is calculated. There are three eigenvectors of each matrix, which represent the components of the matrix. One layer of the original image is selected to carry out the PCA transform. In this case, the Red layer has been used as the sample to achieve PCA transform, the PCA transform will be as follows:

$$R_1 = \text{Largest eigenvector} \times R \quad (3.2)$$

$$R_2 = \text{Medium eigenvector} \times R \quad (3.3)$$

$$R_3 = \text{Smallest eigenvector} \times R \quad (3.4)$$

$R_1$ ,  $R_2$ , and  $R_3$  represent the components of the covariance matrix;  $R_1$  is the main component and will provide a greater contribution than the other two. The new image size will still be  $M \times N \times 3$ , and the first layer  $R_1$  will consist of the main component of the PCA matrices. The first step has achieved a PCA transform for the original images, in the other types of PCA multi-focus image fusion algorithm, only the first layer will be selected to accomplish the fusion process[11]. In such a case, some of the useful information in other components will be ignored, which could lead to a low performance of the fusion results.

The second step is based on the PCA transform result in building a new fusion matrix which contains both the first and second components of the original images. This is the novel part of the proposed algorithm, which could improve the quality of the fusion result. The new fusion matrix in the proposed algorithm is construct by  $M \times N$  blocks, which represent the pixel group at location  $[x, y]$ ; these blocks have also been named as the fusion unit. Each fusion unit contains four elements, which are the main and second components from both image1 and image 2. Figure 3-2 shows the structure of

fusion matrix.

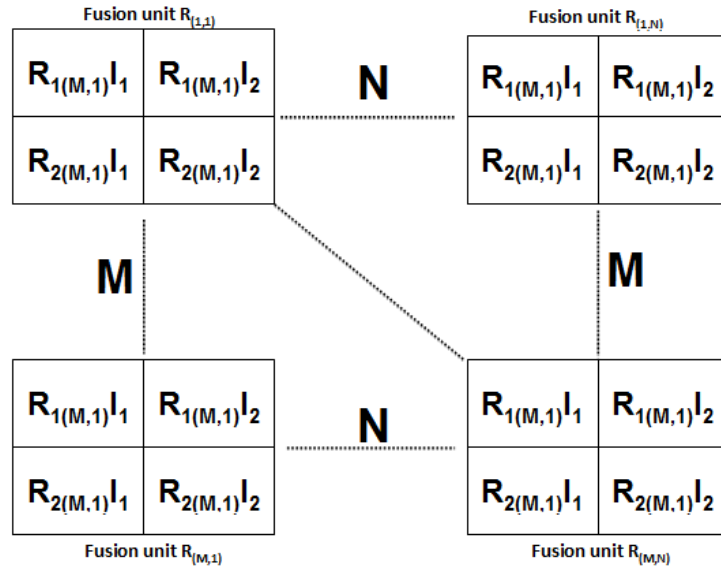


Figure 3-2. Multi-focus image fusion matrix.

In Figure 3-2, it is clear to see that the size of the new fusion matrix is  $M \times N$ , which is based on the original input images size. For each fusion unit, the  $R_{1(x,y)}$  is on the top layer, which is because it is the major component of the original image. In addition, the component from  $I_1$  has been put in the left side, and the component from  $I_2$  has been put in the right side, which means the  $I_1$  is considered as the image base of the fusion result: once the two images show the same information at one particular position, only the information from  $I_1$  will be selected. Each fused unit has no correlation with its neighbourhood. Therefore, the sub-matrix of the new fusion matrix can be used to implement the new decision rules for the image fusion process.

The third step is to extract the feature of the fusion unit and, based on the selection rules, to fuse the input images. In the proposed algorithm, the covariance matrices of the fusion unit have been treated as the feature of the fusion unit, as it can represent the correlation between different dimensions. In this case, if the correlation between each sample can be quantified, then the fusion rules could be designed for comparing

the selected feature of the fusion unit. The covariance matrices of each fusion unit are calculated to give  $M \times N$  matrices of size  $2 \times 2$ . These matrices represent the pixel group's weight in the whole image. The selection rule compares the weight of each pixel group with the corresponding estimate matrix, which is the average of Fusion Matrix Covariance (FMC). In this case, each covariance matrix contains four elements, and each element will be compared separately. If more than two of the elements in the covariance matrix of the fusion unit is greater than the estimate matrix's feature, it means the weight of the pixel group is greater than the estimate matrix. Once this has happened, it means that the pixel in  $I_1$  will represent the fusion result perfectly and vice versa.

After the fusion processing, most of the pixel groups are expected to show their weights clearly across the selection boundary; however, some pixel groups' weights might be too close to the boundary of the selected weight, resulting in a poor image reading performance. Based upon these two factors, an optimisation method is needed to improve the performance of the proposed multi-focus image fusion algorithm.

The last step is to optimise the fusion result, which aims to reduce the computational complexity and improve the fusion result. The optimisation step is an additional step, which can be ignored if there is no high-quality requirement of the fusion result. To reduce the complexity of the algorithm, some unnecessary steps can be skipped. Due to the fact that the principle diagonal of the matrix represents a feature of this matrix, only the principle diagonal is useful in these selection rules, meaning it could be used to help reduce the number of comparison operations  $2 \times M \times N$  times.

The optimisation method for the proposed algorithm is based on the rules of K-Nearest Neighbourhood (K-NN), with the basic model adhering to such an approach. The aim of the optimisation step is to reduce the influence of the noise signal of the fusion

result. To assess whether a particular pixel’s decision value has been influenced by the noise or not, a voting process of the neighbourhood pixels can be used. In the K-NN algorithm, each pixel has eight neighbourhoods, and all these neighbourhoods have the same weight in voting per the decision of pixel K [95]. In general, the K-NN regression algorithm will be used to optimise the fusion result. The benefits of this method are easy to implement and effective. Furthermore, the drawback of this method is that the neighbourhood pixel has its own uncertainty, for it will influence the quality of the fusion result, and, for the corner and edge pixel, it is hard to find enough neighbour pixels. In this case, a novel idea has been introduced here to provide another choice instead of the K-NN regression algorithm. The confidence-level conception from the multi-sensor data fusion area has been used here to represent the weight of the neighbour pixels. The optimisation step will be executed row by row in the fusion result image, starting at the top-left corner of the image and finishing at the right-bottom corner. Figure 3-3 shows the confidence level of neighbour pixels for a normal case in the fusion result.

K1 Confidence level: 1	K2 Confidence level: 1	K3 Confidence level: 1
K4 Confidence level: 1	Current point	K5 Confidence level: 0.5
K6 Confidence level: 0.5	K7 Confidence level: 0.5	K8 Confidence level: 0.5

Figure 3-3. Confidence level of neighbour pixels for a normal case in the fusion result.

Each pixel has eight neighbourhood pixels, which are numbered from K1-K8. The confidence level of the pixel before the current pixel is worth 1 point, as these points have already been determined. The confidence level of the pixel after the current pixel

is not worth 1 point, as these pixels have not been optimised and might be changed later. Since only two images have been taken as the input in this case, the confidence level from  $K5-K9$  equals 0.5. Neighbourhood pixels that have changed or will change later by the fusion decision are marked as 1 whilst the other pixels are marked as 0. Once the sum of the neighbourhood pixels' weight is greater than 3.5 (indicating that more than four neighbourhood pixels have been or will be changed later), then the current point will be changed and vice versa.

The proposed PCA-based multi-focus image fusion algorithm has been based on the existing PCA conception, which can satisfy the basic requirements of the multi-focus image fusion algorithm. The two novelty parts of the proposed algorithm are using the covariance matrix to achieve the feature level multi-focus image fusion and introduced the confidence-level conception to the K-NN regression algorithm. These two novelty parts are the core technique of the proposed algorithm, which are different from other types of PCA-based multi-focus image fusion algorithms. The following section will show the simulation results of the proposed algorithm, which can determine whether the proposed algorithm could reach the higher-level requirements of the multi-focus image fusion algorithm or not.

### **3.3 Simulation Results and Analysis**

This section aims to show the performance of the proposed multi-focus image fusion algorithm within the MATLAB environment. A dataset of the multi-focus images from [www.datafusion.com](http://www.datafusion.com) has been introduced into this experiment, including approximately 140 pairs of multi-focus images. Each pair includes two images that have the same visual angle but a different focus. The classical IHS algorithm, IHS with the K-NN optimisation algorithm, PCA algorithm, PCA with K-NN optimised

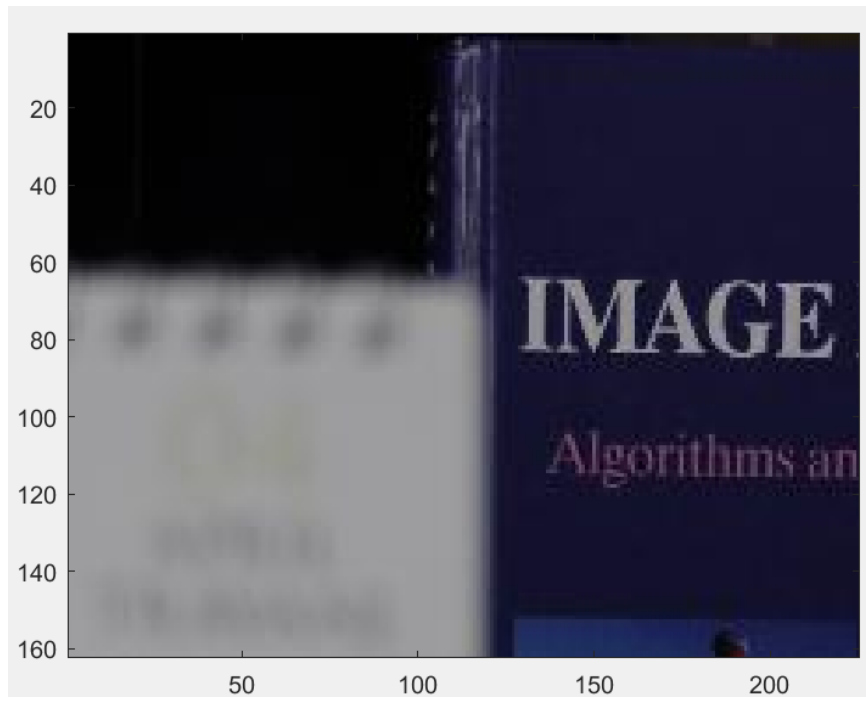
algorithm and proposed fusion algorithms have been employed as candidates for comparison to determine which is most suitable for improving the optical camera of the landmine detection process. The reference image will be the manually selected focus image, known as the ideal fusion result. Evaluation of the algorithms will be conducted across three sections: visual inspection, quantitative evaluation, and complexity level evaluation.

### 3.3.1 Visual Analysis

The simplest way to evaluate an image fusion algorithm is by visually inspecting the fusion result. Four pairs of test images have been selected from the dataset to demonstrate the advantages of the proposed PCA-based multi-focus image fusion algorithm, as illustrated in Figures 3-4, 3-5, 3-6 and 3-7. Figure 3-4 shows the comparison result of all the reference algorithms with the proposed algorithm. Figures 3-5, 3-6 and 3-7 show that the proposed algorithm performs well when the focus points have changed.



(a)



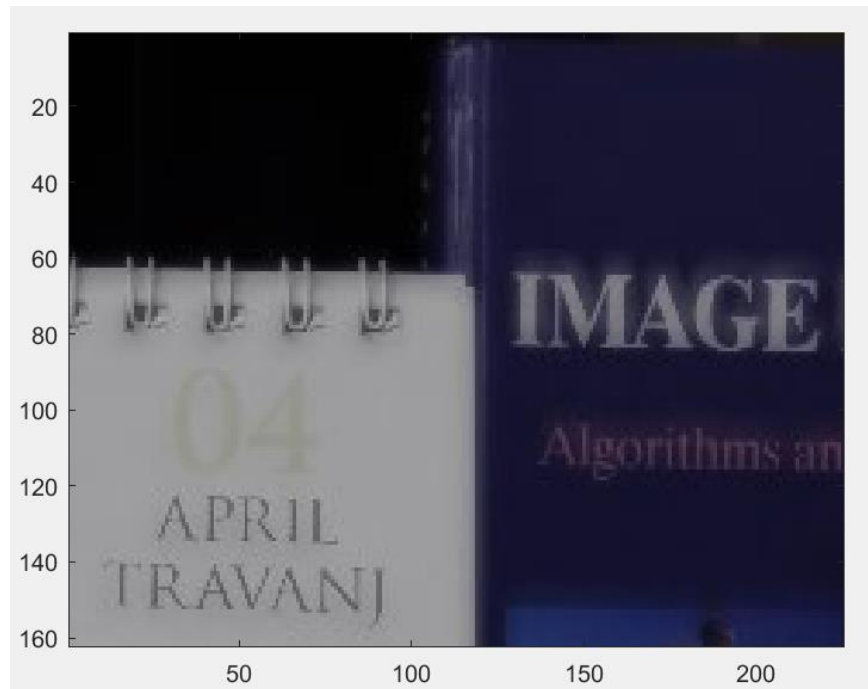
(b)



(c)



(d)



(e)



(f)



(g)



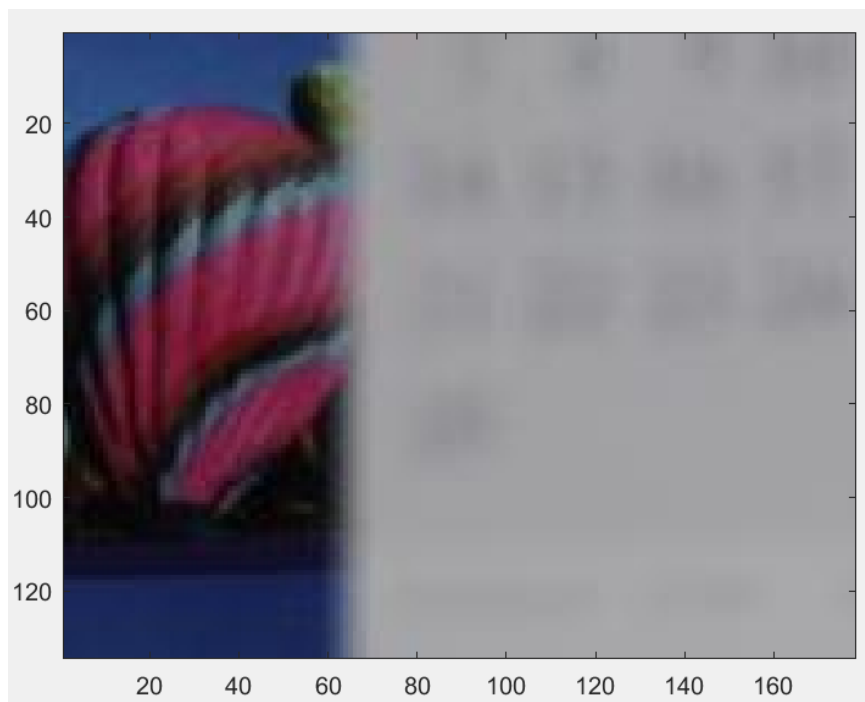
(h)

Figure 3-4. Multi-focus image fusion results.(a) Original left focus image. (b) Original right focus image. (c) Manually cut reference image. (d) Using IHS method to fuse the images. (e) Using IHS method after the optimised fusion of the images. (f) Using PCA method to fuse the images. (g) Using PCA method after the optimised image fusion. (h) Proposed algorithm fusion images (original images from <http://dsp.etfbl.net>).

In Figure 3-4, (a) and (b) are the original multi-focus images, and image (c) is the reference image, which is manually selected for the focus position and montaged to one perfect fusion image. Visual inspection shows that Figure 3-4 (h) represents the best fusion result for the test image, which is quite similar to the reference image. This Figure (e) is also relatively good; however, because the IHS method uses the average of each point, each pixel has suffered from slight distortion. Figures 3-4 (f), (g) are better than (d), although these two images faced the same problem in that the edges are indistinct. To solve this problem, the optimisation method of section 3.2 was partially used.

Figures 3-5, 3-6, and 3-7 represent the results of tests that used three other test images, whereby (a) and (b) are the original images, (c) is the manually cut reference image and (d) is the fusion result achieved by the proposed fusion algorithm. Figure 3-5 shows that the proposed PCA-based fusion algorithm is suitable for images with a left-right focus visual angle. Figure 3-6 shows that the proposed algorithm is suitable for images with a top-bottom focus. Figure 3-7 shows that the algorithm is suitable for images with a diagonal focus.

The visual analysis of the four test cases, as illustrated in Figures 3-4, 3-5, 3-6 and 3-7, shows that the proposed algorithm works well when the focus point changes. The proposed algorithm can identify the clear parts of the input images and is not influenced by the location of the focus point changing. These results show that the proposed algorithm can adapt to different types of focus placement in the original images. In addition, the proposed algorithm belongs to the family of adaptive image fusion algorithms.



(a)



(b)

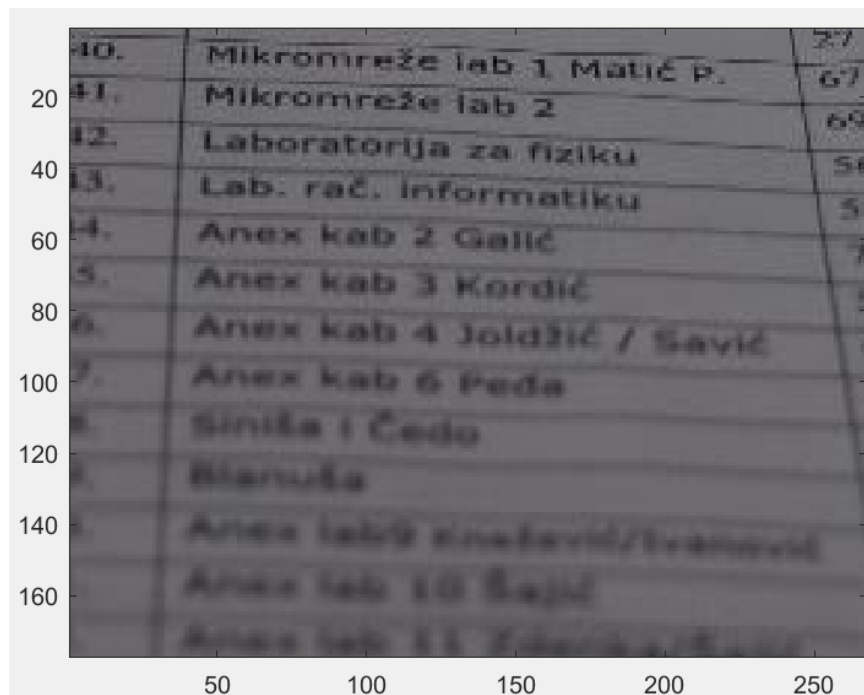


(c)



(d)

Figure 3-5. Multi-focus image fusion result.(a) Original left focus image. (b) Original right focus image. (c) Manually cut reference image. (d) Proposed algorithm fusion result (original images from <http://dsp.etfbl.net>)



(a)

20	40	Mikromreže lab 1 Matić P.	27			
	41	Mikromreže lab 2	67			
	42	Laboratorija za fiziku	69			
	43	Lab. rač. informatiku	5			
	64	Anex kab 2 Gallić	7			
	65	Anex kab 3 Kordić				
	66	Anex kab 4 Joldžić / Savić				
	77	Anex kab 6 Peđa				
	88	Siniša I Čedo				
	99	Blanuša				
	100	Anex lab9 knežević/Ivanović				
	160	Anex lab 10 Šajić				
		Anex lab 11 Zdenka/Šalić				
		50	100	150	200	250

(b)

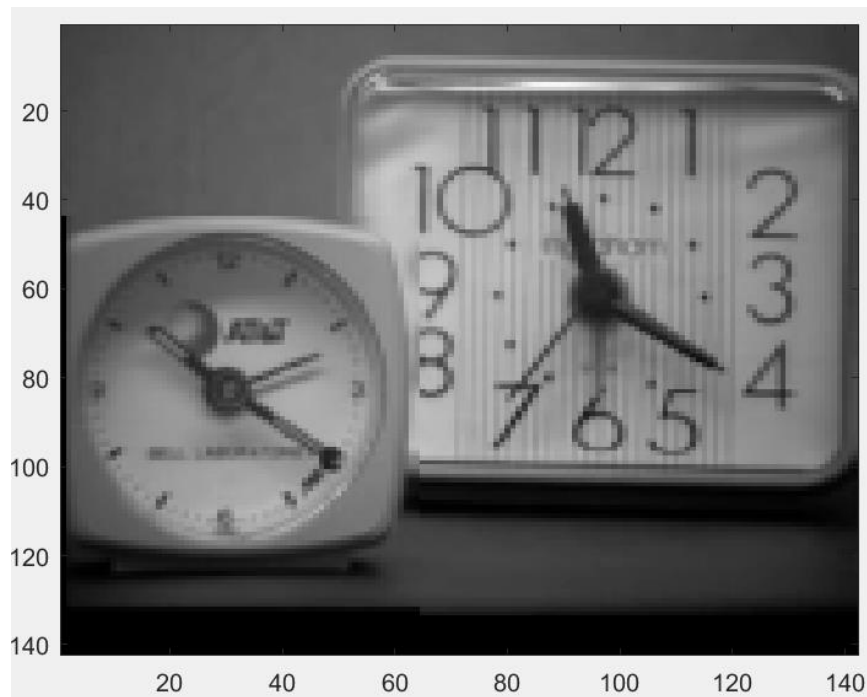
20	40	40.	Mikromreže lab 1 Matić P.	27			
	41	41.	Mikromreže lab 2	67			
	42	42.	Laboratorija za fiziku	69			
	43	43.	Lab. rač. informatiku	5			
	64	44.	Anex kab 2 Gallić	7			
	65	45.	Anex kab 3 Kordić				
	66	46.	Anex kab 4 Joldžić / Savić				
	77	47.	Anex kab 6 Peđa				
	88	48.	Siniša I Čedo				
	99	49.	Blanuša				
	100	50.	Anex lab9 knežević/Ivanović				
	160	51.	Anex lab 10 Šajić				
		52.	Anex lab 11 Zdenka/Šalić				
			50	100	150	200	250

(c)

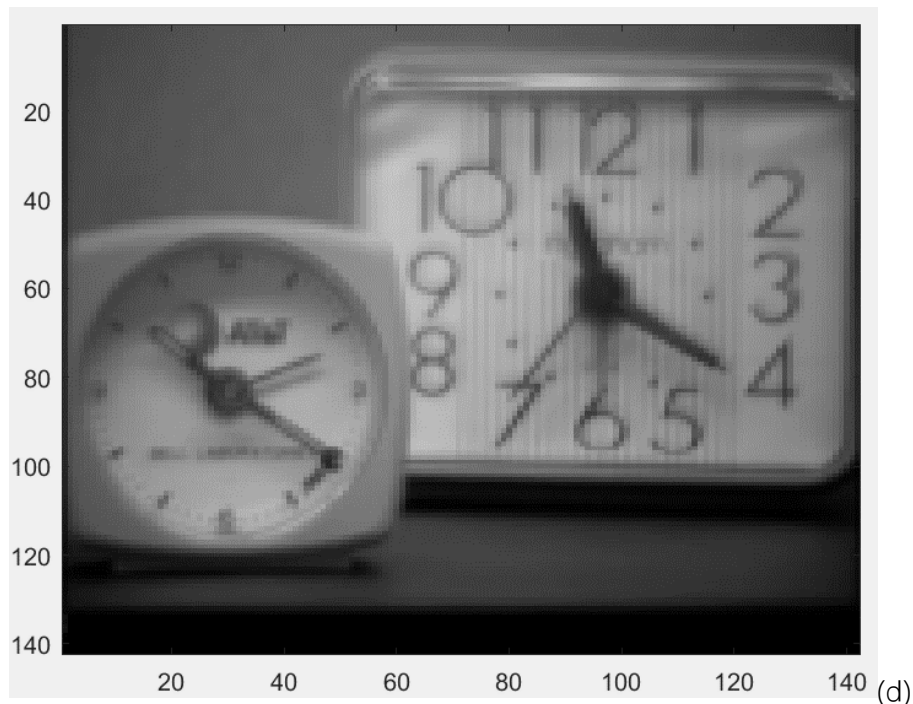




(b)



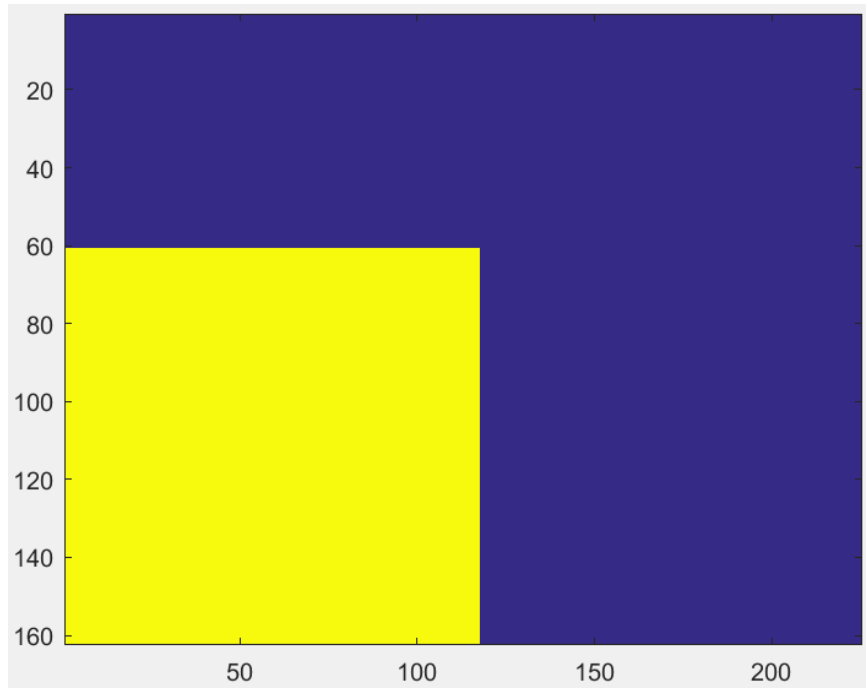
(c)



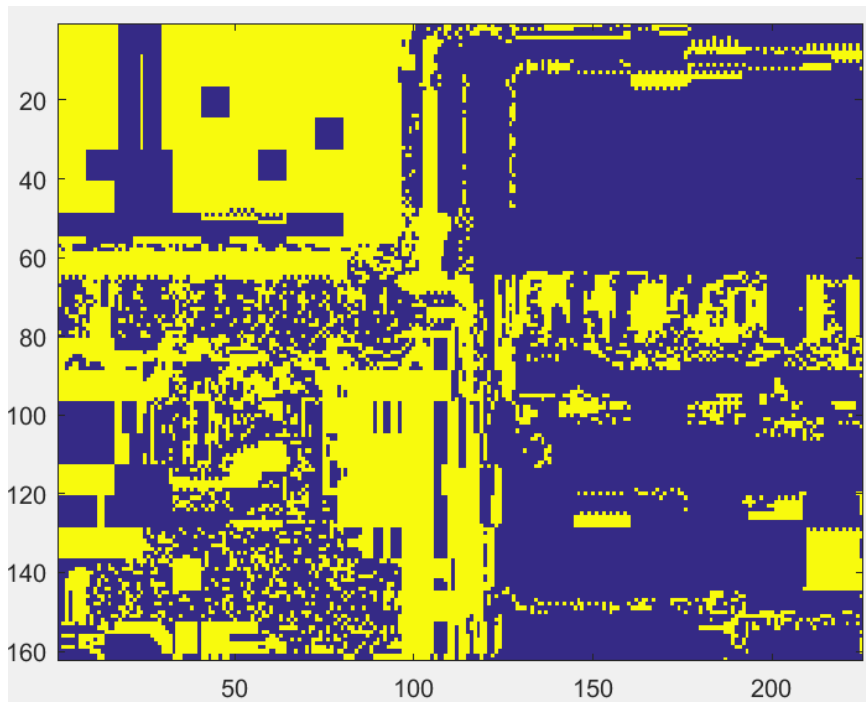
(d)

Figure 3-7. Multi-focus image fusion results.(a) Original top-right focus image. (b) Original left-bottom focus image. (c) Manually cut reference image. (d) Proposed algorithm fusion result (original images from <http://dsp.etfbl.net>).

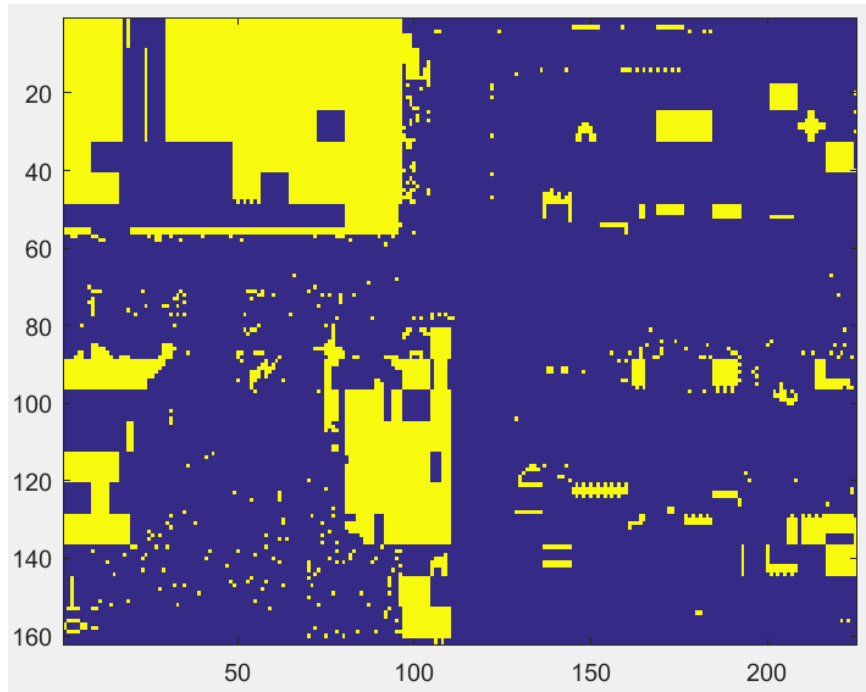
Visual analysis is a means of evaluating multi-focus image fusion algorithms directly; however, in some situations, it is hard to use visual analysis to judge whether an algorithm is effective or not. Some pixels are inconspicuous and require the introduction of a change track technology. Through the change track analysis function, the fusion result has been compared with the reference image, wherein the blue part is the pixel from the original left focus image and the yellow parts is the pixel from the original right focus image. By comparing the change track results, a clear idea about which multi-focus fusion algorithm works most effectively emerges. Figure 3-8 shows the change track applied to each aforementioned algorithm.



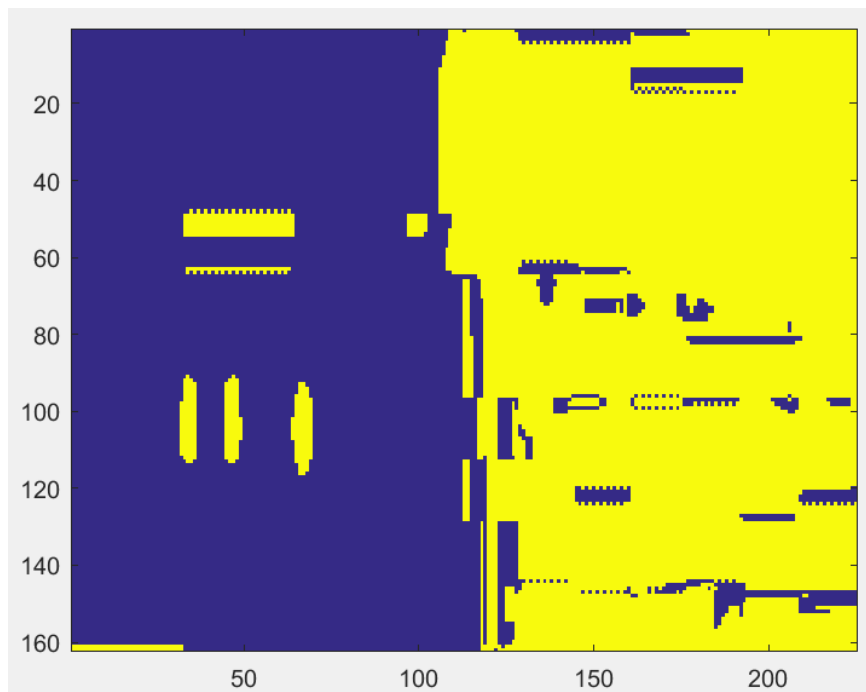
(a)



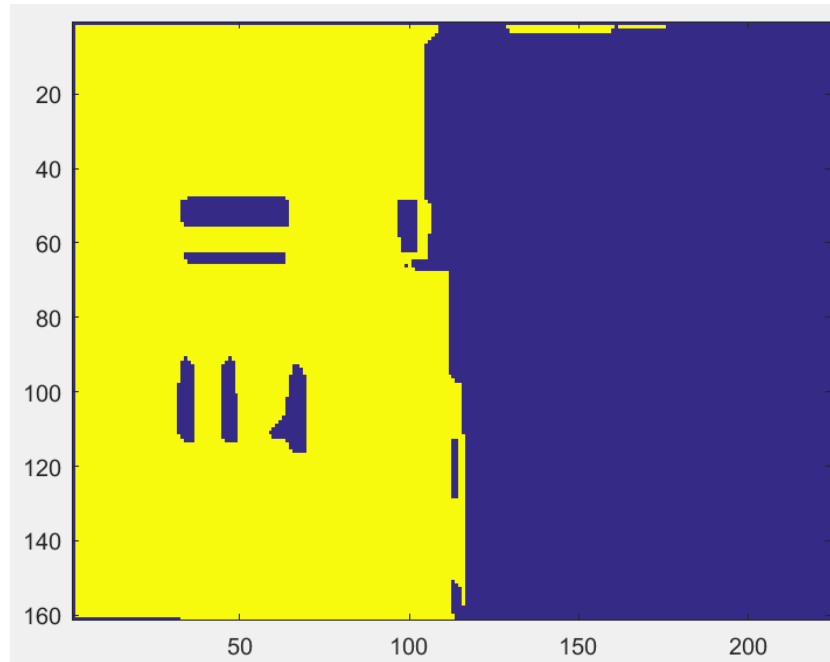
(b)



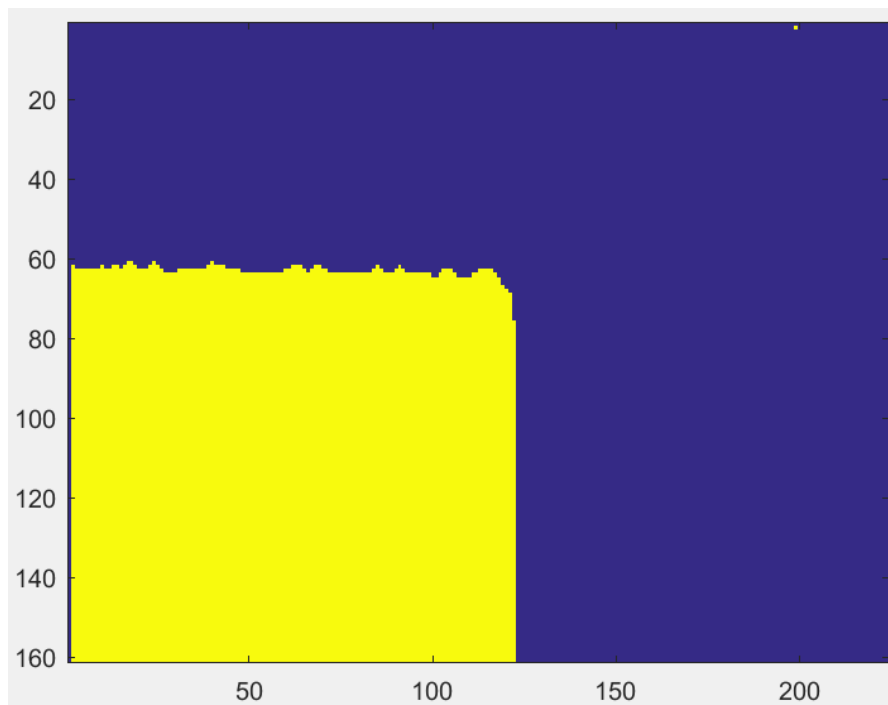
(c)



(d)



(e)



(f)

Figure 3-8. Change track for multi-focus image fusion.(a) Reference change part. (b) IHS method change part. (c) Optimised IHS method change part. (d) PCA method change part. (e) Optimised PCA method change part. (f) Proposed methods change part.

Figure 3-8 (f) shows that the proposed method is most similar to the reference image. The only difference between the reference image and the image resulting from the proposed algorithm are the pixels around the horizontal line in the middle of the left-hand side. This is because the manual cut reference image is made from selected parts of the original images with a simple cut, which might miss some edge information. However, this missing edge information will not be a significant point when judging the multi-focus image fusion algorithms. Figures 3-8 (b), (c), and (d) show that there are some discrete changed points in the right-hand half, which means that the fusion result has suffered from a degree of distortion. Although Figure 3-8 (e) is better than the above methods overall, there are still some holes in the left-hand half, meaning that the selection rules have underperformed, consequently influencing the quality of the fused result.

### 3.3.2 Computational Complexity Evaluation

The novel PCA-based fusion algorithm aims to be low in complexity and capable of being implemented into a resource-constrained embedded system. The resources and the operation time largely depend on the number of computationally intensive operations. Tables 3-1, 3-2 and 3-3 show the number of the operations of addition (ADD), subtraction (SUB), multiplication (MUL), and division (DIV) in each main step of the classical IHS algorithm, classical PCA algorithm and the proposed PCA-based fusion method without the optimisation step, where the size of the image is denoted by the number of rows,  $M$ , the number of columns,  $N$ , and the number of bands,  $L$ . Because the optimisation step is a separate part of the multi-focus image fusion algorithm, it will not count in the calculation of the complexity for all three algorithms.

Table 3-1 Classical IHS Algorithm Complexity Evaluation

STEPS	ADD	SUB	MUL	DIV
IHS transform	$6 \times M \times N \times 2$	0	$9 \times M \times N \times 2$	0
feature extraction	$6 \times M \times N \times 2$	9	$(3 \times M \times N + 5) \times 2$	12
Decision making	$2 \times M \times N \times 2$	$3 \times M \times N \times 2$	$12 \times M \times N \times 2$	0

Table 3-2 Classical PCA Algorithm Complexity Evaluation

STEPS	ADD	SUB	MUL	DIV
Matrix average	$M \times L \times N \times 2$	0	$1 \times 2$	$L \times 2$
Expectation matrix	$(L^2 - L) \times M \times N$	0	$(L^2 - L) \times M \times N$	0
Covariance matrix	0	$L^2 \times 2$	$L^2 - L + 2$	$L^2 \times 2$
Eigen matrix	$5 \times (L-1) \times (L-2) \times (4+2L) \times 2$	$5 \times (L-1) \times (L-2) \times (4+2L) \times 2$	$5 \times (L-1) \times (L-2) \times (14+8N) \times 2$	$10 \times (L-1) \times (L-2)$
PCA transform	$2 \times L \times M \times N \times 2$	0	$L^2 \times M \times N \times 2$	0
Fusion matrix decision making	$M \times N$	$M \times N$	0	1

Table 3-3 Proposed PCA Algorithm Complexity Evaluation

STEPS	ADD	SUB	MUL	DIV
Getting Covariance Matrix	$M \times L \times N \times 2 + (L^2 - L) \times M \times N$	$L^2 \times 2$	$L^2 - L + 4 + (L^2 - L) \times M \times N$	$2 \times L^2 + 2L$
Eigen Matrix	$5 \times (L-1) \times (L-2) \times (4+2L) \times 2$	$5 \times (L-1) \times (L-2) \times (4+2L) \times 2$	$5 \times (L-1) \times (L-2) \times (14+8L) \times 2$	$10 \times (L-1) \times (L-2)$
PCA Transform	$2 \times L \times M \times N \times 2$	0	$L^2 \times M \times N \times 2$	0
Fusion Matrix Covariance	$M \times N \times 3$	4	$M \times N + 3$	6
Comparison and decision making	$M \times N \times 2$	$2 \times M \times N$	0	2

The comparison results show that the IHS algorithm may be the simplest among the evaluated algorithms. The classical PCA algorithm contains a few more calculation steps than the IHS algorithm. The proposed PCA-based algorithm complexity is nearly the same as the classical PCA algorithm. A (256 rows  $\times$  256 cloumns  $\times$  3 layers) test image has been employed to demonstrate the complexity of all the algorithms in terms of operation time. Table 3-4 shows the amount of the numbers of operations and the operation time under the MATLAB environment for the test image

Table 3-4 *Number of Operations and Operation Time*

Method	ADD	SUB	MUL	DIV	Operation Time in seconds
Classical IHS	1,475,008	65,545	3,145,738	12	1.8406
Classical PCA	1,638,600	65,735	1,613,810	45	1.2687
Proposed PCA	1,573,040	131,292	1,639,148	52	1.2706

Table 3-4 shows that the proposed PCA algorithm has the same level operation time as the classical PCA algorithm when processing the same multi-focus images. In addition, the proposed algorithm outperforms the IHS algorithm in terms of both computational complexity and operation time. Therefore, the complexity evaluation results show that the proposed PCA based-multi-focus image fusion algorithm is an efficient algorithm.

### 3.3.3 Quantitative Performance Evaluation

To evaluate the quality of the fused image and the algorithm in a quantitative manner, many parameters can be introduced. This experiment makes use of the spatial frequency (SF), entropy, cross entropy (CE) and fusion-mutual information (FMI) parameters as benchmarks to judge the quality of the fusion result.

SF can be used to indicate the activity degree in the fused image. Below is the equation of SF:

$$SF = \sqrt{RF^2 + CF^2} \quad (3.5)$$

Where RF and CF are row and column frequency, respectively, and given by:

$$RF = \frac{1}{MN} \sqrt{\sum_{x=1}^M \sum_{y=2}^N (I_f(x, y) - I_f(x, y - 1))^2} \quad (3.6)$$

$$CF = \frac{1}{MN} \sqrt{\sum_{x=1}^M \sum_{y=2}^N (I_f(x, y) - I_f(x - 1, y))^2} \quad (3.7)$$

Where  $I$  is the intensity in the image, and  $M$  and  $N$  are the size of the image: the higher the value of spatial frequency, the more detail the target images have and the higher SF the fused image has. In this case, the standard SF value is calculated by using the reference image; the range  $a \pm 0.05$  (around 1%) of the standard SF value will be the acceptable error range, where  $a$  is the SF value of the fusion result.

Entropy is used to measure the information content of the fused image. CE is an extended parameter of entropy and is used to point out similarities between the input images and the fused image. CE is formulated as follows:

$$CE(I_1, I_2: I_f) = \frac{CE(I_1, I_f) + CE(I_2, I_f)}{2} \quad (3.8)$$

$$CE(I_1, I_f) = \sqrt{\sum_{x=0}^L h_{I_1}(x) \log \frac{h_{I_1}(x)}{h_{I_f}(x)}} \quad (3.9)$$

$$CE(I_2, I_f) = \sqrt{\sum_{x=0}^L h_{I_2}(x) \log \frac{h_{I_2}(x)}{h_{I_f}(x)}} \quad (3.10)$$

$I_1$  and  $I_2$  are two input images, and  $I_f$  is the fusion result. Moreover,  $h(x)$  represents the normalised histogram of the image. The acceptable range of the CE is  $\pm 0.05$  (around 1%) of the reference image CE.

FMI represents the dependence degree between fusion image and original image [96]. In the normal case, the bigger the FMI value, the better the fusion result. The joint histogram between original image 1 and fusion result image has been defined as  $h_{I_1 I_f}(x, y)$ , and the same for original image 2. The joint histogram here means the joint probability function of the two input vectors, in this case a simple dimensionality reduction method (insert the column vectors between the two rows), has been employed here to transfer the input 2D image to a 1D vector. Below is the equation for FMI:

$$FMI = MI_{I_1 I_f} + MI_{I_2 I_f} \quad (3.11)$$

$$MI_{I_1 I_f} = \sum_{x=1}^M \sum_{y=1}^N h_{I_1 I_f}(x, y) \log_2 \frac{h_{I_1 I_f}(x, y)}{h_{I_1}(x, y) h_{I_f}(x, y)} \quad (3.12)$$

$$MI_{I_2 I_f} = \sum_{x=1}^M \sum_{y=1}^N h_{I_2 I_f}(x, y) \log_2 \frac{h_{I_2 I_f}(x, y)}{h_{I_2}(x, y) h_{I_f}(x, y)} \quad (3.13)$$

By using these four parameters, a quantitative evaluation can be carried out. If the result of a method is no more than  $\pm 0.05$  (around 1%) of the range of the reference values, this method can be considered effective during the quantitative evaluation.

Table 3-5 shows the quantitative testing results. Here, TI1, TI2, TI3, and TI4 represent test images 1, 2, 3, and 4, shown in Figures 3-4, 3-5, 3-6 and 3-7, respectively. Since test image 3 and 4 (Figures 3-6 and 3-7) are originally a black-white image, the R, G, and B values will be the same.

The testing of the R, G, and B components of the input images was done separately. In Table 3-5, the blue numbers are the SF, CE and FMI results of the reference images. The red numbers in Table 3-5 are the values in the acceptable range of the quantities evaluation parameters. As can be seen from Table 3-5, the proposed method is quantitatively nearly equivalent to the reference image for all four test images according to the four criteria. This demonstrates that the proposed PCA-based multi-focus image fusion algorithm outperforms the IHS-based method and the original PCA methods. Thus, the quantitative evaluation of the proposed method fully corroborates the results of the visual analysis in section 3.3.1 above.

Table 3-5 Quantitative Evaluation of the Multi-Focus Image Fusion Results

Assessment criterion		IHS				Optimised IHS				Original PCA				Optimised Original PCA				Proposed PCA-Based Method				Reference			
Image		TI1	TI2	TI3	TI4	TI1	TI2	TI3	TI4	TI1	TI2	TI3	TI4	TI1	TI2	TI3	TI4	TI1	TI2	TI3	TI4	TI1	TI2	TI3	TI4
Spatial Frequency	Red	5.76	6.86	7.47	8.43	3.62	6.07	7.47	8.48	6.42	6.58	7.42	8.31	6.28	6.57	7.46	8.43	6.20	6.32	9.78	8.95	6.21	6.31	10.45	9.19
	Green	5.70	6.29	7.46	8.43	3.59	5.82	7.47	8.48	6.42	6.25	7.42	8.31	6.27	6.24	7.46	8.43	6.19	5.98	9.78	8.95	6.19	5.95	10.45	9.19
	Blue	5.90	6.78	7.47	8.43	3.70	5.94	7.48	8.48	6.57	6.50	7.42	8.31	6.43	6.42	7.46	8.43	6.38	6.14	9.78	8.95	6.39	6.15	10.45	9.19
Entropy	Red	5.75	6.27	5.44	7.26	5.64	6.29	5.45	7.23	5.56	6.30	5.47	7.26	5.58	6.31	5.49	7.25	5.55	6.33	5.65	7.23	5.56	6.33	5.63	7.24
	Green	5.69	6.19	5.46	7.24	5.60	6.20	5.48	7.23	5.50	6.23	5.51	7.25	5.49	6.22	5.53	7.24	5.45	6.26	5.70	7.23	5.46	6.26	5.69	7.24
	Blue	6.05	6.27	5.52	7.24	5.94	6.27	5.53	7.24	5.87	6.35	5.51	7.26	5.89	6.37	5.52	7.24	5.85	6.36	5.72	7.23	5.85	6.36	5.71	7.24
Cross Entropy	Red	0.36	0.33	0.36	0.19	0.39	0.33	0.34	0.19	0.36	0.31	0.17	0.12	0.36	0.31	0.19	0.12	0.36	0.33	0.29	0.15	0.36	0.34	0.29	0.13
	Green	0.49	0.44	0.39	0.18	0.52	0.38	0.37	0.19	0.36	0.34	0.18	0.12	0.37	0.33	0.18	0.13	0.37	0.36	0.31	0.15	0.37	0.37	0.30	0.13
	Blue	0.35	0.37	0.37	0.18	0.38	0.37	0.35	0.19	0.36	0.36	0.52	0.12	0.37	0.35	0.54	0.12	0.38	0.37	0.29	0.15	0.38	0.38	0.29	0.13
	sum	1.20	1.14	1.12	0.55	1.29	1.08	1.06	0.57	1.08	1.01	0.87	0.36	1.10	0.99	0.91	0.37	1.11	1.06	0.89	0.45	1.11	1.09	0.88	0.39
	average	0.40	0.38	0.37	0.18	0.43	0.36	0.35	0.19	0.36	0.34	0.29	0.12	0.37	0.33	0.30	0.12	0.37	0.35	0.30	0.15	0.37	0.36	0.29	0.13
Fusion Mutual Information	Red	11.53	12.60	11.15	14.50	11.47	12.60	11.14	14.50	11.37	12.60	11.04	14.50	11.39	12.59	11.08	14.49	11.36	12.62	11.26	14.43	11.36	12.63	11.28	14.40
	Green	11.61	12.53	11.24	14.50	11.54	14.44	11.23	14.49	11.19	12.42	11.13	14.49	11.18	12.43	11.16	14.48	11.14	12.45	11.35	14.43	11.15	12.46	11.39	14.40
	Blue	12.19	12.59	11.31	14.50	12.06	12.59	11.30	14.51	12.02	12.68	11.45	14.50	12.05	12.67	11.48	14.49	12.02	12.68	11.39	14.44	12.02	12.69	11.43	14.40
	average	11.78	12.57	11.23	14.50	11.69	13.21	11.22	14.50	11.53	12.57	11.21	14.50	11.54	12.56	11.24	14.49	11.51	12.58	11.33	14.43	11.51	12.59	11.37	14.40

### 3.4 Summary

This chapter presented a new adaptive algorithm for multi-focus image fusion based on the PCA method, which is suitable for use in embedded systems due to its low implementation cost. The complexity evaluation results indicate that the operation time of the proposed PCA-based algorithm is lower than the IHS algorithm. In addition, the proposed algorithm outperforms the classical PCA algorithm in both parameter evaluation and visual inspection, with nearly the same operation time. The algorithm can perform adaptive fusion of images with differently placed foci, e.g. left-right, top-bottom and diagonal. Hence, the proposed PCA-based algorithm is a low-cost and high-quality multi-focus image fusion algorithm, suitable for multi-layer images as well. The drawback of the proposed algorithm is that, given a fused colour image, there will be some noise signal around the boundary of the focus object. For example, in Figure 3-5 (d), there are some black pixels around the boundary in the fusion result; this is mainly because the optimisation rules consider the black pixel as belonging to the black-coloured parts of original left-focus image. The optimisation step of the proposed algorithm can be improved in future research. In addition, a coordinated correction step can be embedded in the first step of the algorithm; therefore, the limitations of the inputs from the same visual angle will be solved.

The research contribution can be summarised as follows: (i) identification and implementation of two suitable multi-focus image fusion algorithms—IHS and classical PCA; (ii) design of optimised versions of the IHS and the classical PCA algorithms; (iii) proposal of a new adaptive image fusion algorithm, based on the PCA method; and (iv) performance evaluation of all the algorithms using visual and quantitative analysis based on four different multi-focus images.

The new algorithm achieves multi-focus image fusion, combining two or more images with the same visual angle but different focus to output a more informative image than the state-of-the-art methods according to the four main criteria. In addition, the proposed algorithm is less complex than the IHS method, which can save a lot of operation time in the embedded systems.

This algorithm can be employed in an object detection sub-system of landmine detection systems. The double-eye systems have been widely used in both EOD robot systems and autonomous driving currently. The proposed PCA-based multi-focus image fusion system could help to fuse the output images from the double-eye system, since they are always multi-focus images. The fusion result of the proposed algorithm can help the system to understand the environment well; also, it can contribute to measuring the distance between the double-eye system and the object of interest. In particular, it can be used to generate the total close-range input image, thus providing more in-depth information about the environment of the suspected area. In addition, the multi-focus image fusion algorithm can improve the landmine detection process in the visual check step. Since the multi-focus image fusion output can extract the information of the focus point, the de-miner will have a clear idea of where the actual landmine is in the suspect area.

# **Chapter 4: Design of Landmine Detection Algorithms for a Single Sensor**

This chapter mainly focuses on the design of landmine detection algorithms for a single landmine detection subsurface sensor.

Section 4.1 presents the landmine detection definitions. Section 4.2 outlines GPR test data from both an outdoor simulated mine area and indoor lab environment collections. Section 4.3 proposes three different kinds of landmine detection algorithms: entropy-based, statistics-based and a GPR array feature-based. Section 4.4 compares the three algorithms proposed in section 4.3 in terms of their Receiver Operating Characteristics (ROC) and computational complexity. Section 4.5 presents a general discussion on the proposed algorithms and summarises the novel contributions.

The algorithms proposed in this chapter could process MD, GPR and IR data (see Appendix B, C and D). However, the GPR sensor has been used as a default sensor to test the proposed algorithms, as it is an important sensor that has been widely used in current landmine detection projects.

## **4.1 Landmine Detection Definitions**

As highlighted in the previous section, research into landmine detection algorithm design seeks an accurate and low computational complexity method, which can help to identify the actual location of the landmines with an acceptable locational accuracy. In the normal case, the killing range of an AP mines are circle area with 40~60 cm diameter; in addition, the maximum acceptable locational accuracy range for detection process will be 15cm[25]. Therefore, the strategies used to evaluate landmine

detection algorithms play an important role in the detection process. The literature review has shown that the majority of existing projects have tended to use the ROC curve to demonstrate the landmine detection results as these incorporate the Detection Rate (DR), as well as the False Alarm Rate (FAR) [9, 97]. However, different publications have proposed different definitions of  $P(d)$  and  $P(fa)$ . Some authors use correct detections per square meter as the DR unit, and false alarms per square meter as the FAR unit. For instance, P. Gader used the ratio of the detection or false alarms numbers and the total time taken by one detector to scan the field once as the FAR [18]. All these definitions for  $P(d)$  and  $P(fa)$  can be used for describing the performance of the close-range landmine detection algorithm. However, the detections per square meter or per minute are influenced by the ground truth information. For example, if evaluating the landmine detection algorithm in large area with few landmines, there will be a very low  $P(d)$ . To avoid this, in this research, the DR and FAR are determined by the ground truth maps. The ratio of the correct detection pixels against the total landmine pixels in the ground truth map is used to define DR, and the ratio of the false alarm pixels against the total number of pixels, marked as negative in the ground truth map, is used to define the FAR.

A discriminant function has been developed by F. Cremer to distinguish a detected landmine from the background of the minefield [51], expressed by the equation below:

$$\theta(\vec{c}) = \begin{cases} \mathbf{1} & \text{if } \theta(\vec{c}) \geq t \\ \mathbf{0} & \text{if } \theta(\vec{c}) < t \end{cases} \quad (4.1)$$

$$\text{if } \theta(\vec{c}) = 1, \text{ assign } (\vec{c}) \rightarrow \text{landmine} \quad (4.2)$$

$$\text{if } \theta(\vec{c}) = 0, \text{ assign } (\vec{c}) \rightarrow \text{background or clutter} \quad (4.3)$$

where  $\theta_{(\vec{c})}$  is a specific point in the landmine detection result;  $c$  denotes the confidence level of the landmine detection sensors output;  $(\vec{c}) = (c_1, c_2, c_3 \dots c_N), c_i \in [0,1] \forall i \in [1, N]$  is the output vector with  $N$  as the number of landmine detection sensors (in this case  $N=1$ , as only one GPR sensor array is used);  $t$  is the threshold value of the detection algorithm; and *assign* is a decision-making function.

Using Cremer's discriminant function, the probability of detection and false alarms can be defined as follows. The *assign* function aims to identify if the output of a single sensor in a specific location is a landmine or not. For the GPR array sensor, a decision based on  $\theta_{(\vec{c})}$  should be made for the output vector of each specific location. Let the location be denoted by  $a$ , then the presence of a landmine at the location  $a$  can be represented as below:

$$\text{There is a landmine: } \theta_{(\vec{c})} = 1 \rightarrow \text{Detect } (a)$$

$$\text{There is no landmine: } \theta_{(\vec{c})} = 0 \rightarrow \text{Undetect } (\bar{a})$$

Let the ground truth map information be denoted by  $G$ , and the corresponding location by  $A$ . Through comparison with the ground truth ( $G$ ) information, the following two cases will be implemented as shown below:

$$\text{There is a landmine: } \theta_{(G)} = 1 \rightarrow \text{Detect } (A)$$

$$\text{There is no landmine: } \theta_{(G)} = 0 \rightarrow \text{Undetect } (\bar{A})$$

The combinations of the decision probabilities are as below:

$$P\theta_{(\vec{c}|G)} = p(a|A) \quad (4.4)$$

$$P\theta_{(\vec{c}|G)} = p(a|\bar{A}) \quad (4.5)$$

$$P\theta_{(\vec{c}|G)} = p(\bar{a}|A) \quad (4.6)$$

$$P\theta_{(\vec{c}|G)} = p(\bar{a}|\bar{A}) \quad (4.7)$$

Equation (4.4) evaluates the probability of detection (true positive rate). Equation (4.5) evaluates the probability of incorrect detection, whereby the system treats a background signal as a landmine, giving a false alarm (false positive rate). Equation (4.6) also evaluates the probability of incorrect detection, but here the system treats the landmine signal as background (false negative rate). Equation (4.7) evaluates the probability of correct detection of the background (true negative rate). False negative detection is not acceptable in a landmine detection system, since it is dangerous to the operator. In the ideal case, the false negative detection rate will be equal to 0.

Therefore, the probability of detection  $P(d)$  and the false alarm rate  $P(fa)$  are defined as follows:

$$P(d) = P\theta_{(\vec{c}|G)} = p(a|A) \quad (4.8)$$

$$P(fa) = P\theta_{(\vec{c}|G)} = p(a|\bar{A}) \quad (4.9)$$

The ROC curve of the landmine detection process can use  $P(d)$  against  $P(fa)$  to fulfil its function. The detection rate is equal to the ratio of the landmines correctly marked by the system against the total number of landmines in the ground truth map [37]. The FAR is equal to the ratio of the incorrectly detected landmines against the total number of real negative cases in the truth data.

For evaluate the landmine detection process effectively, the two well-known evaluation parameters FAR and Detection rate have been used to judge whether an

algorithm is effective or not. The balance between these two competing objectives is quantified by what is known as a ROC curve, as shown in Figure 4-1 [1].

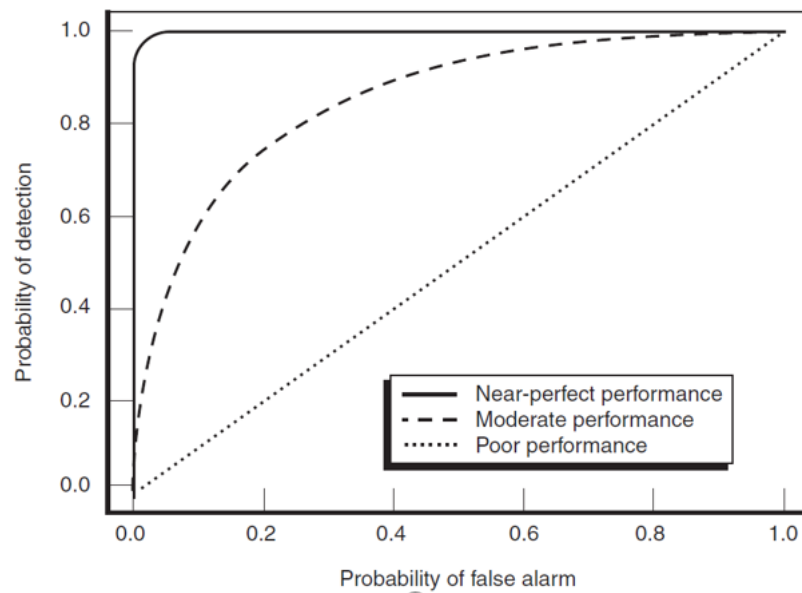


Figure 4-1. ROC curve of the landmine detection process.

In Figure 4-1, the ideal result occurs when the landmine detection equipment is able to detect 100% of the landmines without false alarm. Poor performance occurs when every suspect object detected by the landmine detection equipment is proven false. The aim of signal sensor landmine detection process is to improve the landmine detection rate and thus reduce the number of FARs. The detection result should be nearly the same as the ideal ROC curve.

## 4.2 GPR Sensor Test Data

Given the landmine detection definition define above, the next step for designing a landmine detection algorithm is finding and understanding the data of the landmine area. In this research, both indoor and outdoor GPR data have been used to demonstrate the signal sensor landmine detection algorithm. This section gives

information about both the outdoor and indoor simulated landmine test data used in this research.

#### **4.2.1 GPR Data from the Naples Outdoor Simulated Landmine Area**

The outdoor environment landmine test dataset is obtained from the D-Box project (see section 5.1). As part of the D-Box project, a simulated landmine area was built in Naples, Italy, which was used for testing the performance of landmine detection sensors and data fusion algorithms in an outdoor environment. The GPS coordinates of the Naples simulated landmine area is (40.933366, 14.119095). The Naples test centre included three different test zones distinguished by the surface soil types: humid, desert and high vegetation areas. In this section, the desert landmine zone is used as an example to show the performance of the proposed single-sensor landmine detection algorithms under an outdoor working environment.

There are 16 mines in total in the desert test area, which can be divided into three categories: ATM and two different types of APM. The ATM is located in the centre of the testing area; the AT mine is simulated by a metal can filled with beeswax with a diameter of 30cm and height of 11cm. The other 15 are APM, which are located in two parallel lines, the south (nearest) line has seven mines and the north (farthest) line has eight mines. There are four markers representing both ends of the lines, the purpose of which is to help remember the location of the landmines for the one who buried it. The middle five landmines on the south line are Yugoslavian PMA-1A, simulated by a plastic box with dimensions of 3cm (width)  $\times$  14cm (height)  $\times$  7cm (length), and there is a small electric component inside the plastic box as well. The other 10 AP mines are PMN/PMA-3, which is simulated by a plastic cylinder with a diameter of 11cm and height of 4cm. In Figure 4-2 below, the left image shows the

top view of the desert landmine area, which is taken by an optical camera carried by a UAV. In the left image of Figure 4-2, the white part is the simulated landmine area in the desert environment. The size of this area is around 25 metres long, 10 metres wide and 0.5 metres high from the ground to the surface of the area. As mentioned before, the four blue plates (diameter:10cm) on the white surface are markers to help remember the location of the landmines. In addition, some red circles are drawn around the markers by editing the original image, which can emphasise the markers. All 16 landmines were buried under the surface around 10cm to 15cm depth; the actual location of the landmines can be traced by using the right image in Figure 4-2. The right image shows the position information of the targets via reference markers. The four blue stars on the right image correspond to the blue points on the left image of Figure 4-2. It is clearly shown that one ATM is buried around the middle of the landmine area, the distance between the ATM to long side and wide side of the box edge is 1318cm and 982cm correspond. The numbers 1~8 between the top two markers and 1~7 between the bottom two markers are the position of the 15 APM. The numbers 2~6 on the bottom line are the PMA-3, are small plastic landmines which are hard to be detected by the GPR and MD sensor. The other 10 mines are PMA-1. The large numbers between landmine positions are the distance value in the unit of centimetres.

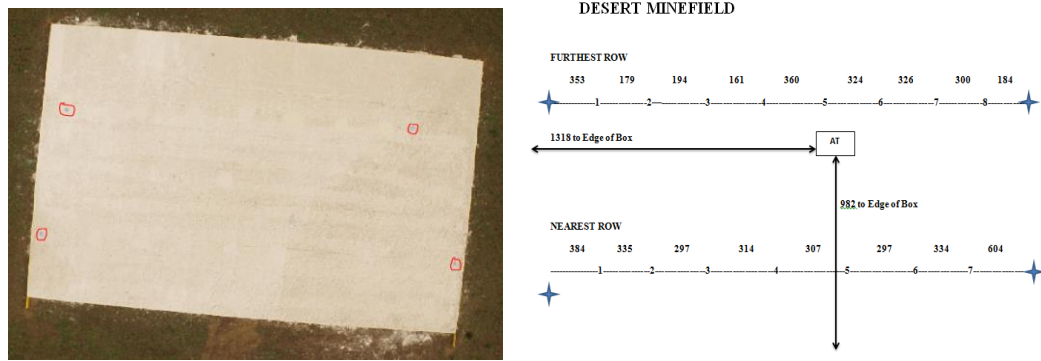


Figure 4-2. UAV image and the position of the landmine targets in the Naples simulated desert landmine area.

Several landmine detection sensors, including GPS, GPR, MD, and IR camera, have collected data from the simulated desert landmine area. However, as there isn't a ground truth map for the Naples test dataset, the only reference for determining the landmine location is the position map and the markers. The performance of the landmine detection algorithms cannot be evaluated without a correct ground truth map. Therefore, it is very important to build a correct ground map. The ground truth map of the desert landmine area has been built based on the measurement data from the GPS system, GPR system, and the target-position map. The scenario of the GPR data collection in the outdoor environment in Naples uses a GPR array which carries a high-accuracy GPS sensor to scan the test area. The GPR array and the GPS sensor are time synchronised, so each set of GPR output data will have a corresponding GPS location. The GPS coordinates of the marker, boundaries and landmines are given by the landmine area set-up document. Details on the pre-processing of the GPR and GPS data are presented in Appendix E and F, respectively. Figure 4-3 below shows the flowchart of building the ground truth map of the outdoor environment:

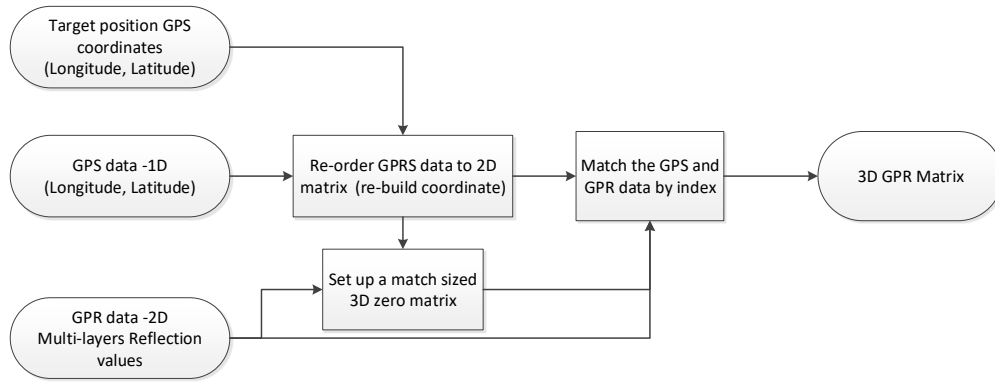


Figure 4-3. Outdoor environment ground truth map-building process.

In Figure 4-3, the target position and the GPS data consist of longitude and latitude values. In addition, the input data from the GPR array are a multi-layer signal consisting of the reflection values under different scanning frequencies. The first step of the ground truth map building is to transfer the longitude and latitude values into a two-dimensional plane coordinate system, where the smallest longitude value and the smallest latitude value will be the origin of the coordinate system. The axis grade of the coordinate system is determined by the accuracy of the GPS system; in this case, it is 5cm. The second step of the ground truth map-building process is to set up a 3D zero matrix which can match the size of the target position map, GPS input data and the GPR input data. The zero matrix is the base of the ground truth map; the following step replaces the matrix value with the index number of the GPS sensor input, and then replacing the index numbers with the corresponding GPR reflection values. In addition, the GPR input data have been transferred to a 3D-GPR array at this step, which can also be used to test the single sensor landmine detection algorithm. The final step is matching the position target input to the 3D ground truth map and highlighting the marker, boundaries and position of the landmines. Figure 4-4 below shows the ground

truth map of the Naples simulated desert landmine area via the proposed processing method:

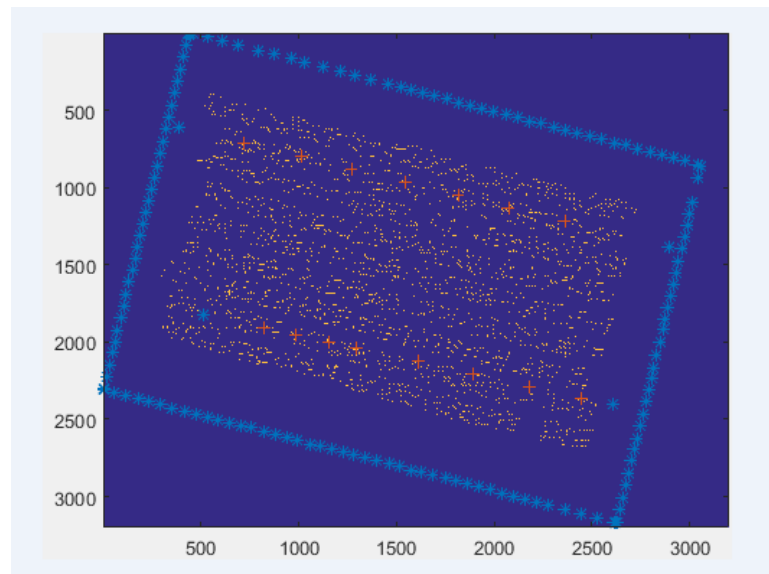


Figure 4-4. Ground truth map of the Naples simulated landmine area.

In Figure 4-4, the blue points are the GPS system data, showing the boundary and the marker in the landmine area. The red plus signs are the landmine locations which are calculated based on the position map. For each GPR signal data collection point, there is a corresponding GPS signal collection point, which could help to improve the detection results for the GPR sensor. The yellow points in the image are high-accuracy GPS signals, which correspond with the GPR sensor.

#### 4.2.2 GPR Data from an Indoor Simulated Landmine Area

The indoor environment landmine detection results are based on a published dataset of GPR arrays [18]. The data were collected in an indoor  $1.8 \times 1.8$ m sandbox with a clean surface. Ten landmines and mine simulants were used in the sandbox, including VS-1.6, VS-2.2, TMA-5 anti-tank mines, and TS-50, PFM-1, M-14 anti-personnel mines. In addition, four clutters (5.08cm sphere, rock, crushed can, and nylon cylinder)

were included in the sandbox. Two transmitters, four receivers, and a GPR array were used to scan the sandbox. The scanning frequency ranged from 60MHz to 8.06GHz.

The ground truth of the sandbox is shown as Figure 4-5 below:

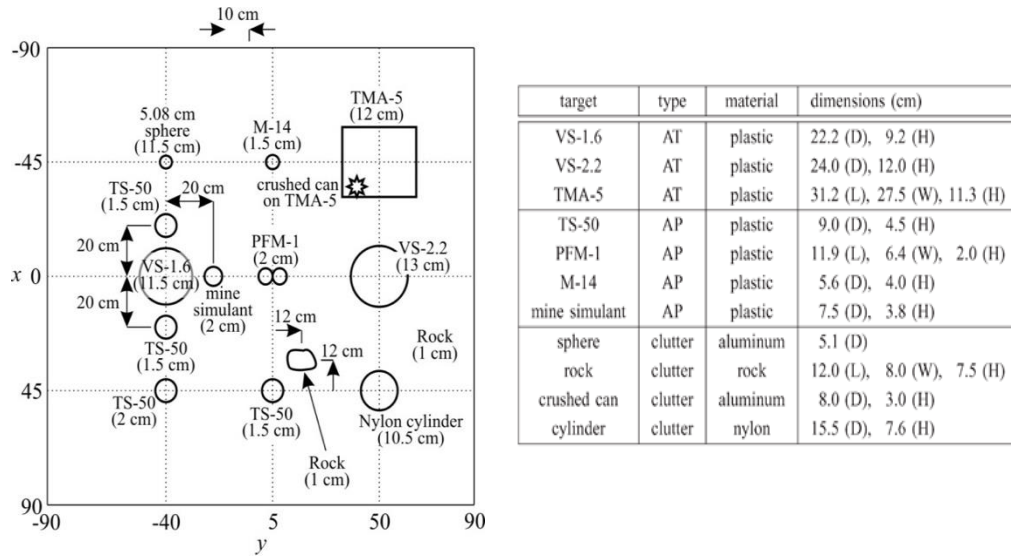


Figure 4-5. Position and nature of the targets in the public domain test area.

The public domain GPR data resource came from the Wrocott research group [43]. The GPR source contains 8 (groups)  $\times$  401 (frequencies)  $\times$  91 (rows)  $\times$  91 (columns) to represent the complex values. According to T. Counts et al., ‘The real part of this image is what is normally obtained using the standard time-domain backprojection algorithm. The magnitude of the complex image can be viewed as the envelope of the standard time-domain backprojection algorithm’ [47]. Thus, the magnitude domain of the data can be worked out with the formula (4.10).

$$\begin{aligned}
 \text{Magnitude}(x, y, z, p) & \quad (4.10) \\
 & = \sqrt{\text{Re}(x, y, z, p)^2 + \text{Im}(x, y, z, p)^2}
 \end{aligned}$$

$x$  and  $y$  are the rows and columns of the pixels  $x \in [1,91]$ ,  $y \in [1,91]$ , while  $z$  is the scanning frequencies from 60MHz–8.06GHz per 20MHz, resulting in frequency

indexes that range from 1 to 401  $z \in [1,401]$ . The different channels of the scanning data are  $p$ , from  $T1R1$  to  $T2R4$   $p \in [1,8]$ .

The eight channels of the dataset are used to adjust the scanning result, after which equation (4.11) is used to process the eight channels of the scanning data into one channel.

$$Magnitude'(x, y, z) = \sum_{p=1}^N Magnitude(x, y, z, p) \quad (4.11)$$

A ground truth table was built based on the ground truth map, which can be used as the truth map in the landmine detection process. In order to evaluate the landmine detection and fusion algorithm, all the detection results will be compared with the rebuilt truth map. The  $P(d)$  and the  $P(fa)$  are calculated by equations (4.8) and (4.9) based on the truth map as well. The rebuilt truth map is shown as Figure 4-6 below:

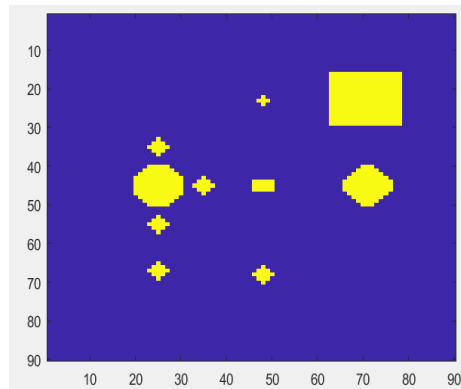


Figure 4-6. Rebuilt ground truth map of the public domain test area.

In the rebuilt truth map, the blue parts represent background or clutter in the detection process, and the yellow parts indicate landmines in the test area based on the location, size and shape of the actual landmine.

### **4.3 Landmine Detection Algorithm Design**

A GPR sensor can detect buried objects by emitting radio waves into the ground and then analysing the return signals generated by reflections of the waves at the boundaries of materials with different indexes of refraction caused by differences in electrical properties. Generally, reflections occur at discontinuities in the dielectric constant, such as at the boundary between soil and a landmine or between soil and a large rock [13]. A GPR system consists of an antenna or series of antennae that emit the waves and then pick up the returning signals. A computerised signal-processing system interprets the signal to determine the object's shape and position. The result is a visual image of the object, which is compared with a mine reference library to indicate whether its shape resembles a landmine [20, 98]. Although the GPR sensor can detect most existing types of landmine, it still has some limitations in the demining process as GPR performance can be highly sensitive to complex interactions between mine metal content, interrogation frequency, soil moisture profiles, and the smoothness of the surface boundary.

In this section, three different kinds of close-range landmine detection algorithms are proposed. The first algorithm is an entropy-based algorithm which is suitable for a large detection area and fast detection, and the second algorithm is a statistics-based algorithm which is suitable for a small range and accurate detection. The last algorithm is a GPR feature-based detection algorithm which is only suitable for GPR sensors.

### 4.3.1 Entropy-based Algorithm

There are two different methods to analyse a 3D-GPR image. One is cross-track analysis; the other one is down-track analysis. The cross-track analysis treats the 3D-GPR image as a multi-spectral image, which means that, for each layer, it presents separate information of the landmine area at different depths. Therefore, in each cross-track sub-image, the opportunity to find a landmine can be treated as an independent repeated trail. As mentioned in section 2.3.3, the region-selection thresholding algorithm uses the maximum rules in each region of the input signal to detect the landmines. The disadvantage of that algorithm is it will be influenced by the noise signals, and it is hard to select the thresholding values. To solve this problem, this research proposed a novel region-based landmine detection algorithm: an entropy-based algorithm.

The entropy-based algorithm belongs to the region-based landmine detection algorithm, which cuts the original landmine area into small piece areas and then, based on selection rules, determines which small region contains landmines. The core techniques of the region-based landmine detection algorithm are how to choose the feature of the regions and how to design the mapping rules. The novel part of the proposed entropy-based algorithm is that it uses the entropy value as the feature of the regions in the 3D GPR array cross-track image, which have not been mentioned by other researchers. The working principle of the entropy-based algorithm is to assess whether the edge of the suspect object is different from the background. The entropy value can measure the disorder degree of each region, helping differentiate the suspect object from the background. The limitation of the entropy feature when comparing it with other candidate features of the region-based landmine detection algorithm (maximum values, standard division and variance) is its computational complexity.

However, in terms of detection performance it outperforms the other candidates.

Figure 4-7 below shows the flowchart of the entropy-based algorithm:

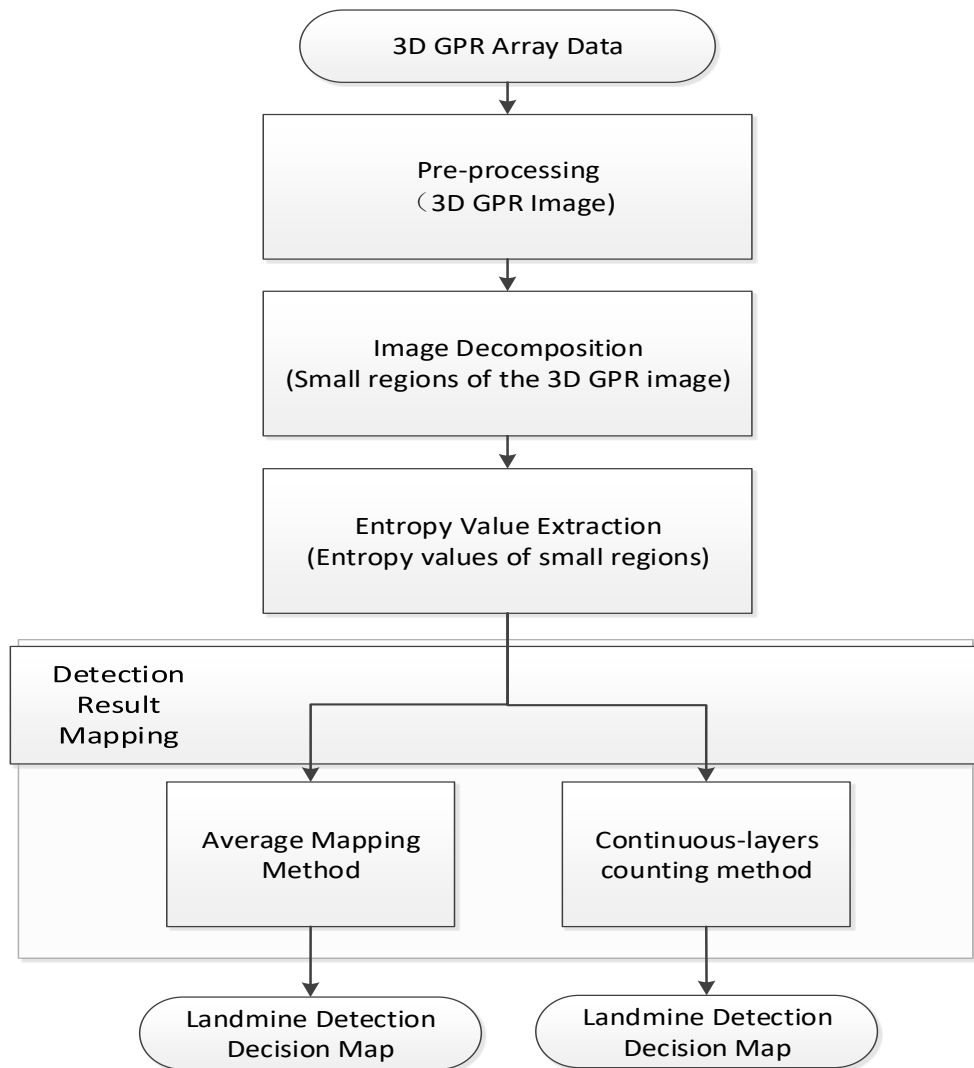


Figure 4-7. Flowchart of an entropy-based algorithm.

In general, the entropy-based single-sensor landmine detection algorithm could be divided into three main steps: pre-processing, feature extraction and detection result mapping.

Since the original input of the proposed entropy-based algorithm is the 3D GPR raw array data, a pre-processing step is necessary to transfer the raw data into the 3D GPR

image format (one transfer method is shown in section 4.2.2). The second step of entropy-based algorithm is to cut the 3D GPR array image to small regions. The size of the window selection for cutting the small regions should follow three rules:

1. All the window sizes must be the same, because the entropy value of each region will be compared in the following step. If the window size is different, it will lead a no reasonable comparison.
2. The edge of the window must be between the size of the smallest predicted landmine and the double size of the smallest predicted landmine on the field. Since the region-based algorithm can only detect one landmine in each region, if the size is too large, it will miss some landmines in the same region. In addition, if the size is too small, it will increase the rate of false alarms.
3. The window should include pixels as much as it can: the more samples in the region, the more differences between each region will be shown.

By following these rules, the window size of both outdoor environment and indoor environment can be determined, which are 20cm square and 10cm square respectively. After the 3D GPR image has been cut into small regions, the next step is to extract the feature of each region.

For feature extraction, the raw C-scan 3D GPR image has been subdivided into several same-sized small regions. For each subdivided region, the entropy value will be selected as the feature. Equations (4.12) and (4.13) show how to calculate the feature value of a subdivided unit.

$$S(X, Y) = - \sum_{x=1, y=1}^{x=m, y=n} p_{(x,y)} \log p_{(x,y)} \quad (4.12)$$

$$p(x, y) = \frac{\text{occurrence value of } I(x, y)}{m \times n} \quad (4.13)$$

Where  $X, Y$  represent the index of the subdivided region,  $I$  represents the subdivided region and  $x, y$  represent the index of the measurement pixel in the subdivided region. In addition,  $S$  represents the entropy value of the selected region, and  $m$  and  $n$  represent the edge size of the subdivided region. The entropy value represents the disorder rate of the small region. High entropy values of a subdivided unit can indicate that the small region might contain parts of a suspect object, which might be a landmine. Lower entropy values of small regions can indicate the background of the landmine area. The background region will show exactly the same entropy value if the landmine area does not have soil-type changes under the ideal case. However, given the clutter signal and the uncertainty of the GPR sensor, the entropy value of each small region will show differences. Therefore, a simple moving average image filter is needed before the feature-extraction step to reduce the effect from the clutter signal in small regions, where the window size is equal to region unit size.

To map the landmine detection result, the 2D detection report is calculated based on the 3D entropy value array. Two different methods are used here to produce this report: simple average and continuous-layer counting.

The simple-average method takes the average value for all down-track subdivided unit feature values to build a one-layer detection report. The principle of the simple average method is treat each layer in the 3D GPR array as having an equal chance to detect the landmines. Therefore, the average value of the cross-track 3D GPR array's feature represents the detection probability of the proposed feature-based algorithm. Equation (4.14) shows how the simple-average algorithm works.

$$2D \text{ detection map } (X, Y) = \frac{\sum_{i=1}^N S(X, Y, i)}{N} \quad (4.14)$$

Where  $N$  is the total layers of the 3D GPR image, and  $i$  is the layer index of the down-track subdivided unit.

By following the entropy-based algorithm above, the landmine decision map will be built. Figure 4-8 shows the entropy-based algorithm test result with the average mapping method for the indoor test set.

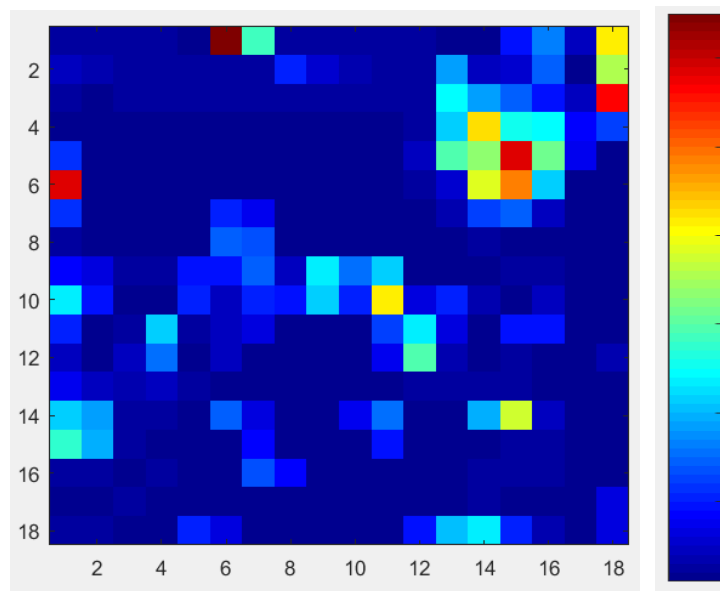


Figure 4-8. Average mapping result of an entropy-based algorithm.

In Figure 4-8, the axis is the index number of the regions. The right-hand side of the image is the colour bar, which shows the entropy feature from low to high, the dark blue is low entropy and the dark red is the high entropy. In this image, each small region represents a 10cm by 10cm square in the real world. If the small region does not show a dark blue colour, it means a landmine has been detected in this small region. The probability of the decision being correct or not has been represented by the colour of the small region, where the red colour means it has a very high probability of

detecting the landmines. When comparing the decision map with ground truth map (Figure 4-5), most of the landmines area has been marked, demonstrating that the average mapping method with the entropy-based algorithm can help to achieve the landmine detection process.

Since Figure 4-8 has indicated that the proposed entropy-based algorithm has the ability to detect landmines in the lab environment, the next step is to apply the proposed algorithm in the outdoor environment. Figure 4-9 shows the entropy-based algorithm test result with the average mapping method under the Naples outdoor GPR dataset.

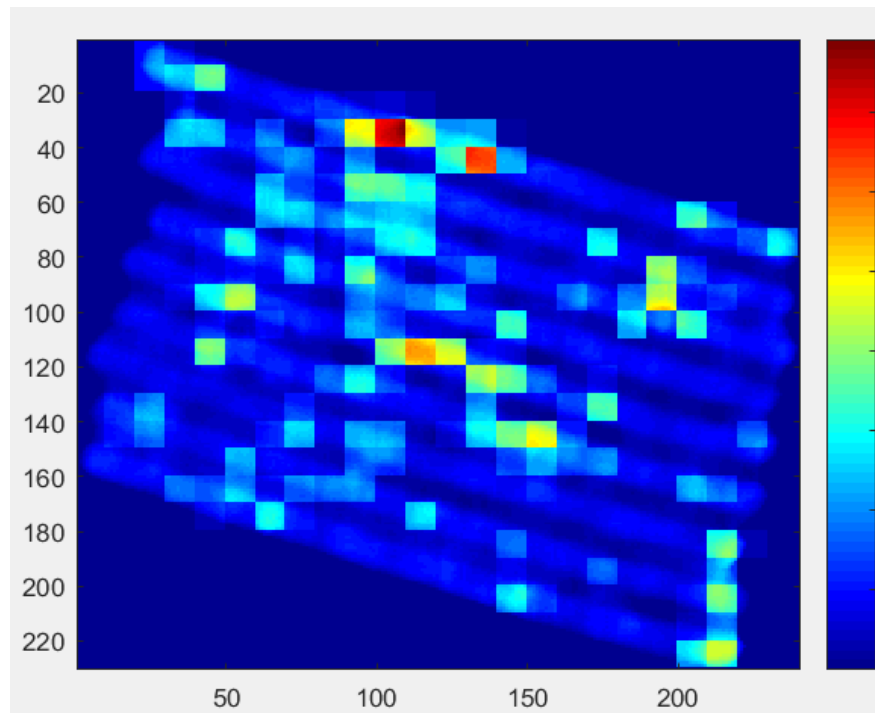


Figure 4-9. Entropy-based algorithm test result with the average mapping method using the Naples GPR dataset.

In Figure 4-9, the dark blue colour area is the unknown area, which means the GPR sensor does not collect data for that area. The blue area is the safe area, which means there is a very low probability of finding landmines buried there. The yellow and red

areas are the dangerous areas, meaning they might contain landmines. The horizontal and vertical axis represent the GPR data collecting point index. The testing results show that 5 of 15 AP mines are miss-detected by using the entropy-based algorithm. The miss detection here means the false negative of the decision, which shows the detection algorithm treat the landmines as a safe area. It is important to reduce the miss detection in the landmine detection process since it will be dangerous to de-miners.

The second mapping method is continuous-layers counting, which aims to count the numbers of repetition in two continuous layers in detecting the same landmines. This mapping method can effectively reduce the influence of noise signals. Since, in the 3D GPR image, the layer index represents the depth information, if two or more continuous layers show the same decision of the landmine detection process, it can improve the credibility of the detection result. The number of the continuous-layers repeats can represent not only the probability of the landmine but also the size of the suspect object. Equations (4.14) and (4.15) show how the continuous-layers method works:

$$\mathbf{2D\ detection\ map\ (X,Y)} \tag{4.14}$$

$$= \sum \mathbf{Single\ layer\ decision}_{(X,Y)}(i)$$

$$\mathbf{Single\ layer\ decision}_{(X,Y)}(i) = \begin{cases} 1 & |L + 1_{(X,Y)} - L_{(X,Y)}| \neq 0 \\ 0 & |L + 1_{(X,Y)} - L_{(X,Y)}| = 0 \end{cases} \tag{4.15}$$

In equation (4.15), the single-layer decision (X,Y) represents the decision of the landmine detection process at layer L, position (X,Y).

Figure 4-10 below shows the decision map of the indoor environment test set by using the continuous-layer counting mapping method, which is the same type as Figure 4-8.

When comparing this figure with Figure 4-8, it can be clearly seen that the alarm range has been reduced effectively, and all the landmines has been detected.

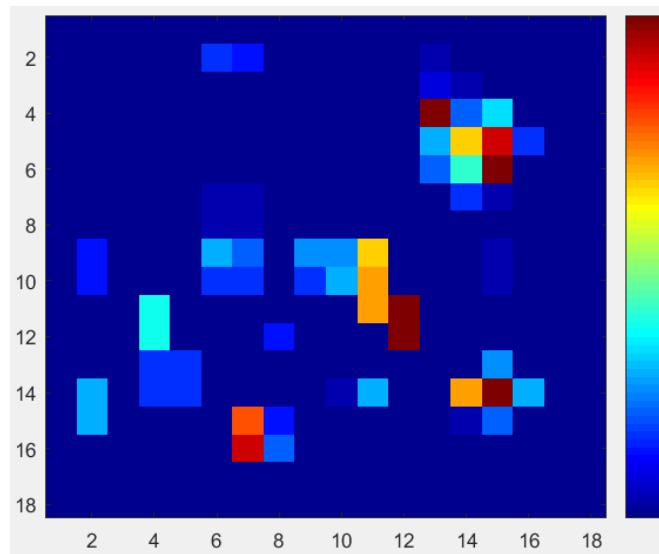


Figure 4-10. Continuous-layer counting method for entropy-based algorithm for an indoor environment.

In Figure 4-10, the dark blue area means a safe area; in addition, the other colour points include light blue, meaning a landmine has been found. The yellow and red colours mean a high decision level of the detection result.

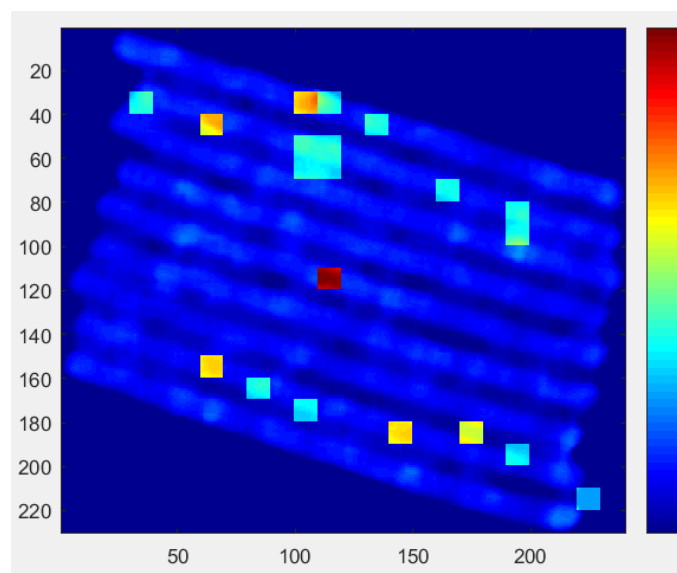


Figure 4-11. Continuous-layers counting method for entropy-based algorithm test results using the Naples GPR dataset.

In Figure 4-11, the dark blue parts are the unknown area, not scanned by the GPR array. The light-coloured parts are the detection results via the continuous-layers counting method. Compared with Figure 4-9, it can be clearly seen that some of the false alarm detection points have been reduced.

The detection results show that the proposed entropy-based algorithm can help to detect the landmines. However, it cannot localise an accurate position, which is a common drawback of the region-based landmine detection algorithm. Therefore, the statistics-based algorithm is proposed in the next section.

### 4.3.2 Statistics-based Algorithm

The entropy-based algorithm analyses the 3D-GPR array data by cross-track, and, in this sub-section, a down-track-based landmine detection algorithm, which is a statistics-based algorithm, is proposed. Normally, in the down-track signal, each pixel represents the reflection value under a different scanning frequency from low to high. The statistics-based algorithm is designed for a fine-grained landmine detection process, which targets the location of landmines in a small area. The term *fine-grained* means the detection via centimetre-level precision.

The literature survey (section 2.2.3) has shown that, in general, most down-track landmine detection algorithms are based on the B-scan GPR images, including the edge-energy detection algorithm. However, the drawback of the existing B-scan-based down-track landmine detection algorithm is computational complexity. In this case, the A-scan-based landmine detection algorithm for a down-track GPR image has been designed, which is a statistics-based algorithm. The core technique of the statistics-based algorithm is based on the background information to generate a model signal which compares the model signal with the A-scan GPR signal to generate the decision

map. The statistics-based algorithm can be divided into two main steps: model signal build and comparison rules design. Figure 4-12 shows the flowchart of the proposed statistics-based landmine detection algorithm.

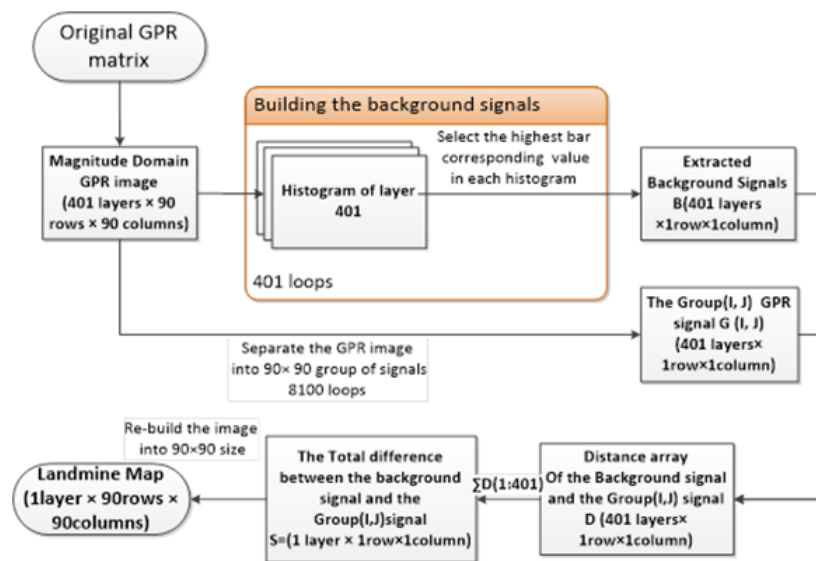


Figure 4-12. Flow chart of the statistics-based algorithm.

In Figure 4-12, the original GPR matrix is a 3D-GPR image, corresponding to the indoor-environment test dataset (section 4.2.2) used here as an example to show how the data are processed. The model signal build seeks the most frequent value in each layer of the C-scan GPR images, which represents the background value. Then, based on the background value, the model signal will be set up. Comparison rules will be used to compare the model signal with the A-scan signal to determine where the landmines are. Finally, a landmine detection map will be built based on the comparison result. The following paragraphs will introduce the model signal build and the comparison rules block separately.

For the model signal build, a statistics-based algorithm aims to generate a model signal by using background information. The working principle of the model signal is, when

using a GPR sensor to scan the ground surface with different frequencies, the reflection curve (A-scan GPR signal) will be nearly the same if the ground environment does not change and there is nothing buried under the ground. Therefore, the reflection curve under the mine clean environment can be defined as the model signal. Since the ground environment does not change in the landmine area, if a unique A-scan GPR signal has been found when comparing with the model signal, it means a landmine has been detected.

Figure 4-13 below shows the A-scan GPR signal plot for different types of objects in an indoor environment, which aims to demonstrate the proposed working principle of the statistics-based algorithm. The horizontal axis of all the sub-figure in Figure 4-13 represents the length of the A-scan GPR signal and the vertical axis represents the strength of the reflection A-scan signals. In Figure 4-13, the image (a) is an A-scan signal of the mine clean position, image (b) represents an A-scan signal of the TS-50 AP mine in the sandbox, and image (c) is an A-scan signal of TMA-5 AT mine in the sandbox. By comparing these three signals, a significant difference emerges between the landmine absent signal and the landmine present signal. If a landmine is present, the A-scan signal will show great reflection value changes and vice versa. In addition, the first several pixels of each A-scan signal represent the values with a very small difference; this is because these pixels represent the information before the radar signal reaches the ground surface, known before the ground reflection. These pixels will not be important in the down-track comparison process.

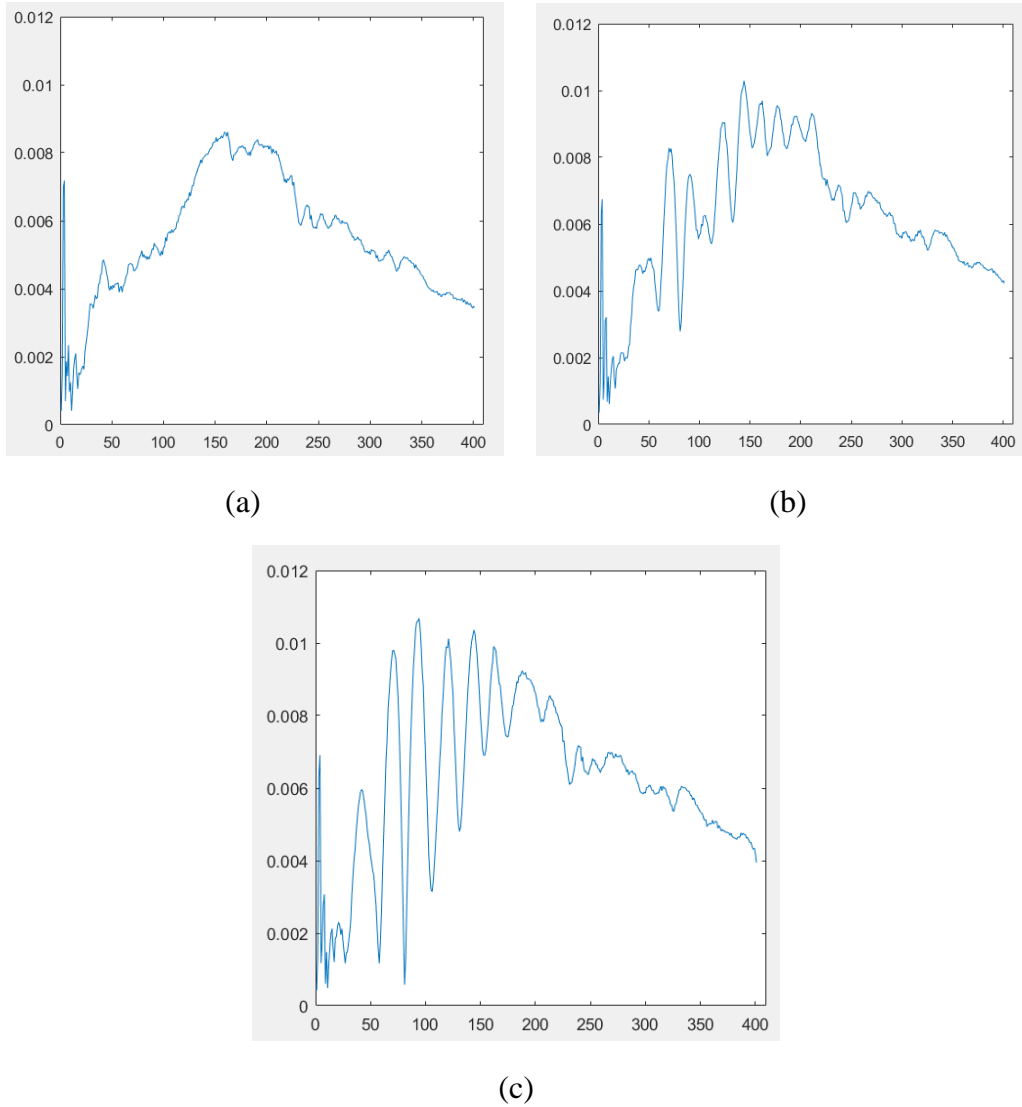


Figure 4-13. Pixel plot of the GPR signal.

The model signal building has two steps which are building the histogram for each layer of the C-scan GPR images and selecting the peak value in the histogram to generate the model signal. The following notation is used in the proposed GPR feature based algorithm:  $C$  denotes the C-scan 3D GPR image,  $x, y, z$  represent the length, width and layer number of the 3D GPR image, respectively,  $N$  is the largest index value of  $(x, y, z)$ ;  $\forall x, y, z \in [1, N]$ ,  $C(z)$  is the layer  $z$  in the C-scan GPR image,  $A(x, y)$  is the A-scan signal at the location  $(x, y)$  in the C-scan GPR image,  $A(z)$  is the pixel value of the A-scan GPR signal at layer  $z$  for fixed values of  $(x, y)$  and vector  $M(z)$

is the model signal, which represents the common background information in the C-scan GPR image, as below:

$$M(z) = \max(\text{hist}(C(z))) \quad (10)$$

where the *hist* function calculates the histogram of layer  $z$  of the C-scan GPR signal  $C(z)$ ; the *max* function determines the peak value of the histogram in layer  $z$ . Following the equation 4.16, the model signal of the indoor environment 3D-GPR image has been built, shown in Figure 4-14 below:

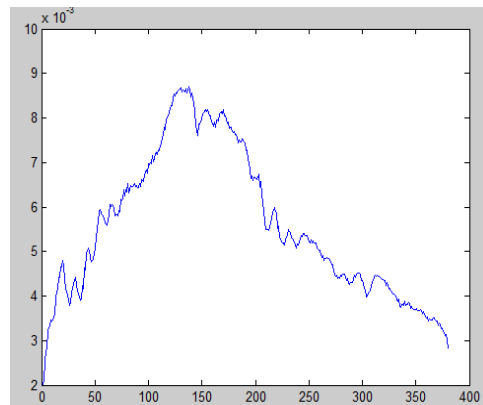


Figure 4-14. Model signal of the GPR array signal (public domain dataset).

In Figure 4-14, the blue line represents the model signal of the public domain GPR array dataset. The model signal is composed of the average reflection value of the test area under different scanning frequencies.

Since most of the A-scan GPR signals in a C-scan GPR image result in a background signal, the landmine signal is unique, and it is concentrated in a small area. The model signal will represent the common background information in the C-scan GPR image. When the difference between the model signal and A-scan signals is significant enough, this is an indication that there might be a landmine present. In this proposed

algorithm, two different methods are used to quantify the difference between the model signal and A-scan signals.

First, the cross-comparing method aims to compare the absolute difference between two signals. Assume  $D$  is the quantised difference value. Equation (4.17) shows how the first method works:

$$D_{(x,y)} = \sum \sqrt{(A_{(x,y,z)} - M_{(z)})^2} \quad (4.17)$$

Figure 4-15 below shows the detection result of the public domain dataset by using equation (4.17). In Figure 4-15, the colour bar goes from blue to red, which means that the blue colour is the safe colour and the red means a landmine is present. Comparing Figure 4-15 with the ground truth map (Figure 4-4), it can be clearly seen that the landmine in the left row and the right row has been marked as red, yellow, and light blue. However, there are still lots of false alarms which influence the detection result.

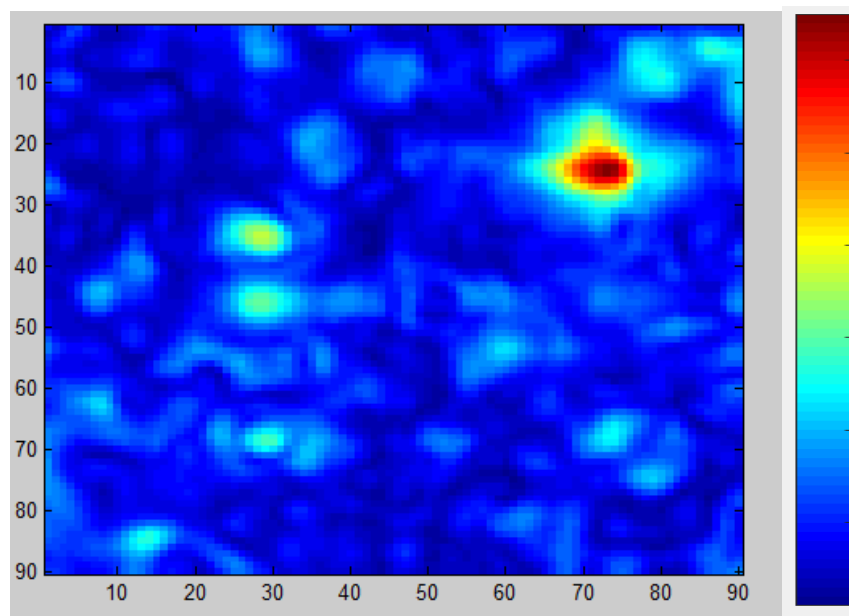


Figure 4-15. Cross-comparing method of statistics-based algorithm for the public domain dataset.

The self-comparing method aims to compare the self-difference between the model signal and the A-scan signals. The working principle of this method is that the increment of reflection signals is proportional to the increment of the transmitting signals. This means that, if using a constant increment step scanning frequency to scan the ideal mine clear area, there will be a constant increase value in each layer as the scanning frequency increases.

Once the sum of the self-difference of one A-scan signal is much higher than the model signal, it means a landmine is present. Equation (4.18) shows how the second statistics-based algorithm works:

$$D_{(x,y)} \tag{4.18}$$

$$= \sum \sqrt{\left( \sqrt{(A_{(x,y,z+1)} - A_{(x,y,z)})^2} - \sqrt{(M_{(z+1)} - M_{(z)})^2} \right)^2}$$

Figure 4-16 below shows the detection result of the public domain dataset by using equation (4.18). In Figure 4-16 the colour bar goes from blue to red, where the colour blue means landmine absence and yellow and light blue means a landmine is present. When compared with the ground truth map (Figure 4-4), the result shows that most of the landmine in the left and right row has been detected, and, in the middle row, the landmine area can be distinguished against the background.

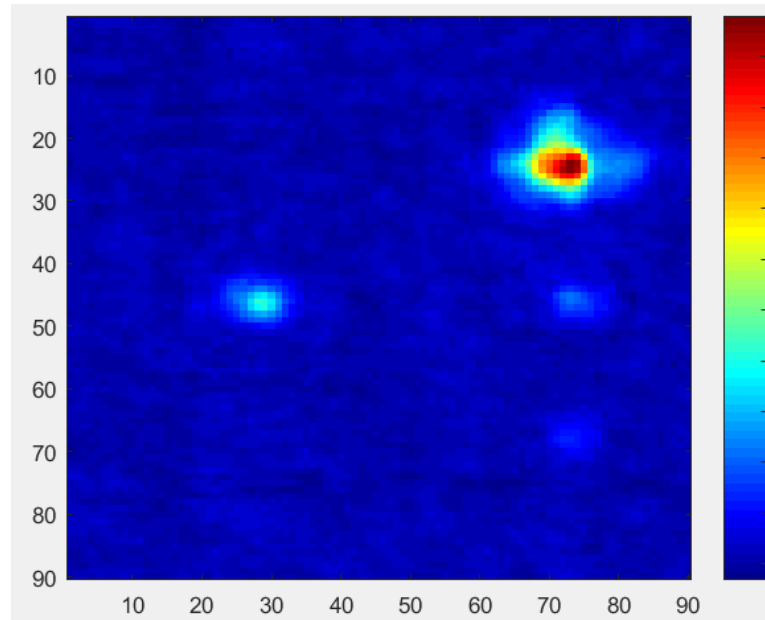


Figure 4-16. Self-comparing method of statistics-based algorithm for the public domain dataset.

### 4.3.3 GPR Array Feature-based Algorithm

As mentioned in section 2.3.3, the spectral feature, spatial region feature and the spatial edge feature are the main features of the 3D GPR image, which can be used in the landmine detection algorithm research area. Currently, most of the existing algorithms focus on using one feature for detection work. A novel idea of combining two or more different types of features of the 3D GPR image to improve the detection performance of the algorithm has been proposed in this research. The GPR feature-based algorithm combines a spectral feature and a spatial edge feature of the GPR signals to form a new oscillation feature, which can represent the reflection value change between the layers of a C-scan GPR image.

The oscillation feature of the GPR signals are defined as follows. When a GPR signal trend changes from an increase to decrease and from a decrease to increase in an A-scan GPR signal, it exhibits an oscillation. The increment of the signal reflection

absolute value tends to oscillate as the scanning frequency increases step by step. The spectral feature of the GPR array signal is the distance between the peaks of an A-scan signal, and its lowest value is the signal oscillation range. The oscillation frequency represents the spatial edge feature of the GPR array signals. If the sum of the absolute oscillation distances for an A-scan signal is greater than the absolute oscillation distance of the background signal, this indicates a presence of a landmine target. In addition, a signal corresponding to a landmine will also have a lower oscillation frequency value.

The working principle of the proposed algorithm generates a model signal by using the background information from the C-scan 3D GPR image, thereby comparing the differences between each A-scan GPR signal with the model signal to extract the oscillation features. Since most of the A-scan signals result in a background signal, the landmine reflections are unique and concentrated in a small area. By comparing the model signal with the A-scan signals, the presence of a landmine could be established in case of a large difference in value between the two signals. Figure 4-17 below shows the flowchart of the proposed GPR feature-based landmine detection algorithm.

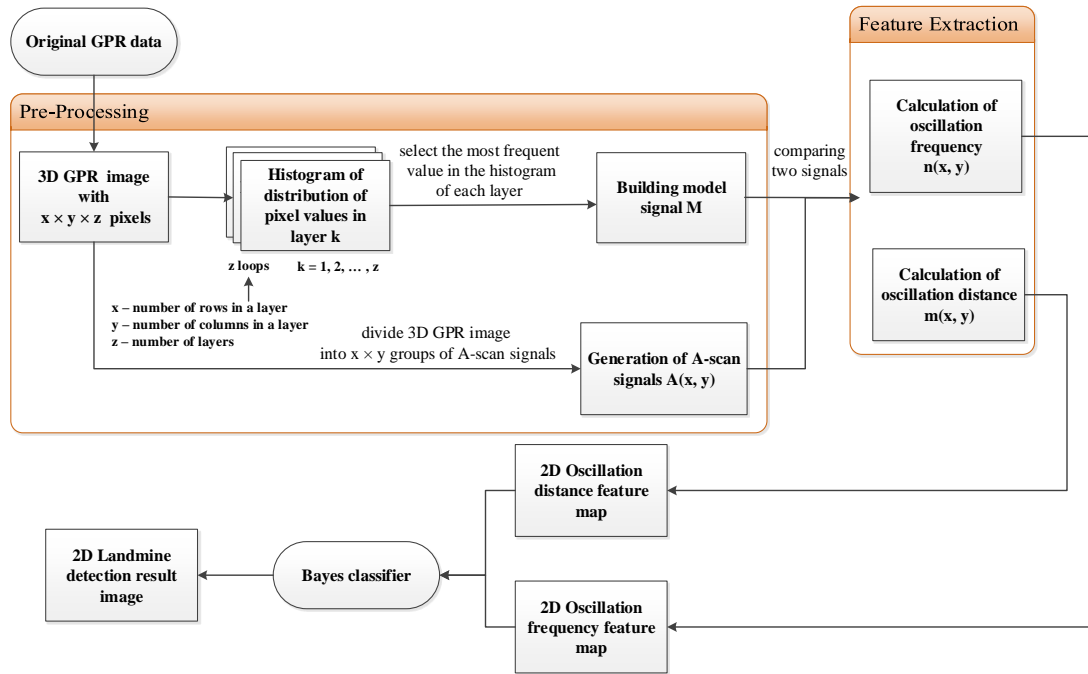


Figure 4-17. Flowchart of the GPR feature-based landmine detection algorithm.

In Figure 4-14, the proposed algorithm can be divided into three main steps: pre-processing, feature extraction and decision making. The pre-processing block aims to build the model signal and divide the original 3D GPR array matrix into A-scan GPR signals, preparation for feature extraction. The first step of the pre-processing block is formatting the original GPR data into 3D GPR image, which is a 3D matrix, and each pixel inside represents the reflection value of the corresponding GPR scanning frequency. The second step is to divide the 3D-GPR image into A-scan GPR signals, which aim to compare the model signal in the feature extraction blocks. The model signal will be build based on equation (4.16) in chapter 4.3.2.

The feature extraction block aims to calculate the oscillation features of the model signal, which includes the oscillation frequency and the oscillation range. The standard oscillation range  $r$  is equal to  $1/N$  of the sum of the oscillation distances of the model signal, as expressed by equation (4.19) below. In equation (4.19), the sum of the

oscillation distances of the model signal represent the absolute spectral information changing range.  $N$  represents the total layer of the C-scan 3D GPR image; therefore, the  $r$  represents the average changing range of the spectral information. Once the spectral information of two adjacent pixels in the A-scan signal is higher than  $r$ , it means a unique oscillation has been found, which might be caused by a landmine. Then, based on equations (4.20) and (4.21), the oscillation frequency of the A-scan GPR signal  $n$  (starting from 0) and the sum of the absolute oscillation distances of the A-scan GPR signal  $m$  are obtained.

$$r = \frac{1}{N} \times \sum_{i=1}^n \sqrt{(M(z+1) - M(z))^2} \quad (4.19)$$

$$n = \begin{cases} n+1 & \text{if } \sqrt{A(z+1) - A(z)}^2 - r > 0 \\ n & \text{if } \sqrt{A(z+1) - A(z)}^2 - r < 0 \end{cases} \quad (4.20)$$

$$m = \sum_{i=1}^n \sqrt{(\sqrt{A(z+1) - A(z)}^2 - r)^2} \quad (4.21)$$

After getting  $m$  and  $n$ , the same oscillation features of each A-scan signal will be calculated. By comparing A-scan signals with the model signal, two  $x \times y$ -sized matrices will be generated. One represents the difference in the oscillation times between the model signal and each A-scan signal while the other represents the sum of the total oscillation distance.

Figure 4-18 below shows the new algorithm result when using the public domain image. In Figure 4-18, the left-hand side image represents the feature of the oscillation distance, the blue colour in the image represents the high oscillation distance (landmine present) and the yellow parts represent low oscillation distance (landmine absence). Comparing the left image with Figure 4-5, it can be clearly seen that most

of the buried object has been detected; only the TS-50 and PFM-1 in the middle row are missing. The right-hand side image represents the oscillation time, the yellow colour represents the high oscillation numbers (landmine absent) and the blue colour represents the low oscillation numbers (landmine present). When comparing the right-hand side image of the figure with the ground truth map, the landmine in the left row is not that clear; however, the TS-50 and PFM-1 in the middle row have been detected.

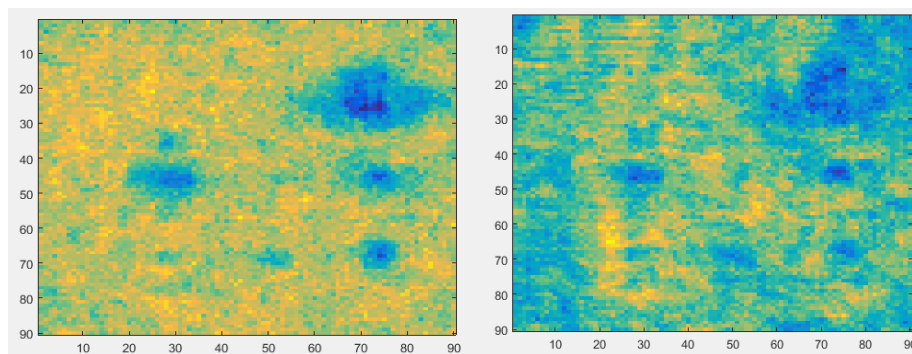


Figure 4-18. Testing result of the feature-based algorithm. Left: oscillation distance. Right: oscillation numbers.

After the two different feature maps have been built based on the proposed algorithm, a fuzzy fusion rule (see section 5.4) is applied to select the lowest oscillation number and largest oscillation distance pixels, as the landmine present. Then, based on the fusion result, a 2D feature map is built. Figure 4-19 below shows the testing result of the GPR feature-based algorithm under the public domain dataset.

From Figure 4-19, it can be clearly seen that the yellow parts are the objects obtained by the GPR sensor; this is accurate detection when compared with the ground truth map. The testing result proves that the proposed feature-based algorithm is able to achieve accurate landmine detection in a small test area.

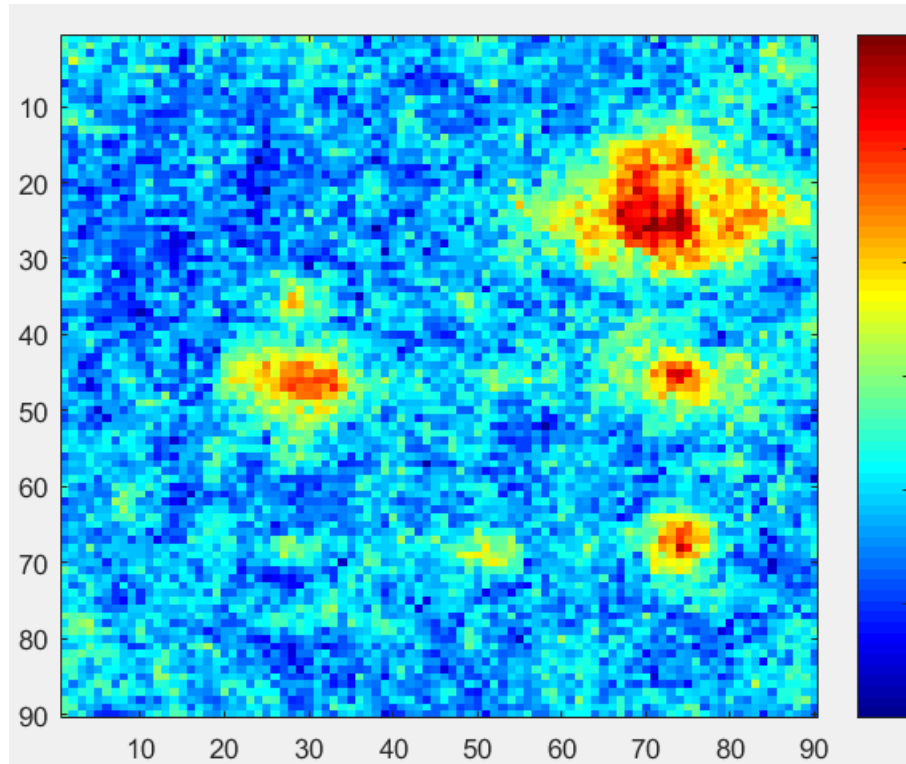


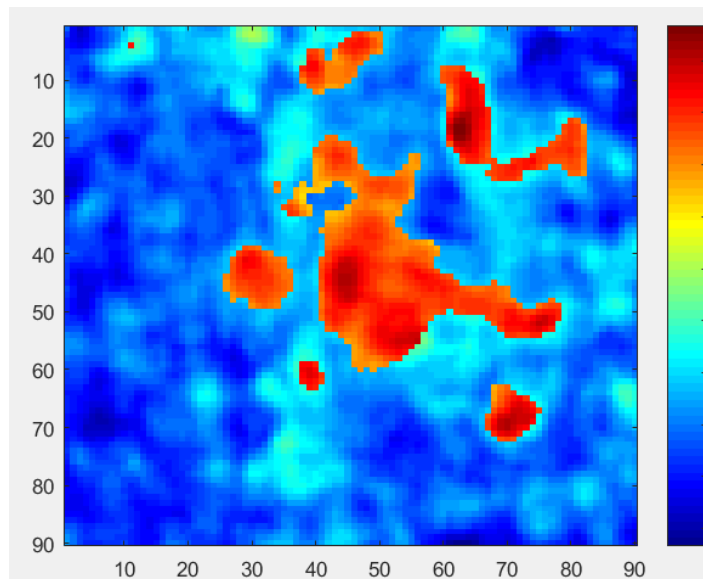
Figure 4-19. 2D detection map of the feature-based algorithm.

## 4.4 Evaluation of the Algorithms

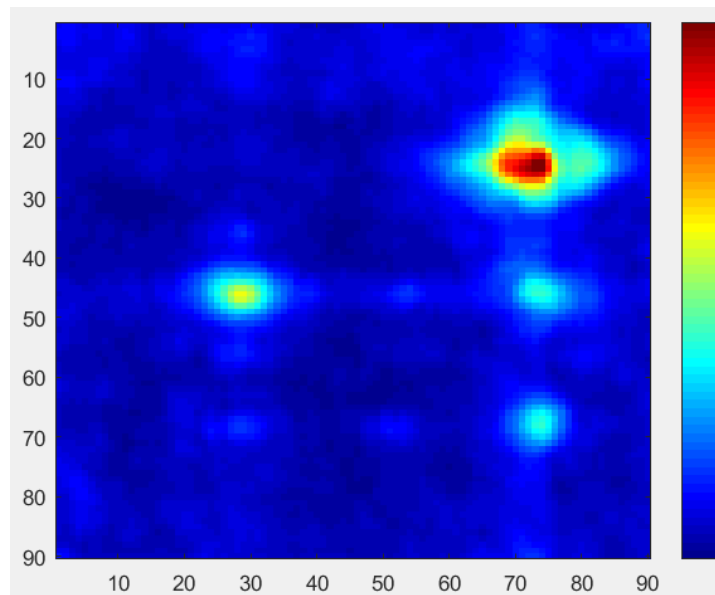
### 4.4.1 ROC Curve Analysis

The ROC curve, introduced in section 4.1.1, is a very popular method for evaluating performance of landmine detection algorithms. The edge-energy method (section 2.3.3), region-selection thresholding method and EHD method are employed as reference algorithms in this section due to their strong detection performance, comparable to the best-performing state-of-the-art algorithms [56, 65]. In this case, the detection accuracy has been set at 1cm for the indoor environment, which means that the detection algorithm needs to locate the landmines in the right position only. The 1cm accuracy range is only used for testing the limitations of the proposed algorithms; in a normal case, the accuracy range for a deminer would be 40cm to 60cm.

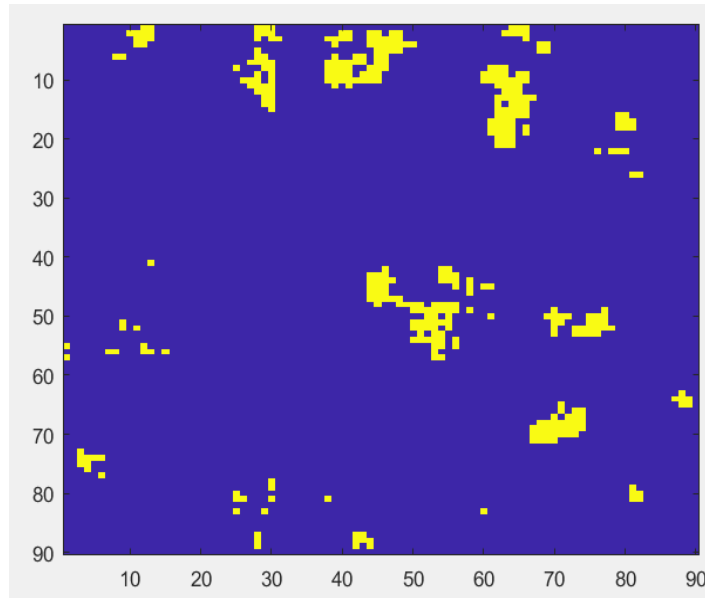
Figure 4-20 below shows the landmine detection results by running the three reference algorithms with the indoor environment dataset:



(a) EHD algorithm



(b) Edge energy algorithm



(c) Region selecting thresholding method

Figure 4-20. Reference algorithms' test results with the indoor environment dataset.

Figure 4-20 shows the test result of the existing popular landmine detection algorithms within an indoor environment. Figure 4-20(a) is the result of the EHD algorithm mentioned in section 2.2.3. The window size was set as  $10 \times 10 \times 10$ , which means that, in each window, there are 1000 pixels. The  $\theta$  value has been chosen from 0.20~0.50, and the final  $\theta$  value in this case is 0.27, since, in the original algorithm, the  $\theta$  is an experience value. Figure 4-20(b) is the result of the edge-energy algorithm; the test results show the accurate location of the buried landmines. Figure 4-20(c) is the region-selecting thresholding method test result. Since the comparing algorithm is the entropy-based algorithm, in this case, region size has been selected as  $5 \times 5$  square, the same size as the entropy-based algorithm window size.

Five different proposed algorithms and three reference algorithms are implemented in this chapter. All eight algorithms have been used for processing the indoor environment dataset. The visual detection results have shown that all the eight

algorithms can detect most buried landmines. However, some algorithms introduce more false alarms than others. Therefore, a ROC analysis has been made by comparing the detection results of the eight algorithms with the ground truth map, thereby evaluating the detection accuracy of all eight algorithms. Figure 4-21 below shows the ROC analysis results:

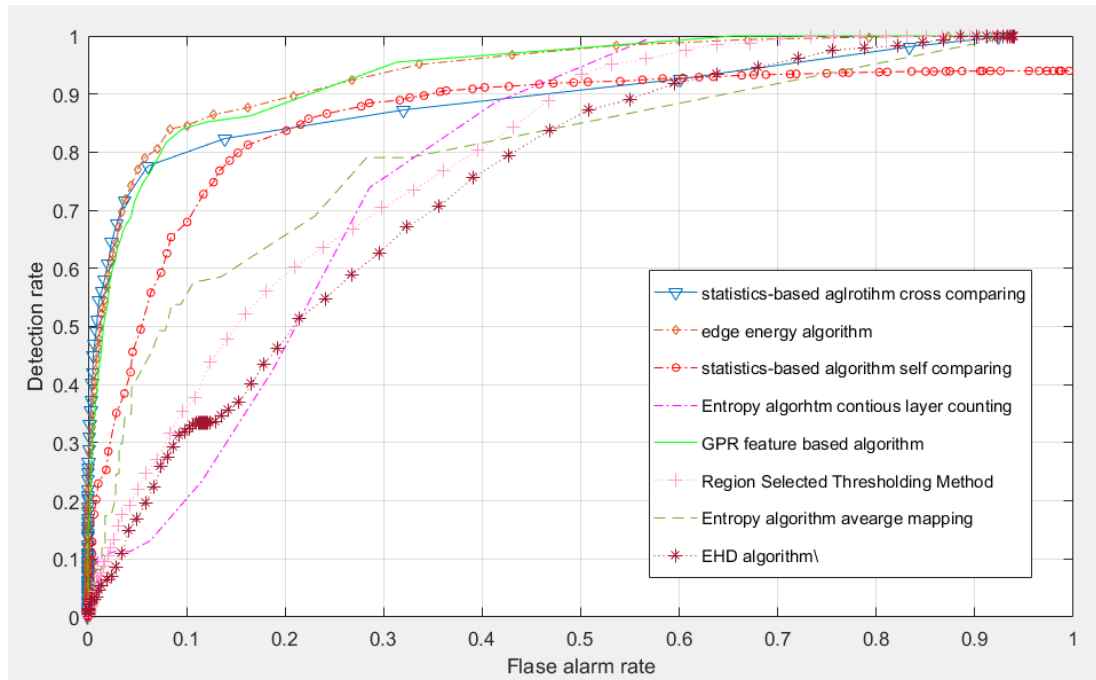


Figure 4-21. ROC curve of the proposed algorithms for the indoor test dataset (section 4.2.2).

As it can be seen from Figure 4-21 that the edge-energy algorithm and the GPR feature based algorithm have the best ROC curve with a high detection rate and low false alarm rate. It also proves that both the GPR feature-based algorithm and the statistics-based algorithms perform well in the ROC curve. In fact, there is no significant difference in performance between the edge-energy and the GPR feature-based algorithm. All the proposed spatial-feature algorithms are outperforming the EHD algorithm. The detection ability of the statistics-based algorithms has reached a 35% and 46% false alarm rate with a 90% detection rate for the self-comparing and cross

comparing algorithms, respectively. The GPR feature based algorithm has reached a 22% FAR with a 90% detection rate, which is a great improvement. The existing low boundary of the detection ability is demonstrated by the EHD algorithm with a 60% FAR at a 90% detection rate. The entropy-based algorithms and region-selecting thresholding methods do not show a good ROC curve. This is because these three algorithms realise a region-based detection, whereby all the pixels in the same region will have the same decision. However, the ROC curve of the entropy-based algorithm reaches a 33% FAR at a 80% detection rate, outperforming the existing region selecting thresholding algorithm (40% FAR at 80% detection rate).

#### **4.4.2 Detection Accuracy Range Analysis**

Detection accuracy range is the distance between the position of the landmine when triggering an alarm and the centre or edge point of the landmine. In a normal case, the detector will define a distance or ‘halo’ around the target centre or edge (edge will be used in this case), and any alarm within this range will be considered a detection. The distance or ‘halo’ is difficult to define; in fact, each detector has its own experience in selecting the detection accuracy range based on environmental conditions and the sensor’s location-estimate uncertainties. The literature has shown that most detectors define the halo radius around 40cm (edge case) or 60cm (centre case) for safety reasons[38].

In this case, the detection accuracy range is calculated by counting the largest distance between the landmine alarm position to the edge of the landmine. Table 4-1 below shows the detection accuracy range for all the eight algorithms using the indoor environment dataset.

In Table 4-1, the red coloured numbers represent the highest maximum detection accuracy range of the algorithms: most of the algorithms' detection accuracy ranges are around 20cm radius, smaller than the standard range. The GPR feature-based algorithm outperforms the edge-energy algorithm in the maximum accuracy range. The blue coloured numbers represent the lowest maximum detection accuracy range of each object. The edge-energy algorithm outperforms the other algorithms with five objects having the lowest maximum detection accuracy range. However, the GPR feature-based algorithm also has three objects getting the lowest accuracy range. Table-4-1 thus demonstrates that the proposed algorithm can satisfy the standard detection accuracy range for demining works.

Table 4-1 *Detection Accuracy Range Analysis*

	Entropy-based average	Entropy-based CLC	Statistics-based self-comparing	Statistics-based cross-comparing	GPR feature based algorithm	EHD algorithm	Edge energy-based algorithm	Region selecting thresholding algorithm
Sphere	-	10cm	-	8cm	6cm	8cm	4cm	-
TS-50 (1)	20cm	10cm	10cm	-	6cm	8cm	6cm	-
VS-1.6	10cm	10cm	12cm	16cm	10cm	8cm	8cm	-
TS-50 (2)	10cm	10cm	10cm	-	6cm	6cm	4cm	-
TS-50 (3)	10cm	10cm	8cm	10cm	6cm	8cm	10cm	-
M-14	-	-	6cm	-	-	18cm	-	14cm
PFM-1	10cm	10cm	20cm	22cm	18cm	6cm	4cm	12cm
TS-50 (4)	10cm	0cm	4cm	-	8cm	-	12cm	-
TMA-5	20cm	20cm	12cm	10cm	16cm	8cm	20cm	16cm
VS-2.2	20cm	10cm	12cm	4cm	4cm	10cm	12cm	8cm
Cylinder	10cm	20cm	14cm	4cm	6cm	14cm	8cm	14cm

### 4.4.3 Operation Time Analysis

Operation time is another important parameter used to evaluate landmine detection algorithms. Since the ultimate goal of the landmine detection algorithm design is to achieve real-time operations for use in handheld or vehicle-based landmine removal tools, a short operation time for the algorithms is desirable. In some of mine area reduction work, the operation time is now that important, however, for military used landmine detection and some urgent detection work the operation time will be an important point. Figure 4-22 below shows the operation times for all the proposed algorithms in this chapter in the MATLAB environment, using the public 3D GPR image, described in sec. 4.2.2.

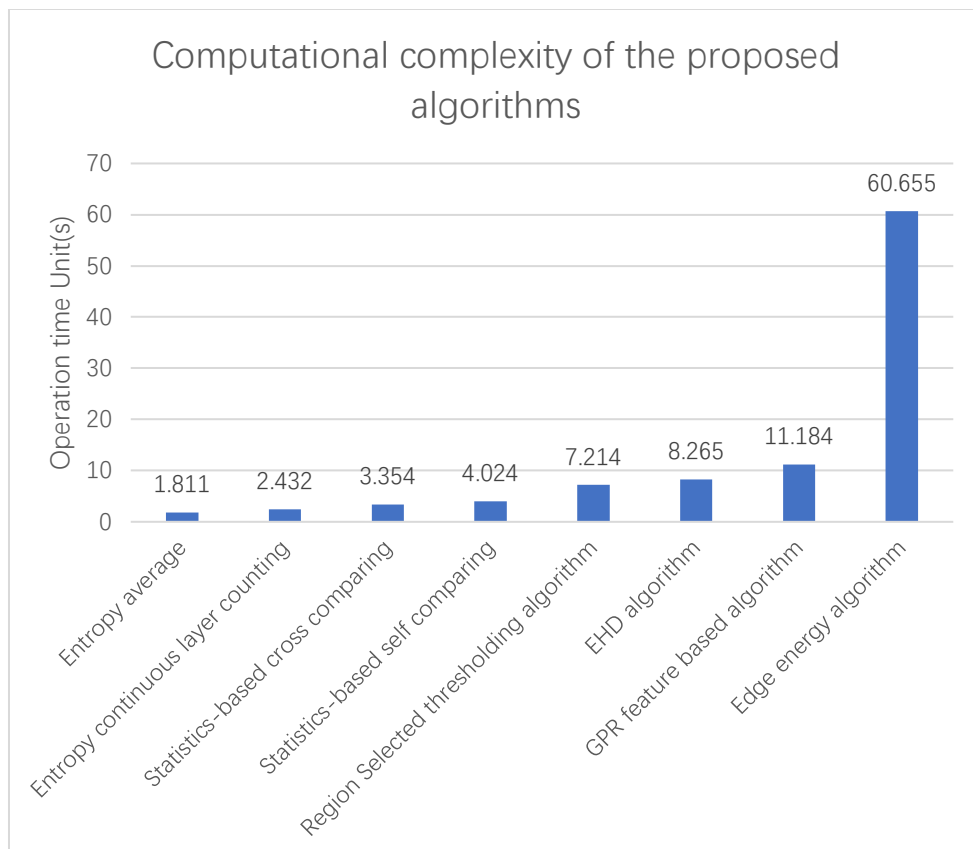


Figure 4-22. Operation time of the proposed algorithms in the MATLAB environment.

According to Figure 4-22, the entropy-based algorithm has the lowest operation time when processing the same size data, which means that the algorithm is suitable for detection within a large mined area. In addition, the entropy-based continuous-layer counting method has saved 66.2% computation time compared with the region selection thresholding method. The edge-energy algorithm has the highest operation time when processing the same size data, which means it is only suitable for detection of small areas. The GPR feature-based algorithm has the second-highest operation time; however, it is significantly faster than the edge-energy algorithm, having showed 81.5% evaluation time. The statistics-based algorithm has a higher operation time than the entropy-based algorithm but lower than the edge-energy and the EHD algorithm, which is a good choice for landmine detection processes in a small area. The statistics-based self-comparing method requires 51.1% less computation time than the EHD algorithm. In addition, the analysis of the computational complexity of the proposed algorithm has been made (see Appendix G).

Finally, we observe that the two existing popular algorithms used in embedded systems, the EHD and the region-based selection algorithm have operation times, which are higher than four of the proposed algorithms but lower than one of them in Figure 4-22. In conclusion, the operation time analysis results suggest that the proposed algorithms can fulfil the requirements of the existing landmine detection processes.

#### **4.4.4 Memory Usage Analysis**

To evaluate the embedded-system algorithm, there are two main parameters: operation time, as discussed in section 4.4.3, and the memory usage of the program. In the normal case, the memory usage of a program can be divided into three parts: input

memory usage, the program memory usage and the derived variable memory usage during the program running.

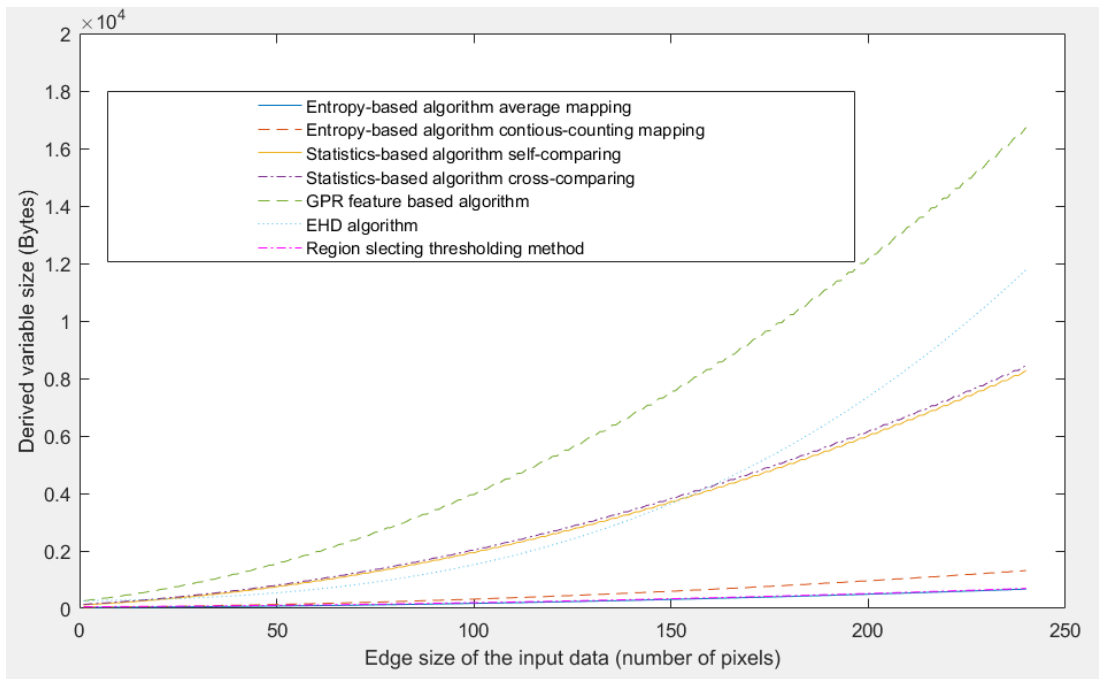
In a landmine detection case, the memory used by the data inputs is the same (for the indoor environment, the input files size is 37.14MB). In addition, memory usage by the program very less (all eight algorithm files are less than 1KB). Therefore, the memory usage analysis in this case will mainly focus on evaluating the size of the total derived variables during the program running. The memory usage analysis will consider the size of the input 3D GPR array data as  $M \times N \times K$ , where the  $M$  and  $N$  represent the horizontal and vertical size of the input data, and  $K$  represents the depth index. For each pixel in the 3D GPR array, the data values will be 16 bit-long numbers which use two bytes. In addition, for all the region-based algorithms, the window size will be  $x \times y \times z$ . The memory usage analysis aims to calculate the derived variable size produced by the program. Table 4-2 below shows the total memory usage by all the eight algorithms.

Table 4-2 *Memory Usage by the Landmine Detection Algorithms*

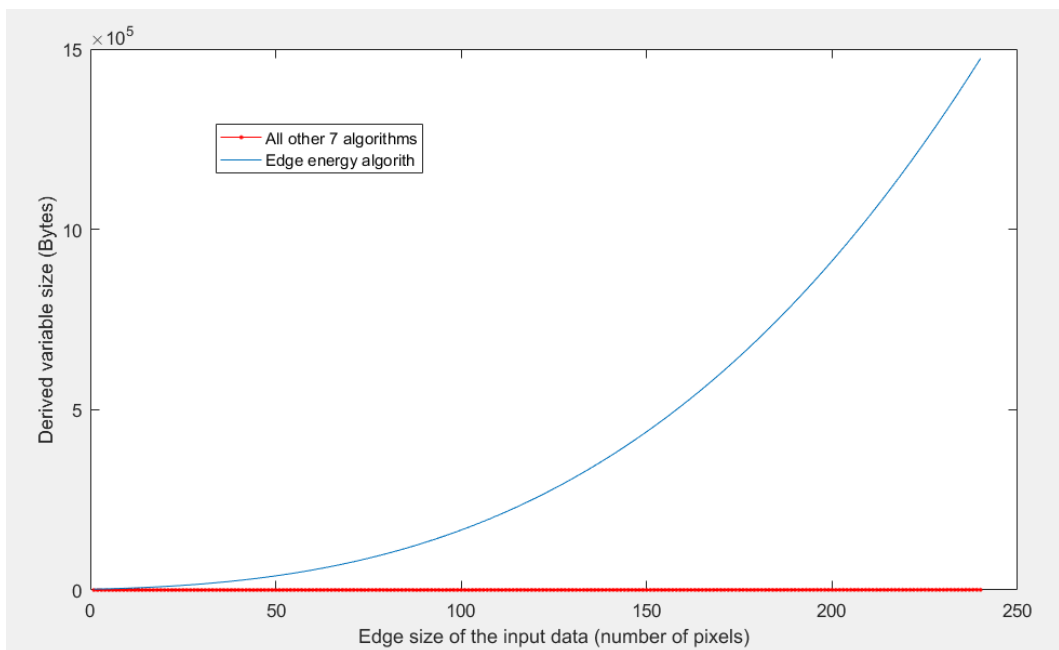
	Entropy-based average	Entropy-based continues layer counting	Statistics-based self-comparing	Statistics-based cross-comparing	GPR feature based algorithm	EHD algorithm	Edge energy-based algorithm	Region selecting thresholding algorithm
Input size	$M \times N \times K \times 2\text{Byte}$	$M \times N \times K \times 2\text{Byte}$	$M \times N \times K \times 2\text{Byte}$	$M \times N \times K \times 2\text{Byte}$	$M \times N \times K \times 2\text{Byte}$	$M \times N \times K \times 2\text{Byte}$	$M \times N \times K \times 2\text{Byte}$	$M \times N \times K \times 2\text{Byte}$
Program size	Less than 1KB	Less than 1KB	Less than 1KB	Less than 1KB	Less than 1KB	Less than 1KB	Less than 1KB	Less than 1KB
Derived variable size	$(x \times y + \frac{M}{x} \times \frac{N}{y} \times 2) \times 2\text{Byte}$	$(x \times y + \frac{M}{x} \times \frac{N}{y} \times 4) \times 2\text{Byte}$	$(3 \times K + M \times N) \times 2\text{Byte}$	$(3 \times K + M \times N) \times 2\text{Byte}$	$(6 \times K + M \times N \times 2) \times 2\text{Byte}$	$(x \times y \times z \times 2 + \frac{M}{x} \times \frac{N}{y} \times \frac{K}{z} \times 2) \times 2\text{Byte}$	$(M \times K \times 2 + N \times K \times 2 + M \times N \times K \times 2 + M \times N) \times 2\text{Byte}$	$(x \times y \times 2 + \frac{M}{x} \times \frac{N}{y} \times 2) \times 2\text{Byte}$

Table 4-2 shows memory usage when the program runs; it can be seen that the edge energy will use more memory than other algorithm, which is because the edge-energy algorithm will fuse two edge matrices, which is the same size as the original input data. This also explains why the edge-energy algorithm has the longest operation time among the eight algorithms. The GPR feature-based algorithm also contains the fusion step; however, the fusion input are two decision maps which do not use too much memory. Figure 4-19 shows the memory usage change trends when the input size of data increases. In Figure 4-19, the size of the input image has been set between  $10 \times 10 \times 10$  (around 8KB) to  $90 \times 90 \times 90$  (around 729KB), and the window size of the region-based algorithm has been set to  $5 \times 5 \times 5$ .

Figure 4-23 (a) shows the memory usage of all detection algorithms except the edge-energy algorithm. The entropy-based averaging method and the region-selection thresholding method will use less memory in the embedded system. The statistics-based algorithm and the entropy-based continuous-layer counting method reach the same memory level as the EHD algorithm, which is an existing popular algorithm. The GPR feature algorithm has a high memory usage size; however, it is still on the same level as the EHD algorithm. Figure 4-23(b) shows the memory usage of the edge-energy algorithm and the other seven algorithms. It can be clearly seen that the edge-energy algorithm will use more memory than the other algorithms, which limits the edge-energy algorithm to systems that can provide large memory blocks.



(a)



(b)

Figure 4-23. The memory usage change trend.

## 4.5 Summary

This chapter focused on the design and evaluation of single sensor landmine detection algorithms. Two different GPR-based landmine datasets were introduced in order to evaluate the performance of the proposed algorithms.

Three different landmine detection algorithms suited to C-scan 3D GPR images were proposed. The entropy-based algorithm is appropriate for fast detection over a large area, the statistics-based algorithm is fast and shows good performance in a small area, and the feature-based GPR sensor detection algorithm is suitable for a small area and results in a high detection rate. The proposed algorithms could be used for close-in landmine detection work, generating a 2D landmine decision map based on 3D GPR images. The 2D landmine decision map could assist current landmine detection systems locate suspected landmines in the field. All the proposed algorithms have accomplished the detection boundary of the existing single sensor detection algorithms, i.e. 60% FAR at 90% detection rate for APM. In addition, the 2D decision map is suitable for both feature- and decision-level fusion with other types of sub-surface landmine detection sensors.

The performance of each of the proposed algorithms was evaluated via visual inspection, detection accuracy range analysis, operation time comparison and memory usage estimation. The entropy-based algorithm uses the entropy value instead of the maximum energy value of the existing region-based detection algorithm and it outperforms the latter on both detection rate and operation time. The statistics-based algorithm uses A-scan GPR signals to detect landmines, which reduces the GPR data size in comparison to the GPR B-scan signals, used by most of the existing algorithms. In addition, the statistics-based algorithm has outperformed the EHD algorithm on

both detection rate, detection accuracy range and operation time. The GPR feature based algorithm has proposed a new feature of the GPR signals which is the oscillation feature. By using the oscillation feature, the proposed algorithm has achieved detection ability of 22% FAR at 90% detection rate, which is the same level as the best existing edge energy algorithm.

The Naples outdoor dataset demonstrated that the entropy-based algorithm has the ability to reduce the suspected landmine area effectively. The dataset is collected from a simulated landmine area, which includes lots of clutter signals and uncertain objects, however the entropy-based algorithm still detects all the landmines in that field. It is a notable accomplishment showing that the proposed algorithm will not only work in an ideal environment but also in a real outdoor environment. The experimental results based on the public domain indoor dataset have confirmed that both the statistics-based algorithms and the GPR feature-based algorithm could achieve accurate landmine detection in a small area.

In conclusion, the new landmine detection algorithms that have been proposed in this chapter show a good performance, featuring a low operation time and memory usage, which are required characteristics in EOD systems.

# **Chapter 5: Data Fusion System Design for Landmine Detection**

This chapter aims to design heterogeneous multi sensor data fusion systems for landmine detection. The work is demonstrated using the close-in detection scenario of the EU D-Box project.

Section 5.1 presents the background and data fusion concept of the D-Box project as well as the available resources for the fusion process. Section 5.2 proposes two novel data fusion systems, Kalman-Bayesian and fuzzy-logic based; a reference Dempster-Schafer Theory-based data fusion system is introduced too. Section 5.3 provides evaluation results. Section 5.4 summarises the chapter.

## **5.1 D-Box System and Data Resources**

One of the work packages in the D-Box project was related to heterogeneous multi-sensor data fusion. This section describes the data fusion system structure developed to achieve the requirements of the D-Box task WP4.5.1 [99], in which the author was involved.

The two main humanitarian mine actions that may benefit from multi-sensor data fusion technology are close-range mine detection and mined area reduction as shown in Figure 5-1. The goal of the close-range mine detection activity is to identify and locate landmines in the minefield, discriminating them from other objects. The mined area reduction activity aims to identify the mine free area from the mine suspected areas (MSA).

As shown in Figure 5-1, the multi-sensor data fusion process for the APM clearance task can be separated into two tasks: mined-area reduction and close-in detection of

APM. The mined area reduction task aims to fuse satellite images with three dimensional images in order to reduce the suspected landmine area. The close-in AP mines detection aims to fuse data obtained primarily by sub-surface detectors, in order to identify the actual landmines in a small working area.

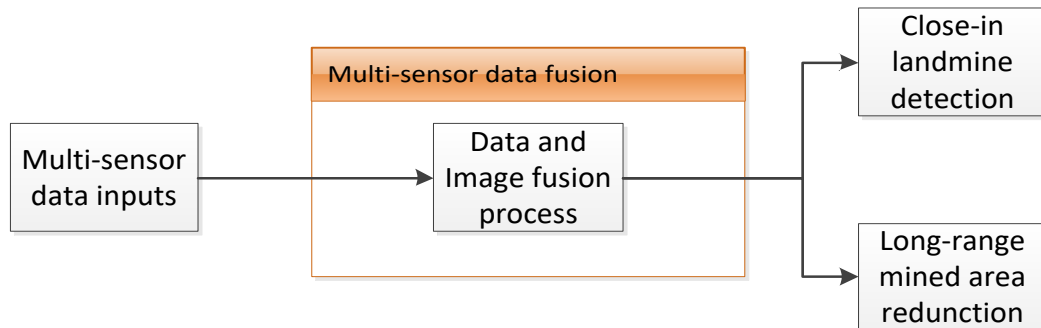


Figure 5-1. Multi-sensor data fusion for AP landmine clearance.

The objective of task WP4.5.1 in the D-Box project is to develop a sensor-fusion tool that takes heterogeneous sensor data sets as input and outputs a more informative landmine detection report.

### 5.1.1 D-Box System Design

There are several types of heterogeneous sensors used in close-in landmine detection systems, including electromagnetic induction (EMI) sensors, ground-penetrating radar (GPR), infra-red cameras, etc. Metal detectors are based on EMI technology and are the dominant sensors in current demining practices. An induced magnetic field is measured over a target via a time-varying magnetic field over the respective target. This technology is good for detecting buried mines in non-metallic soils, but it generates a very high rate of false alarms. Data fusion with other sensors, e.g. GPR and IR, could help to discriminate between mines and other objects in order to reduce the false alarm rate of EMI sensors. GPR detects discontinuities in the ground

including landmines with little or no metal content (high detection rates), but there could be also a high rate of false detections due to being quite sensitive to the type of soil and its conditions, surface cover and terrain [22]. Thermal infrared cameras can image thermal differences between shallow-buried objects.

The goal of fusing heterogeneous sensors in demining is to detect antipersonnel mines in different mined areas with a variety of surface covers, such as soil, grass, tussocks, etc. Since different sensors will produce different output data, it is necessary to find a common reference point. Previous projects have used confidence levels of sensors as a common point for fusion work. It is worth noting that most of the previous landmine detection projects have been tested with training datasets rather than blind field test data, showing very good performance (high detection rates and low FAR).

Figure 5-2 shows the proposed close-range detection system on a functional level. Sub-surface sensors such as MD, GPR and IR could be fused to detect landmines. Environmental data from surface sensors and the results of long-range area reduction could be fused to finalise the mine suspected area. After that, binary decision results from landmine detection and the MSA could be combined to get an overall fusion result, presented in the form of a GIS map with landmine markings.

A multi-sensor close range landmine detection system has been proposed based on the existing Naïve Bayes data fusion system (Figure 2-3) and the available landmine detection sensors in the D-Box project. The proposed algorithm includes three parts: image pre-processing, image feature extraction, and landmine decision-making. Figure 5-3 below shows the proposed top-level design of the landmine detection system, for the D-Box close-range detection task WP4.5.1.

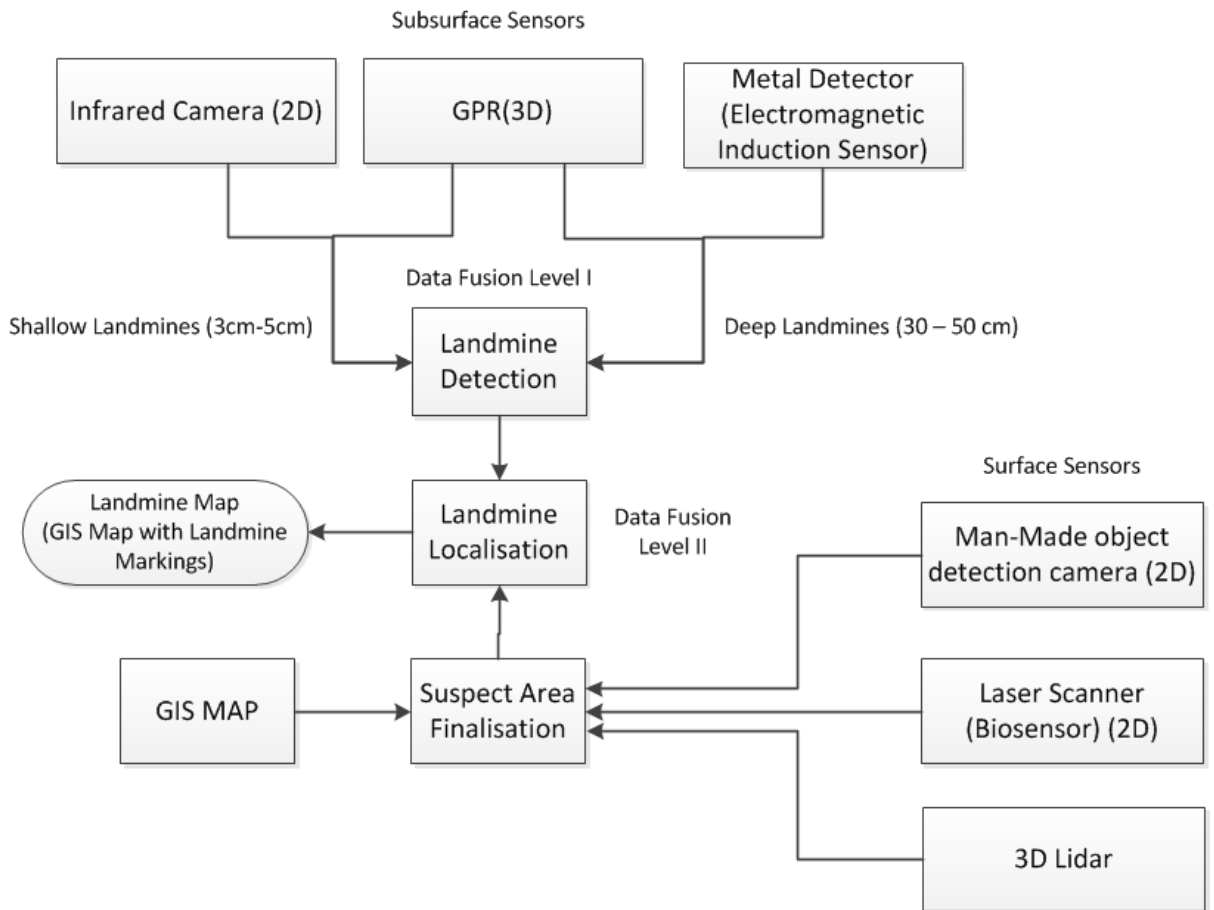


Figure 5-2. Close range detection sensor data fusion functionality.

The image pre-processing unit requires that all of the input types are geo-referenced images. The main work of the image pre-processing unit is to correct the input signals, allowing the raw fusion images to become pixel-matched images. The output of the image pre-processing unit will be three different pixel-matched images.

The image feature-extraction step aims to build the danger map for each pixel-matched image. In this case, we select the entropy value as the main feature of the pixel-matched image. Since, in GPR, IR and MD images, the detected object shape can be seen easily, the edge of the object will show a high entropy value. This research has try to using the IR images as the input of the data fusion system (see Appendix H), however, the IR images is unmatched with the GPR or MD signal, the IR images will

not be introduced into this research. The feature of the landmine detection sensor could be extracted similarly as in the GPR feature-based algorithm proposed in section 4.3.3.

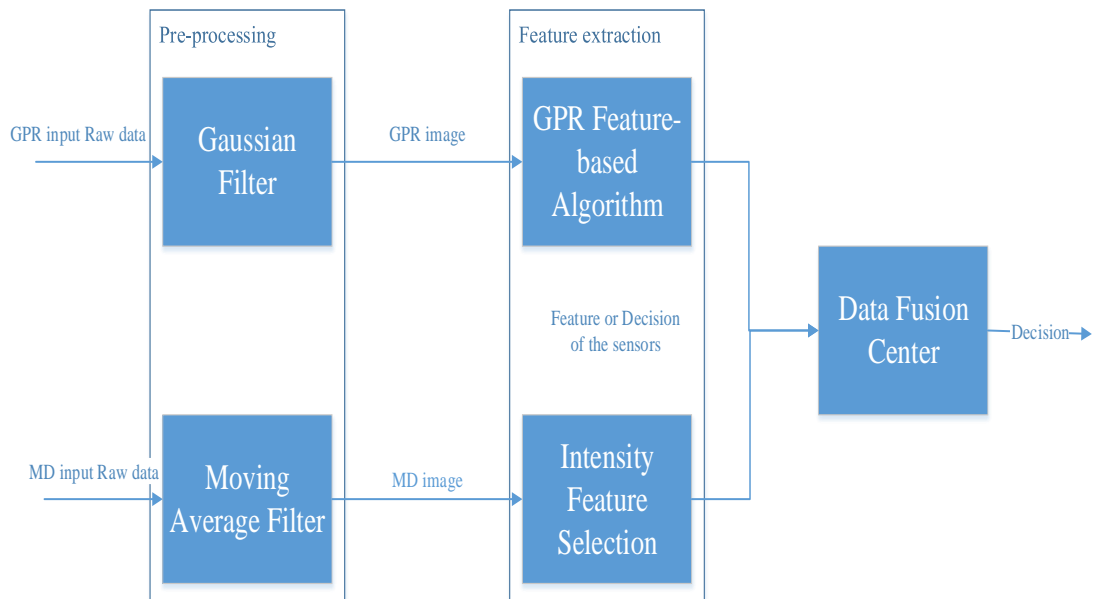


Figure 5-3. Centralized feature level Naïve Bayes fusion system flowchart.

In Figure 5-3 the pre-processing step for both GPR and MD data aims to reduce the sensor noise. Due to the Gaussian noise is the mainly noise of the GPR sensor[4] , a Gaussian filter has been employed in the GPR pre-processing step to improve the 3D GPR images. For the MD the mainly noise is random noise, therefore a moving average filter has been introduced to reduce the noise level. The feature extraction blocks aim to extract the feature of the input data, the GPR array feature based algorithm (section4.3.3) detection result and intensity value of the MD will be used as the feature of the input GPR and MD data. The Data fusion centre aims using feature-level or decision-level fusion method to fuse the MD and GPR image.

### 5.1.2 Robot Arm Data Re-build

The D-Box project provided a tele-control robot for the metal detector data collection. (Details on the D-Box MD data are included in Appendix I.) Figure 5-4 below shows

the image of the robot and the MD sensor. The robot arm has two freedoms, meaning the robot arm data have two angle vectors: one is used for describing the angle between the arm and the robot platform; the other one is used for describing the distance between the centre of the MD and the robot. Since the data for the GPS are on the robot platform but not on the MD, it is very important to calculate the actual location of the MD detector when the tele-control robot is working in this case.

A program was written for calculating the location of the round MD detector by using the existing measurement data. The process of the program is shown below:

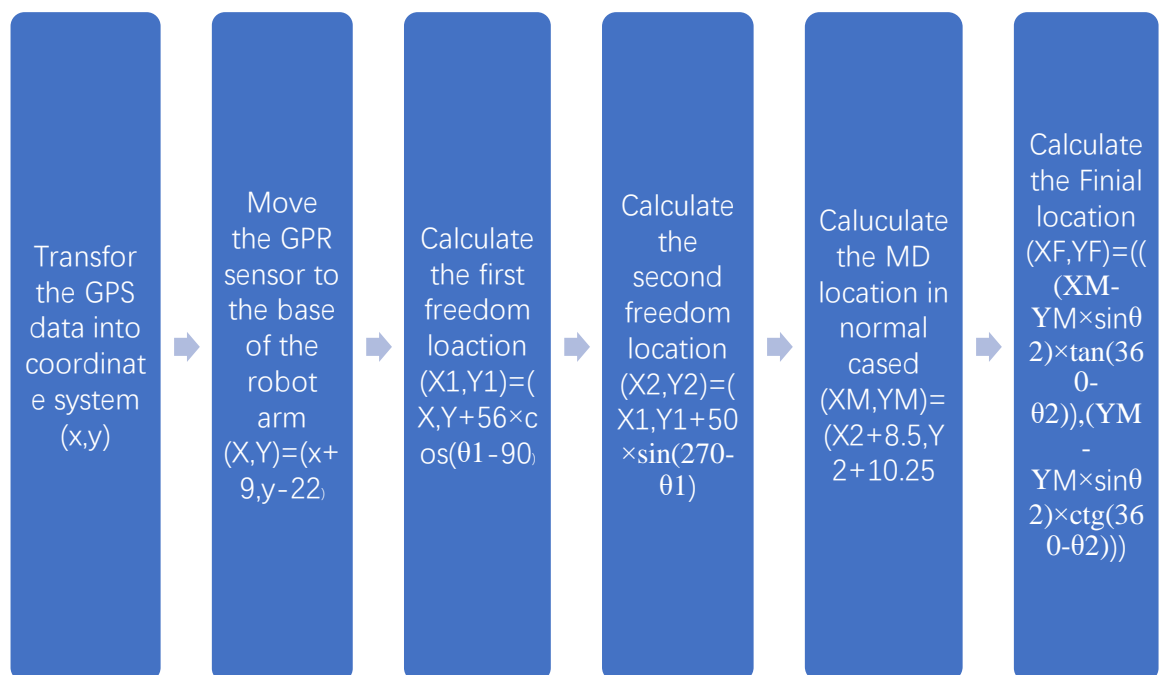


Figure 5-4. How to re-build the position of the MD arm.

By using this function, the GPS data can be added into the arm location data, helping to identify the GPS coordinates of the MD.

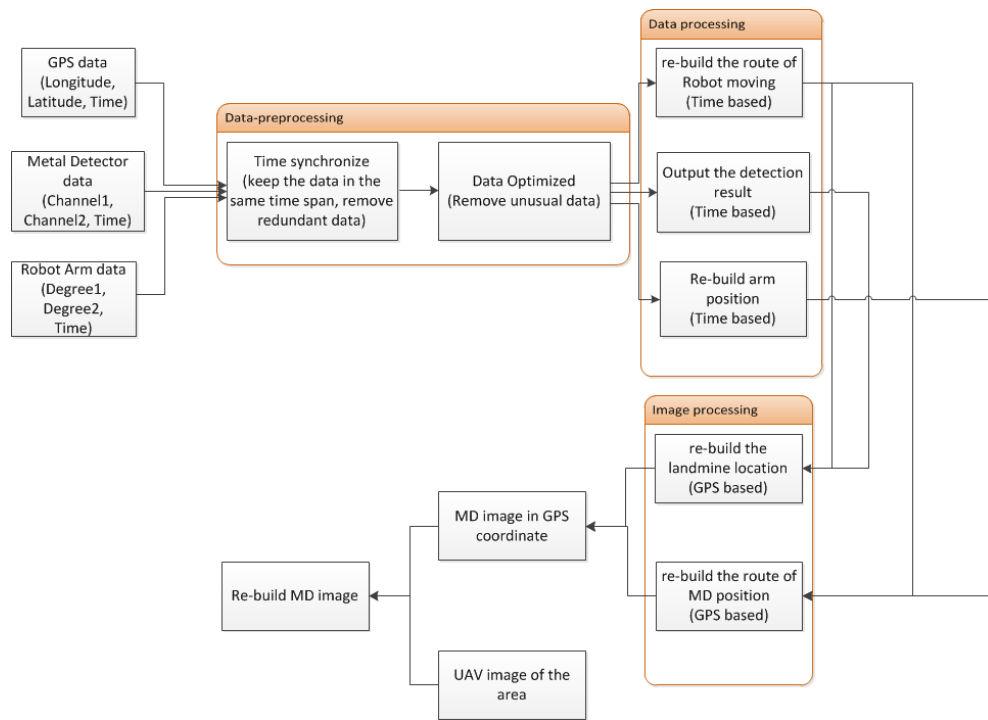


Figure 5-5. Metal detector image re-build process flowchart.

The flowchart in Figure 5-5 shows the process of rebuilding the MD image. Three types of input data were obtained, which are GPS data, metal detector data and robot arm data. All these types of the data are time-based signals. The aim of the pre-processing part is to synchronise these three types of data based on the time correlation. The time spans of the three types of the sensors, which are the effective inputs are cut manually. Then, the unusual data of each sensors meaning the bad signals, are removed; thus, if one point in one signal is removed, the corresponding point in the other signal should be removed as well. The output of the data pre-processing parts contains three different signals of the sensors, with the same time span and matched time point sensors.

The data-processing step for each sensor is different. For a GPS sensor, the aim of the data processing is to re-build the route of moving via a latitude and longitude coordinate system for robot. For the MD sensor, the landmines in a unit of time can

be detected via data processing. For the robot arm sensor, data processing is used to re-build the coordinate system to the centimetre level and to improve the robot's route. The image processing parts aim to fuse the three types of sensors into a readable image. The landmine location in the longitude and latitude coordinates is re-built by fusing the GPS sensor and the MD sensor. The MD's moving route image is obtained by fusing the GPS sensor and the robot arm sensor. When the output of the above results are fused, an image of the route of the MD sensor moving and the location of the landmines are detected.

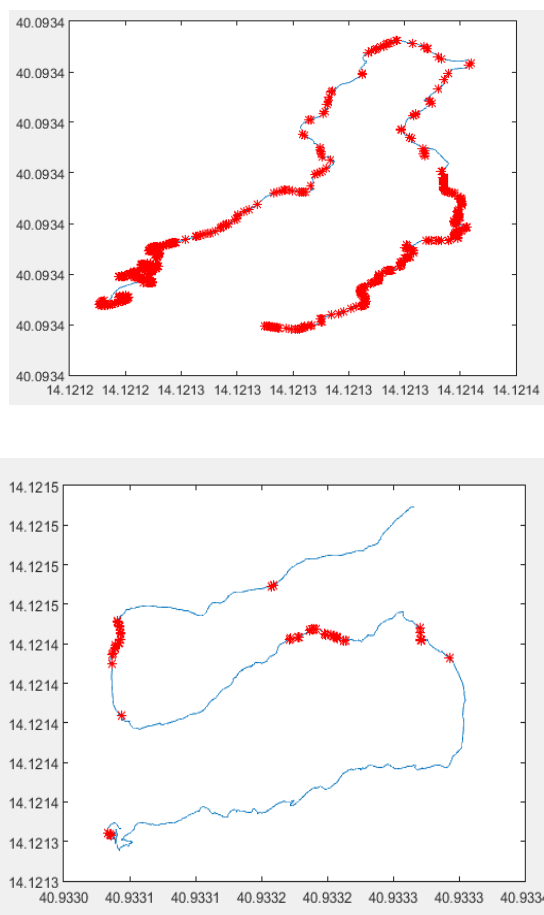


Figure 5-6. Re-built landmine location (grass in the top, desert in the bottom).

In Figure 5-6, the top image is the MD detector image for the high organic area and the bottom image is for the desert area. The red points in the figure represent that a

metal containing object has been detected. In addition, the blue line is the moving track of the centre of the MD. The image shows that by using the proposed MD image building method, the route of the MD sensor moving has been combined with the GPS signals. By comparing the MD carried GPS signals with the GPR carried GPS signals, these two types sensor can be fused. The MD result in the high organic area shows lots of the clutter signals, this is because the soil environment of the high organic has contained lots of metal objects, which will reduce the detection ability of the MD. The MD detector result for the desert area shows only a few things has been detect, this is because the technique problem of the MD. The MD detector in the D-Box system was supposed to be a 16-bit continuous-wave MD, however, during the test only the first 12 bits of the MD signals were recorded, which made the MD dataset unusable. Therefore, the Naples out-door environment data could not be utilised for the data fusion system design in this research.

### **5.1.3 Metal Detector Image Simulation**

Since the MD sensor from the D-Box project was not able to produce useful data, a simulated MD output image will be created instead to provide data input from the MD to the fusion system. The metal detector could detect both metal and very low-metal-containing objects in the landmine area. The MD sensor is very sensitive and can detect the trigger system of a plastic landmine, which means that the MD could find most of the landmines[100]. However, since the metal sensor is influenced by other metal objects in the landmine area, every metal-containing object will be a source of alarm in the detection process. The MD sensors do not provide image signals directly, since they normally generate sound signals. The strength of the sound signals depends on the depth of the object, the distance of the MD to the object, and the amount of metal that the object contains.

For the distance from the MD to the object, the function (5.1) was used to represent the signal attenuation.

$$y = x \quad (5.1)$$

For the depth of the object, the function (5.2) was used to represent the signal attenuation, since the landmine is buried in the soil.

$$y = \log x \quad (5.2)$$

For the material of the object, function (5.3) was used to represent the signal attenuation, where A is the total metal contained in the object.

$$y = A \cdot \log x \quad (5.3)$$

Based on the equations (5.1-5.3) and the ground truth map (Figure 4-3), the simulated MD image was built, as shown in Figure 5-7.

An intensity map approach was used to assure that the inputs of the data fusion system are of the same format. The intensity map is constructed through normalising the output values of the landmine detection algorithm between 0 and 1. In this thesis, the intensity value of 1 means the presence of a landmine and 0 means presence of background.

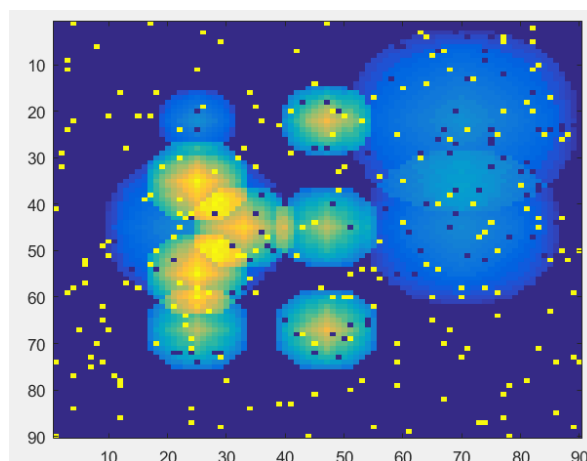


Figure 5-7. Simulated metal detector image output.

The Figure 5-7 shows the simulated metal detector image, which will be using for testing the performance of the data fusion system. For the reason of introduce the uncertainty of MD sensor, the “salt and pepper” noise has been added to metal detector image.

#### **5.1.4 GPR Image Analysis**

Since the sample of MD input image of the data fusion system has been selected, as shown in Figure 5-7, the following step is to generate the GPR input image samples. The GPR image sample used for the data fusion system is chosen from the detection result in chapter 4. Since the data fusion system aims to evaluate the fusion method, there is no difference between using the eight detection results from chapter 4 as the GPR input.

The GPR feature based algorithm detection result for the in-door environment has been selected as the GPR input of the data fusion system, which is shown in Figure 4-19. In order to reduce the operating time of the detection algorithm, all the algorithms included in chapter 4 omit the noise reduction step. However, as the data fusion system aims to achieve an accurate detection process, it will be important to reduce the noise level of the GPR input image. A Gauss filter (window size  $5 \times 5$  and  $\sigma=0.5$ ) has been employed here to reduce the Gauss noise in the detection result. In addition, a moving average filter (window size  $5 \times 5$ ) was added after the Gauss filter, which aims to make the image smooth. Figure 5-8 below shows the input GPR image for the data fusion system:

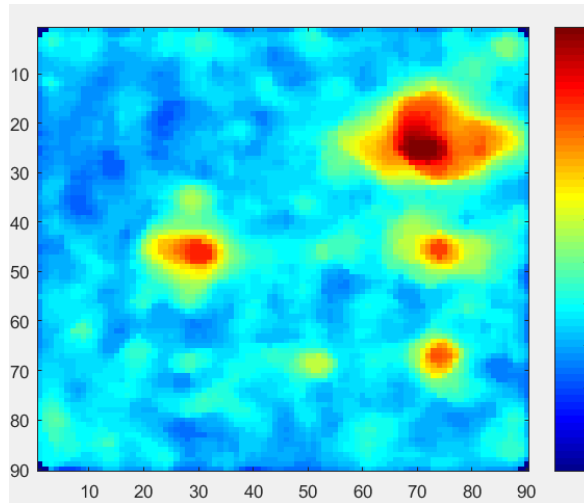


Figure 5-8. GPR image input for data fusion system

Comparing Figure 5-8 with Figure 4-19, it can be clearly seen that the noise signal has been reduced. In addition, the AP mine Ts-50 can be clearly seen in Figure 5-8.

## 5.2 Fusion System Design

After the MD input and GPR input for the data fusion system has been generated, the next step is to design the data fusion system. Two popular data fusion architectures were studied: the Joint Directors Laboratories' (JDL) [120] and the National Bureau of Standards (NBS) [121] fusion models. The JDL data fusion architecture, which can be used in most data fusion systems, is a functionally oriented model. The NBS data fusion architecture can meet real-time requirements and is more focused on communication. It is mostly used in robotic applications and is suitable for EOD systems. The design of the fusion systems proposed in this section is targeted at the NBS fusion model. (A review of the existing data fusion models is presented in Appendix J.)

This research employs three kinds of classical data fusion methods: the Bayes method, the Dempster-Schafer method, and the Fuzzy Logic method. The following section will demonstrate these fusion algorithms.

### 5.2.1 Kalman-Bayes Fusion System Design

The Bayes based fusion method is a fundamental statistical approach to the problem of pattern classification[101]. The advantage of the Bayes system is that it performs best in all statistical fusion methods[102]. The disadvantage of the Bayes fusion method is that it normally requires the joint probability density functions of the inputs to be known, which are normally not available or can be hard to estimate from data in the landmine detection process. A centralized feature level Kalman-Bayes fusion system has been proposed in this subsection. The proposed Kalman-Bayes fusion system aims to fuse the GPR data with the MD data, which can be divided into two parts: to estimate the sensors confidence level, and to fuse the detection decision from different sensors.

The sensor confidence level is an important parameter in the data fusion system, which represents the probability of the data fusion system trusting the detection sensors. The proposed data fusion system will use the Bayes theory to estimate the sensor confidence level. In the ideal case each detection sensor will be working properly without noise, and the surface environment of the landmine area will not affect the detection result. Therefore, the data fusion system will consider that all sensors will have an equal confidence level. Considering the Bayes based data fusion system has  $n$  inputs sensors, then the confidence level of each sensor will be equal to  $\frac{1}{n}$ , which is shown as equation (5.4).

$$P(s_i) = \frac{1}{n} \quad (5.4)$$

In equation 5.4, the  $P(s_i)$  is a priori probability in the Bayes system, representing the probability of the system to trust the sensor  $x_i$ , where  $\forall i \in [1, n]$ . As mentioned in chapter 4, the detection sensor will output the probability value for each position in the landmine area to demonstrate the level of dangerous of that position, which is  $P_{si(x,y)}(d)$ . The  $x, y$  represent the position of the landmine area and  $d$  represents the case that a landmine has been detected. If using  $P_{fused(x,y)}(d)$  to represent the fusion result at position  $(x, y)$ , the fusion step will show as equation 5.5.

$$P_{(x,y)}(d) = \sum_{i=1}^n P_{si(x,y)}(d)P(s_i) \quad (5.5)$$

In equation 5.5, the  $P_{si(x,y)}(d)$  is also known as  $P_{(x,y)}(d|s_i)$ , therefore the equation 5.6 will be deduced based on the Bayes equation.

$$P_{(x,y)}(s_i|d) = P(s_i) \frac{P_{(x,y)}(d|s_i)}{P_{(x,y)}(d)} \quad (5.6)$$

As mentioned earlier, in equation 5.6, the  $P(s_i)$  is the a priori probability of the sensor confidence level, the  $\frac{P_{(x,y)}(d|s_i)}{P_{fused(x,y)}(d)}$  is the likelihood, and the  $P_{(x,y)}(s_i|d)$  is the posterior probability of the sensor confidence level that will be used in the fusion process. The following will show how a two inputs data fusion system calculate the confidence level for each sensor.

Consider two decision maps B1 and B2 from two different detection sensors, one is MD the other one is GPR. The  $P(B1)$  and  $P(B2)$  represent the a priori sensor confidence value, which is 0.5 in this case. In the fused process, the pixels from B1

and B2 have different probability values ranging from 0 (landmine absence) to 1 (landmine presence), which is denoted by  $P_{B1}(x) \in [0,1]$  and  $P_{B2}(x) \in [0,1]$ .

$P(x|B1)$  denotes the probability of the landmine represent from MD

$P(x|B2)$  denotes the probability of the landmine represent from GPR

The probability of the presence of a landmine in the fusion result  $P_{fuse}(x)$ , can be determined by the average decision of each sensor which is shown as equation 5.7

$$P_{fuse}(x) = P(x|B1) P(B1) + P(x|B2) P(B2) \quad (5.7)$$

Based on the Bayes equation the posterior sensor confidence level will be calculated as shown in equation (5.8):

$$P(B1|x) = P(B1) \frac{P(x|B1)}{P_{fuse}(x)} \quad (5.8)$$

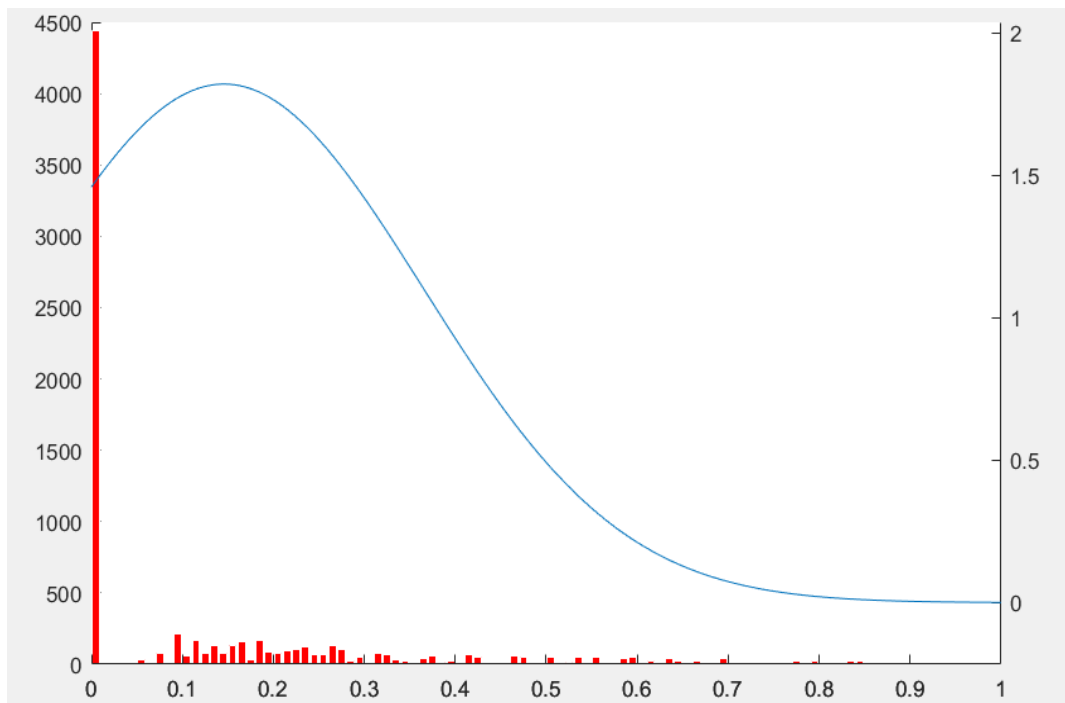
$$P(B2|x) = 1 - (B1|x)$$

For each pixel in the detection area, there will be a posterior sensor confidence value, therefore the average of the posterior sensor confidence values will be selected as the system sensor confidence values.

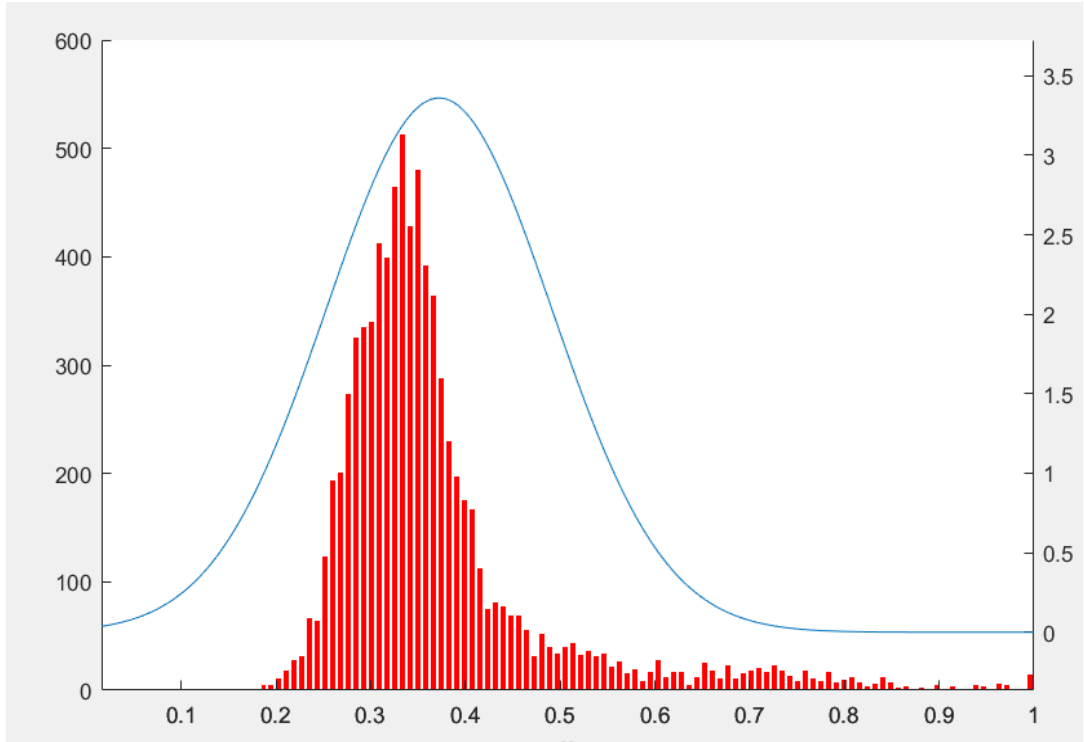
Once the system sensor confidence value has been estimated, the next step is to introduce uncertainty into the system. The uncertainty of the sensor ( $u_{GPR}$  and  $u_{MD}$ ) can take two main forms. One is ambiguity which means “*the inability to specify exactly a measurable parameter or to assign a precise attribute to an object*[103]”, this type of uncertainty is due to the random noise of the sensor. The other uncertainty of the sensor is vagueness, which means the sensor cannot describe the meaning of the concepts properly[103]; this type of uncertainty is due to the imprecision of the sensor. The normal frameworks to model ambiguity are Bayes theory and Dempster-Schafer

theory. In addition, the framework to model vagueness is the Fuzzy Logic (section 5.2.3)[104]. In addition, the uncertainty of the detection sensor cannot be avoided during the fusion process and the uncertainty is not constant[105].

In order to analyse the uncertainty of the sensor the first step is to understand the data distributions of the detection sensors. Figure 5-9 below shows the distribution of the output for both MD and GPR sensors. It can be seen that the output distributions of the MD and GPR sensor can be represented by the normal distribution. The two blue lines in Figure 5-9 represent the simulated normal distribution of the MD and GPR sensor, where the  $\mu = 0.1457 (MD), 0.3721(GPR)$  and  $\sigma = 0.2190(MD), 0.1187(GPR)$  respectively.



(a)



(b)

Figure 5-9. Distributions of the sensor output (a) MD, (b) GPR.

Since both the MD and GPR sensor outputs follow the normal distribution, the uncertainty in the sensor measurement will be equal to the  $\sigma^2$  value of the Gauss distribution[106]. Therefore, the sensor uncertainty for the MD is  $U_{MD} = 0.2190$  and the sensor uncertainty for GPR is  $U_{GPR} = 0.1187$ . The  $U_{MD} = 0.2190$  means, in this case, that both the MD and GPR sensors have a 21.9% probability of not working properly. Since, the Gaussian noise is the predominant noise of the fusion system, the popular approach of using a Gaussian filter to reduce the noise was implemented. In this research, a Kalman filter was used to reduce the system noise, in the fusion system.

*“The Kalman filter providing optimal estimation of observable, but often non-directly measurable, physical quantities, represents the best tool for data fusion, well consolidated in the avionic field”*[107]. The Kalman filter has been often used in the

data fusion system to reduce the noise of sensor data[108]. The equations 5.9 and 5.10 below show the core technique of the Kalman filter:

$$T_k = A \cdot T_{k-1} + B \cdot U_k + u_s \quad (5.9)$$

$$O_k = H \cdot T_k + u_{mk} \quad (5.10)$$

In equation 5.9,  $A$ ,  $B$  and  $H$  are system variables, which can be set to 1.  $T_k$  represents the true state of the system at time  $K$ ,  $T_{k-1}$  represent the true state of the system at time  $K-1$ ,  $U_k$  represents the control variable of the system at time  $K$ , for the simple Kalman system  $U_k = 0$ .  $O_k$  represents the observation value of the system at time  $K$ , in addition, the  $u_s$  and  $u_{mk}$  are the system error and measurement error at time  $K$ . In the Kalman equation, if the noise and the control variable are not considered, then  $O_k = A \cdot T_{k-1}$ , therefore,  $T_{k-1}$  can be used to predict the system observation value at state  $K$ , which has been represented by  $P_{K|K-1}$ . When adding the system noise,  $P_{K|K-1} = A \cdot T_{k-1} + \text{noise}$ . The noise here will be equal to the difference between the observing value and the system estimate value. The Kalman gain (Kg) has been introduced here to represent the related weight value between the observing value and estimate value. The equations 5.11, 5.12 and 5.13 will show how the Kalman filter calculated the true value of state  $K$ .

$$P_{K+1|K} = T_k = T_{k-1} + \text{Kg}(O_k - P_{K|K-1}) \quad (5.11)$$

$$\text{Kg} = \frac{|u_s^2 + u_{k-1}^2|}{|u_s^2 + u_{k-1}^2| + u_s^2} \quad (5.12)$$

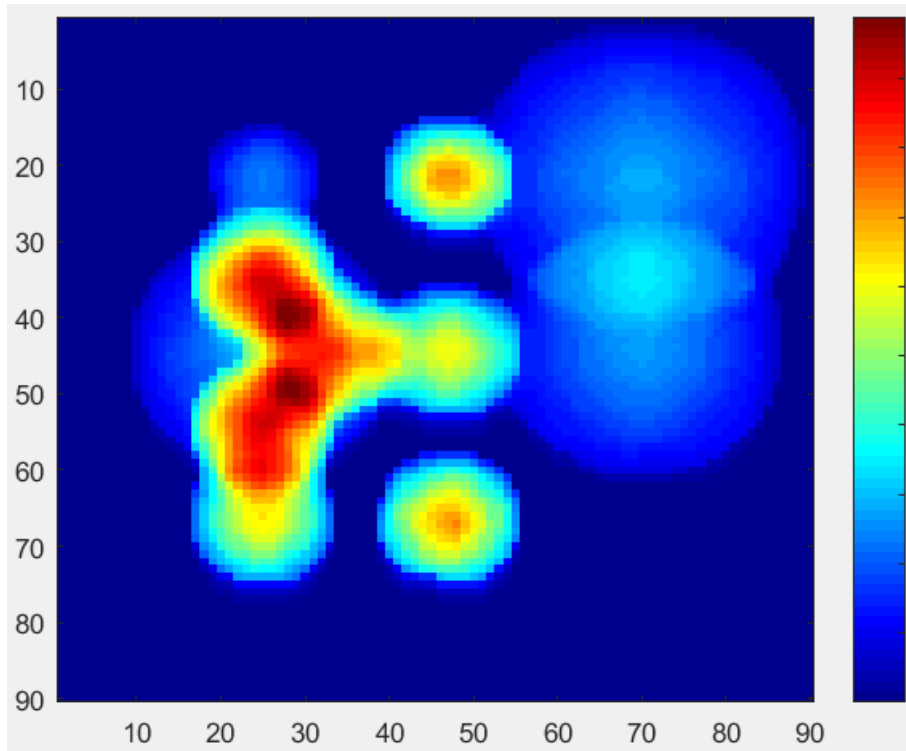
$$u_k = \sqrt{(1 - \text{Kg}) \times u_s^2} \quad (5.13)$$

To calculate the true value of the next system state  $K+1$ , the original observing value and the true value of the system as state  $K$  will be set to  $K-1$ . The following paragraph

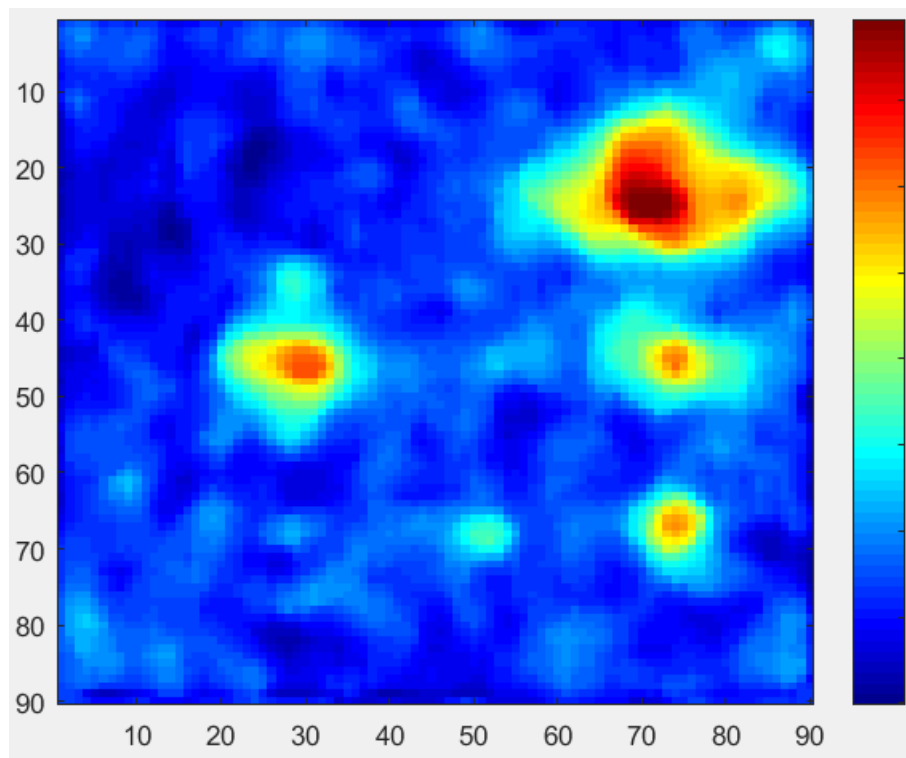
will use the GPR sensor as an example to show how the Kalman filter reduced the system noise.

As stated previously, the uncertainty for the GPR sensor in this case is  $u = 0.1187$ , and the first output data from the GPR sensor will be treated as the true value of the  $K-1$  state which is  $T_{GPR}(K-1) = 0.3345$  with the measurement uncertainty  $u_m(k-1)=0$  and the system uncertainty  $u_s=0.1187$ . In addition, the predicted value of state  $K$  at state  $K-1$  will be  $P_{GPR}(K|K-1) = 0.3345$ . The second output data from the GPR sensor will be treated as the observation value of the  $K$  state, which is  $O_{GPR}(K) = 0.3575$  with uncertainty  $u_s$ . By following the Kalman equation the Kalman gain can be calculated, which is  $Kg = \frac{(0.1187^2+0^2)}{(0.1187^2+0^2)+0.1187^2} = 0.5$ . Hence, the true value of the GPR sensor output at state  $K$  will be  $T_{GPR}(K) = 0.3345 + 0.5 \times (0.3575 - 0.3345) = 0.3460$ . After the true measure value of state  $K$  has been calculated, the measurement uncertainty value of state  $K$  will be updated by using the Kalman equation, which is  $u_m(k-1) = \sqrt{(1-0.5) \times 0.1187^2} = 0.0840$ . The true measurement value at state  $K$  of the GPR sensor can be used as the predict value of the state  $K+1$ , which is  $P_{GPR}(K+1|K) = 0.3460$ . By using the Kalman filter the true measurement value of the following state will be calculated.

Figure 5-10 below shows the Kalman filter result of the sensor inputs for both MD and GPR:



(a)



(b)

Figure 5-10. Kalman filter result of the input sensor (a) MD (b) GPR.

By comparing Figure 5-10 with Figure 5-7 (input signal of MD) and Figure 5-8 (input signal of the GPR image) it can be seen that the noise of the input sensor has been reduced; in addition, the detection parts have been enhanced.

Once the sensor confidence value has been estimated and the uncertainty of the sensor has been considered, the next step is to fuse the decision value from the different sensors. The existing fusion method is set so that the fusion decision value will be equal to the sum of the sensor decision multiplied by the sensor confidence level, which is shown as equation 5.14.

$$P_{decesion}(x) = P(x|B1) P(B1|x) + P(x|B2) P(B2|x) \quad (5.14)$$

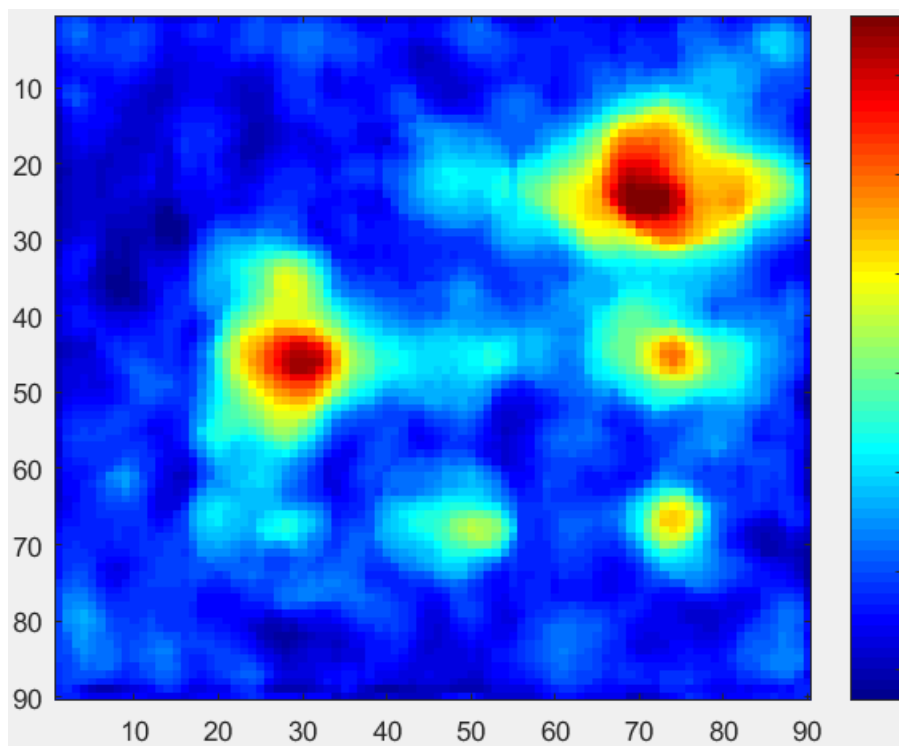


Figure 5-11. Bayesian fusion existing method fusion result.

Figure 5-11 shows the fusion result of the re-calculation method Bayes fusion system, the red colour and yellow colour represent the landmine presence and the blue colour

represents the landmine absence. It can be clearly seen that all the landmines have been identified. However, there are some false alarms affecting the detection result. To evaluate the fusion process the distribution of the fusion result can be used. Figure 5-12 below shows the distributions of the Bayesian fusion system:

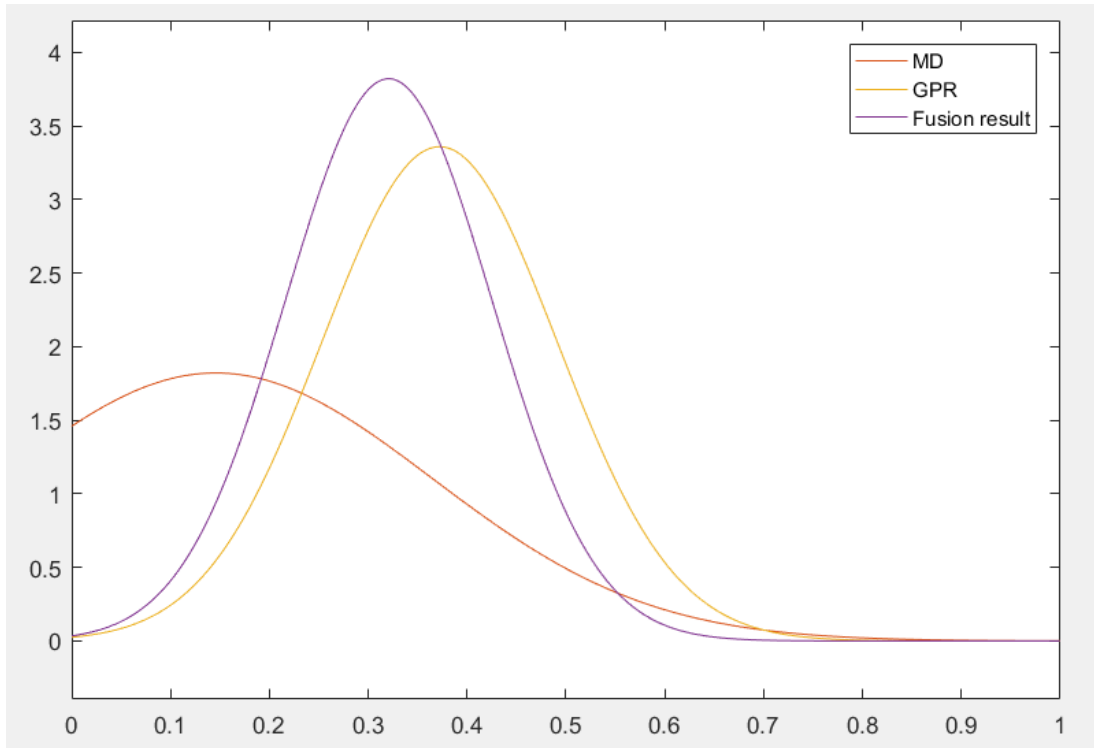


Figure 5-12. Distributions of the Bayes fusion system.

In Figure 5-12, the red line is the Gaussian distribution of the MD sensor output, the yellow line is the Gaussian distribution of the GPR sensor output and the purple line is the Gaussian distribution of the fusion results. Figure 5-12 has proved that the Bayesian fusion method can improve the original single sensor outputs.

The existing Bayesian fusion system can achieve a multi-sensor data fusion work. However, the sensor confidence values in the existing system are fixed values during the fusion process. In the Bayes fusion process the system will use the average of the

posterior sensor confidence value to evaluate the sensor output. However, in the real time system the sensor confidence value will always be changing, since the surface environment will also be changing. To solve this problem a Kalman theory based fusion framework has been introduced here to improve the existing Bayes fusion system, which is one of the main unique contributions of this research.

In the Bayes-Kalman fusion system, the a priori probability of the sensor confidence level will be the state  $K-1$ , the posterior probability of the sensor confidence level will be the state  $K$ , in addition, the standard deviation of the posterior probability will be the system uncertainty. Then, by using the Kalman equation as described earlier in this section, the true sensor confidence level will be calculated. The fusion result will be equal to the sensor output value multiplied by the true sensor confidence level. Figure 5-13 below shows the fusion result of the Bayesian-Kalman system:

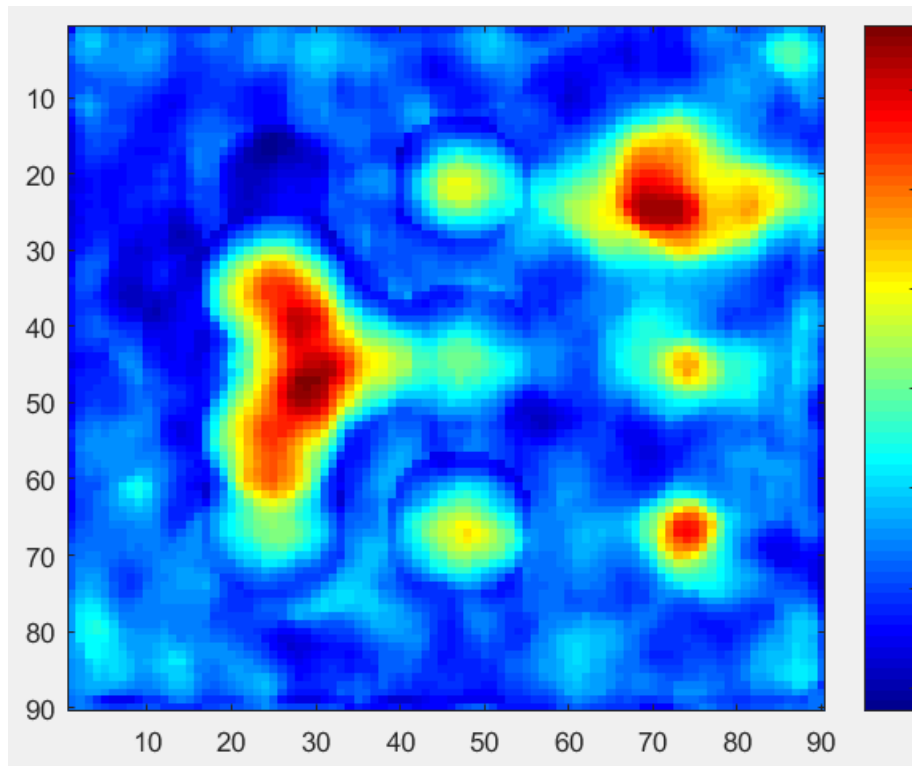


Figure 5-13. Bayesian-Kalman method fusion result.

By comparing Figure 5-13 with Figure 5-11, the results show that in Figure 5-13 all the landmine areas have been marked clearly, and on the left and middle line, the Bayesian-Kalman fusion system can target the landmines more accurately than the existing Bayes system.

### 5.2.2 Dempster-Schafer Theory-Based System Design

The Dempster-Schafer fusion method is another statistical fusion method. In general, there is not a significant difference between the Dempster-Schafer theory fusion system and the Bayesian fusion system. The Dempster-Schafer method assigns its masses to all of the subsets of the entities that comprise a system [109, 110].

The mass function is the core technique of the Dempster-Schafer theory. In a standard case, each landmine detection sensor will have three kinds of outputs states for a pixel: the probability of the pixel to be a landmine, the probability of the pixel to be a safe area, and the probability of the pixel to be an unknown state[37]. The unknown output state is also known as the uncertainty of the detection sensor.

In the proposed Dempster-Schafer fusion system the uncertainty of the GPR and MD sensor has been chosen as 0.1. The following paragraph describes the Dempster-Schafer fusion system. In a GPR sensor the output probability mass assigned to a landmine is  $m_{GPR}(M)$ , the output probability mass assigned to background is  $m_{GPR}(\bar{M})$ , and the unassigned probability mass is  $m_{GPR}(M \cup \bar{M})$  (the uncertainty of the GPR sensor). Therefore, the corresponding  $m_{MD}(M)$ ,  $m_{MD}(\bar{M})$  and  $m_{MD}(M \cup \bar{M})$  represent the output state of the MD sensor[51]. For the fusion work, the confidence level of the sensor  $C_{GPR}$  and  $C_{MD}$  are also required. In the standard case, the sensor's confidence level will change based on the surface environment, however,

in the training dataset, both the MD and GPR sensors' confidence level will be set as 0.5. The equations (5.15-5.17) show the mass function of the two-input sensors of the Dempster-Schafer fusion system.

$$m_{GPR}(M) = (1 - u_{GPR}) \times C_{GPR} \quad (5.15)$$

$$m_{MD}(M) = (1 - u_{MD}) \times C_{MD}$$

$$m_{GPR}(\bar{M}) = (1 - u_{GPR}) \times (1 - C_{GPR}) \quad (5.16)$$

$$m_{MD}(\bar{M}) = (1 - u_{MD}) \times (1 - C_{MD})$$

$$m_{GPR}(M \cup \bar{M}) = u_{GPR} \quad (5.17)$$

$$m_{MD}(M \cup \bar{M}) = u_{MD}$$

The fusion rules of the GPR and MD have been built based on the Dempster-Schafer theory, which is shown in Table 5-1.

Table 5-1 The *Dempster-Schafer Fusion Rules*

$m_{GPR}(M)$	$m_{fusion}(M)$	$m_{fusion}(M \cup \bar{M})$	$m_{fusion}(M)$
$m_{GPR}(\bar{M})$	$m_{fusion}(M \cup \bar{M})$	$m_{fusion}(\bar{M})$	$m_{fusion}(\bar{M})$
$m_{GPR}(M \cup \bar{M})$	$m_{fusion}(M)$	$m_{fusion}(\bar{M})$	$m_{fusion}(M \cup \bar{M})$
	$m_{MD}(M)$	$m_{MD}(\bar{M})$	$m_{MD}(M \cup \bar{M})$

By following the fusion rules from Table 5-1, the equation (5.18) will be derived, which is known as the decision of the fusion result.

$$m_{fusion}(M) = m_{GPR}(M) \times m_{MD}(M) + m_{GPR}(M) \times m_{MD}(M \cup \bar{M}) \quad (5.18)$$

$$+ m_{GPR}(M \cup \bar{M}) \times m_{MD}(M)$$

By following equations (5.15-5.17) the fusion decision map will be calculated. Figure 5-14 below shows the fusion result of the Dempster-Schafer fusion system, where the uncertainty of both sensors equals 0.1 and the confidence level of both sensors equals 0.5.

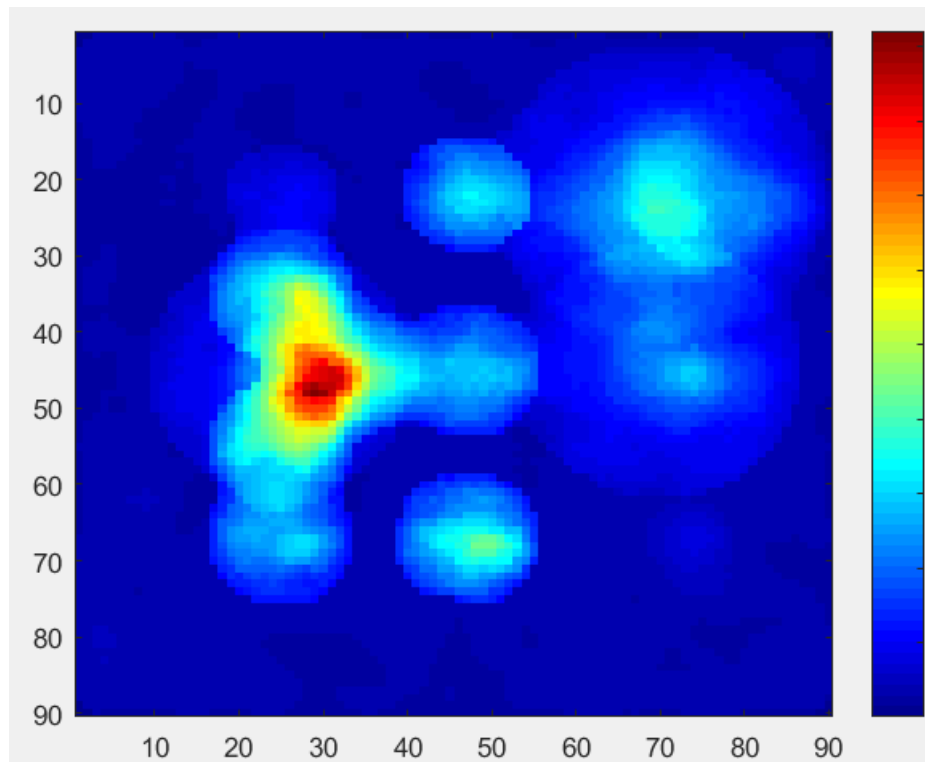


Figure 5-14. Dempster-Schafer theory fusion result.

Figure 5-14 shows that the fusion result has outperformed the single sensor detection result, most of the landmines have been identified, and the number of false alarms has been reduced to a low level.

The difference between the proposed Dempster-Schafer fusion system and the existing Dempster-Schafer fusion system is in the fusion rules. The existing fusion system will

be an unknown state for fuse  $m_{GPR}(M)$  with  $m_{MD}(\bar{M})$ , whereas in the proposed fusion system the decision will be  $m_{fusion}(M \cup \bar{M})$  [101]. The new proposed Dempster-Schafer fusion system is more efficient than the existing Dempster-Schafer fusion system in terms of operating time. Since the unknown state will lead the sum of the mass function less than 1. In the training dataset of the Dempster-Schafer theory fusion system the uncertainty value was set as 0.1. However, in the real demining case, the uncertainty value will be determined by the sensor manufacture. The following experiment aims to determine how the uncertainty of the sensor influences the fusion result. In this case, the uncertainty value for both MD and GPR will be chosen from 0.1 to 0.9, the ROC curve will be employed to evaluate the performance of the fusion result. Figure 5-11 below shows the Dempster-Schafer fusion result when  $u_{GPR} = 0.5$  and  $u_{MD} = 0.3$

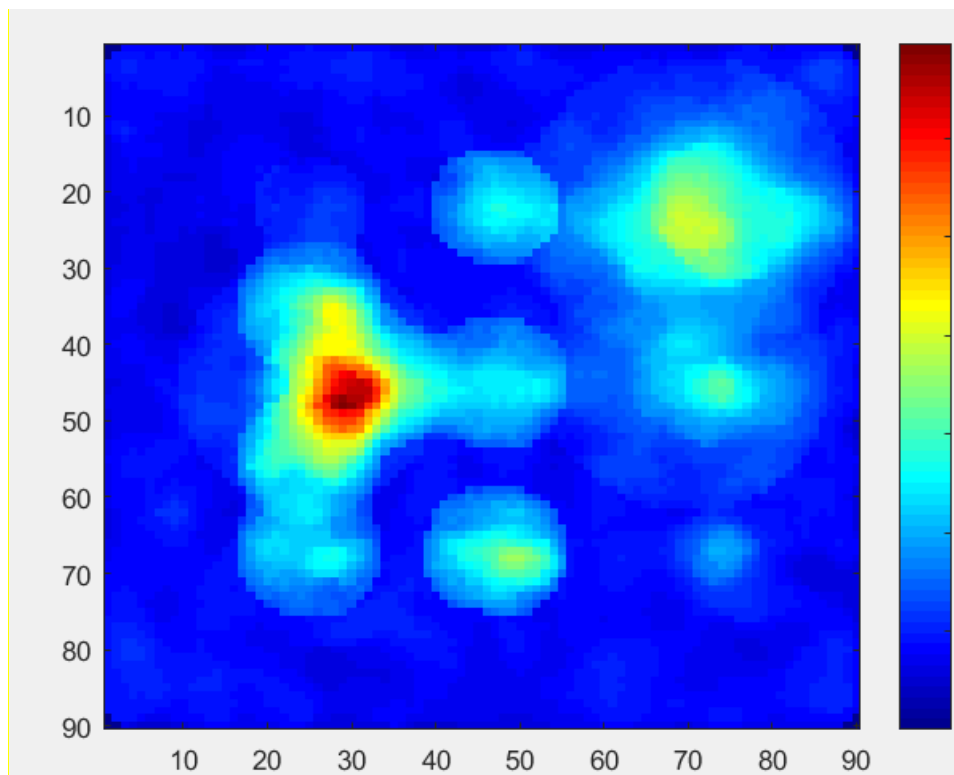
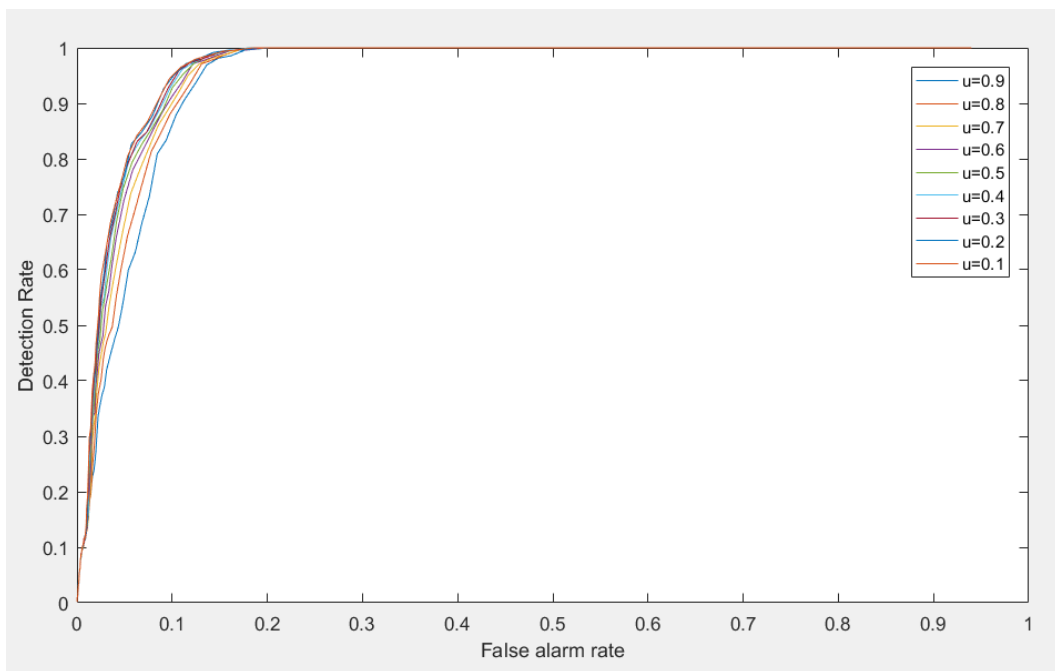
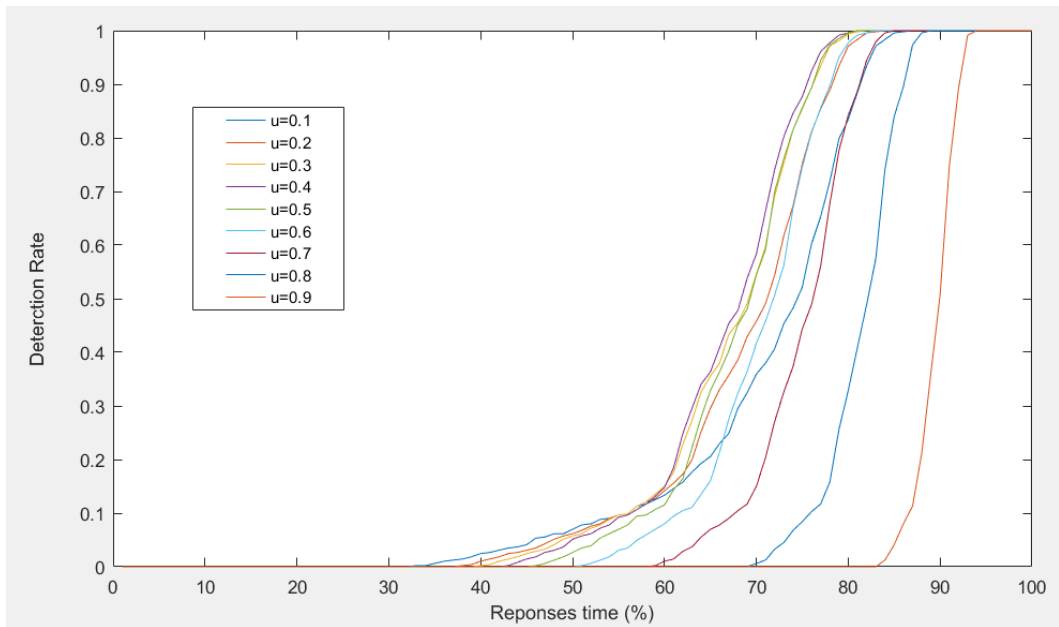


Figure 5-15. Dempster-Schafer fusion result  $u_{GPR} = 0.5$  and  $u_{MD} = 0.3$ .

By comparing Figure 5-15 with Figure 5-14, it is apparent that the background colour has changed from dark blue to light blue, which means that the incidences of false alarms has increased. For example, in Figure 5-15 the bottom left (10,60) shows a false alarm has been discovered, which is not shown in Figure 5-14. Figure 5-16 below shows how the uncertainty rate of the sensor influenced the fusion result in the Dempster-Schafer system:



(a) ROC analysis of the uncertainty rate in the Dempster-Schafer system



(b) Response time analysis of the uncertainty rate in the Dempster-Schafer system

Figure 5-16. The influence of the uncertainty rate changed in Dempster-Schafer System

Figure 5-16(a) shows that as the uncertainty rate of the sensor increased, the performance of the fusion result decreased. This suggests that as the uncertainty rate of the sensor increases, the Dempster-Schafer system will make more false detections. Figure 5-16(b) shows that as the uncertainty rate increases the response time of the fusion system also increases.

### 5.2.3 Fuzzy Logic Data Fusion System Design

A Mamdani-type fuzzy inference (or Fuzzy Logic) system [43] was proposed to fuse the detection result of the GPR sensor and the MD sensor in this section. The fusion process includes fuzzifying inputs of the data fusion system, i.e. two corresponding features from a co-incident pair of detection feature maps, combining the fuzzified

inputs according to the prescribed logic, and then de-fuzzifying the result to generate the detection map.

Fuzzification of the input values is achieved using the input membership functions.

Figure 5-17 and equation 5.19 below shows the membership function of the inputs for both the GPR and MD sensors.

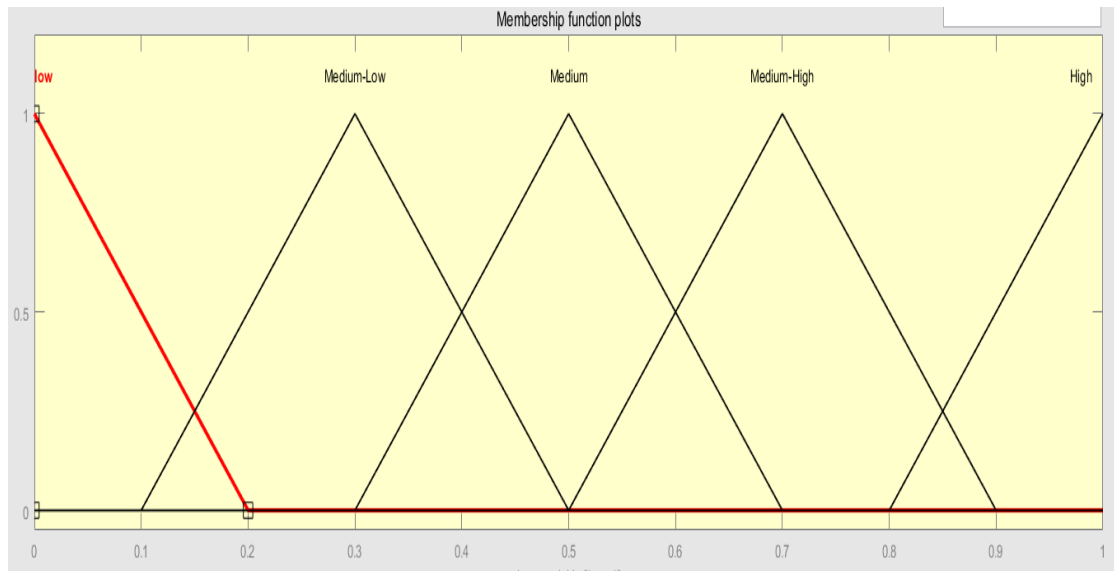


Figure 5-17. Membership function of GPR and MD sensor input data.

$$\text{Input State} = \begin{cases} \text{Low} & P < 0.2 \\ \text{Medium - low} & 0.1 < P < 0.5 \\ \text{Medium} & 0.3 < P < 0.7 \\ \text{Medium - high} & 0.5 < P < 0.9 \\ \text{High} & 0.8 < P \end{cases} \quad (5.19)$$

Figure 5-17 shows that the input value is divided into five different membership functions: low, medium-low, medium, medium-high, and high intensity. When a pair of detection intensities (normalised between 0 and 1) are supplied to the membership functions, the degree to which they correspond to each of the membership function classifications is calculated by determining the height of each input membership function at the x value, defined by the input detection values. For example, if a pixel

in the GPR detection inputs represents 0.6, this means that the pixel will have an equal chance of belonging with the medium or medium-high group. In addition, the range of the membership function is a temp value, in the real case the value will be changed based on the surface condition of the landmine area and the human experts' suggestions. This research aims to improve the fusion performance of the existing fuzzy fusion system, therefore, all the fuzzy fusion system will use the same range of the membership function.

The degree to which the detection intensity corresponds to each input membership function is then processed by the prescribed logic. This logic consists of 25 rules (one for each possible combination of degrees) that determine how a given pair of degrees corresponds to an output membership function. The output membership functions are a collection of four overlapping curves centred on 0.00, 0.40, 0.60, and 1.00, and represent safe, danger, buried landmine, and landmine fused detection decisions respectively. Figure 5-18 and equation 5.20 show the membership function of the outputs.

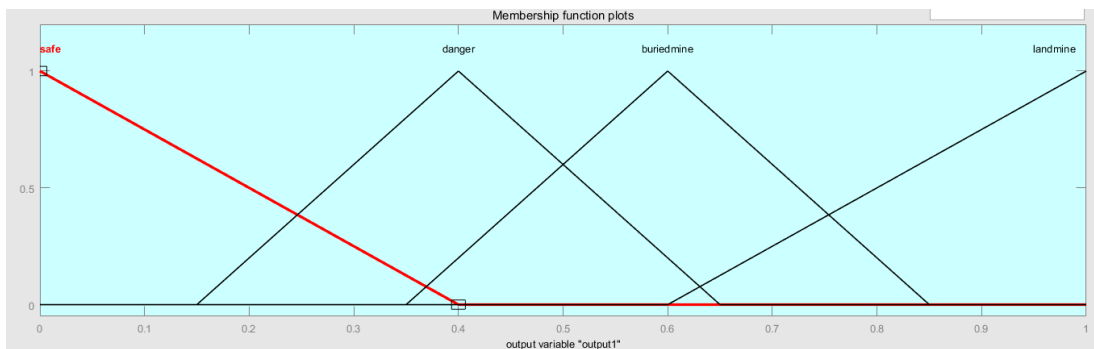


Figure 5-18. Membership function of the output.

$$Output\ State = \begin{cases} safe & P < 0.4 \\ danger & 0.15 < P < 0.65 \\ buried\ landmine & 0.35 < P < 0.85 \\ landmine & P > 0.6 \end{cases} \quad (5.20)$$

Based on the input and output membership function, a series of fuzzy rules was set to output the fuzzy fused result. Figure 5-19 shows the surface map of the designed fuzzy rules.

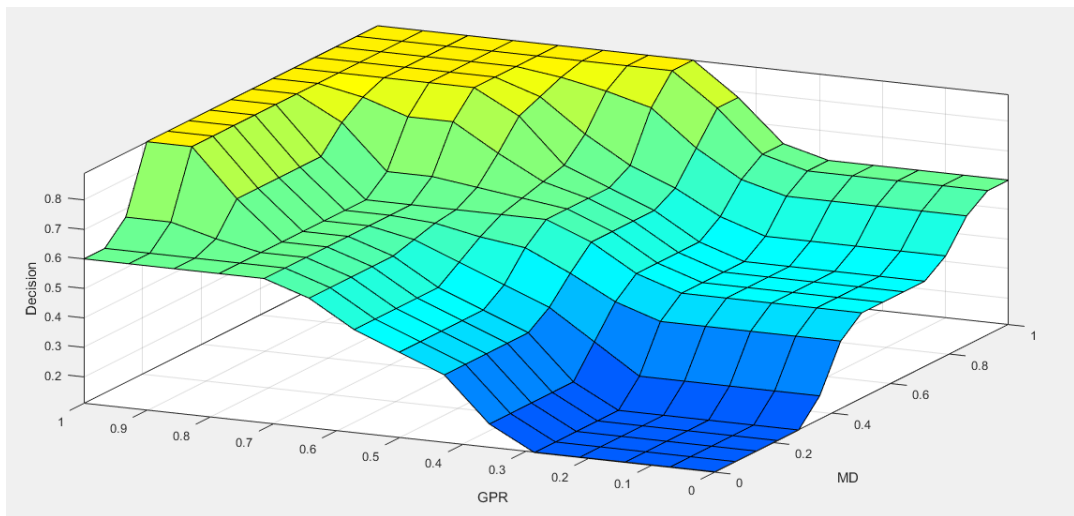


Figure 5-19. Fuzzy rules surface map.

In Figure 5-19 the two horizontal axes represent the detection probability of the input data (MD and GPR). The vertical axes represent the probability of detection of the fusion result. i.e. if the MD inputs equal 0.4 and the GPR inputs equal 0.6, the fuzzy fusion system will consider the MD inputs as medium-low or medium level and consider the GPR inputs as medium or medium-high level. Therefore, by checking the table of Fuzzy Logic mapping rules (table5-3), a fusion table can be made as with table 5-2. By checking the fuzzy fusion table, the result shows that the example pixels will have 75% chance to identify a buried mine or 25% chance to identify a danger area.

Table 5-2 *Fuzzy Fusion Table*

MD (probability)	GPR (probability)	Fusion decision(probability)
Medium-Low (0.5)	Medium (0.5)	Danger (0.25)

Medium (0.5)	Medium (0.5)	Buried mine (0.25)
Medium-Low (0.5)	Medium-High (0.5)	Buried mine (0.25)
Medium (0.5)	Medium-High (0.5)	Buried mine (0.25)

Table 5-3 details the output membership function that is activated by each pairwise combination of input degrees.

Table 5-3 *Fuzzy Logic Mapping Rules*

1 <sup>st</sup> input detection	2 <sup>nd</sup> input detection	Fused detection
intensity	intensity	intensity
Low	Low	Safe
Low	Medium-low	Safe
Low	Medium	Danger
Low	Medium-high	Buried Mine
Low	High	Buried Mine
Medium-Low	Low	Safe
Medium-Low	Medium-low	Safe
Medium-Low	Medium	Danger
Medium-Low	Medium-high	Buried Mine
Medium-Low	High	Landmine
Medium	Low	Danger
Medium	Medium-low	Danger

Medium	Medium	Buried Mine
Medium	Medium-high	Buried Mine
Medium	High	Landmine
Medium-high	Low	Danger
Medium-high	Medium-low	Danger
Medium-high	Medium	Buried Mine
Medium-high	Medium-high	Landmine
Medium-high	High	Landmine
High	Low	Buried Mine
High	Medium-low	Buried Mine
High	Medium	Landmine
High	Medium-high	Landmine
High	High	Landmine

---

The smaller of the two-degree values in each of the 25 pairwise combinations of degrees is used to truncate the corresponding output membership function's height. The 25 truncated output membership functions are then combined into a single output profile by taking the least truncated occurrence (maximum values) of each of the output membership functions. This output profile is then de-fuzzified to produce a crisp output value, and the fused detection resulting from the two detection inputs into the process. The de-fuzzification of the output profile is achieved by calculating the x

position of its centroid (the expected value). The fused detection map is formed by calculating this value for each corresponding pixel of the input detection image.

Figure 5-20 shows the test result for the proposed fuzzy fusion algorithm, fusing the GPR detection image with the MD image. When comparing the test result with the ground truth map (Figure 4-6), it could be seen that most of the suspect target area has been marked as the landmine area.

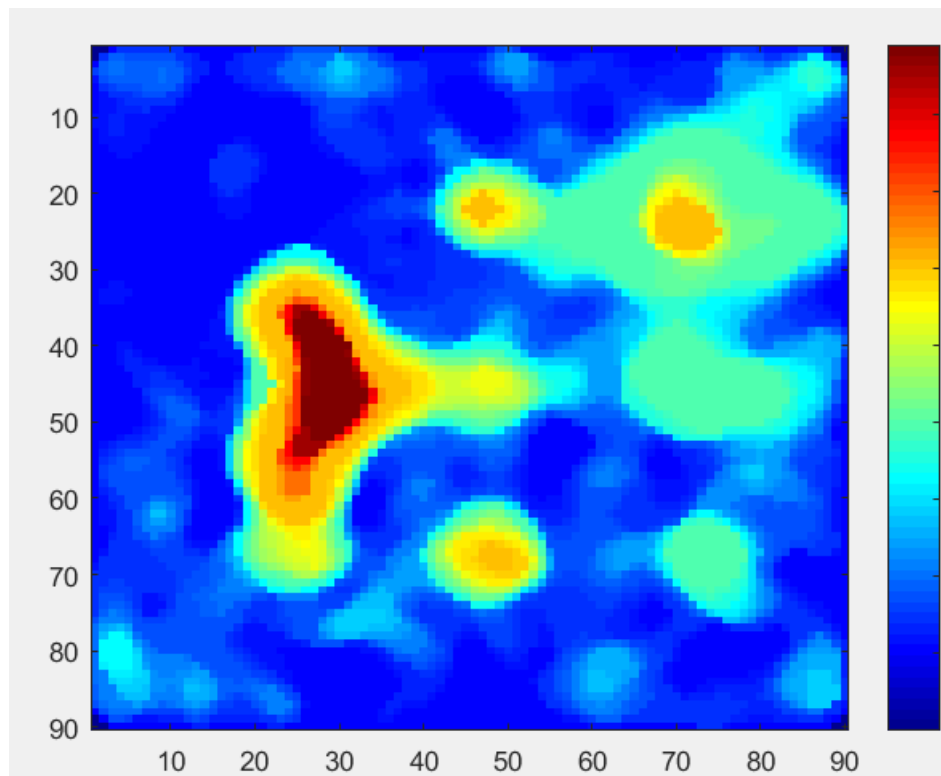


Figure 5-20. Fuzzy fusion algorithm test result.

In Figure 5-20 the red parts represent the landmine on the surface, the orange colour represents the landmines which might be buried under the surface level, the light green colour represents the danger area that is the detection accuracy range of the landmines, and the blue parts represent the safe area that do not contain landmines. As the uncertainty in both the MD and GPR inputs cannot be fully removed, the fusion result

shows some false detection of the danger area on the left-side and bottom of the detection result.

As a classical fuzzy fusion system has been built and the fusion result shows that some noise will still affect the fusion result there are two aspects that can be improved upon in order to reduce the noise in the fusion result: improving the single sensor detection and filtering algorithm (see chapter 4), and to improve the fuzzy fusion system.

The P.D Grader group proposed a fuzzy fusion system[43, 106], which shows that using the Gaussian output membership function with different width and centred will improve the fuzzy fusion result. Therefore, an identical fuzzy fusion system has been built with the same width and position of each distribution of output membership function, in order to improve the fusion system. Figure 5-21 shows the output membership function of P.D Grader group.

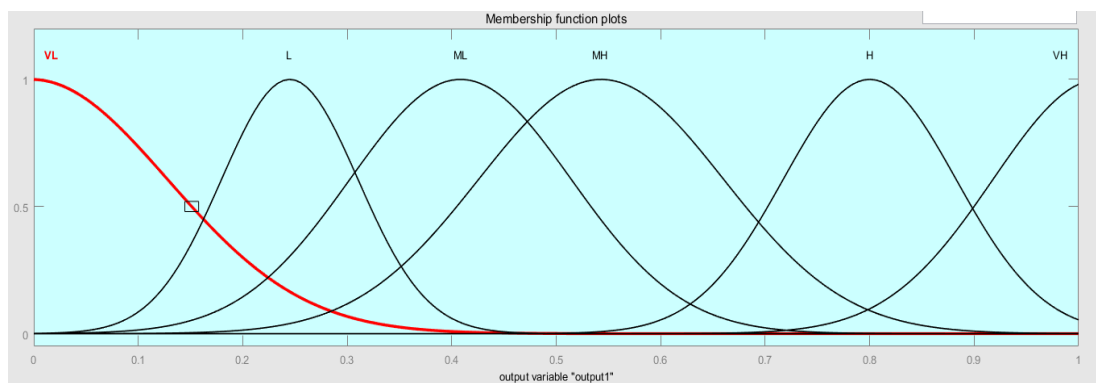


Figure 5-21. P.D Grader research group's fuzzy fusion system output function.

Figure 5-21 show the membership function from the P.D Grader group. The six output functions present the detection results: very low, low, medium-low, medium-high, high, and very high. All the output function uses Gaussian distribution since the normal distribution is most suitable in an unknown environment. The width and the

centre of the output function has been determined by demining experts and a pervious detection test. Figure 5-22 below shows the fuzzy fusion result of the MD and GPR image by using the same fuzzy fusion rules and membership function as the P.D Grader research group. By comparing Figure 5-22 with Figure 5-20 some of the false alarms have been removed. However, there are still a number of false alarms remaining on the top and bottom of the image. In addition, the centre of the landmines has been emphasised showing that the accuracy of detection has been improved.

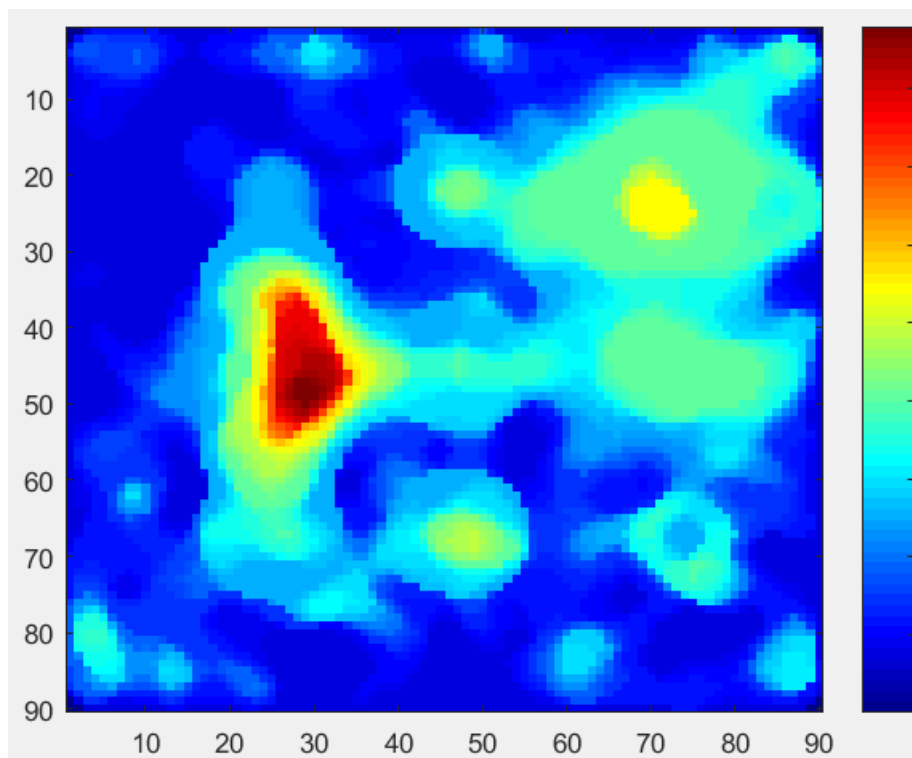
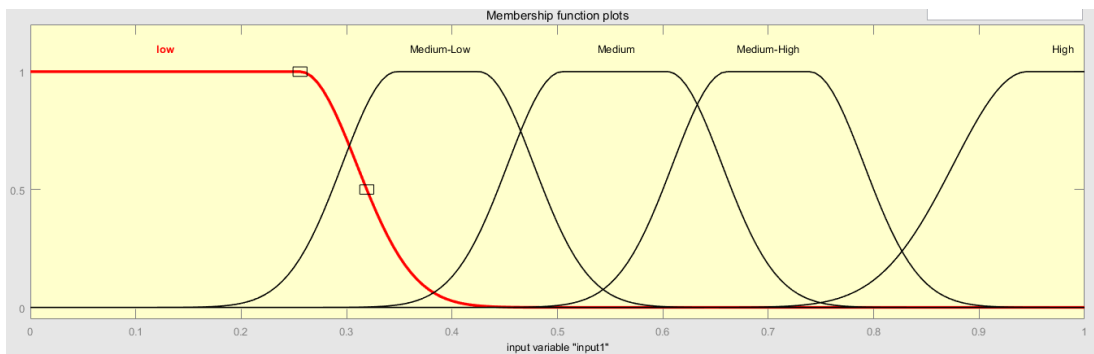


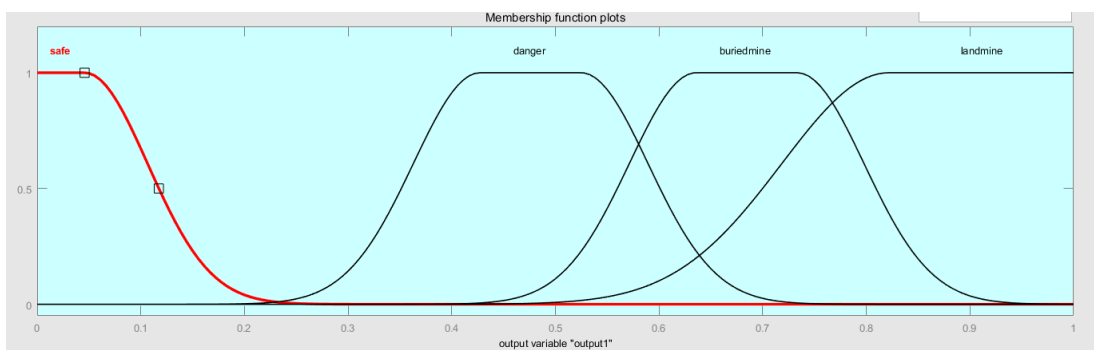
Figure 5-22. Fuzzy fusion result by using Gaussian output membership function.

The fuzzy fusion system from P.D Grader group has proved that the fusion result has been affected by the membership function and the fusion rules. Since the fusion rules of the fuzzy system is determined by human demining experts, which is outside of the scope of the research, subsequent improvements will use the same fuzzy fusion rules as the classical fuzzy system.

In the classical fuzzy fusion system, the membership functions as a crisp triangular shape, and the system is easy to implement. However, it does not smooth at the corner point specified by the parameters. In the P.D Grader group’s fuzzy system using the Gaussian distribution membership function is smooth this time however, for both the input and output membership functions a scale is needed on the top of the distribution to improve the stability of the fusion system. The two-scale Gauss distribution has been introduced here to achieve the membership function. Figure 5-23 shows both the input and output membership function distribution of the novel fuzzy fusion system.



(a)



(b)

Figure 5-23. Input and output membership function of the novel fuzzy fusion system.

In Figure 5-23, the (a) is the input membership function of the novel fuzzy fusion system, and the input distribution has been changed to the two-scale Gaussian distribution, where a scale has been added to top of each membership function. The range of each membership function has been changed slightly, which aims to smooth out the output of the fuzzy system. Figure 5-24 below shows the fusion result of the novel fuzzy fusion system.

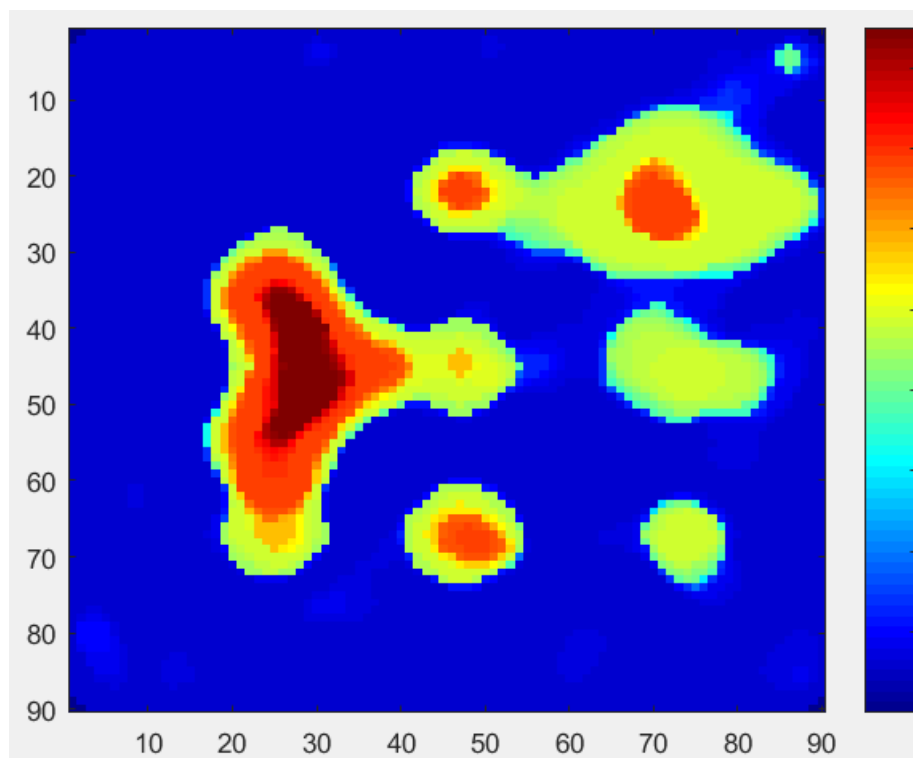


Figure 5-24. Fusion result of the novel fuzzy fusion system.

In Figure 5-24, the red parts are the centre of the landmines, the yellow parts are the killing range of each object, and the blue and green parts are the safe area. Comparing this figure with Figure 5-22 and 5-20, it can be seen that most of the false alarms have been removed. The only false alarm is on the top right side. Comparing with the input data (Figure 5-7 and Figure 5-8), the fusion result also shows a very good performance.

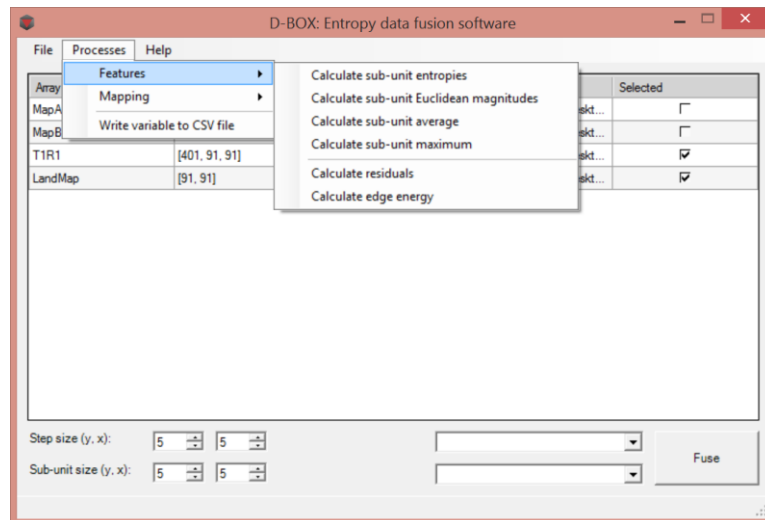


Figure 5-25. Screenshot of the C# D-Box software.

The prototype of the proposed fuzzy logic fusion system was developed in the Matlab environment. It was then implemented under the C# environment [7, 111]. This software can calculate both the entropy features and the statics features in the input image; in addition, it has a Mamdani style fuzzy logic fusion capability. Figure 5-25 shows the user interface of the C# software tool for close-in landmine detection and fusion of GPR and MD sensor data at feature level, which is based on the Matlab prototype developed by the author.

### 5.3 ROC Analysis

The ROC analysis which is discussed in section 4.1.1 and section 4.4.1 is a popular method of assessing the outcome of the landmine detection process. In this subsection, all the fusion results produced by the proposed fusion systems will be compared. Since the fusion system is not required to be a real time system in the detection process, the ROC analysis will be the main result to evaluate the proposed fusion system. Figure 5-26 below shows the ROC analysis result of the proposed fusion system.

In Figure 5-26 the blue line is the GPR single sensor detection result and the orange line is the simulated MD single sensor detection result. Figure 5-26 shows that all the fusion results outperform the single sensor detection system and all the fusion result has reach the detection rate boundary of existing data fusion system which is 10% FAR rate on 90% detection rate. The Bayes fusion system and the D-S fusion system have the same level fusion result, since both are statistics based fusion systems and the D-S system is an improvement on the Bayes system. The result shows the Kalman-Bayes system detection ability can reach 7.8% FAR on 91.1% detection rate, which is outperforms than the Bayes system. All the fuzzy based fusion systems also show good detection ability. The existing outstand fuzzy fusion system has reach 7.25% FAR with 92.4% detection rate, which is a very good result. However, the proposed fusion system detection ability can reach 6.30% FAR with 92.4% detection rate, which is an improvement of the existing landmines fuzzy system. The ROC analysis result clearly demonstrates that both proposed Kalman-Bayes system and proposed fuzzy fusion system has the ability to fuse different landmine detection sensors output and that the fusion result outperforms the existing fusion systems.

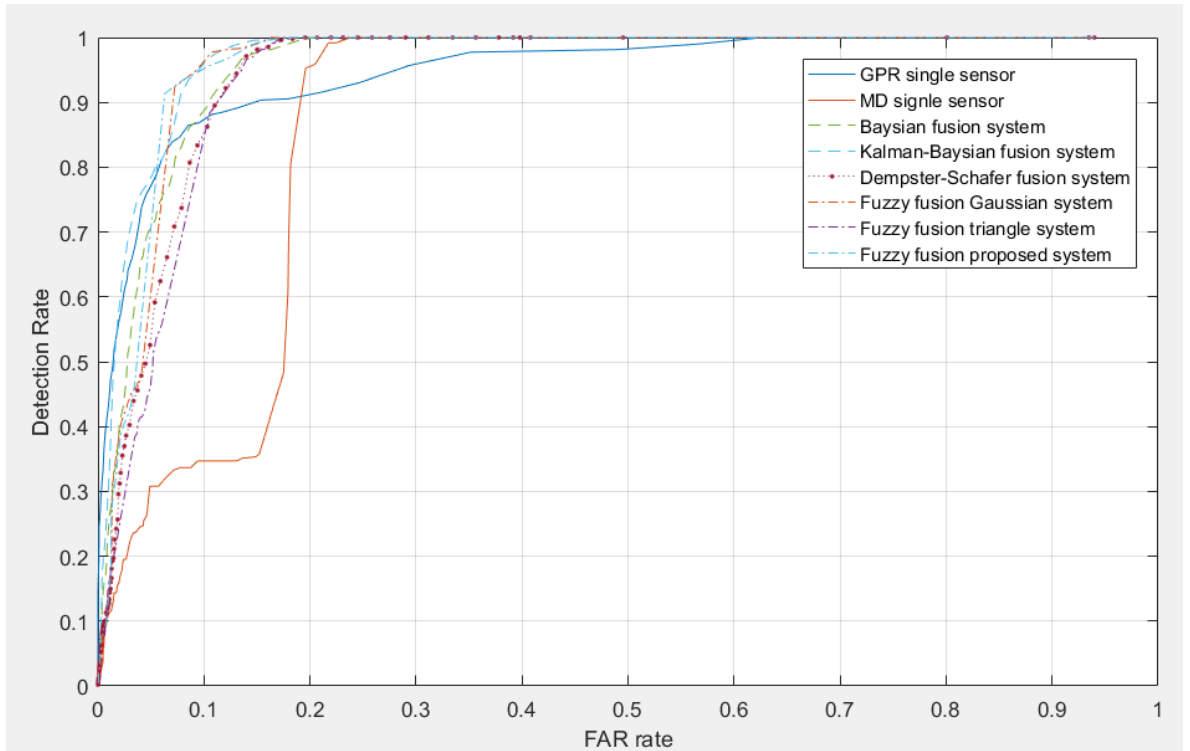


Figure 5-26. ROC analysis of the fusion system.

## 5.4 Summary

This chapter has focused on the design of a data fusion system for landmine detection processing, whereby the D-Box project close-in detection scenario was used as an example to demonstrate the multi-sensor data fusion. The aim of the data fusion in the D-Box project is to achieve the close-in range landmine detection, the available sensors have included GPR, MD and IR camera.

A novel Kalman-Bayes data fusion system was proposed in this chapter, through adding a Kalman filtering process before the decision level fusion to improve the detection ability of the Bayes-based data fusion system. The detection ability analysis has shown that the proposed Kalman-Bayes data fusion system can reach 7.8% FAR

with 91.1% detection rate, which has crossed the boundary of the existing landmine detection data fusion system of 10% FAR with 90% detection rate.

The Dempster-Schafer data fusion system has been built as a reference fusion system in this chapter as well. The detection ability analysis has shown that this system has also reached the boundary of the existing fusion system. In addition, the influence of the sensor uncertainty has been analysed in the Dempster-Schafer data fusion system.

A novel fuzzy logic-based data fusion method was proposed in this chapter too. The proposed method transfers the landmine detection map to the fuzzy membership functions. Then landmine detection experts experience is used to design the fusion rules for the fuzzy based data fusion system. The test results showed that by using the novel fuzzy logic data fusion method, the detection rate has been improved which could be seen from the detection ability analysis. The proposed fuzzy logic data fusion system has reached 6.3% FAR with 92.4% detection rate, outperforming the existing landmine detection system.

The fusion system design proves that the detection results achieved when using data fusion methods are better than when a single sensor is employed for the landmine detection task. The D-Box project final demonstration included a MD with a matching GPR sensor and GPS sensor, however due a technical problem, the two of the most important bits of the collected MD sensor data have been lost, which lead to the MD dataset being unsuitable for fusion. Therefore, a simulated MD image was used with the matching in-door 3D-GPR array as the inputs to the data fusion systems.

However, it is very difficult in general to find matching sensors for collection of test data in an out-door environment, which is suitable for fusion. The problem here are

the GPS sensors, as it is very hard to assure that the data collected from the out-door environment could match at a pixel-level.

## **Chapter 6: Case Study - Multi-Sensor Data Fusion using the MsMs Dataset**

This chapter will use the MultiSensor Mine Signatures (MsMs) dataset as an example to prove that the proposed algorithms can be used in an outdoor environment.

Section 6.1 will provide an overview of the settings of the MsMs landmine area and select the most useful sensor for the data fusion process. Section 6.2 will detail the results of the landmine detection sensor's analysis of the MsMs dataset. Section 6.3 will show the landmine detection results by using the data fusion technology to fuse the MD sensor and the GPR sensor. Finally, Section 6.4 will summarise the chapter.

### **6.1 Overview of the MsMs Project**

The MsMs project was conceived as a relatively simple way to provide experimental data suitable for developers of data fusion algorithms for demining [44]. The MsMs test site was located in the European Commission's Joint Research Centre in Ispra, Italy. Figure 6-1 below shows the area map of the test lane. Seven different kinds of soils were used as the surface environment of the landmine area (the number 7 is off-camera), with each area being a 6m-by-6m square. The numbers 1-7 will represent the surface environment with grassy, loam, sandy, pure sand, clay, high organic and ferromagnetic, respectively. All the landmines used in the MsMs dataset are simulated landmines with the same size, shape and material as a real landmine. The simulated landmine areas are open to the sky and separated from each other by textile membranes; only plot 4 has a cover to maintain it as a dry environment. Each plot has 48 targets, which include the surrogated mines, calibration objects, simulated clutter, and position markers.

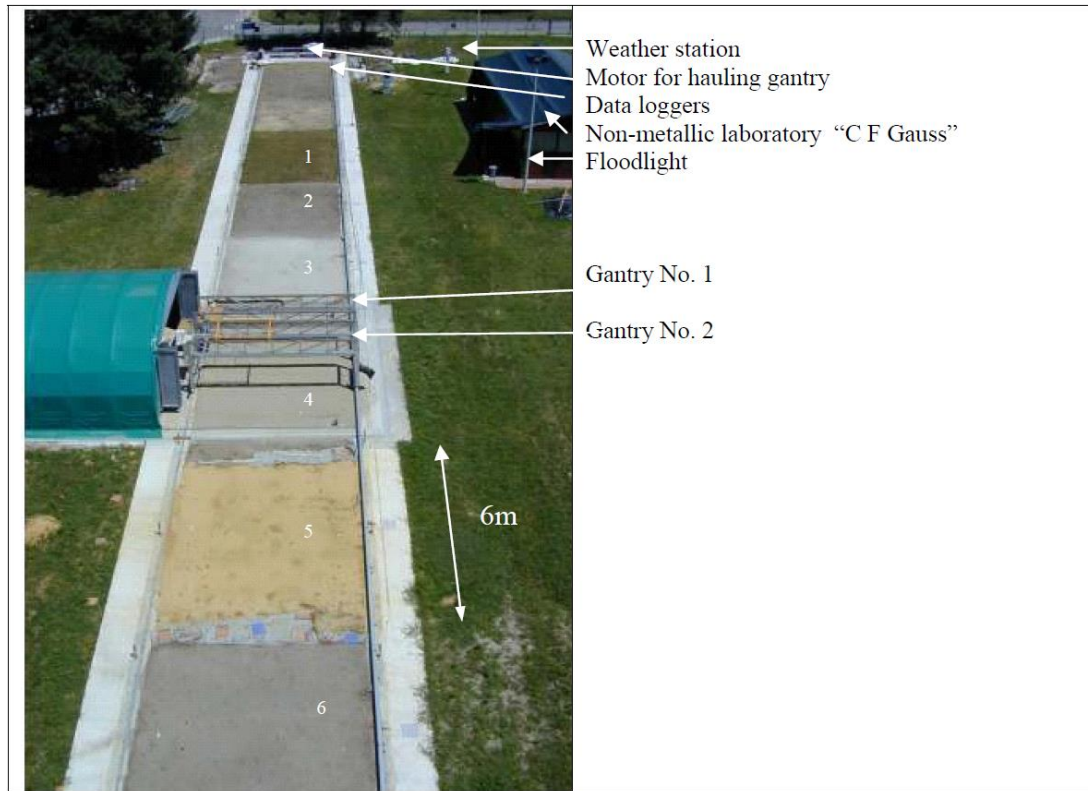


Figure 6-1. Area map of the test lane [44].

The ground truth information of the landmine area is the same for each surface environment, given in Figure 6-2. In Figure 6-2, the 6m-by-6m square has been divided into three 2m-by-6m areas, called *A*, *B*, and *C*. There are 16 objects buried in each area in the same position; eight of them are simulated landmines. There are two differences between the three areas. The first is the clutter type; each area contains six clutters selected from the clutter dataset, consisting of spheres, stones, barbed wire, drink cans, plastic boxes, wooden cylinders, and spent cartridges. All the clutter has been marked on the ground truth map (Figure 6-2). The second difference is the diameter of the simulated landmines; for each area, there are two types of simulated landmines. The *A* type contains a low amount of metal, while the *B* type contains a medium amount. For areas *A*, *B*, and *C*, the diameter of the simulated landmines is

50mm, 80mm, and 110mm respectively, which means, in Figure 6-2, *M1A*, *M2A* and *M3A* represent the low-metal surrogate and *M1B*, *M2B* and *M3B* represent the medium-metal surrogate with the diameter mentioned. The *PT* represents the positioning target with a diameter of 30mm. The *RE1* and *RE2* represent the calibration sphere with diameters of 50mm and 1mm. The *CL1* represents a stone with 60mm length and about 10mm in height and width. The *CL2* represents barbed wire with a 50mm length. The *CL3* represents a drink can with a 66mm diameter and 115mm height. The *CL4* represents a plastic box with length of 60mm, width of 60mm and 30mm in height. The *CL5* represents a wooden cylinder with a length of 60mm and 15mm in diameter. The *CL6* represents a spent cartridge of around 60mm in length. The *TS* in Figure 6-2 means the temperature sensor, *MS* means the Moisture Sensor and the *DT* represents the Delta T moisture sensor; this type of sensor aims to record weather conditions. Since most of the measurement sensors are at the edge of the test lane, they will not influence the data collection for the test lane.

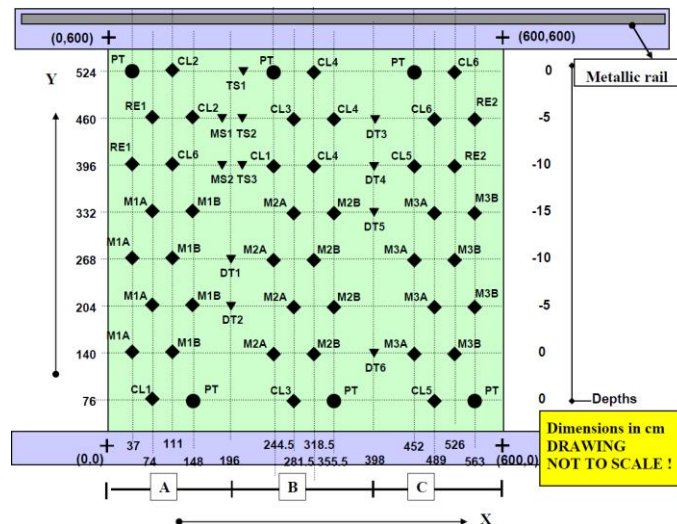


Figure 6-2. Ground truth information of the MsMs dataset [44].

The MsMs dataset contains several types of sensor-testing data, such as MD, GPR, IR camera, and magnetometer, details of which are given in Appendix K. In this case study, the MD and GPR sensors were selected as the default sensors, and the sandy surface area A (3A) was chosen as the default testing area to investigate the proposed landmine detection algorithm (section 4.2) and data fusion systems (sections 5.2 and 5.3). All seven kinds of surface environments were used in the algorithm test process.

Figure 6-3 below shows a ground truth map of area 3A.

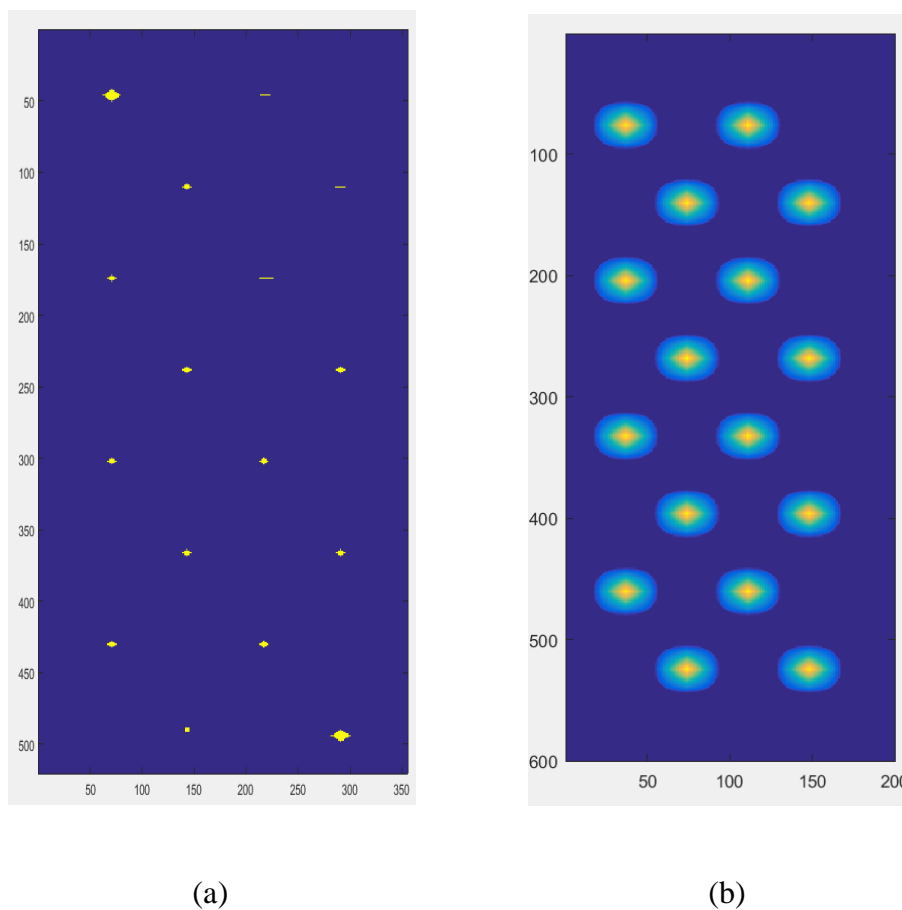


Figure 6-3. Ground truth map of area 3A (a), Dangerous range of the area 3A (b)

In Figure 6-3, the left image is the ground truth map of landmine area 3A, the yellow point means that an object has been buried by the MsMs project team. All the other objects out of this range are unexpected clutter objects, which were already in place

before the MsMs was set up. The right image is the dangerous area of the ground truth map for landmine area 3A. The dangerous area for each object is the 20cm radius from the centre of the object, which is normally 30cm radius for the existing detection algorithms (section 4.4.2). In addition, each detection point addressed in this area will be treat as a successful detection and for the detection point outside of this area will be marked as the false alarm.

## **6.2 Sensor Data Analysis**

This section will analyse the detection results of the landmine detection algorithms, proposed in this thesis, using the MsMs data for selected landmine detection sensors. Section 6.2.1 will present the results of both the entropy-based and MD sensor feature-based algorithms based on the MD sensor data. Section 6.2.2 will present the results of the entropy-based algorithm, statistics algorithm, and GPR feature-based algorithm based on the GPR sensor data.

### **6.2.1 MD Sensor Data Analysis**

MD was selected as the default sensor for the data fusion process in the MsMs dataset because this type of sensor is widely used in existing landmine detection systems. In the military, most landmine detection work makes use of the MD since it is very cheap and has a fast response. However, the limitations of this type of sensor are also obvious; it only displays a good performance in areas that do not contain metal' as the clutter signal will result in an increased number of false alarms.

Two types of metal detectors have been used in the MsMs dataset: the Pulsed Induction Metal Detector (*MD01*) from Vallon, and the Continuous Wave Metal Detector (*MD02*) from Foerster. Since the *MD01* was previously discussed in the data

fusion chapter (see section 5.1), in this chapter, *MD02* is used as the default sensor to test the proposed entropy-based landmine detection algorithm.

Figure 6-4 below shows a typical detection signal feature of the *MD02* in the MsMs dataset. In Figure 6-4, the  $x$  axis is the horizontal movement of the *MD02* sensor, while the  $y$  axis is the reflection signal strength. It can be clearly seen that, if a metal object represents the centre of the object, it will show the same level of reflection signal strength as an area without landmines; in contrast, a change in signal strength near the centre of the object indicates a sine wave signal.

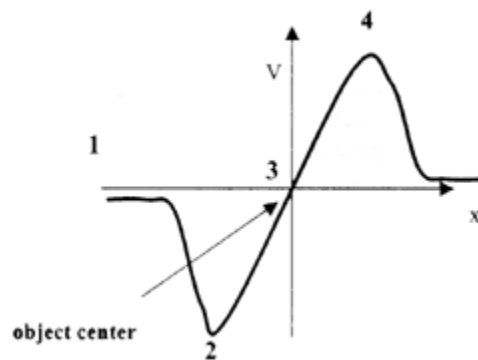


Figure 6-4. A feature of MD02 signals.

Figure 6-5 depicts the data collected by the MD sensor in the A area of the sand surface environment, denoted as MD image *MD023A01*. The marker and clutter in the landmine area produce a very strong signal, as it can be found easily by matching it with the ground truth map (Figure 6-3). The change in the reflection signal is presented via two different colours—the blue on the left-hand side, and the red on the right. The centre of the object can be found in the middle of the two colours' area of coverage.

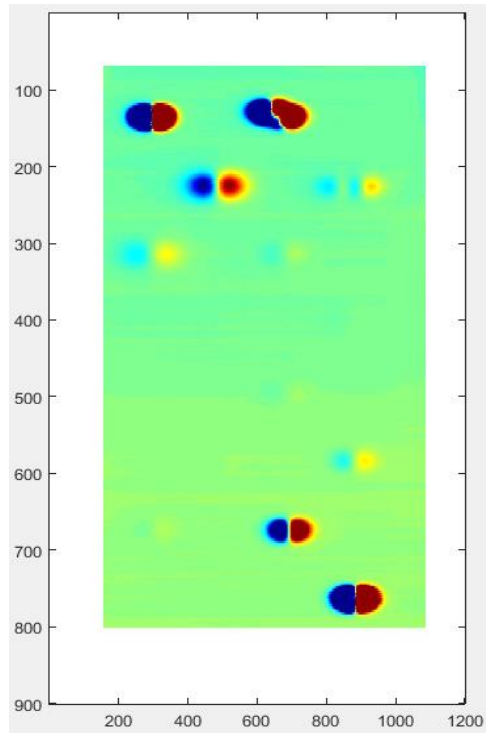


Figure 6-5. The MD023A01 output data.

Based on the features of the MD image, the entropy-based algorithm has been slightly changed. Figure 6-6 represents the flowchart of the entropy-based landmine detection algorithm for the MD image within the MsMs dataset. The first step is to separate the raw image into two different images: red-based, representing the high-reflection signal, and blue-based, representing the low-reflection signal. The second step is building the entropy map using the proposed entropy-based algorithm, which can highlight the suspected area in both the red- and blue-based images. The third step is to fuse the red-based image with the blue-based image in order to produce an entropy-map, thereby helping to reduce the landmine affected area.

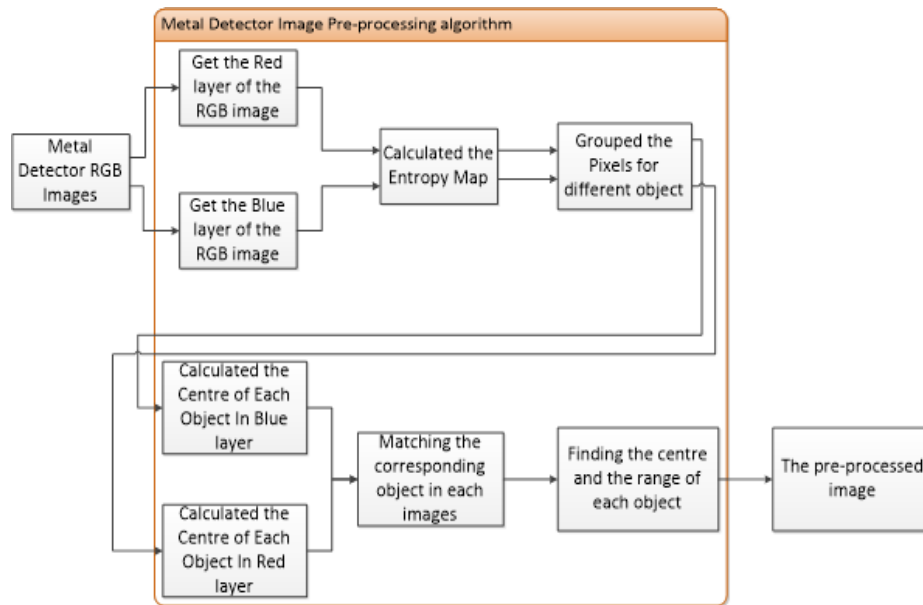


Figure 6-6. Flow chart of the metal detector image pre-processing algorithm.

Using the proposed flowchart, the entropy map of the MD images has been built. Figure 6-7 shows the entropy map of the *MD023A01* image. The colour bar runs from blue to red, in which the dark blue colour is the safe area marked by the entropy-based algorithm, while the other colour is the landmine affected area. Comparing Figure 6-7 with the ground truth image (Figure 6-3), two kinds of unwanted problems appear. The first is that some of the landmines in the middle of the image are not obvious in Figure 6-7; this is because these mines are buried more than 15cm away from the ground surface (some of the targets are 30cm below the surface), thus reaching the limitation of the MD sensor, so detection result do not show an obvious change compared with the surface signal in the MD output result. The other problem is that the marker and the clutter objects in the *MD023A01* image have been marked as the landmine affected area; this is due to the limitations of the MD. Since the MD is sensitive to all object made of or containing metal, the marker and clutter that contain metal will be treated as landmines in the detection process.

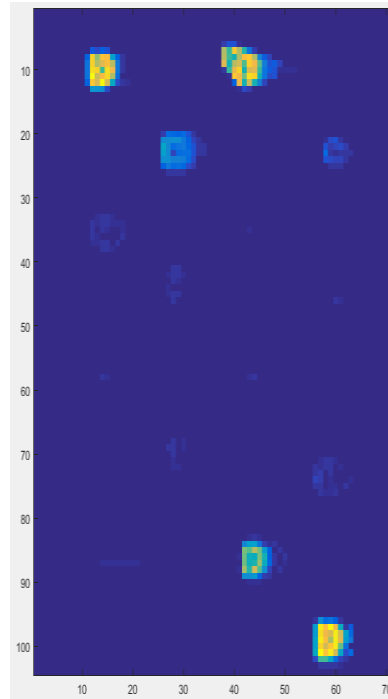


Figure 6-7. Entropy average mapping algorithm detection result for MD sensor in area 3A.

Figure 6-7 shows that the entropy-based algorithm average mapping can detected the buried landmine effectively, when comparing with the ground truth map Figure 6-3(b), it can be clearly seen that nearly all the landmines and object has been founded by using the entropy algorithm, except the bottom left one.

A metal detector feature-based algorithm is proposed here to improve the detection performance of the Counties Wave metal Detector (CWMD) sensor. The working principle of the proposed algorithm is to detect the sine wave signal reflection of the CWMD, using the CWMD to scan the landmine area. The steps of MD feature-based image detection algorithm are shown below:

1. Transfer the RGB image into a linear group, with the index for each pixel of coordinated information.

2. Apply a second-order Butterworth band-pass filter [112] in the frequency domain to reduce the noise of the raw data; the cut-off frequencies for this filter are 0.3 and 0.06.
3. Pick up the index number for each sine wave feature in the linear group.
4. Calculate the centre point of each small sine wave as the detection point.
5. Rebuild the detection result and use the nearest neighbour-based method to optimise the detection results.

Taking the *MD023A01* image as an example, Figure 6-8, shows the detection results of the CWMD sensor, using the feature-based detection algorithm. In Figure 6-8, the left-hand image is the optimised detection result (the red circle means that the object represents the same place as the ground truth image), showing that all landmines, markers and several items of clutter have been detected. The right-hand image is the combined image of the detected result and the ground truth (Figure 6-3), the red circle represents the false alarms, which include the marker, bullet, calibration sphere and some unknown clutter. It can be clearly seen that all landmines marked on the ground truth map have been detected with only 13 false alarms.

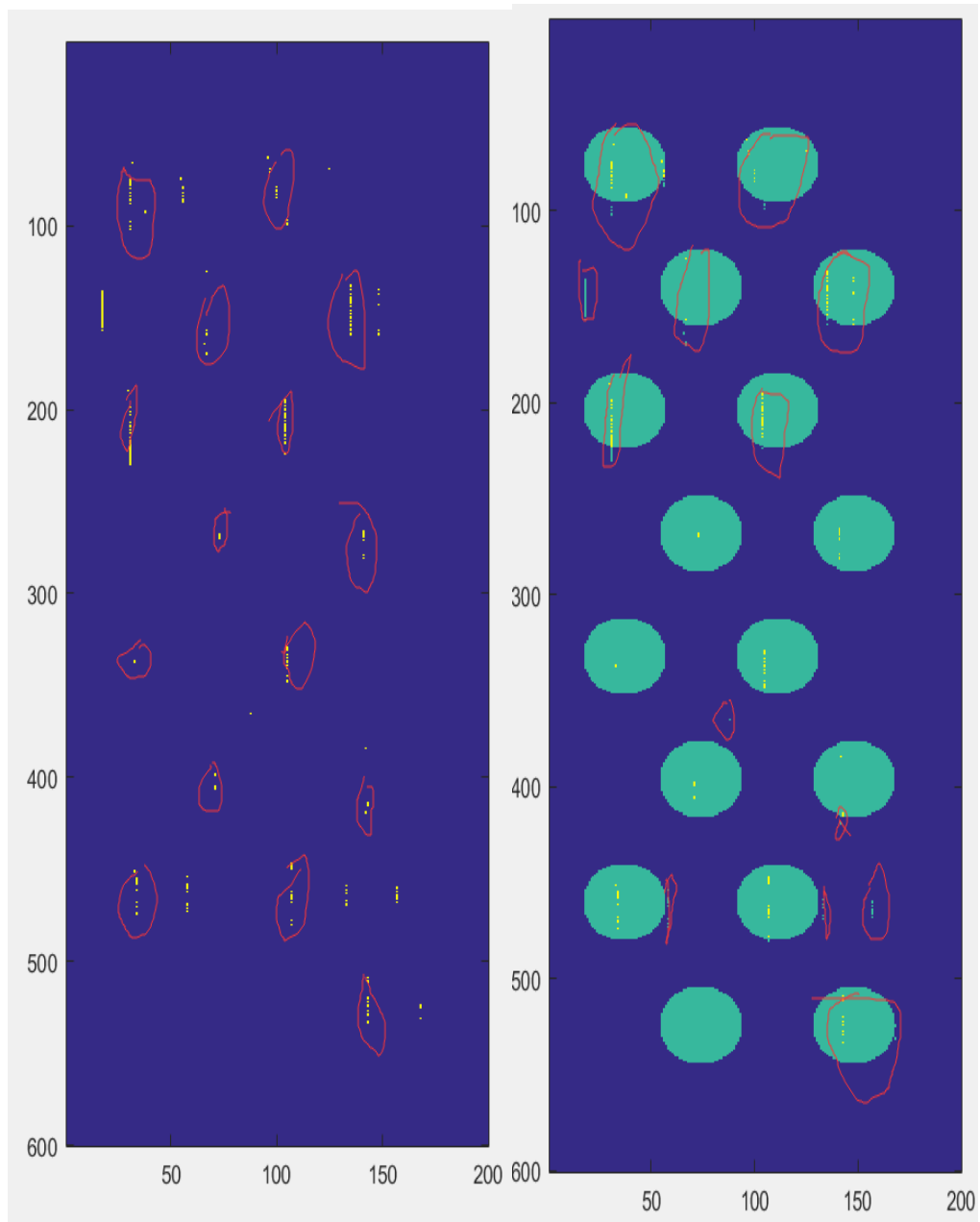


Figure 6-8. The detection result of the MD sensor; left, the optimised image; right, compared to ground truth.

Using the proposed algorithm, all the images of the CWMD in the MsMs dataset have been tested; the results are depicted in Table 6-1.

Table 6-1 *Detailed Results of the MD Detection*

Surface	Detection and FAR number A		Detection and FAR number B		Detection and FAR number C	
Cluttered Grass	6/8	22	7/8	27	8/8	19
Clean loam	8/8	18	8/8	17	8/8	18
Sandy	8/8	13	8/8	15	8/8	16
Pure sand	8/8	12	8/18	14	8/8	14
Clay	8/8	15	8/8	14	8/8	18
High organic	7/8	19	8/8	21	8/8	24
Ferromagnetic	7/8	21	7/8	20	8/8	23

In Table 6-1, each area contains eight landmines, and the detection rate shows how many landmines were detected by the proposed CWMD feature-based detection algorithm. The FAR number details how many false alarms were made when comparing the test result with the dangerous range map of the ground truth. It can be clearly seen that, as the metal content of the object increases, the detection ability of the MD improves. In area C, most of the landmines have been detected, except one landmine within the ferromagnetic environment. The test results demonstrate that the proposed algorithm is suitable for a variety of surface environments except high-organic and ferromagnetic surfaces. The MD detection results will be used as the fusion inputs for the data fusion system in section 6.3.

### 6.2.2 GPR Sensor Data Analysis

The GPR sensor data in the MsMs dataset were collected by a one-metre GPR array from ERA Company, also known as GP04 in the MsMs dataset. The GPR array contains 32 channels; for each channel, an A-scan has been made, making up 256

signals. The GPR array ran on a 1cm step cross-track path to sample the test area, which means the size of the GPR array output is 32 channels×256 signals×600cm.

The data format for the GP04 in the MsMs dataset is a '.rad' file, which is raw radar output binary data. This type of file cannot be opened directly in the MATLAB environment; therefore, a section of the C++ code has been introduced here to read the .rad file. This part of the code was run under the QT creator platform, which reads the binary data from the .rad file and saves the data in ".txt" format for GP043A01. The Figure 6-9 shows the details of the C++ code.

```
QString          strRadFilename          =
"//uol.le.ac.uk/root/staff/home/h/hj76/Desktop
Files/msms/GPR01/era_data/HT          115/Cluttered
Grass/GP04_3A_01.rad";//

short* sData;

QFile file(strRadFilename);

file.open(QIODevice::ReadOnly);

QByteArray ba = file.readAll();

sData = (short*)ba.data();

QFile data("GP04_3A_01.txt");

if (data.open(QFile::WriteOnly | QIODevice::Truncate))
{
QTextStream out(&data);

For (int i=0; i<ba.size()/2;i=i+1)

{

QString::number(sData[i]);

Out<<sData[i]<<" ";

If((i+1) % 256==0)

{

Out<<'r';

}

}
```

```
    }  
    }  
file.close();  
qDebug() << sData[1] << ba.size();
```

Figure 6-9. C++ code for reading the .rad file.

After the GPR array data have been read in the MATLAB environment, the next step is to match the GPR array data with the ground truth information. The size of the raw GP043A01 image is 32 channels×585cm×256 signals, which needs to match the ground truth map (200cm×600cm). The 256 signals will not affect the matching process since it is carried out in along the vertical dimension. The 585cm can be matched with the 600cm-long side of the testing area using the adjusted value given by the MsMs dataset. The only challenge here is to match the 32 signal channels with the 200cm-wide side. This was achieved following Dittmer’s helpful suggestions [113] to add a linear number between each channel to smooth the 3D C-scan GPR image.

After the 3D C-scan GPR image has been built, the next step is to test the algorithms proposed in section 4.3. Figure 6-10 below shows the testing results achieved by the entropy-based algorithm and the statistics-based algorithm.

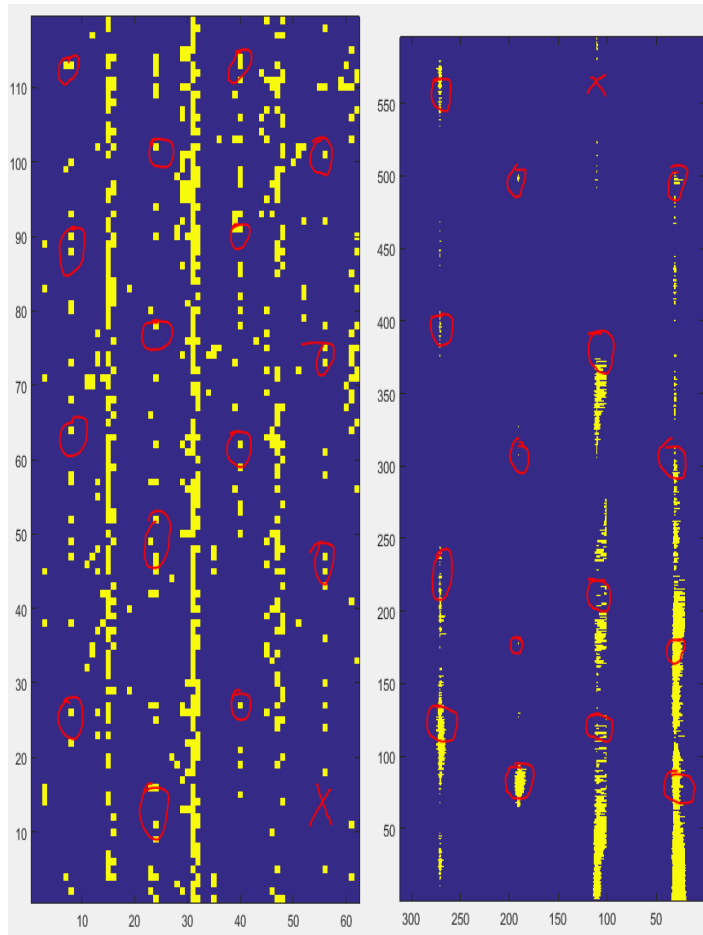


Figure 6-10. The detection result of the GPR sensor. On the left, the entropy-based algorithm; on the right, the statistics-based algorithm.

The left image in Figure 6-10 is the result of the entropy-based landmine detection method using the GP043A01 image, showing that all the landmine affected area have been marked as a suspect area. All the proposed algorithms, entropy, statistics-based and the GPR feature based, can detect all eight mines in the test area. However, there were also many false alarms around the detection area; this is because the data input from the GPR sensor is in a different format. For the vertical axis, the distance between two samples is 1cm; for the horizontal axis, the distance between the two samples is nearly 6cm. In general, the GPR array output unit in the lab environment is 1cm×1cm square; however, in a real case, the GPR array data would not show the same accuracy as in the lab environment. This indicates that the statistics-based algorithm does show

the ideal performance as in the lab environment; nevertheless, it still reveals a high detection rate.

Figure 6-11 below shows the testing results achieved by the GPR feature based algorithm.

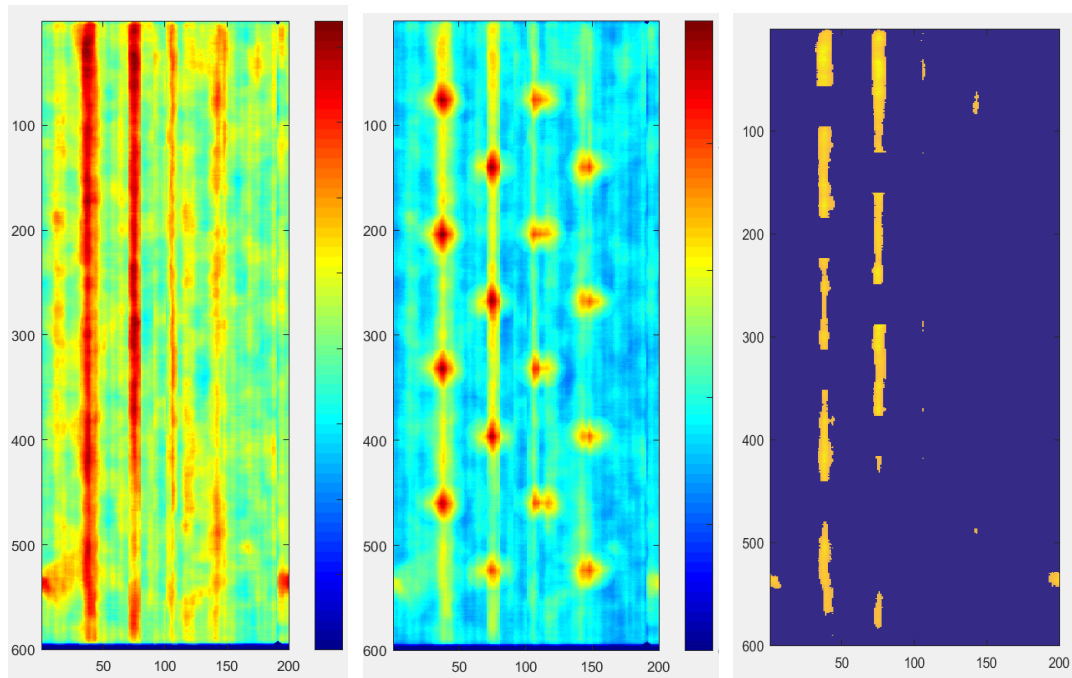


Figure 6-11. The detection result of the GPR feature algorithm. left, the GPR feature based algorithm detection result; middle, detection object counting; right, false alarm counting of the detection result.

In the Figure 6-11, the left image is the GPR feature based algorithm detection result, the red colour represents the high dangerous area and the blue colour represents the background. The middle image is comparing the detection result with the dangerous area of the ground truth map. The result has shown that all the centre of the buried object has been marked as red colour, which means that all the buried object has been detected by the proposed GPR feature based algorithm. This has proved that the GPR feature based algorithm is suitable for an outdoor environment landmine area. The right-hand side image is the false alarm counting image, it can be clearly seen that

there are 16 false alarm areas in the image. In addition, there are eight marked objects in the landmine area are not landmines, therefore the total false alarm of the GPR feature based algorithm is 24. By using the proposed GPR feature-based algorithm, all the MsMs GPR data have been processed. Table 6-2 below shows all the test groups in the MsMs dataset using the GPR feature based algorithm.

Table 6-2 Detailed Results of the GPR Detection Test

Surface	Detection and FAR number A GPR		Detection and FAR number B GPR		Detection and FAR number C GPR	
	8/8		8/8		8/8	
Cluttered grass	8/8	29	8/8	31	8/8	27
Clean loam	8/8	26	8/8	18	8/8	16
Sandy	8/8	24	8/8	19	8/8	17
Pure sand	8/8	23	8/8	17	8/8	21
Clay	8/8	26	8/8	24	8/8	21
High organic	8/8	32	8/8	28	8/8	31
Ferromagnetic	8/8	34	8/8	32	8/8	36

According to Table 6-2, as the metal content of the object increases, the detection ability of the MD improves. In area C, most of the landmines have been detected, except one landmine within a high organic environment. The test result demonstrates that the proposed GPR feature based algorithm is suitable for a variety of surface environments, except the highly organic and ferromagnetic surfaces.

## 6.3 Evaluation Results

Both the Kalman-Bayes fusion system and the fuzzy-based fusion system were employed to fuse the GPR and MD data in the MsMs database. Figure 6-11 details the results of the data fusion, using the fuzzy-based fusion system to fuse the MD detection result and the GPR detection result. Since the MD image and the GPR image do not have the same data size, a normalised step is required to ensure that the MD output and the GPR output have the same data size. In Figure 6-12, the left-hand side is the simulated MD detection image, which is based on the MD detection result (Figure 6-8), and the right side is the processed GPR image.

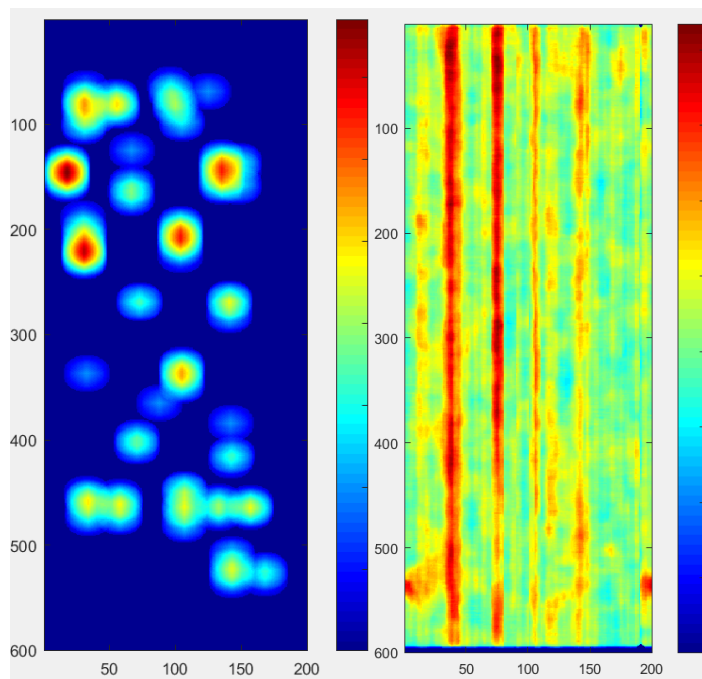
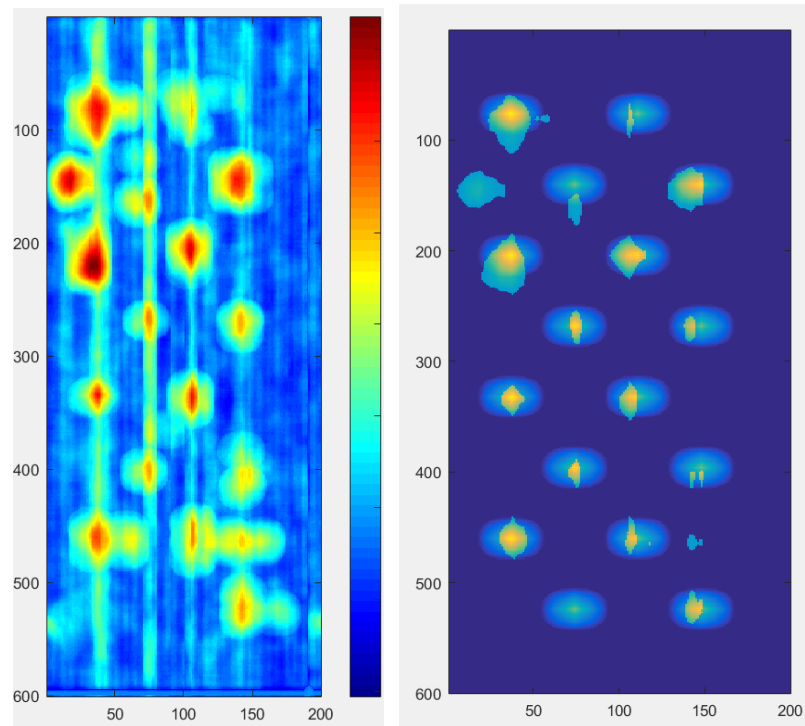
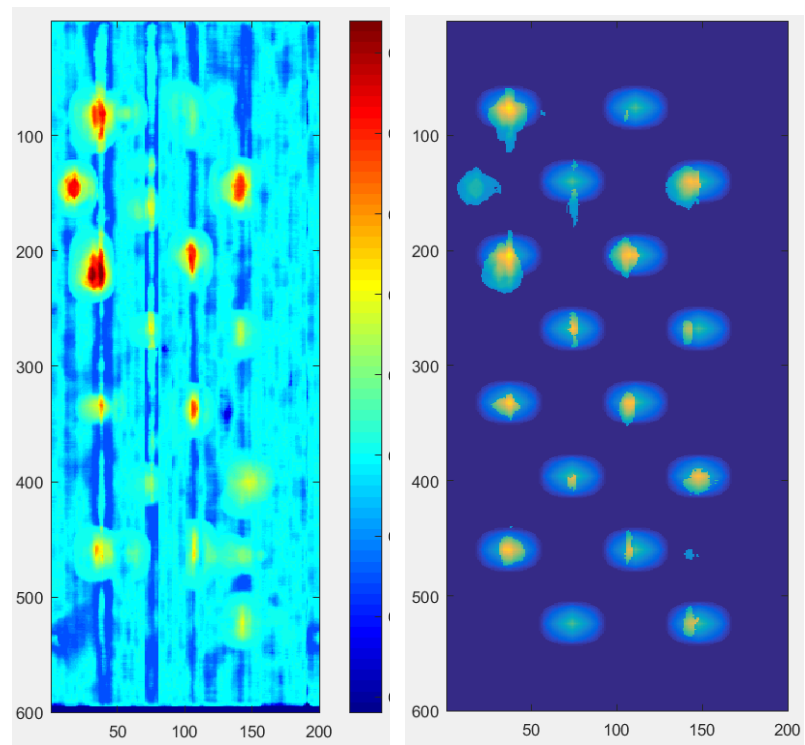


Figure 6-12. Data fusion system inputs. Left: MD image; right: GPR image.

Both images in Figure 6-12 display false alarms, but, via the Kalman-Bayes fusion method and the fuzzy fusion system, the number of false alarms has been effectively reduced, as shown in the of Figure 6-13.



(a)



(b)

Figure 6-13. Data fusion system result. (a): Kalman-Bayes fusion system; (b): fuzzy fusion system.

Figure 6-13 shows the fusion results using area 3A in the MsMs dataset. In Figure 6-13 the part (a) shows the fusion result produced by the Kalman-Bayes fusion system, where the left image is the fusion result and the right image is the false alarm counting. From the fusion result it can be clearly seen that all the objects have been marked by the red colour, in addition, only two unexcepted objects have been marked on the decision map. In addition, the false alarm counting image has shown that the Kalman fusion system has reduced the false alarm to 10, which include 3 unexcepted objects and 7 known clutter. The false alarm counting for the MD sensor is 13 and for the GPR sensor is 24, the result has proofed that the Kalman-Bayes fusion system can reduce the false alarm in the detection process. In Figure 6-13 part (b) the images show the fusion result produced by the proposed fuzzy fusion system. The left image is the detection result, which has shown that all the objects have been marked as yellow or red colour, which means that the fuzzy system is not as sensitive as the Kalman-Bayes system, however, all the landmines have been marked. The right image is the false alarm counting result; it shows that the fuzzy fusion system can reduce the false alarms compared with a single sensor input. Figure 6-13 has proved that the fuzzy fusion system also can be used in an outdoor environment.

Table 6-3 below shows the detailed results of the fusion of the MD and GPR data, under the MsMs dataset by using both Kalman-Bayes fusion system and the fuzzy-based data fusion system in section 5.2. According to Table 6-3, the proposed data fusion system could improve the detection rate and reduce the false alarm rate in the landmine detection process. Figure 6-3 (the ground truth map of MsMs dataset in area A) also shows that the proposed algorithm has been influenced by the surface environment. It works well on dry surfaces, but when used for grass, high organic, and ferromagnetic areas, the results are inferior.

Table 6-3 Detailed Fusion Results with the MsMs Dataset (a) Kalman-Bayes fusion system, (b) fuzzy fusion system

(a)

Surface	Detection and FAR number A fusion		Detection and FAR number B fusion		Detection and FAR number C fusion	
	8/8		8/8		8/8	
Cluttered grass	8/8	10	8/8	11	8/8	12
Clean loam	8/8	7	8/8	9	8/8	8
Sandy	8/8	10	8/8	8	8/8	8
Pure sand	8/8	7	8/8	8	8/8	8
Clay	8/8	11	8/8	14	8/8	13
High organic	8/8	12	8/8	16	8/8	12
Ferromagnetic	8/8	14	8/8	12	8/8	15

(b)

Surface	Detection and FAR number A fusion		Detection and FAR number B fusion		Detection and FAR number C fusion	
	8/8		8/8		8/8	
Cluttered grass	8/8	11	8/8	13	8/8	11
Clean loam	8/8	9	8/8	11	8/8	9
Sandy	8/8	11	8/8	13	8/8	11
Pure sand	8/8	8	8/8	9	8/8	8
Clay	8/8	10	8/8	13	8/8	11
High organic	8/8	14	8/8	18	8/8	17
Ferromagnetic	8/8	19	8/8	16	8/8	18

## 6.4 Summary

This chapter has focused on evaluating and proving the proposed landmine detection algorithms and data fusion system using the MsMs dataset. The MsMs dataset was introduced. In this chapter, the landmine area 3A of the MsMs dataset was selected as

the default area to test the proposed algorithms in section 4. A central feature of this chapter is the proposed MD feature-based detection algorithm that can automatically detect metal-containing objects with a low false alarm rate.

The MD data analysis has shown that the proposed entropy-based algorithm can reduce the landmine affected area effectively. In addition, the MD feature-based algorithm works well, achieving a very high detection rate and a low false alarm rate in dry areas. The GPR data analysis section proposes a method based on the QT creator, which can transfer the raw radar data to a text file. The test results of the proposed algorithms have proved that the entropy-based algorithm can reduce the landmine affected area, and the statistics-based algorithm achieves high rates of landmine detection. The data fusion result section has demonstrated that, via the proposed fuzzy-based data fusion system, the false alarm rate can be reduced.

Through this case study based on the MsMs dataset, the performance of the proposed algorithms, the Kalman-Bayes fusion system and the fuzzy-based data fusion system has been verified. Currently, the landmine detection system works on the training dataset, processing the sensor collection data in real-time. In addition, since the MsMs dataset comes from an outdoor environment, the proposed algorithm has the ability to work in the real world. The results of the data fusion system also demonstrate that the surface environment influences the proposed algorithms, working well in a dry environment but, when moved to a high-organic environment, the performance level is reduced.

## **Chapter 7: Conclusions and Future Work**

### **7.1 Research Summary**

This research has focused on advancing the state-of-the-art of landmine detection systems by using data fusion technology. Two types of data fusion methods have been used to demonstrate that the data fusion technology could improve the existing landmine detection process. The first method uses data fusion technology to reduce redundant data in a single landmine detection sensor, which could improve the detection ability of a single sensor. The second method uses data fusion technology to fuse several different types of landmine detection sensors' output, helping to improve the detection result of landmine detection systems.

This thesis has reviewed relevant studies concerning data fusion system design for landmine detection. Based on the literature review, three different research gaps were identified and targeted: multi-focus image fusion, landmine detection at the sensor data level and heterogeneous multi sensor data fusion for landmine detection.

The thesis has thus proposed a novel PCA-based multi-focus image fusion algorithm. In comparing the new proposed algorithm with other multi-focus image fusion algorithms, the test results show that the new proposed algorithm could achieve a low computational complexity and high-quality fusion result. The proposed PCA-based multi-focus image fusion algorithm can be employed as a double-eye system in landmine detection as well as other relevant image processing systems. For surface landmine detection, the multi-focus image fusion algorithm can help the system to understand the detection area environment. In non-landmine detection, the multi-focus image fusion algorithm is important as well. In actual fact, it is one of the most important steps of image data pre-processing. For example, autonomous car driving

systems need a multi-focus image fusion algorithm to fuse the multi-focus images captured from different optical cameras. Once multi-focus image fusion has been completed, distance detection and routing calculation processing can be started.

Three different types of landmine detection algorithms for the GPR sensor have also been proposed in this thesis. The proposed entropy-based algorithm is appropriate for fast detection in a large area. In addition, the entropy-based algorithm also shows good performance in the landmine area reduction process. The statistics-based algorithm is fast and also shows good performance in a small area. The test results show that it presents a good performance with low computational complexity. The feature-based GPR sensor detection algorithm, which is only suitable for GPR sensors, shows the best results among the three proposed algorithms. The evaluation results have shown that all the proposed algorithms could be used for close-in landmine detection work, generating a 2D landmine decision map based on 3D GPR images.

With regards to data fusion system design, this research overcomes the limitations of the existing Bayesian fusion approach. A new Kalman-Bayes based fusion system is proposed which reduces the system uncertainty and improves the fusion process. Two Gaussian membership functions are introduced, which take into account the input signals' distributions. The existing Bayes, Dempster-Schafer and fuzzy logic based fusion systems have been implemented in this research as reference systems. The test results have shown that the data fusion system could effectively combine the GPR sensor output with the MD sensor output. The proposed Kalman-Bayes and the improved fuzzy fusion system outperform both the existing Bayes and fuzzy logic based fusion system in terms of detection ability.

The MsMs dataset has been used as an example to demonstrate the proposed algorithms and data fusion systems. The test results indicate that both the proposed algorithms and the proposed data fusion systems are suitable for outdoor environments.

## 7.2 Novel Contributions

The novel contributions of this research will be summarised as follows:

1) *Firstly*, three new single-sensor sub-surface landmine detection algorithms have been proposed in this thesis: the entropy-based algorithm, the statistics-based algorithm and the GPR feature-based algorithm. The evaluations of these algorithms show that they advance the state-of-the-art in several ways.

The entropy-based algorithm requires low computational time and memory usage, producing good detection results, which outperform the state-of-the-art region-selection thresholding algorithm. In addition, the statistics-based algorithm and the GPR feature-based algorithm require lower computational time, low memory usage and, at the same time, produce the same level of performance, as the state-of-the-art edge energy detection algorithm and EHD algorithm. The detection ability of the GPR feature based algorithm has reached 22% FAR with a 90% detection rate, which is beyond the state-of-the-art boundary performance for a single sensor detection algorithm: 60% FAR with 90% detection rate.

The proposed entropy-based algorithm and statistics-based algorithm are not only applicable to the GPR sensor, but can also work with other types of multi-layer sensor data. Being capable of higher detection performance the proposed single sensor detection algorithms would enhance the final detection result of a multi-sensor data fusion system. In addition, the single sensor detection algorithms could be used for buried object detection, metal flaw detection and other detection processes.

2) *Secondly*, this thesis has proposed two novel data fusion systems: the Kalman-Bayesian fusion system and the fuzzy logic-based system. The evaluation results have shown that both proposed systems improve the output result of the landmine detection process outperforming the state-of-the-art Bayes fusion system, Dempster-Schafer fusion system and fuzzy fusion system.

The detection ability of the Kalman-Bayes fusion system has reached 7.8% FAR with 91.1% detection rate, which outperforms the boundary performance of the state-of-the-art landmine detection system (10% FAR with 90% detection rate). The proposed fuzzy fusion system outperforms state-of-the-art fuzzy logic based landmine detection systems in terms of detection ability. This is due to the innovative membership functions design, which takes into account features of the input signals.

The proposed multi-sensor data fusion techniques have demonstrated a significant increase in the detection rate when comparing the fusion results with the single-sensor detection results. The proposed Kalman-Bayes fusion system is suitable not only for landmine detection, but can also be used for other heterogeneous multi sensor data fusion processes.

3) *Thirdly*, the proposed novel multi-focus-image fusion algorithm can assist surface landmine detection systems by reducing redundant information. The proposed multi-focus image fusion algorithm outperforms most of the state-of-the-art algorithms.

The multi-focus image fusion research builds upon the existing PCA multi-focus image fusion algorithm adding an innovative new step, i.e. a fusion process, to it. The test results have shown that the proposed multi-focus image fusion algorithm outperforms both the existing PCA and IHS algorithm.

The multi-focus image fusion algorithm could also be applied to double-eye detection systems in autonomous robotic applications.

4) *Finally*, the case study of the MsMs dataset has demonstrated that the proposed single sensor detection algorithms and data fusion systems are suitable for outdoor environment detection work, making them applicable to a wide range of applications.

### **7.3 Future Work**

Future research should focus on improving the computational time of both landmine detection algorithms and the data fusion systems. The ultimate goal of this research is to build a real-time, low-power and reliable landmine detection system for use by human operators in the field.

The highest priority future work with respect to the development of the C# D-Box Software is comprehensive testing and characterisation of the performance of the developed and implemented algorithm using real measurement data from close-in detection sensors (e.g. GPR, MD etc.), as opposed to simulated data. The implementation of other processes such as mapping methods is also a high priority for future work with respect to the development of the C# D-Box Software. The development and derivation of sets of fuzzy logic rules that take into account the type of input data to be fused would likely improve the data fusion aspects of the software.

Implementing a more diverse range of options associated with the determination of a threshold for use in the count of qualifying mapping methods would both be simple to achieve, as well as likely to broaden the applicability of the mapping methodologies to more diverse datasets.

Future work should also focus on the design and implementation of the proposed algorithms and data fusion systems within embedded systems. Improving detection performance will require particular attention to finding a trade-off between performance and power consumption of hardware designs aimed at portable embedded platforms.

Finally, future research on the multi-focus image fusion algorithm should focus on improving the quality of the fusion image and reducing operation time.

# Appendices

## Appendix A: Surface Landmine Detection Algorithm

Based on the existing multi-modal image fusion algorithm, a novel algorithm which could fuse the visible image with the IR image has been proposed. The proposed algorithm could be used for detecting the surface landmine in the landmine detection process. The flow chart of the proposed fusion algorithm is shown in Figure B-1.

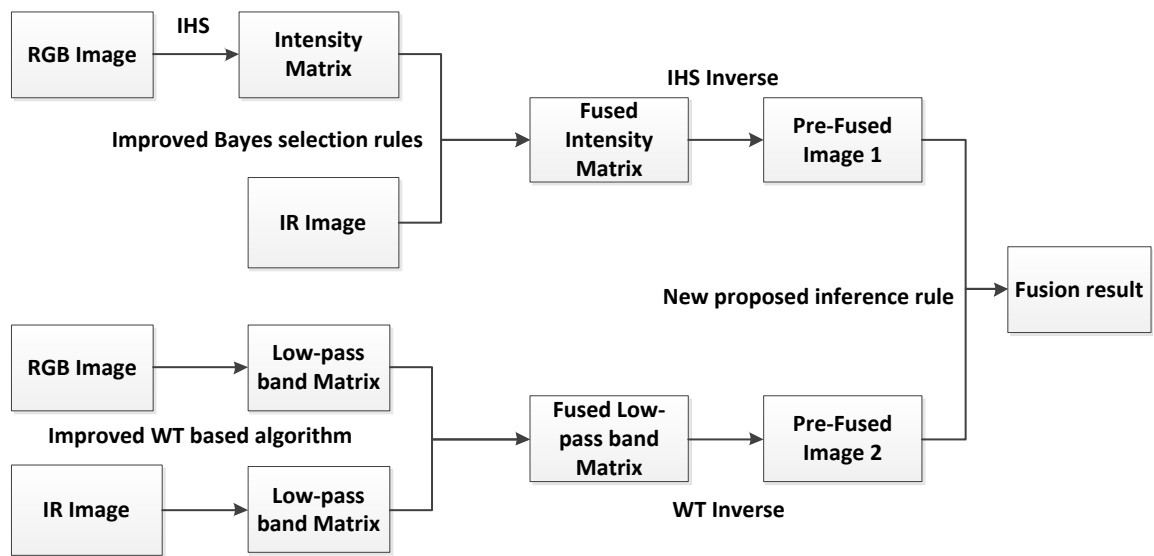


Figure B-1. Flow chart of the proposed multi-modal image fusion algorithm.

The features of the visible image are the edge information and the colour information. However, the edge information cannot be extracted from the original image directly. The WT is an effect image decomposed method, which can decompose the original image into different bands. Then, the useful information from each band could be fused to produce a good fusion result. The classical wavelet transform is shown below [75]:

$C_o$  = the odd column of the image and  $C_s$  = the even column of the image.

Firstly, the original image is decomposed into H and L bands:

$$H = (Co-Cs) \text{ and } L=(Co+(H/2))$$

Secondly, the wavelet transform decomposes the L and H bands into LH, LL, HL and HH bands based on the raw image.

$$\begin{aligned}
 LH &= L_{\text{odd}} - L_{\text{even}} & LL &= L_{\text{even}} + (LH/2) \\
 HL &= H_{\text{odd}} - H_{\text{even}} & HH &= H_{\text{even}} + (HL/2) \\
 H_{\text{odd}} &= \text{odd row of H} & L_{\text{odd}} &= \text{odd row of L} \\
 H_{\text{even}} &= \text{even row of H} & L_{\text{even}} &= \text{even row of L}
 \end{aligned} \tag{a.8}$$

Then, the LL band is selected as the fusion band and the maximum inference rules are used to fuse the visible image and IR image. The equation of the maximum inference rules is shown as below:

$$F2_{(x,y)} = \begin{cases} IR_{(x,y)} & IR_{(x,y)} > V_{(x,y)} \\ V_{(x,y)} & IR_{(x,y)} < V_{(x,y)} \end{cases} \tag{a.9}$$

Based on the maximum inference rules, the pre-fused image 2 (F2) can be calculated, which contains most feature of the visible image. The previous steps provide two pre-fused images: the feature of the visible image and the feature of the IR image. The following step marks the changed pixels in each pre-fused image. For each changed pixel, the city-block distance algorithm is used to measure the changing probability of the pixel. The city-block is shown below:

$$\begin{aligned}
 & \text{changed pixels value of pre – fused image 1} \\
 & = \begin{cases} 0 & F1(x, y) = VI(x, y) \\ 1 & F1(x, y) \neq VI(x, y) \end{cases} \tag{a.10}
 \end{aligned}$$

*changed pixels value of pre – fused image 2*

$$= \begin{cases} 0 & F2(x, y) = IR(x, y) \\ 1 & F2(x, y) \neq IR(x, y) \end{cases} \quad (\text{a.11})$$

$$P(F_m(x, y)) = \text{changed pixels matrix} * \frac{1}{16} \begin{bmatrix} 1 & 2 & 1 \\ 2 & 4 & 2 \\ 1 & 2 & 1 \end{bmatrix} \quad (\text{a.12})$$

$$F(x, y) = \begin{cases} F1(x, y) & P(F1(x, y)) > P(F2(x, y)) \\ F2(x, y) & P(F2(x, y)) > P(F1(x, y)) \end{cases} \quad (\text{a.13})$$

The final fused image is re-built based on the compared result of the probability of the changing rate.

## Appendix B: General GPR Analysis

The first step of the GPR sensor research to use this GPR image as the reference image to build the landmine danger map. The next step is to work out a pre-processing method to get the dangerous level of the GPR image. The readable GPR image for an 'G' label on the surface after the pre-processing is shown in Figure A-1.

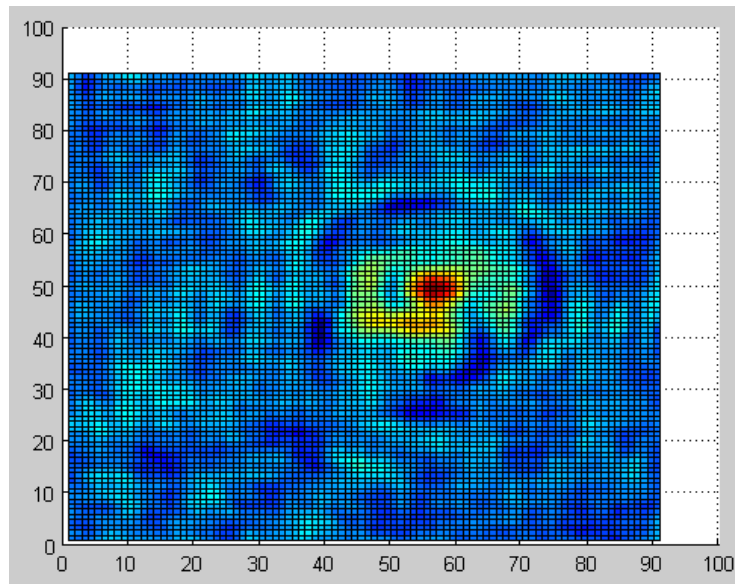


Figure A-1. 'G' label GPR image.

Figure A-1 indicates that a highlight point is on the center of the GPR image and the location is (60,50). The highlight points which look like a Big G (yellow and red color) are also shown in the figure. These highlight points in the GPR image means that there will be an object at that layer. This is the actual surface environment of the GPR system.

## Appendix C: TIR Image Analysis

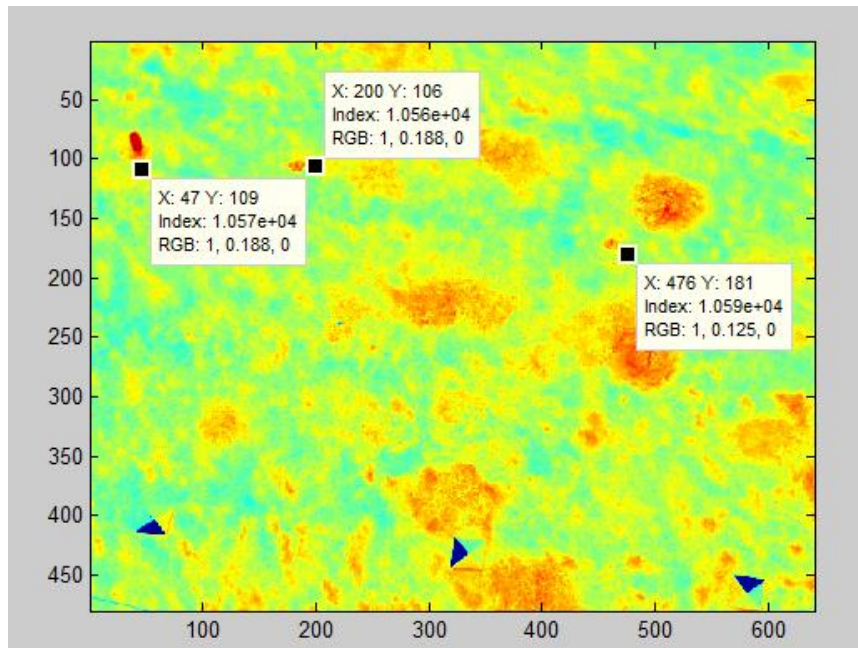


Figure D-1. TIR image for the landmine area.

The TIR image in Figure D-1 is a part of landmine area zone 1. Three AP mines on the surface could be found in this adjusted image, shown as black points. However, it is hard to identify the buried landmines from the original image.

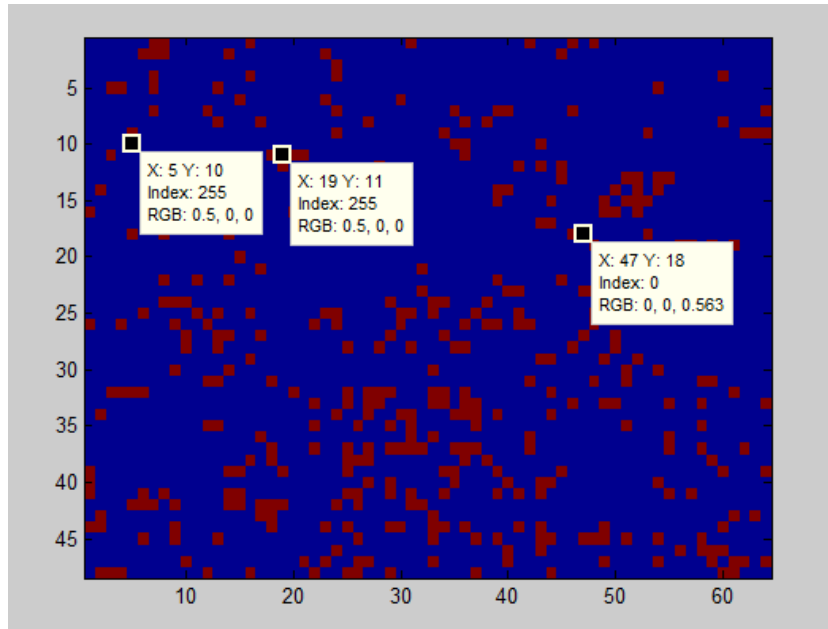


Figure D-2. Entropy-based algorithm for TIR image detection

Entropy-based fusion algorithm is applied to the TIR image. All the surface landmines are identified but with many false alarms. The current equation requires a re-design in order to match the algorithm to the detection result.

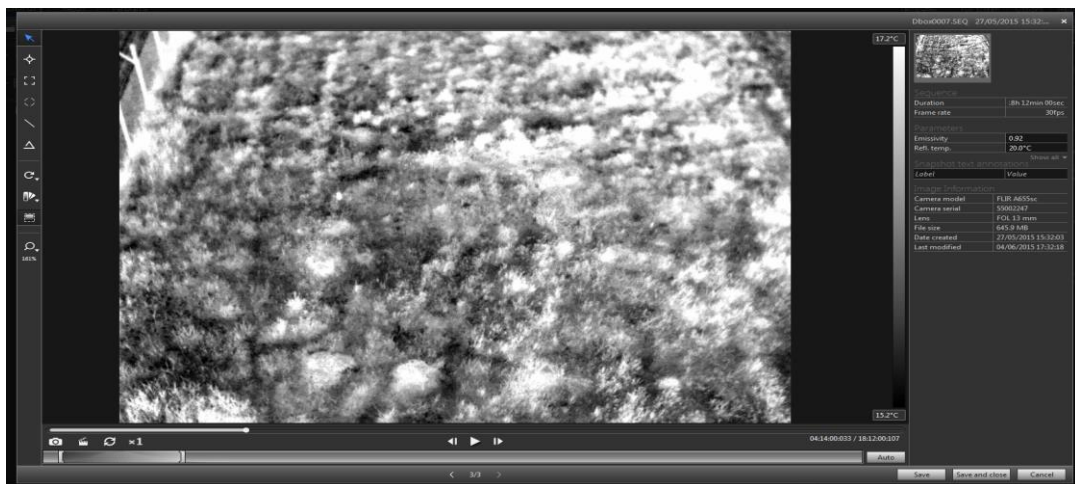


Figure D-3. FLIR landmine area normal image.

Figure D-3 shows the normal FLIR thermal image of the landmine area 1 in May in Poland. Most of the area in this image is white, and it is very hard to find the landmines.

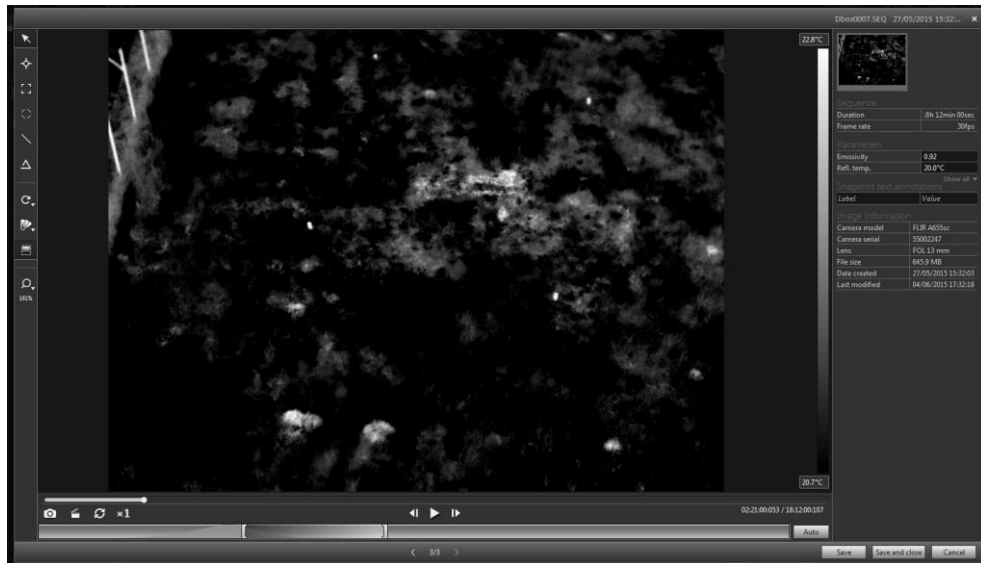


Figure D-4. GLIR landmine area image with filter.

Figure D-4 is processed by using the high pass filter, whereby some small white objects in the middle of the image can be found; when compared to Figure D-5 the ground truth information of the landmine area, these can be identified as landmines.

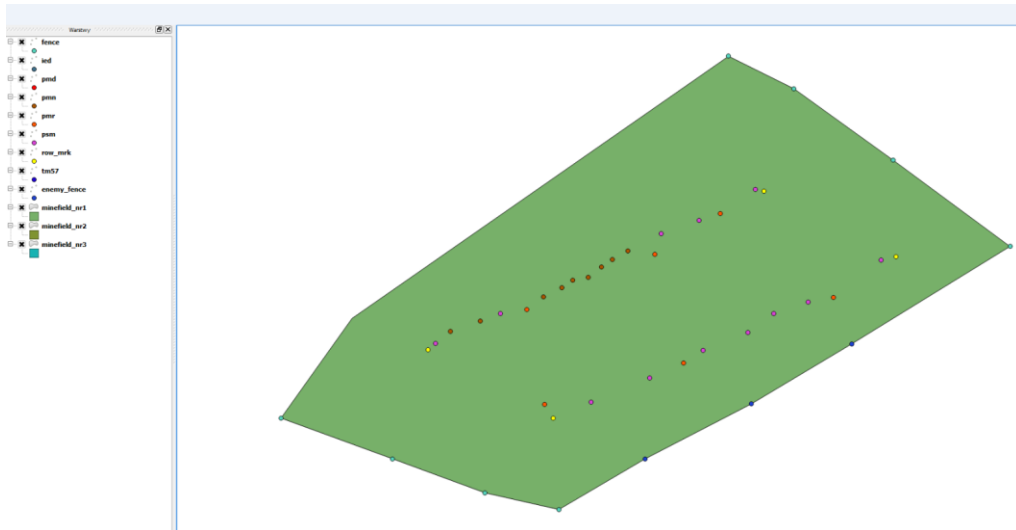


Figure D-5. Ground truth of landmine area.

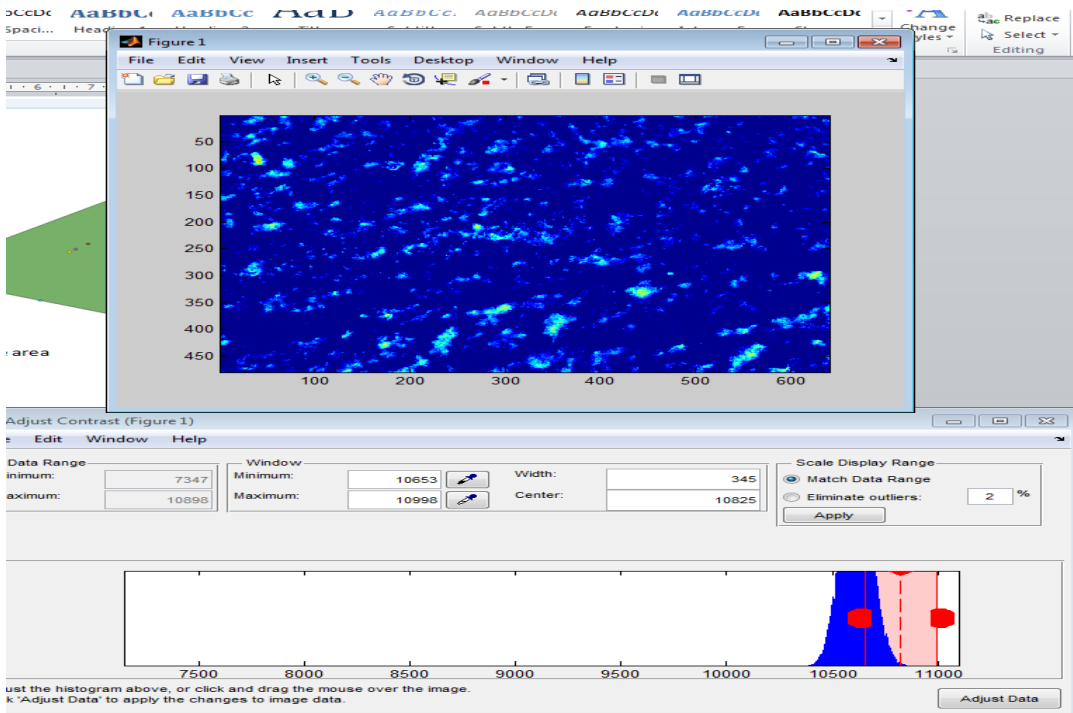


Figure D-6. Landmine area TIR image in MATLAB version with filter.

Two landmines in this area can be detected by using the high pass filter in the MATLAB file for the Poland March image.

## Appendix D: Metal Detector Image Re-build

The U-blox is used to open the GPR information. The altitude information is very strange, and it is quite difficult to understand why the altitude information changed in such a big range. This file is opened in the MATLAB, which demonstrates the same information.

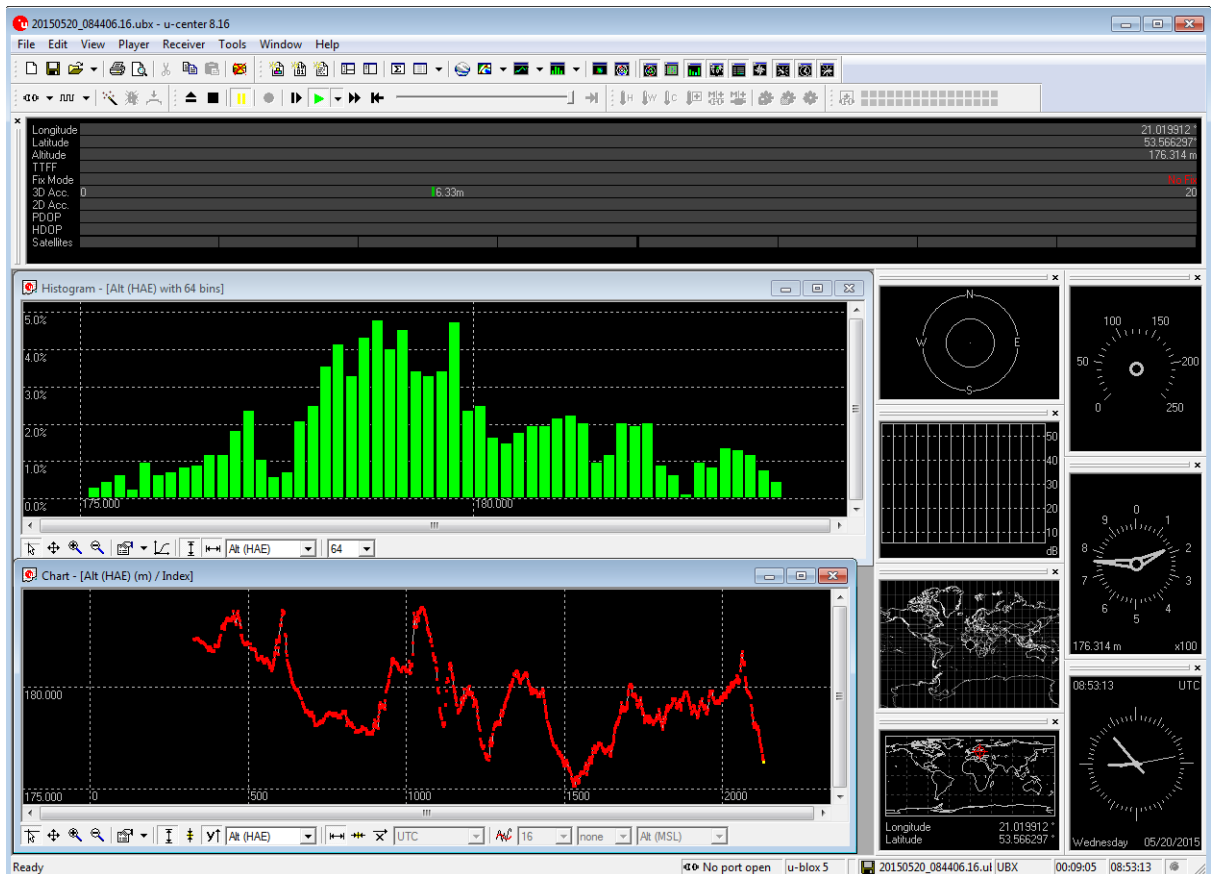


Figure E-1. U-blox version of MD altitude information.

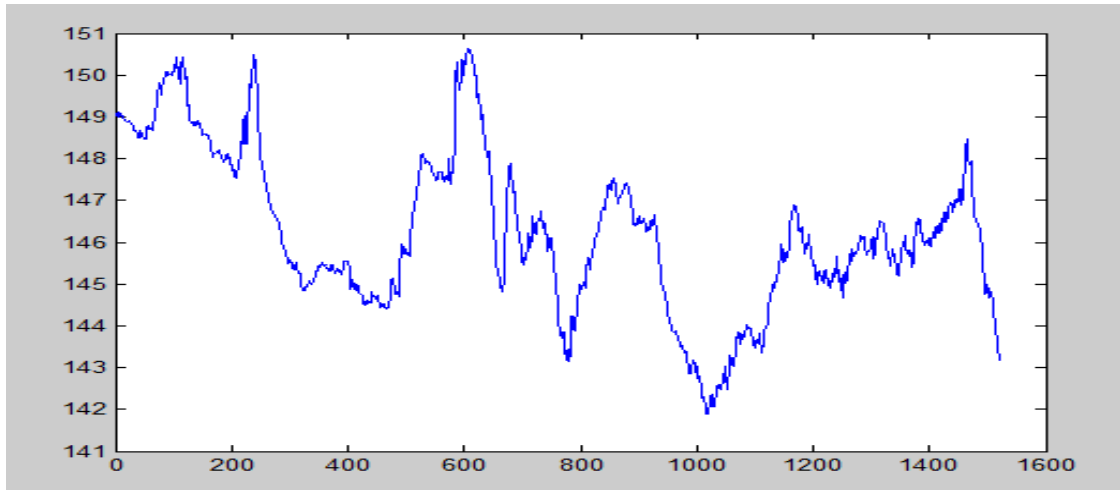


Figure E-2. MATLAB version of MD altitude information.

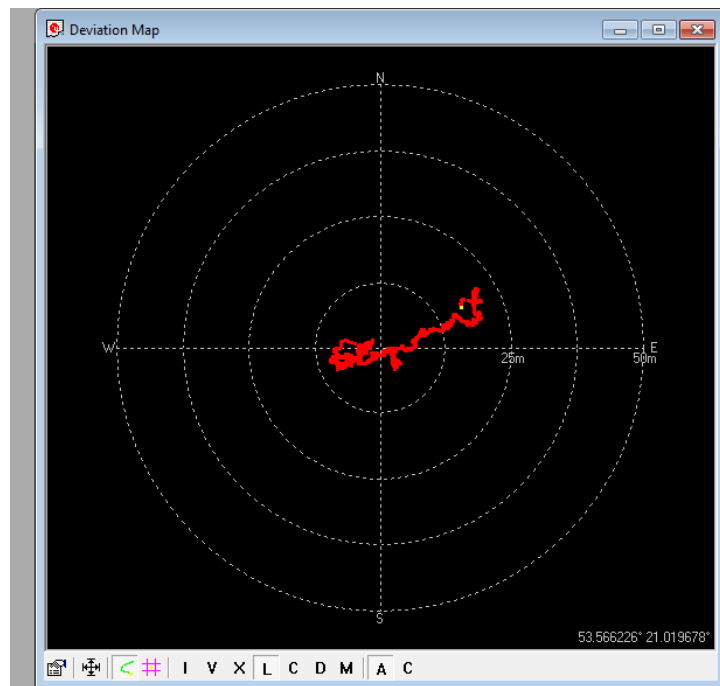


Figure E-3. U-blox version of the deviation map.

Figure E-3 shows the deviation map of the GPS information. The red line may be the route of the MD operator. This file is opened in MATLAB, shown in Figure E-4.

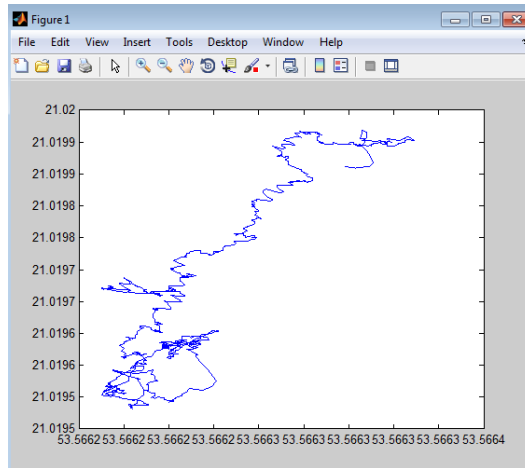


Figure E-4. MATLAB version for the route of MD operator.

## Appendix E: Re-built GPR Image

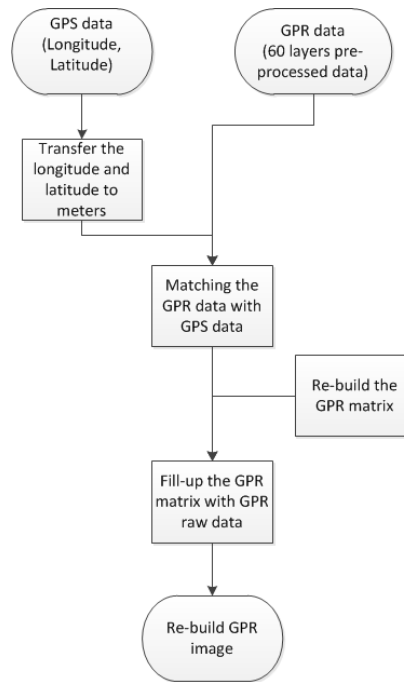


Figure F-1. Flow chart of the re-building GPR image.

The flow chart of the re-build GPR image is processed by using MATLAB.

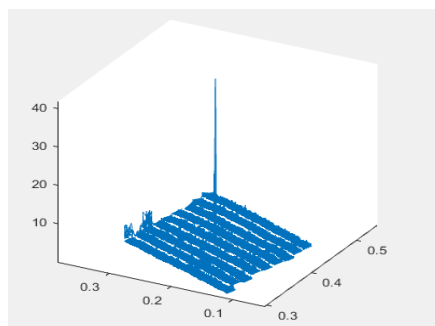


Figure F-2. Anti-tank mines in a desert area.

Re-building the desert area requires creating a same sized zeros matrix and putting the GPS data into the zeros matrix based on the relation of the GPS data. In the desert case,

the whole length of the signals is 176883; thereafter, the two sizes of the zeros matrix are created: 300\*300 and 500\*500. The plot in Figure F-2 shows the average of the signals of the sixty layers. In the centre of the plot are the anti-tank mines. The anti-personnel mines are not very clear in the plot, because the anti-tank signals have the largest reflection values.

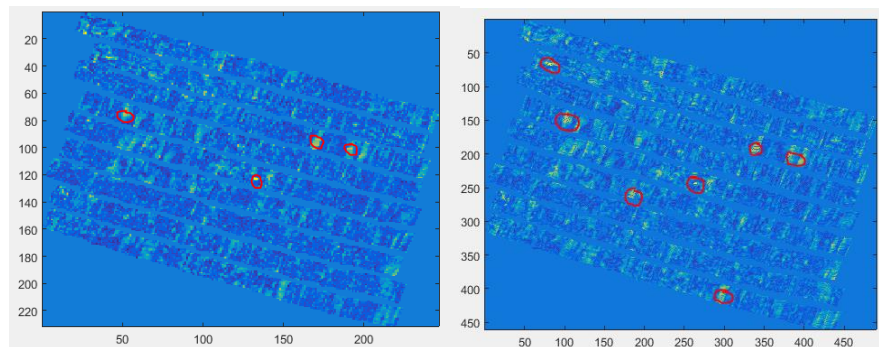


Figure F-3. 300\*300 matrix (left) and 500\*500 matrix (right) of the statistics algorithm result.

Figure F-3 shows how the 300\*300 and 500\*500 matrices represent the landmines after the statistics algorithm s processed. There is a higher resolution of in the 500\*500 matrix than 300\*300 matrix. Thus, more suspect landmines are found in the right image.

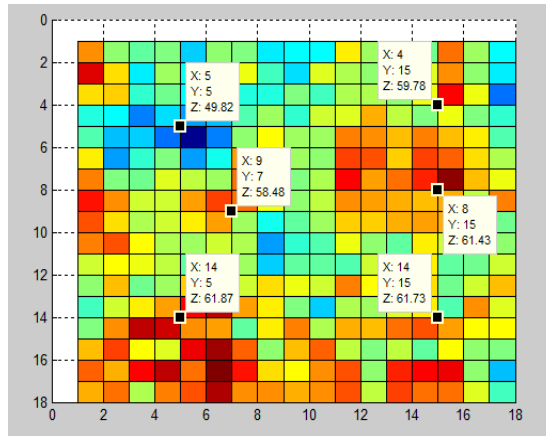


Figure F-4. GPR entropy map using the simple average method.

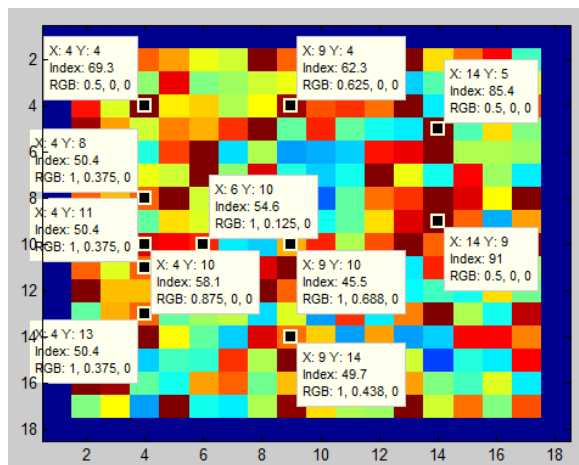


Figure F-5. GPR entropy map using the threshold value method.

Figures F-4 and F-5 show the entropy map built using the simple average method and the threshold value method. In the entropy map, dark red blocks represent the highest probability of landmine presence. Figures F-4 and F-5 demonstrate that most of the landmines can be identified based on the neighbourhood algorithm, compared to the ground truth map shown in Figure 4-5.

## Appendix F: GPS Location Analysis

The function of a GPS location is to transfer the longitude and latitude data into a coordinate system. The actual landmine location can be calculated by using the coordinate system. Data are shown by a .ubx file. The longitude and latitude data from the .ubx file can be extracted using the RTKlib software. However, the U-blox software was not usable (I contacted the radio lab system group but received no response.) Figure J-1 shows the attempt to convert the ubx file into a renix file with the correct file and the correct format.

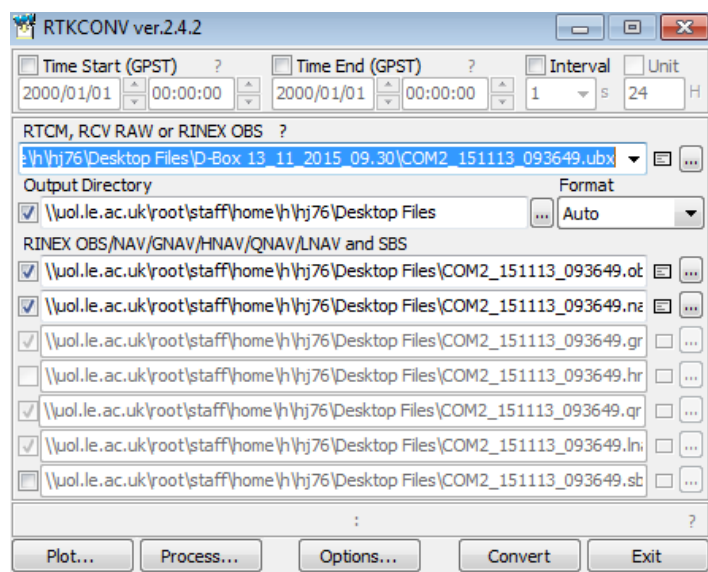


Figure J-1. Operation surface of the RTKCONV software.

The route map of the .ubx file is plotted and shown in Figure J-2:

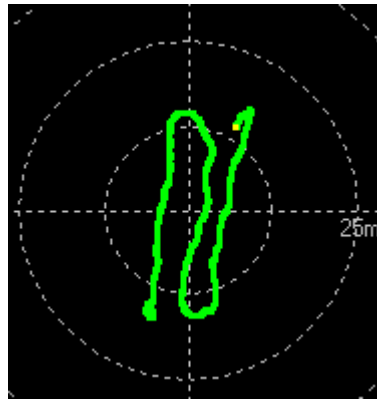


Figure J-2. GPS route of the Poland landmine area.

The yellow point represents the final point, and the start point of the robot is (14.121347,40.933097).

## Appendix G: Computational Complexity of Single-Sensor

### Detection Algorithms

Computational complexity aims to estimate the number of the computationally intensive operations, which is another important parameter of algorithm evaluation. An algorithm which has low computational complexity is easier to implement in resource-constrained, real-time embedded systems. Tables H-1 and H-2 show the results of a comparison of the computational complexity of the proposed algorithms in this thesis.

Consider a 3-D GPR image represented by a matrix  $M \times N \times L$ , where  $M$  and  $N$  are the number of rows and columns, respectively, and  $L$  is the layer of the GPR matrix (corresponding to a particular scanning frequency), the sub-unit size is  $m \times n$ , where  $M$  and  $N$  are multiples of  $m$  and  $n$ , respectively. The complexity for each algorithm is summarised in Table H-1, which shows the numbers of the main mathematical operations that are required for the algorithms' realisation.

Table H-1 shows that the entropy-average algorithm has the lowest complexity of all the algorithms, and that the edge-energy algorithm has the highest complexity. If we consider the GPR matrix size as  $(91 \times 91 \times 401)$ , and the sub-unit size as  $5 \times 5$ , then the operation numbers for all algorithms can be calculated, as shown in Table H-2.

The computational complexity analysis and evaluation demonstrates that all the proposed algorithms have lower computational complexity than the edge-energy method, meaning that the proposed algorithms have improved the processing time of

the landmine detection process, while keeping the detection quality at the same level as the edge energy-based algorithm.

Table H-1 Computational Complexity Analysis for Proposed Algorithm

Process name	ADD	SUB	MUL	DIV	Complex operation
Entropies-Average	$M \times N \times L + \left(\frac{M}{m} \times \frac{N}{n}\right) \times (m \times n - 1) \times L + M \times N \times (L - 1)$	0	$M \times N \times L$	$M \times N \times L + M \times N$	Log $2 \times M \times N \times L$
Entropies-thresholds	$M \times N \times L + \left(\frac{M}{m} \times \frac{N}{n}\right) \times (m \times n - 1) \times L + M \times N \times (L - 1)$	0	$M \times N \times L$	$M \times N \times L$	Log $2 \times M \times N \times L$ Comparing with Threshold Values: $\left(\frac{M}{m} \times \frac{N}{n}\right) \times L$
Statistics cross-comparing	$M \times N \times L \times 2 + M \times N \times (L - 1)$	$M \times N \times L + M \times N \times L$	0	$M \times N \times L$	Bit shift $M \times N \times (L - 1)$
Statistics self-comparing	$M \times N \times L \times 2 + M \times N \times (L - 1)$	$M \times N \times L + M \times N \times L \times 2 + M \times N$	0	$M \times N \times L$	Bit shift $3 \times M \times N \times (L - 1)$
GPR feature based algorithm (Bayesian fusion)	$M \times N \times L \times 2 + M \times N \times L$	$M \times N \times L \times 4$	$M \times N \times L \times 2$	$M \times N \times L$	Bit shift $4 \times M \times N \times L$
Edge energy	$2 \times M \times N \times L$	$2 \times M \times N \times L$	$18 \times M \times N \times L$	$(M + N) \times L + M \times N \times L$	0

Table H-2 Computational Complexity Analysis for Proposed Algorithm with the Public Domain GPR Image

Process name	ADD	SUB	MUL	DIV	Complex operation
Feature extraction method					
Entropies-Average	9751257	0	3320681	3328962	Log 6641362
Entropies-thresholds	9751257	0	3320681	3320681	Log 6641362 Comparing with Threshold Values: 129924
Statistics cross-comparing	9953762	6641362	0	3320681	Bit shift 3312400
Statistics self-comparing	9953762	9970324	0	3320681	Bit shift 9937200
GPR feature based algorithm (Bayesian fusion)	9962043	13282724	6641362	3320681	Bit shift 13282724
Edge energy	6641362	6641362	59772258	3393663	0

## Appendix H: Simulation of the IR Camera Image

Infrared cameras are commonly used to detect landmines. The operating principle of IR is based on measuring very small temperature differences [39]. Physically, there is a difference between characteristics of the heating and cooling time of the ground surface with and without buried objects. These phenomena can be utilised to obtain thermal maps of the ground surface [114], which can be found on the surface or close to the surface of the objects by using an IR camera. However, it takes a very long time for the IR image to collect the sample data. In this case, the simulation IR image is used to achieve the landmine dangerous map to build work. The simulation principle is based on a high-energy object which has higher signals than a small object. The simulation image is shown in Figure C-1.

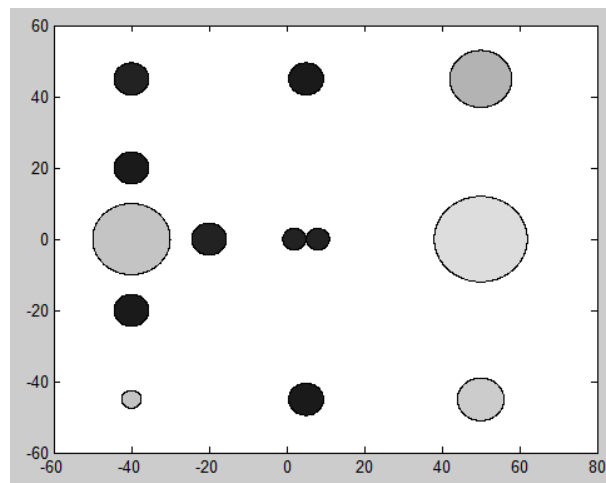


Figure C-1. Simulation IR camera's landmine map.

## Appendix I: The Metal Detector Data Analysis

Metal detector data include time data and two different channels of MD data. The normal value of the metal detector is 0X3E00, which is 16191 in decimal. When the metal object is detected by MD, one of the channels will start to reduce the value from

16191 to 0. Therefore, a value going down from high to low at any time anywhere means that there is something made of metal that is detected by the MD. Figure 8-19 shows the result of metal detector detection in a sandbox environment.

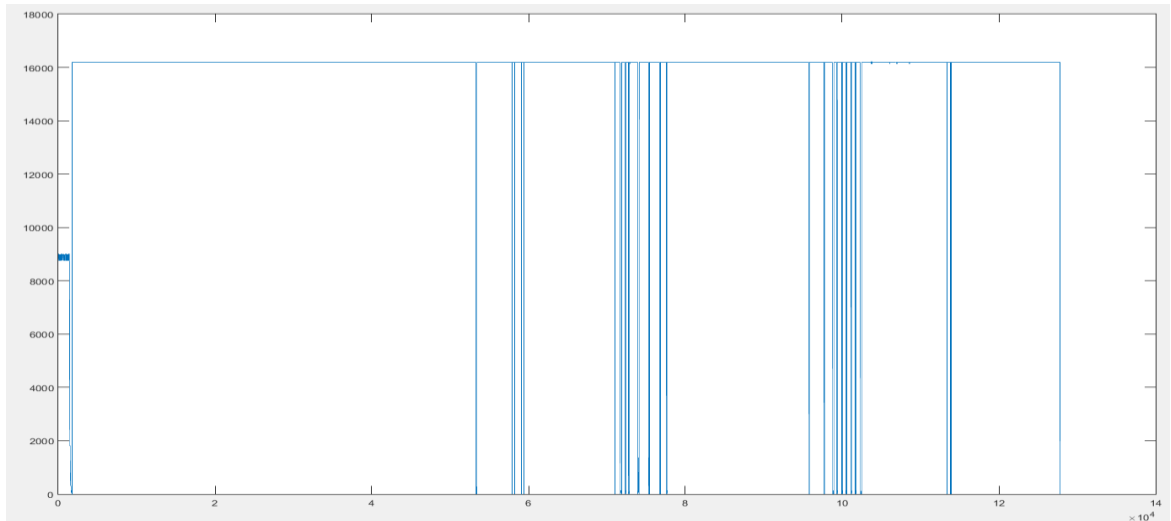


Figure G-1. Robot-based MD detection result from Naples.

There are 127811 samples in this vector. The top part in Figure G-1 is the metal-detecting robot, not an actual landmine. In FigureG-1, the metal detector found around 11 objects made of metal. Although most things were AP landmines, some signals were generated by other metal items.

The time stamps are used to match the GPS signals with metal detector data, which could identify the location of the landmines.

## **Appendix J: Data Fusion Models Review**

Data fusion technology has been used in many applications in both the Department of Defense (DOD) area and non-DOD areas [28]. The DOD applications include automated target recognition (for smart weapons), guidance for autonomous vehicles,

remote sensing, and battlefield surveillance. These kinds of application often need more than one entity to fulfil their functions. For example, Figure K-1 shows how data fusion technology used in battlefield surveillance is combined with different information from other entities, such as aeroplanes or ships [115]. The non-DOD data fusion applications include the monitoring of complex machinery, medical diagnosis, smart buildings, and landmine area clearing. Non-DOD applications are characterised as having a low-cost and high-performance data fusion system, whereby all sensors typically integrate into one entity. Research into explosive detection systems seek an intelligence data fusion system that is low cost and has high-integration performance [116].

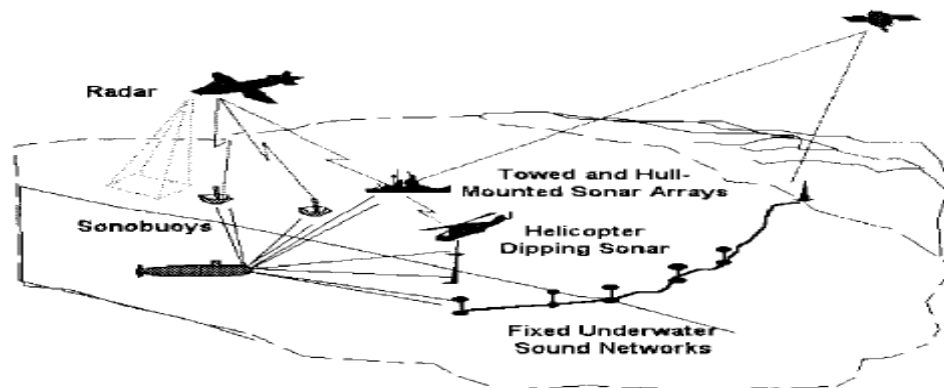


Figure K-1. Multisensory ocean surveillance [28].

A data fusion technique is defined as fusing data from different sensors by setting an algorithm to output an expected representation [107]. However, many definitions for data fusion exist, with different organisations and publishers having their own depending on their particular research area.

For instance, Pohl and Van Genderen [117] claimed that ‘image fusion is the combination of two or more different images to form a new image by using a certain

algorithm'. This definition is focused on image fusion, a subtopic of data fusion, and the key words of this sentence are 'combination', 'image', and 'certain algorithm' [115]. This definition is a little too narrow to apply to a landmine detection system. Mangolini defined data fusion as a 'set of methods, tools, and means using data coming from various sources of a different nature, in order to increase the quality of the requested information' [118]. Although this definition covers most of the research area, 'tools' are not usually present in the robot system, making the definition too general to be applicable. Hall and Llinas also published a definition for data fusion: 'Data fusion techniques combine data from multiple sensors and related information from associated databases, to achieve improved accuracy and more specific inferences that could be achieved by the use of a single sensor alone' [118, 119]. Despite this definition being more suitable for the robot system, the term 'combine' is not appropriate, as the data fusion system needs to be capable of selecting several relevant sensors to carry out a fusion process. The 'output' part of Hall and Llinas's definition focuses on accurate results and inferences, which is more applicable. As such, data fusion for an EOD system can be defined as a framework that inputs data from various sensors, processing units, and associated databases before processing the input through a fixed algorithm or selection rules to either create a set of data more informative than the original or to make a decision.

The main issues in building a data fusion system could be summarised in seven parts: architecture, algorithm, effect, accuracy, optimisation, environment and conditions. The term 'architecture' describes the structure of the fusion system, which normally includes the Joint Directors of Laboratories (JDL) [120], the National Bureau of Standards (NBS) [121], and constraint-based sensor fusion architecture. Suitable fusion architecture can reduce system redundancy and unnecessary variable headers.

The term ‘algorithm’ includes the necessary calculation steps, as well as the selection or evaluation rules. An intelligent EOD system needs to integrate more than one algorithm, which can consequently provide more informative fusion. The terms ‘effect’, ‘accuracy’ and ‘optimisation’ refer to the working performance of the fusion system, focusing on how individual sensor data are processed to extract the maximum amount of information, the degree of accuracy obtainable using data fusion technology, and how the fusion process can be optimised in real systems. ‘Environment’ and ‘condition’ determine the situation in which the data fusion system can be used.

The complexity of the data fusion system is determined by data fusion system architecture. A suitable architecture can save a lot of unnecessary memory and power. Fundamentally, the fusion nodes may be arranged in three different ways (topologies), or architectures: centralised, decentralised and hierarchical [6]:

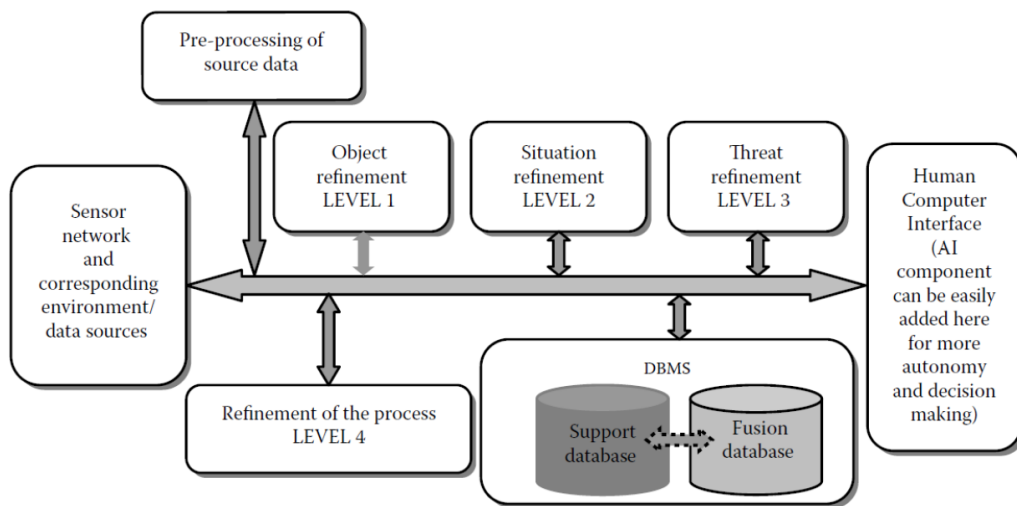
- In a centralised system, the sensor fusion unit is treated as a central processor or node that collects all information from the different sensors. All decisions are made at this node, and instructions or task assignments are given out to the respective sensors.
- In a decentralised system, the sensor measurements—or information—are fused locally using a set of local fusion nodes rather than by using a single central fusion node. The main advantage of decentralised architecture is the lack of sensitivity regarding the correct alignment of the sensors.

Hybrid architecture can be taught as a design, in which the centralised and decentralised systems are mixed together. The hierarchical architecture combines the advantages of the centralised and decentralised architectures without some of their

disadvantages. For example, the performance of the hierarchical architecture is relatively insensitive to any errors in the correct alignment of the sensors.

Data fusion models represent a system view of data fusion activity. The Joint Directors of Laboratories (JDL) fusion model, originating from the US Department of Defence, has become very popular. The JDL model comprises four levels of data processing and a database as shown in Figure K-2. These levels are interconnected by a common bus and can be executed concurrently [122].

This classic data fusion model was developed by the JDL data fusion working group, established in 1986. The JDL data fusion architecture is a functionally oriented model [123] and a two-layer hierarchy system. The input of this model is usually at the post detection, extracted parameter level of signal processing. The output is a minimally ambiguous identification and characterisation of the target entities. This system can be considered as a data-in-decision-out system.



FigureK-2. The top layer of JDL model [122].

In fact, the JDL fusion model has six levels. The pre-processing of the source data could be considered as level 0, whilst the human computer interface as level 5. The explanation of each level is outlined as follows:

The source of information comes from data collected from corresponding local sensors or other databases such as reference information. This input can be at the data, feature, or decision level.

In Level 0, the data carry out the pre-processing, ensuring that the sensory array fits the processing array. In addition, this step forces the data most pertinent to the current situation to turn on.

In Level 1, Processing (object refinement), the basic function of level 1 is to transform sensor data into a consistent set of units, refine and extend the estimated time of an object's position, and identity or classify the data from the relevant entity.

Level 2, Processing (situation refinement), focuses on the relationship between objects and observed events depending on the environment. Moreover, this level uses the data and analyses the situation of level 1, targeting the outside environment. This is in the feature level.

Level 3, Processing (threat refinement), derives from the information of the previous level, processing the current situation of objects into the future to draw inferences regarding potential threats. Decisions made at this level ultimately decide future trends.

Level 4, Processing (process refinement), seeks to detect current performance to provide information about real-time control. In addition, this level finds and improves upon unreliable information as well as allocates and directs the sources to achieve mission goals.

Level 5, human-computer interface, offers possibility refinement and improvement by human experts, allowing humans to make decisions.

The JDL model is suitable for most data fusion systems. This hierarchical model ensures that the fused data are reliable in each level of the system and that uncertain

signals are filtered in the pre-processing level [124]. Furthermore, this model is easy to understand and achieve. However, the drawback of this system is that it is necessary for the data to be transmitted from different levels, which may lead to variables becoming redundant and data being distorted. As the data fusion centre of the JDL model is always in the higher level, it is difficult for the data fusion process to meet real-time requirements.

Architecture from the National Bureau of Standards [121] is another classic data fusion structure often used in robotic systems [125]. The main principle of this architecture is the division of whole tasks into smaller, more achievable tasks. When compared with the JDL model, the NBS model is more focused on information interaction in the same levels. Figure K-3 shows the structure of the NBS module.

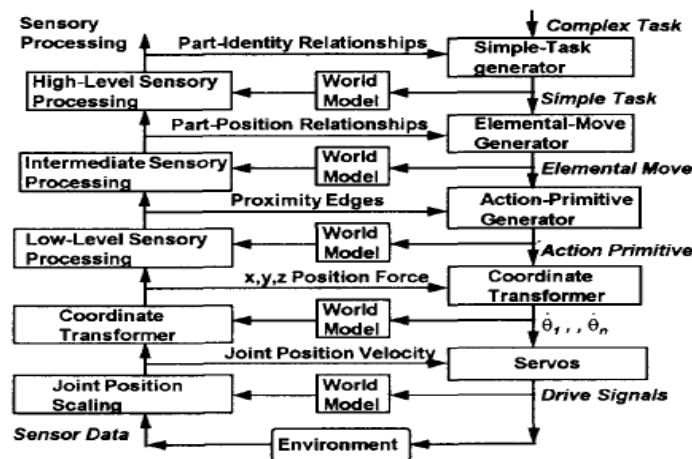


Figure K-3. NBS hierarchy model [19].

The graph shows how NBS data fusion architecture deals with a complex set of tasks. Specifically, environmental sensory data are collected from the environment and passed through a series of processes before reaching the fusion centre. The fusion centre makes the decisions and divides the complex tasks into many simple tasks, which use the corresponding register and generator to prepare relevant action. Only once this process has reached its conclusion can the complex task be achieved. The

feature of the NBS model is that data from different levels share their information using the world model [126]. The architecture thus allows decisions to be made without authorisation from the fusion centre.

The world model is used to ascend sensory processing as well as to assign or control tasks in the lower level. The world model achieves deviation detection from the low-level sensor data, which also helps it make decisions at the high level [121]. The NBS model is suitable for EOD systems, as it provides more reliable data and decisions during the fusion processing. In addition, the NBS model is capable of meeting the real-time requirements, as the world model can make decisions without the higher-level command in most situations. However, the system architecture is a little too complex.

## Appendix K: MsMs Landmine Detection Sensor Analysis

The MsMs database includes several types of landmine detection sensors, including metal detector, GPR array, GPR, thermal camera, magnetometer, microwave, and SLDV.

The metal detector is used to detect metal objects in a test area. The performance of the metal detector is shown in Figure I-1. The centre of the object contains a blue colour in the left and red colour in the right.

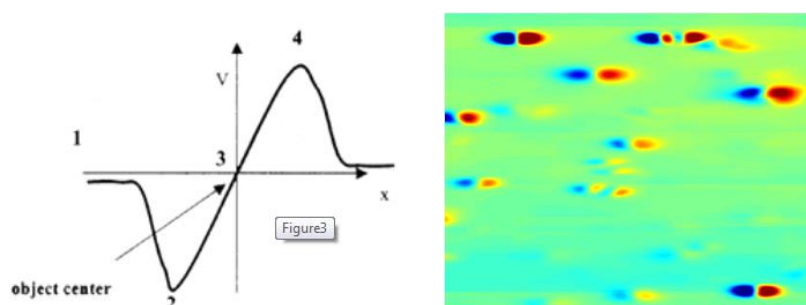


Figure I-1. CW metal detector data.

Data fusion in the image level can be achieved as the data of the metal detector are geo-referenced data. The environment sensor is mainly used for recording weather conditions in the test area. Environmental data include the soil moisture data and soil temperature data. These types of data can be used for learning how the environment influences landmine detection sensors. Environmental information and soil information must be compared in the future.

FGAN GPR data, given by a uncommon file, is also used in the MsMs database. However, the file is not able to be read.

The GPR01 may be the full data for the ERA GPR array. This database includes most of the test area and should be fused with metal data. Infrared data are also available in the MsMs database. This type of data should be fused with the MD and GPR data.

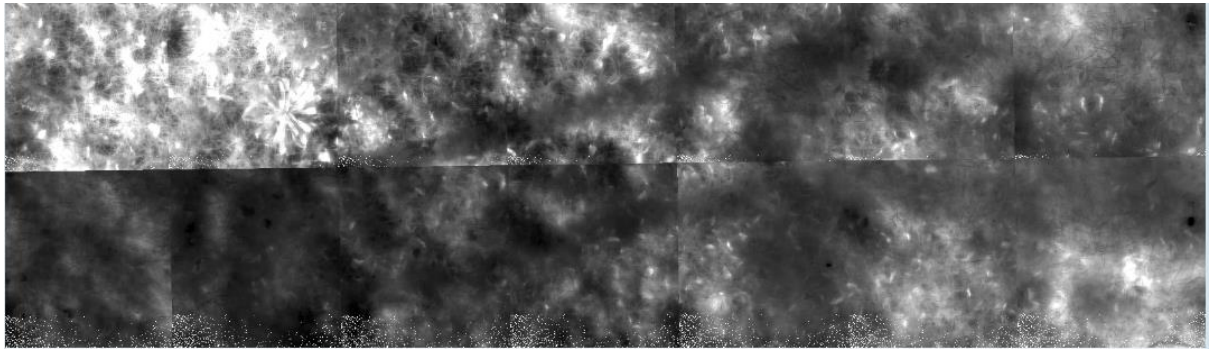


Figure I-1. Infrared camera output of MsMs dataset.

The principle of the magnetometer is almost the same as the metal detector and can be used to detect low-metal mines. The data fusion algorithms of the feature level or decision level are used to fuse the magnetometer with the metal detector. Figure 8-22 shows a sample image of the magnetometer.

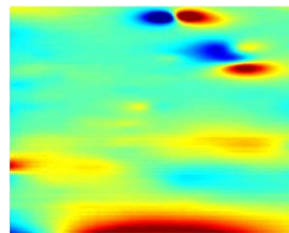


Figure I-3. Magnetometer output in the MsMs dataset.

The working principle of a microwave sensor is similar to the GPR. A landmine buried under ground can be detected by microwave sensors. The MsMs database contains several images for the microwave sensor, used to achieve feature-level fusion. The

database also contains the raw data for the microwave sensor. However, it is hard to read; it is better to use the microwave sensor for feature-level fusion only.

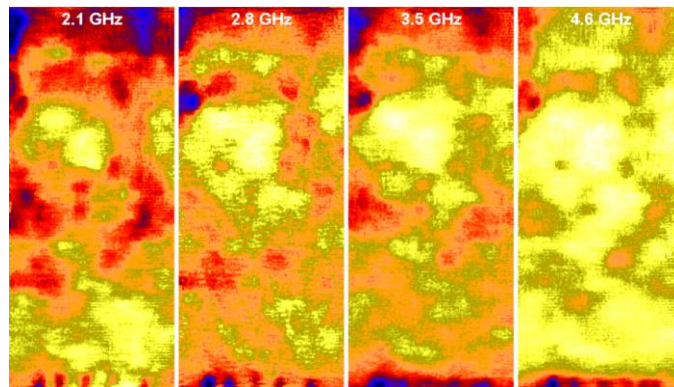


Figure I-4. Scanning Laser Doppler Vibrometry Sensor of MsMs dataset.

A Scanning Laser Doppler Vibrometry Sensor (SLDV) is also included in the MsMs database, saved in a .mat file format. The SLDV data are much clearer than the GPR data. The feature-level data fusion algorithm is also necessary to be applied on the SLDV image.

## References

1. MacDonald, J., et al., *Alternatives for landmine detection*. 2003, DTIC Document.
2. Hussein, E.M. and E.J. Waller, *Landmine detection: the problem and the challenge*. *Applied Radiation and Isotopes*, 2000. 53(4): p. 557-563.
3. Schubert, H. and A. Kuznetsov, *Detection and disposal of improvised explosives*. Vol. 6. 2006: Springer.
4. Jing, H. and T. Vladimirova. *Image Fusion for an EOD Robot Wireless Visual Module*. in *2013 Fourth International Conference on Emerging Security Technologies*. 2013. IEEE.
5. Marc, A. and Y. Yann, *Mine suspected Area Reduction Using Aerial and Satellite Images*.
6. Yvinec, Y. and A. Renaissance. *A validated method to help area reduction in mine action with remote sensing data*. in *Proc. of the 4th International Symposium on Image and Signal Processing and Analysis (ISPA 2005)*, Zagreb, Croatia. 2005.
7. Bennett, D., et al. *Generation and Fusion of Landmine Detection Intensity Maps using a Three Stage Algorithm*. in *14th IARP Workshop on Humanitarian Demining and Risky Intervention*. 2016. Beograd, Croatia.
8. Malof, J.M., et al., *A Probabilistic Model for Designing Multimodality Landmine Detection Systems to Improve Rates of Advance*. *IEEE Transactions on Geoscience and Remote Sensing*, 2016. 54(9): p. 5258-5270.

9. Milisavljevic, N., I. Bloch, and M. Acheroy, *Multi-sensor data fusion based on belief functions and possibility theory: Close range antipersonnel mine detection and remote sensing mined area reduction*. Humanitarian Demining: Innovative Solutions and the Challenge of Technology, MK Habib Ed, 2008: p. 392-418.
10. Schutte, K., et al. *ARC: A camcopter based mine field detection system*. in *Presented at the Fifth International Airborne Remote Sensing Conference*. 2001. Citeseer.
11. Singh, S., *Sensors—An effective approach for the detection of explosives*. *Journal of hazardous materials*, 2007. 144(1-2): p. 15-28.
12. Almeida, G.T.B., *Development and implementation of multi-sensor data fusion algorithms for landmine detection*. 2015.
13. Gonzalez-Huici, M., I. Catapano, and F. Soldovieri, *A comparative study of GPR reconstruction approaches for landmine detection*. 2014.
14. Harding, G., *X-ray scatter tomography for explosives detection*. *Radiation Physics and Chemistry*, 2004. 71(3): p. 869-881.
15. Khanna, S.M., et al., *Landmine detector with a high-power microwave illuminator and an infrared detector*. 2002, Google Patents.
16. Yvinec, Y., et al. *SMART: Space and Airborne Mined Area Reduction Tools—Presentation*. in *Proc. of EUDEM2-SCOT-2003 International Conference on requirements and Technologies for the Detection, Removal and neutralization of Landmines and UXO-Vrije Universiteit Brussel*. 2003.
17. Bielecki, Z., et al., *Sensors and systems for the detection of explosive devices—an overview*. 2012.

18. Gader, P.D., M. Mystkowski, and Y. Zhao, *Landmine detection with ground penetrating radar using hidden Markov models*. Geoscience and Remote Sensing, IEEE Transactions on, 2001. 39(6): p. 1231-1244.
19. Ho, K., et al., *Discrimination mode processing for EMI and GPR sensors for hand-held land mine detection*. Geoscience and Remote Sensing, IEEE Transactions on, 2004. 42(1): p. 249-263.
20. Ho, K. and P.D. Gader, *A linear prediction land mine detection algorithm for hand held ground penetrating radar*. Geoscience and Remote Sensing, IEEE Transactions on, 2002. 40(6): p. 1374-1384.
21. Nuzzo, L., et al. *A new densely-sampled Ground Penetrating Radar array for landmine detection*. in *Ground Penetrating Radar (GPR), 2014 15th International Conference on*. 2014. IEEE.
22. Nguyen, M.K., J.M. Lewis, and M.S. Korman, *Modeling acoustic landmine detection using a soil-plate oscillator*. The Journal of the Acoustical Society of America, 2016. 139(4): p. 2094-2094.
23. Masarik, M.P., et al. *Enhanced buried UXO detection via GPR/EMI data fusion*. in *SPIE Defense+ Security*. 2016. International Society for Optics and Photonics.
24. Steinway, W.J., et al. *Multi-sensor system for mine detection*. in *Geoscience and Remote Sensing Symposium Proceedings, 1998. IGARSS'98. 1998 IEEE International*. 1998. IEEE.
25. Lameri, S., et al. *Landmine detection from GPR data using convolutional neural networks*. in *Signal Processing Conference (EUSIPCO), 2017 25th European*. 2017. IEEE.

26. Liggins II, M., D. Hall, and J. Llinas, *Handbook of multisensor data fusion: theory and practice*. 2017: CRC press.
27. Zhai, X., H. Jing, and T. Vladimirova. *Multi-sensor data fusion in Wireless Sensor Networks for Planetary Exploration*. in *Adaptive Hardware and Systems (AHS), 2014 NASA/ESA Conference on*. 2014. IEEE.
28. Hall, D.L. and J. Llinas, *An introduction to multisensor data fusion*. Proceedings of the IEEE, 1997. 85(1): p. 6-23.
29. Ferrari, S. and A. Vaghi, *Demining sensor modeling and feature-level fusion by Bayesian networks*. Sensors Journal, IEEE, 2006. 6(2): p. 471-483.
30. Dempster, A.P., *A generalization of Bayesian inference*. Journal of the Royal Statistical Society. Series B (Methodological), 1968: p. 205-247.
31. Shafer, G., *A mathematical theory of evidence*. Vol. 1. 1976: Princeton university press Princeton.
32. Abdelgawad, A. and M. Bayoumi, *Resource-Aware data fusion algorithms for wireless sensor networks*. 2012: Springer.
33. Gupta, I., D. Riordan, and S. Sampalli. *Cluster-head election using fuzzy logic for wireless sensor networks*. in *Communication Networks and Services Research Conference, 2005. Proceedings of the 3rd Annual*. 2005. IEEE.
34. Kacelenga, R., D. Erickson, and D. Palmer. *Voting fusion adaptation for landmine detection*. in *Information Fusion, 2002. Proceedings of the Fifth International Conference on*. 2002. IEEE.
35. Kacelenga, R., D. Erickson, and D. Palmer, *Voting fusion adaptation for landmine detection*. IEEE aerospace and electronic systems magazine, 2003. 18(8): p. 13-19.

36. Santana, P., et al. *A multi-robot system for landmine detection*. in *Emerging Technologies and Factory Automation*, 2005. *ETFA 2005. 10th IEEE Conference on*. 2005. IEEE.
37. Cremer, F., E. den Breejen, and K. Schutte. *Sensor data fusion for anti-personnel land-mine detection*. in *Proceedings of the International Conference on Data Fusion (EuroFusion98)*. 1998. Citeseer.
38. McFee, J.E., et al. *Multisensor vehicle-mounted teleoperated mine detector with data fusion*. in *Aerospace/Defense Sensing and Controls*. 1998. International Society for Optics and Photonics.
39. Susek, W., *Thermal microwave radiation for subsurface absolute temperature measurement*. *Acta Physica Polonica-Series A General Physics*, 2010. 118(6): p. 1246.
40. Koscho, M.E., R.H. Grubbs, and N.S. Lewis, *Properties of vapor detector arrays formed through plasticization of carbon black-organic polymer composites*. *Analytical chemistry*, 2002. 74(6): p. 1307-1315.
41. Daniels, D.J., *Ground penetrating radar*. Vol. 1. 2004: Iet.
42. ; Available from: <http://www.cytterra.com/products/anpss14.htm>.
43. Gader, P.D., et al., *Fuzzy logic detection of landmines with ground penetrating radar*. *Signal Processing*, 2000. 80(6): p. 1069-1084.
44. Lewis, A.M., et al., *Multisensor Mine Signatures Final Report*. 2004 july.
45. Sahli, H., et al., *Remote Sensing Minefield Area Reduction: Semantic Knowledge-based Image Understanding*". *Proceedings of ESA-EUSC 2004: Theory and Applications of Knowledge driven Image Information Mining, with focus on Earth Observation*, 2004: p. 17-18.
46. ARC, *ARC Final Public Report*.

47. Counts, T., et al., *Multistatic ground-penetrating radar experiments*. Geoscience and Remote Sensing, IEEE Transactions on, 2007. 45(8): p. 2544-2553.
48. Maathuis, B. and J.v. Genderen, *A review of satellite and airborne sensors for remote sensing based detection of minefields and landmines*. International Journal of Remote Sensing, 2004. 25(23): p. 5201-5245.
49. Duston, B.M. and C. Chatterjee. *Multisensor combination for vehicle-based mine detection*. in *Signal Processing, Sensor Fusion, and Target Recognition VII*. 1998. International Society for Optics and Photonics.
50. SMART, *SMART Public Report*.
51. Cremer, F., et al., *A comparison of decision-level sensor-fusion methods for anti-personnel landmine detection*. Information fusion, 2001. 2(3): p. 187-208.
52. Almeida, G.T.B., *Development and implementation of multi-sensor data fusion algorithms for landmine detection*. 2005.
53. Cremer, F., et al. *Comparison of vehicle-mounted forward-looking polarimetric infrared and downward-looking infrared sensors for landmine detection*. in *AeroSense 2003*. 2003. International Society for Optics and Photonics.
54. van der Mark, W., et al. *Camera-based platform and sensor motion tracking for data fusion in a landmine detection system*. in *AeroSense 2003*. 2003. International Society for Optics and Photonics.
55. Gader, P.D., J.M. Keller, and B.N. Nelson, *Recognition technology for the detection of buried land mines*. Fuzzy Systems, IEEE Transactions on, 2001. 9(1): p. 31-43.

56. Smock, B., J. Wilson, and M. Milner. *Improved landmine detection through context-dependent score calibration*. in *SPIE Defense+ Security*. 2016. International Society for Optics and Photonics.
57. F. Curatella, P.V., G. Rizzo, T. Vladimirova, L. De Vendictis, T. Emter, J. Petereit, C. Frey, D. Usher, I. Stanciugelu, J. Schaefer, E. den Breejen, L. Gisslén, D. Letalick. , *Towards a Multifaceted Platform for Humanitarian Demining*, in *13th IARP Workshop on Humanitarian Demining and Risky Intervention*. 27-28 April 2015: Beograd, Croatia.
58. Esmiller, B., et al., *FP7 Integration Project D-Box (“Comprehensive Toolbox for Humanitarian Clearing of Large Civil Areas from Anti-Personal Landmines and Cluster Munitions”)*. 2013.
59. Bruschini, C. and B. Gros, *A survey of research on sensor technology for landmine detection*. *Journal of Conventional Weapons Destruction*, 2016. 2(1): p. 3.
60. Frigui, H. and P. Gader, *Detection and discrimination of land mines in ground-penetrating radar based on edge histogram descriptors and a possibilistic-nearest neighbor classifier*. *Fuzzy Systems, IEEE Transactions on*, 2009. 17(1): p. 185-199.
61. Yuksel, S.E. and P.D. Gader, *Context-based classification via mixture of hidden Markov model experts with applications in landmine detection*. *IET Computer Vision*, 2016. 10(8): p. 873-883.
62. Ho, K., et al., *An investigation of using the spectral characteristics from ground penetrating radar for landmine/clutter discrimination*. *IEEE transactions on Geoscience and Remote Sensing*, 2008. 46(4): p. 1177-1191.

63. Giannakis, I., A. Giannopoulos, and A. Yarovoy, *Model-Based Evaluation of Signal-to-Clutter Ratio for Landmine Detection Using Ground-Penetrating Radar*. IEEE Transactions on Geoscience and Remote Sensing, 2016. 54(6): p. 3564-3573.
64. Frigui, H. and P. Gader, *Detection and discrimination of land mines in ground-penetrating radar based on edge histogram descriptors and a possibilistic  $k$ -nearest neighbor classifier*. IEEE Transactions on Fuzzy Systems, 2009. 17(1): p. 185-199.
65. Torrione, P. and L.M. Collins, *Texture features for antitank landmine detection using ground penetrating radar*. IEEE Transactions on geoscience and remote sensing, 2007. 45(7): p. 2374-2382.
66. Wang, R. and L. Du, *Infrared and visible image fusion based on random projection and sparse representation*. International Journal of Remote Sensing, 2014. 35(5): p. 1640-1652.
67. Zou, H., et al., *Multimodal Remote Sensing Data Fusion via Coherent Point Set Analysis*. 2013.
68. Marcello, J., A. Medina, and F. Eugenio, *Evaluation of Spatial and Spectral Effectiveness of Pixel-Level Fusion Techniques*. 2013.
69. Russ, J.C., *The image processing handbook*. 2006: CRC press.
70. Xia, Y., H. Leung, and E. Bossé, *Neural data fusion algorithms based on a linearly constrained least square method*. Neural Networks, IEEE Transactions on, 2002. 13(2): p. 320-329.
71. Petrou, M. and C. Petrou, *Image processing: the fundamentals*. 2010: Wiley.com.

72. Modersitzki, J., *Numerical Methods for Image Registration (Numerical Mathematics and Scientific Computation)*. 2004: Oxford university press USA.
73. Kenneth, R., *Castleman, Digital image processing*. 1996, Prentice Hall Press, Upper Saddle River, NJ.
74. Haykin, S. and K.R. Liu, *Handbook on array processing and sensor networks*. Vol. 63. 2010: John Wiley & Sons.
75. Lavanya, A., et al. *Image fusion of the multi-sensor lunar image data using wavelet combined transformation*. in *Recent Trends in Information Technology (ICRTIT), 2011 International Conference on*. 2011. IEEE.
76. Wu, H. and Y. Xing. *Pixel-based image fusion using wavelet transform for SPOT and ETM+ image*. in *Progress in Informatics and Computing (PIC), 2010 IEEE International Conference on*. 2010. IEEE.
77. Arbelaez, P., et al., *Contour detection and hierarchical image segmentation*. *Pattern Analysis and Machine Intelligence, IEEE Transactions on*, 2011. 33(5): p. 898-916.
78. Lightstone, M., E. Majani, and S.K. Mitra, *Low bit-rate design considerations for wavelet-based image coding*. *Multidimensional systems and signal processing*, 1997. 8(1-2): p. 111-128.
79. Patil, U. and U. Mudengudi. *Image fusion using hierarchical PCA*. in *Image Information Processing (ICIIP), 2011 International Conference on*. 2011. IEEE.
80. Chibani, Y. and A. Houacine, *The joint use of IHS transform and redundant wavelet decomposition for fusing multispectral and panchromatic images*. *International Journal of Remote Sensing*, 2002. 23(18): p. 3821-3833.

81. Alparone, L., et al. *Fusion of multispectral and SAR images by intensity modulation*. in *Proc. 7th Int'l Conf. Information Fusion (Fusion 2004)*. 2004.
82. Kano, M. and Y. Nakagawa, *Data-based process monitoring, process control, and quality improvement: Recent developments and applications in steel industry*. *Computers & Chemical Engineering*, 2008. 32(1): p. 12-24.
83. Malviya, A. and S. Bhirud. *Multi-focus image fusion of digital images*. in *Advances in Recent Technologies in Communication and Computing*, 2009. *ARTCom'09. International Conference on*. 2009. IEEE.
84. Li, H., B. Manjunath, and S.K. Mitra, *Multisensor image fusion using the wavelet transform*. *Graphical models and image processing*, 1995. 57(3): p. 235-245.
85. Mallat, S.G., *Multifrequency channel decompositions of images and wavelet models*. *Acoustics, Speech and Signal Processing, IEEE Transactions on*, 1989. 37(12): p. 2091-2110.
86. Dong, Z., et al., *SPOT5 Multi-spectral (MS) and Panchromatic (PAN) Image Fusion Using an Improved Wavelet Method Based on Local Algorithm*. *Computers & Geosciences*, 2013.
87. Santos, M., et al., *A new wavelets image fusion strategy*, in *Pattern Recognition and Image Analysis*. 2003, Springer. p. 919-926.
88. Chen, D.-k. and K. Wang. *Second fusion algorithm of satellite images by à trous-Curvelet transform*. in *Signal Processing*, 2008. *ICSP 2008. 9th International Conference on*. 2008. IEEE.
89. Yan, W., L. Ming, and L. Guisheng. *Image fusion by means of à trous discrete wavelet decomposition*. in *Control, Automation, Robotics and Vision Conference*, 2004. *ICARCV 2004 8th*. 2004. IEEE.

90. Hong, L., K. Yang, and X. Pan. *Multispectral and Panchromatic Image Fusion Based on Genetic Algorithm and Data Assimilation*. in *Image and Data Fusion (ISIDF), 2011 International Symposium on*. 2011. IEEE.
91. Ranchin, T. and L. Wald, *Fusion of high spatial and spectral resolution images: the ARSIS concept and its implementation*. *Photogrammetric Engineering & Remote Sensing*, 2000. 66(1): p. 49-61.
92. Yang, L., B. Guo, and W. Ni, *Multimodality medical image fusion based on multiscale geometric analysis of contourlet transform*. *Neurocomputing*, 2008. 72(1): p. 203-211.
93. Li, S. and B. Yang, *Hybrid multiresolution method for multisensor multimodal image fusion*. *Sensors Journal, IEEE*, 2010. 10(9): p. 1519-1526.
94. Jing, H. and T. Vladimirova. *Novel PCA based pixel-level multi-focus image fusion algorithm*. in *Adaptive Hardware and Systems (AHS), 2014 NASA/ESA Conference on*. 2014. IEEE.
95. Ho, K. and P.D. Gader, *A linear prediction land mine detection algorithm for hand held ground penetrating radar*. *IEEE Transactions on Geoscience and Remote Sensing*, 2002. 40(6): p. 1374-1384.
96. Wells III, W.M., et al., *Multi-modal volume registration by maximization of mutual information*. *Medical image analysis*, 1996. 1(1): p. 35-51.
97. Park, S., K. Kim, and K.H. Ko, *Multi-Feature Based Multiple Landmine Detection Using Ground Penetration Radar*. *Radioengineering*, 2014. 23(2).
98. Van Der Merwe, A. and I.J. Gupta, *A novel signal processing technique for clutter reduction in GPR measurements of small, shallow land mines*. *Geoscience and Remote Sensing, IEEE Transactions on*, 2000. 38(6): p. 2627-2637.

99. FOI, et al., *Preliminary version of software tools*, in *Deliverable D4.5.1 D-Box* 2014.
100. Bruschini, C., et al., *Ground penetrating radar and imaging metal detector for antipersonnel mine detection*. *Journal of Applied Geophysics*, 1998. 40(1-3): p. 59-71.
101. Challa, S. and D. Koks, *Bayesian and Dempster-Shafer fusion*. *Sadhana*, 2004. 29(2): p. 145-174.
102. Frigui, H., et al., *An evaluation of several fusion algorithms for anti-tank landmine detection and discrimination*. *Information Fusion*, 2012. 13(2): p. 161-174.
103. Oxenham, M.G., D.J. Kewley, and M.J. Nelson. *Measures of information for multilevel data fusion*. in *Signal Processing, Sensor Fusion, and Target Recognition V*. 1996. International Society for Optics and Photonics.
104. Mahler, R.P. *Unified data fusion: fuzzy logic, evidence, and rules*. in *Signal Processing, Sensor Fusion, and Target Recognition V*. 1996. International Society for Optics and Photonics.
105. Bordoni, F. and A. D'Amico, *Noise in sensors*. *Sensors and Actuators A: Physical*, 1990. 21(1-3): p. 17-24.
106. Kumar, M. and D.P. Garg. *Three-dimensional occupancy grids with the use of vision and proximity sensors in a robotic workcell*. in *ASME 2004 International Mechanical Engineering Congress and Exposition*. 2004. American Society of Mechanical Engineers.
107. Carminati, M., et al., *Real-Time Data Fusion and MEMS Sensors Fault Detection in an Aircraft Emergency Attitude Unit Based on Kalman Filtering*. *Sensors Journal, IEEE*, 2012. 12(10): p. 2984-2992.

108. Hong, Y., *an introduction to Kalman filter*. 2008.
109. Wu, H., et al. *Sensor fusion using Dempster-Shafer theory [for context-aware HCI]*. in *Instrumentation and Measurement Technology Conference, 2002. IMTC/2002. Proceedings of the 19th IEEE*. 2002. IEEE.
110. Milisavljevic, N. and I. Bloch, *Sensor fusion in anti-personnel mine detection using a two-level belief function model*. *IEEE Transactions on Systems, Man, and Cybernetics, Part C (Applications and Reviews)*, 2003. 33(2): p. 269-283.
111. Daniel Bennett, H.J.a.T.V.E.S.a.C.R.G., U.o.L. Department of Engineering, and U.K. Leicester, *Validated Software Tool for Close-in Detection of Landmines*, in *D4.6 in D-Box project report*. 2016.
112. Selesnick, I.W. and C.S. Burrus, *Generalized digital Butterworth filter design*. *IEEE Transactions on signal processing*, 1998. 46(6): p. 1688-1694.
113. Dittmer, J., *explanation about the ERA GPR used in the MsMs dataset*. 2016.
114. Esposito, S., et al., *Experimental Validation of an Active Thermal Landmine Detection Technique*. 2014.
115. Wald, L., *Some terms of reference in data fusion*. *Geoscience and Remote Sensing, IEEE Transactions on*, 1999. 37(3): p. 1190-1193.
116. Hariharan, B., A. Sasidharan, and A.V. Vidyapeetham, *iWEDS—an intelligent explosive detection and terrorist tracking system using wireless sensor network*. *IJCSI*, 2011. 8(4): p. 245-250.
117. Pohl, C. and J.L. Van Genderen, *Review article multisensor image fusion in remote sensing: concepts, methods and applications*. *International journal of remote sensing*, 1998. 19(5): p. 823-854.
118. Varshney, P.K., *Multisensor data fusion*. *Electronics & Communication Engineering Journal*, 1997. 9(6): p. 245-253.

119. Llinas, J. and D.L. Hall. *An introduction to multi-sensor data fusion*. in *Circuits and Systems, 1998. ISCAS'98. Proceedings of the 1998 IEEE International Symposium on*. 1998. IEEE.
120. Bedworth, M. and J. O'Brien, *The Omnibus model: a new model of data fusion?* IEEE Aerospace and Electronic Systems Magazine, 2000. 15(4): p. 30-36.
121. Yu, H. *The Research of Hierarchical Data Fusion Based on Three-tiers Wireless Sensor Networks for Urban Real Time Traffic Information Monitoring*. in *Genetic and Evolutionary Computing (ICGEC), 2010 Fourth International Conference on*. 2010. IEEE.
122. Raol, J.R., *Multi-sensor data fusion with MATLAB®*. 2009: CRC press.
123. Bloch, I., *Information combination operators for data fusion: A comparative review with classification*. Systems, Man and Cybernetics, Part A: Systems and Humans, IEEE Transactions on, 1996. 26(1): p. 52-67.
124. Schreiber-Ehle, S. and B. Seifert, *Geographisches Informations-management fur weltweite Einsatze*. EUROPAISCHE SICHERHEIT, 2002. 51(5): p. 47-48.
125. Luo, R.C., M.-H. Lin, and R.S. Scherp, *Dynamic multi-sensor data fusion system for intelligent robots*. Robotics and Automation, IEEE Journal of, 1988. 4(4): p. 386-396.
126. Yick, J., B. Mukherjee, and D. Ghosal, *Wireless sensor network survey*. Computer networks, 2008. 52(12): p. 2292-2330.